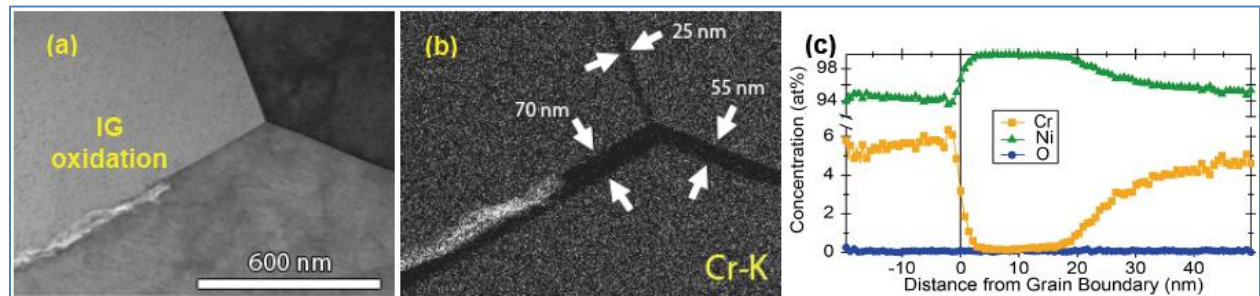
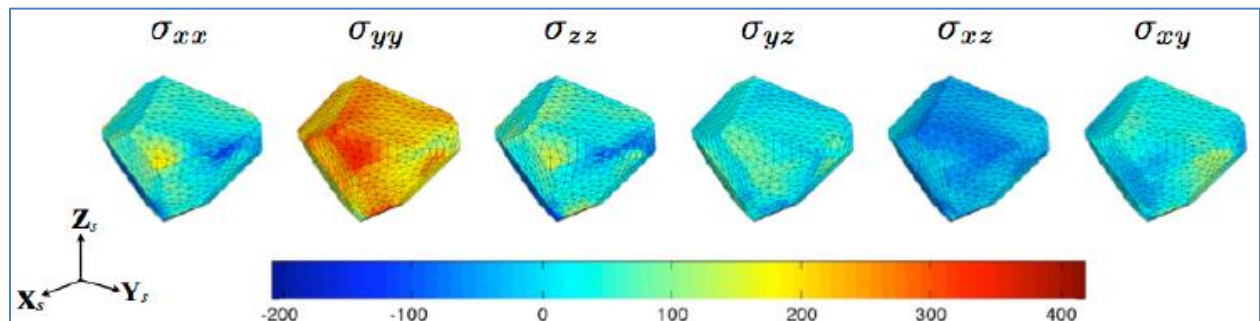
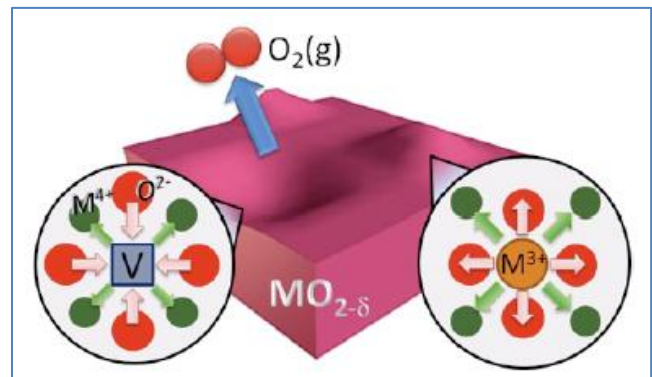
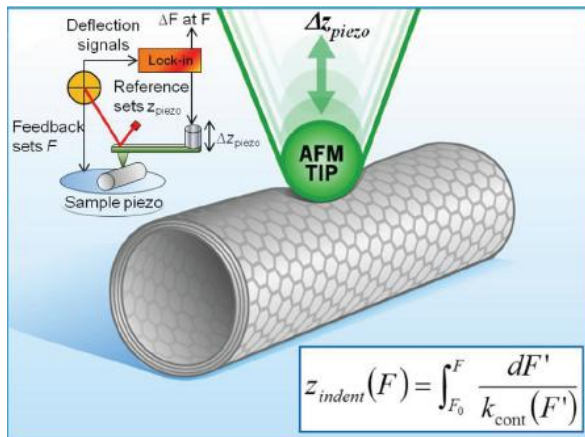


# Mechanical Behavior and Radiation Effects 2013 Principal Investigators Meeting

March 25 - 27, 2013  
Bolger Center, Potomac, MD



U.S. DEPARTMENT OF  
**ENERGY**

Office of  
Science

Materials Sciences and Engineering Division  
Office of Basic Energy Sciences

## Cover

**Top Left:** Cartoon of AFM-based modulated nano-indentation (MoNI) technique used to measure radial elastic properties of BN nanotubes. (Riedo et al., Georgia Tech)

**Top Right:** Schematic of chemical expansion origin – competition of oxygen and cation sublattice relaxations in  $\text{Pr}_x\text{Ce}_{1-x}\text{O}_{2-\delta}$ . (Tuller et al., MIT)

**Middle:** Spatial distribution of the stress components within a target crystal, derived from experiments with a load of 219 MPa. The macroscopic loading direction was “y” and the scale is in MPa. (Miller et al., Cornell)

**Bottom:** TEM and APT analyses of IG oxidation in Ni-5at%Cr: (a) TEM bright-field image of grain boundary oxidation front; (b) TEM - energy dispersive X-ray spectroscopy Cr elemental map showing extensive grain boundary depletion; and (c) APT composition profile across a metallic grain boundary ahead of the oxidation front. (Bruemmer et al., Pacific Northwest National Laboratory)

This document was produced under contract number DE-AC05-06OR23100 between the U.S. Department of Energy and Oak Ridge Associated Universities.

The research grants and contracts described in this document are supported by the U.D. DOE Office of Science, Office of Basic Energy Sciences, Materials Sciences and Engineering Division.

## Foreword

This volume comprises the scientific content of the 2013 Mechanical Behavior and Radiation Effects Principal Investigators (PI) Meeting sponsored by the Division of Materials Sciences and Engineering (DMS&E) in the Office of Basic Energy Sciences (BES) of the U.S. Department of Energy (DOE). The meeting, held on March 25–27 at the Bolger Center, Potomac, Maryland, is the fourth such meeting on this topic and is one among a series of research theme-based PI meetings being held by DMS&E. The meeting’s focus is on research in mechanical behavior and radiation effects of materials, and it also features research that cuts across several other BES core research program areas and Energy Frontier Research Centers where appropriate and relevant.

The studies of mechanical behavior and radiation effects have a long and important history with respect to the generation, transmission, utilization and conservation of energy. It is a tribute to the researchers that they have continued to move the field forward into a number of important areas, as can be seen by the diversity of projects being presented at this meeting. Attendees will note a number of new projects and research directions since the previous meeting, including several new recipients of Early Career Research Program awards and two new projects in “Predictive Theory and Modeling.” These new projects, along with the new ones funded from the “core,” add to the exciting areas of research and cutting-edge techniques that are a hallmark of this program.

The purpose of the Mechanical Behavior and Radiation Effects PI Meeting is to bring together researchers funded by DMS&E in this important area of research on a periodic basis (approximately every three years) in order to facilitate the exchange of new results and research highlights, to nucleate new ideas and collaborations among the participants, and to identify needs of the research community. The meeting will also help DMS&E in assessing the state of the program, identifying new research directions, and recognizing programmatic needs.

I would like to express my sincere thank to all of the attendees for their active participation and for sharing their ideas and new research results. I would also like to express my sincere gratitude to Ms. Teresa Crockett in DMS&E, and Ms. Tammy Click of the Oak Ridge Institute for Science and Education (ORISE) for their dedicated and outstanding work in taking care of all the logistical aspects of the meeting.

John Vetrano  
Program Manager  
Mechanical Behavior and Radiation Effects  
Division of Materials Sciences and Engineering  
Office of Basic Energy Sciences  
U.S. Department of Energy



**Mechanical Behavior and Radiation Effects  
Principal Investigators Meeting  
March 25–27, 2013  
Bolger Center, Potomac, MD**

**Sunday, March 24, 2013**

- 3:00 – 6:00 pm    Registration  
6:00 – 7:00 pm    Reception (No Host, Pony Express Bar & Grill )  
7:00 pm            \*\*\* Dinner (Osgood’s Restaurant – On your own) \*\*\*

**Monday, March 25, 2013**

- 7:00 – 8:00 am    \*\*\* Breakfast \*\*\*  
8:00 – 8:40 am    **Linda Horton**, *Director, Division of Materials Science and Engineering  
Division and Program Updates*  
8:40 – 9:00 am    **John Vetrano**, *Program Manager, Mechanical Behavior and Radiation Effects  
Program Overview*
- Session I**            **Chair: Dan Gianola** (University of Pennsylvania)
- 9:00 – 9:30 am    **Bilge Yildiz**, **Massachusetts Institute of Technology**  
*COFFEI: Chemomechanics of Far-From-Equilibrium Interfaces*  
9:30 – 10:00 am    **William Nix**, **Stanford University**  
*Mechanical Properties of Materials with Nanometer Scale Dimensions and  
Microstructures*  
10:00 – 10:30 am    \*\*\* Break \*\*\*
- Session II**            **Chair: Reiner Dauskardt** (Stanford University)
- 10:30 – 11:00 am    **Jan Schroers**, **Yale University**  
*Using Artificial Microstructures to Understand Microstructure Property  
Relationship-Toughening Mechanisms in Metallic Glass*  
11:00 – 11:30 am    **Ivar Reimanis**, **Colorado School of Mines**  
*Mechanical Behavior in Ceramics with Unusual Thermal-Mechanical Properties*  
11:30 – 12:00 pm    **Rob Ritchie (LBNL)**  
*Lightweight Hybrid Materials*  
12:00 – 1:30 pm    \*\*\* Working Lunch (Scientific Highlights: Discussion and Input from  
Attendees) \*\*\*
- Session III**            **Chair: Qizhen Li** (University of Nevada – Reno)
- 1:30 – 2:00 pm    **Richard LeSar (Ames)**  
*Nanotwinned Materials for Energy Technologies*  
2:00 – 2:30 pm    **Carlos Tomé (LANL)**  
*Stress States Associated with Twin Nucleation and Propagation in Hexagonal  
Materials*

2:30 – 3:00 pm **Samantha Daly, University of Michigan**  
*Deformation and Failure Mechanisms of Shape Memory Alloys*

3:00 – 3:30 pm **\*\* \*Break \*\***

**Session IV** **Chair: Karl Sieradzki** (Arizona State University)

3:30 – 4:00 pm **Gary Was (Michigan)**  
*Localized Deformation and Intergranular Fracture of Irradiated Alloys Under Extreme Environmental Conditions*

4:00 – 4:30 pm **Steve Bruemmer (PNNL)**  
*Crack-Tip Mechanisms Driving Environmental Degradation*

4:30 – 5:30 pm **\*\*\* Break \*\*\***

5:30 – 6:30 pm **\*\*\* Working Dinner (poster introductions ) \*\*\***

6:30 – 9:30 pm **Poster Session I**

## Tuesday, March 26, 2013

7:30 – 8:30 am **\*\*\* Breakfast \*\*\***

**Session V** **Chair: Mitra Taheri** (Drexel University)

8:30 – 9:00 am **Amit Misra (LANL)**  
*High Strength and Deformability of Metal-Ceramic Nanocomposites*

9:00 – 9:30 am **Hussein Zbib (Washington State)**  
*Investigating Deformation and Failure Mechanisms in Nanoscale Multilayer Metallic Composites*

9:30 - 10:00 am **Julia Greer (Cal Tech)**  
*Investigation of Radiation Damage Tolerance in Interface-Containing Metallic Nano Structures*

10:00 – 10:30 am **\*\*\* Break \*\*\***

**Session VI** **Chair: Ryan Ott** (Ames Laboratory)

10:30 – 11:00 am **Kevin Hemker (John Hopkins)**  
*In Situ Characterization of Stress-Coupled Grain Boundary Migration*

11:00 – 11:30 am **Easo George (ORNL)**  
*Multiscale Mechanical Properties and Alloy Design*

11:30 – 12:00 pm **Brad Boyce (SNL)**  
*Nanomechanics and Nanometallurgy of Boundaries*

12:00 – 1:30 pm **\*\*\* Working Lunch (Scientific Highlights: Discussion and Input from Attendees) \*\*\***

**Session VII** **Chair: Lin Shao** (Texas A&M)

1:30 – 2:00 pm **Rod Ewing (Michigan)**  
*Response of Simple, Model Systems to Extreme Conditions*

- 2:00 – 2:30 pm **Ricardo Castro (UC Davis)**  
*Energetics of Radiation Tolerant Nanoceramics*
- 2:30 – 3:00 pm **Bill Weber (ORNL)**  
*Electronic and Atomic Response of Ceramic Structures to Irradiation*
- 3:00 – 3:30 pm **\*\*\* Break \*\*\***
- Session VIII** **Chair: Irene Beyerlein** (Los Alamos National Laboratory)
- 3:30 – 4:00 pm **Carl Boehlert (Michigan State)**  
*Characterization and Modeling of Deformation Induced Damage in Titanium Alloys*
- 4:00 – 4:30 pm **Matt Miller (Cornell)**  
*Understanding Microplasticity Processes Related to Fatigue Damage Using High Energy X-Rays and a Crystal-Based Modeling Formulation*
- 4:30 – 5:30 pm **\*\*\* Break \*\*\***
- 5:30 – 6:30 pm **\*\*\* Dinner (Scientific Highlights of the Day: Discussion and Input from Attendees) \*\*\***
- 6:30 – 9:30 pm **Poster Session II**

### Wednesday, March 27, 2013

- 7:30 – 8:30 am **\*\*\* Breakfast \*\*\***
- Session IX** **Chair: Stephen Foiles** (Sandia National Laboratory)
- 8:30 – 9:00 am **Marisol Koslowski (Purdue)**  
*Plasticity in Ultra-Fine Grained Materials*
- 9:00 – 9:30 am **Mike Miller (ORNL)**  
*Stability of Nanoclusters in Metal Matrices under Extreme Environments*
- 9:30 – 10:00 am **Vasek Vitek (Penn)**  
*Multiscale Modeling of Dislocation Behavior in Non-magnetic Transition Metals and Ferromagnetic Iron*
- 10:00 – 10:30 am **\*\*\* Break \*\*\***
- Session X** **Chair: Ian Baker** (Dartmouth College)
- 10:30 – 11:00 am **Mukul Kumar (LLNL)**  
*Evolution of Grain Boundary Networks in Extreme Radiation Environments*
- 11:00 – 11:30 am **John Allison (Michigan)**  
*Software Center for Predictive Theory and Modeling*
- 11:30 – 12:00 pm **Mike Demkowicz (MIT)**  
*Inferring Grain Boundary Properties from Measurements on Grain Boundary Networks*
- 12:00 – 1:00 pm **\*\*\* Working Lunch (Scientific Highlights of the Day: Discussion and Input from Attendees) \*\*\***
- 1:00 – 1:30 pm Closing Remarks by PM



# Mechanical Behavior and Radiation Effects Principal Investigators Meeting

## Poster Session I

Monday, March 25, 6:30–9:30 pm

- 1.** Materials for Extreme Irradiation Environments  
*Pascal Bellon, University of Illinois – Urbana-Champaign*
- 2.** Crack-Tip Mechanisms During Environmental Degradation  
*Dan Schreiber, Pacific Northwest National Laboratory*
- 3.** Molecular-Reinforced Hybrid Glass Films with Superior Thermo-Mechanical Properties  
*Reiner H. Dauskardt, Stanford University*
- 4.** Modulating Thermal Transport Phenomena in Nanostructures via Elastic Strain at Extreme Limits of Strength  
*Daniel S. Gianola and Brian Piccione, University of Pennsylvania*
- 5.** Effects of High-Dose Irradiation and He on the Microstructure of Nanostructured Ferritic Alloys  
*Chad Parish, Oak Ridge National Laboratory*
- 6.** The Coupling Between Interfacial Charge and Mechanical Deformation at High Temperatures in Ceramics  
*Rishi Raj, University of Colorado – Boulder*
- 7.** Nanomechanics: Elasticity and Friction in Nano-Objects  
*Elisa Riedo, Georgia Tech*
- 8.** Damage-Tolerant Structural Materials  
*Valentina Naglieri and Amy Wat, Lawrence Berkeley National Laboratory*
- 9.** Radiation Responses of Low Dimensional Carbon Systems  
*Lin Shao, Texas A&M*
- 10.** Understanding and Controlling Toughening Mechanisms in Nanotube Reinforced Ceramic Coatings  
*Brian Sheldon, Brown University*
- 11.** Dynamic Fracture in Dealloying Induced Stress Corrosion Cracking  
*Karl Sieradzki, Arizona State*
- 12.** Tunable Hetero-Epitaxial Shape Memory Alloys  
*Alejandro Strachan, Purdue University*

- 13.** Radiation Effects in Nanocrystalline Ceramics: Multi-scale Model and Experiment  
*Izabela Szlufarska, University of Wisconsin*
- 14.** Linking the Correlated Dependence of Grain Boundary Structure and Density to Defect Evolution Mechanisms during Radiation Damage  
*Mitra Taheri, Drexel University*
- 15.** Twin Boundary Serrations: the Controlling Mechanism for Twinning and De-twinning Propagation?  
*Jian Wang, Los Alamos National Laboratory*
- 16.** Chemomechanics of Far-From-Equilibrium Interfaces (COFFEI)  
*Bill Woodford, Massachusetts Institute of Technology*
- 17.** Effects of Electronic and Nuclear Energy Loss: Novel Experimental Approaches  
*Yanwen Zhang, Oak Ridge National Laboratory*
- 18.** EFRC – Center for Materials Science of Nuclear Fuel  
*Anter El-Azab, Idaho National Laboratory*
- 19.** EFRC – Center for Materials at Irradiation and Mechanical Extremes (CMIME)  
*Irene Beyerlein, Los Alamos National Laboratory*

**Mechanical Behavior and Radiation Effects  
Principal Investigators Meeting**

**Poster Session II**

*Tuesday, March 26, 6:30–9:30 pm*

- 1.** DOE Software Innovation Center for Integrated Multi-Scale Modeling of Structural Metals (PRedictive Integrated Structural Materials Science – PRISMS Center)  
*John Allison, University of Michigan*
- 2.** Deformation of Nanostructured Two-Phase B2/L2<sub>1</sub> FeNiMnAl Alloys  
*Ian Baker, Dartmouth University*
- 3.** Nanomechanics and Nanometallurgy of Boundaries  
*Stephen Foiles, Sandia National Laboratories*
- 4.** Multiscale Mechanical Properties and Alloy Design  
*George Pharr and E. P. George, Oak Ridge National Laboratory*
- 5.** Designing Nanoscale Precipitates in Novel Cobalt-based Superalloys to Improve Creep Resistance and Operating Temperature  
*David Dunand, Northwestern University*
- 6.** Evolution of Grain Boundary Networks in Extreme Radiation Environments  
*Mukul Kumar, Lawrence Livermore National Laboratory*
- 7.** Nanotwinned Materials for Energy Technologies  
*Ryan Ott, Ames National Laboratory*
- 8.** Micro-mechanisms and Multiscale Modeling of Cyclic Plastic Deformation of Magnesium Single Crystals  
*Qizhen Li, University of Nevada – Reno*
- 9.** Transformation and Deformation Mechanisms in High Temperature Shape Memory Alloys with Nanoprecipitates  
*Mike Mills, Ohio State University*
- 10.** Development of an Atomistically Informed Interface-Dislocation Dynamics Model for Composite Materials  
*Jian Wang, Los Alamos National Laboratory*
- 11.** Local Morphing, Magneto-mechanical Fatigue and Fracture of Magnetic Shape-Memory Alloy  
*Peter Müllner, Boise State University*

- 12.** Deformed Materials: Towards a Theory of Materials Morphology Dynamics  
*Jim Sethna, Cornell University*
- 13.** Characterization and Modeling of Deformation Induced Damage in Titanium Alloys  
*Chen Zhang, Michigan State University*
- 14.** Response of Simple, Model Systems to Extreme Conditions  
*Maik Lang, University of Michigan*
- 15.** Understanding Microplasticity Processes Related to Fatigue Damage Using High Energy X-rays and a Crystal-Based Modeling Formulation  
*Paul Dawson, Cornell University*
- 16.** The Effect of Temperature, Interfacial Morphology and Chemistry on the Mechanical Behavior of Nanoscale Multilayer Metallic Composites  
*David Bahr, Washington State University*
- 17.** EFRC – Materials Science of Actinides  
*Rod Ewing, University of Notre Dame*
- 18.** EFRC – Energy Frontier Research in Extreme Environments  
*Malcolm Guthrie, Carnegie Institute of Washington*
- 19.** EFRC – Center for Defect Physics  
*Easo George, Oak Ridge National Laboratory*

# ***Table of Contents***



# Table of Contents

<b>Foreword</b> .....	i
<b>Agenda</b> .....	iii
<b>Poster Sessions</b> .....	vii
<b>Abstracts</b>	
<i>DOE Software Innovation Center for Integrated Multi-Scale Modeling of Structural Metals (PRedictive Integrated Structural Materials Science – PRISMS Center)</i>	
<b>John Allison</b> .....	1
<i>Deformation of Nanostructured Two-Phase B2/L2<sub>1</sub> FeNiMnAl Alloys</i>	
<b>I. Baker</b> .....	5
<i>Materials for Extreme Irradiation Environments</i>	
<b>Pascal Bellon</b> .....	9
<i>Characterization and Modeling of Deformation Induced Damage in Titanium Alloys</i>	
<b>Carl J. Boehlert</b> .....	13
<i>Nanomechanics and Nanometallurgy of Boundaries</i>	
<b>B. L. Boyce</b> .....	17
<i>Crack-Tip Mechanisms During Environmental Degradation</i>	
<b>Stephen M. Bruemmer</b> .....	18
<i>Energetics of Radiation Tolerant Nanoceramics</i>	
<b>Ricardo Castro</b> .....	22
<i>Deformation and Failure Mechanisms of Shape Memory Alloys</i>	
<b>Samantha Daly</b> .....	26
<i>Molecular-Reinforced Hybrid Glass Films with Superior Thermo-Mechanical Properties</i>	
<b>Reinhold H. Dauskardt</b> .....	30
<i>Inferring Grain Boundary Properties from Heterogeneous Data</i>	
<b>Michael J. Demkowicz</b> .....	34
<i>Designing Nanoscale Precipitates in Novel Cobalt-Based Superalloys to Improve Creep Resistance and Operating Temperature</i>	
<b>David C. Dunand</b> .....	35

<i>Response of Simple, Model Systems to Extreme Conditions</i> <b>Rodney C. Ewing</b> .....	39
<i>Multiscale Mechanical Properties and Alloy Design</i> <b>E. P. George</b> .....	43
<i>Modulating Thermal Transport Phenomena in Nanostructures via Elastic Strain at Extreme Limits of Strength</i> <b>Daniel S. Gianola</b> .....	47
<i>Investigation of Radiation Damage Tolerance in Interface-Containing Metallic Nanostructures</i> <b>Julia Greer</b> .....	51
<i>In Situ Characterization of Stress-Coupled Grain Boundary Migration</i> <b>Kevin Hemker</b> .....	54
<i>Plastic Strain Recovery in Nanocrystalline Materials</i> <b>Marisol Koslowski</b> .....	58
<i>Evolution of Grain Boundary Networks in Extreme Radiation Environments</i> <b>Mukul Kumar</b> .....	62
<i>Nanotwinned Materials for Energy Technologies</i> <b>Richard LeSar</b> .....	66
<i>Micro-mechanisms and Multiscale Modeling of Cyclic Plastic Deformation of Magnesium Single Crystals</i> <b>Qizhen Li</b> .....	70
<i>Understanding Microplasticity Processes Related to Fatigue Damage Using High Energy X-rays and a Crystal-Based Modeling Formulation</i> <b>Matt Miller</b> .....	74
<i>Formation and Stability of Nanoclusters in a Nanostructured Ferritic Alloy</i> <b>Michael K. Miller</b> .....	78
<i>Transformation and Deformation Mechanisms in High Temperature Shape Memory Alloys with Nanoprecipitates</i> <b>M. J. Mills</b> .....	82
<i>Deformation Physics of Ultra-fine Scale Materials</i> <b>Amit Misra</b> .....	86

<i>Local Morphing, Magneto-mechanical Fatigue and Fracture of Magnetic Shape-Memory Alloys</i> <b>Peter Müllner</b> .....	90
<i>Mechanical Properties of Materials with Nanometer Scale Microstructures</i> <b>William D. Nix</b> .....	94
<i>The Coupling Between Interfacial Charge and Mechanical Deformation at High Temperatures in Ceramics</i> <b>Rishi Raj</b> .....	98
<i>Mechanical Behavior in Ceramics with Unusual Thermal-Mechanical Properties</i> <b>Ivar Reimanis</b> .....	102
<i>Nanomechanics: Elasticity and Friction in Nano-Objects</i> <b>Elisa Riedo</b> .....	106
<i>Damage-Tolerant Structural Materials</i> <b>Robert O. Ritchie</b> .....	110
<i>Using Artificial Microstructures to Understand Microstructure-Property Relationships in Metallic Glasses</i> <b>Jan Schroers</b> .....	114
<i>Deformed Materials: Towards a Theory of Materials Morphology Dynamics</i> <b>James P. Sethna</b> .....	115
<i>Radiation Responses of Low Dimensional Carbon Systems</i> <b>Lin Shao</b> .....	119
<i>Understanding and Controlling Toughening Mechanisms in Nanotube Reinforced Ceramic Coatings</i> <b>Brian W. Sheldon</b> .....	123
<i>Dynamic Fracture in Dealloying Induced Stress Corrosion Cracking</i> <b>Karl Sieradzki</b> .....	127
<i>Tunable Hetero-Epitaxial Shape Memory Alloys</i> <b>Alejandro Strachan</b> .....	131
<i>Radiation Effects in Nanocrystalline Ceramics: Multi-scale Model and Experiment</i> <b>Izabela Szlufarska</b> .....	135
<i>Linking the Correlated Dependence of Grain Boundary Structure and Density to Defect Evolution Mechanisms during Radiation Damage</i> <b>Mitra Taheri</b> .....	139

<i>Stress States Associated with Twin Nucleation and Propagation in HCP Materials</i> <b>Carlos N. Tomé</b> .....	143
<i>Chemomechanics of Far-From-Equilibrium Interfaces (COFFEI)</i> <b>Harry L. Tuller</b> .....	147
<i>Combined Atomistic and Mesoscopic Study of Deformation of Body-Centered-Cubic Transition Metals: Effects of Alloying and Magnetism</i> <b>V. Vitek</b> .....	151
<i>Localized Deformation and Intergranular Fracture of Irradiated Alloys Under Extreme Environmental Conditions</i> <b>Gary S. Was</b> .....	155
<i>Electronic and Atomic Response of Ceramic Structures to Irradiation</i> <b>William J. Weber</b> .....	159
<i>Investigating Deformation and Failure Mechanisms in Nanoscale Multilayer Metallic Composites</i> <b>H. M. Zbib</b> .....	163
<b>EFRC Abstracts</b>	
<i>EFRC Center for Materials Science of Nuclear Fuel</i> <b>Todd Allen</b> .....	167
<i>EFree – An Energy Research Frontier Center</i> <b>H-k Mao</b> .....	171
<i>Center for Materials at Irradiation and Mechanical Extremes (CMIME), an Energy Frontier Research Center</i> <b>Amit Misra</b> .....	172
<b>Author Index</b> .....	173
<b>Participant List</b> .....	175

# ***Abstracts***



## **DOE Software Innovation Center for Integrated Multi-Scale Modeling of Structural Metals (PRredictive Integrated Structural Materials Science – PRISMS Center)**

### **John Allison, Principal Investigator**

HH Dow Building  
2300 Hayward Street  
Ann Arbor, MI 48109-2136  
johnea@umich.edu

### **PROGRAM SCOPE**

The overarching goal is to establish a unique scientific platform that will enable accelerated predictive materials science. This will be accomplished by completing the following objectives:

1. Develop and establish PRISMS (Predictive Integrated Structural Materials Science), a suite of integrated multi-scale computational tools for predicting the microstructural evolution and mechanical behavior of structural metals. This software suite will be open-source/open-executable, extensible, user friendly and efficient.
2. Develop advanced, open source/open executable computational methods for metallic materials.
3. Tightly couple the computational methods with advanced experimental methods for determining model inputs, filling gaps in theory and for validation.
4. Demonstrate this integrated capability by making major advances in the quantitative and predictive understanding of magnesium alloys, in particular the phenomena of:
  - complex, microstructure-dependent deformation processes of magnesium alloys;
  - fatigue, ductility, and stress-strain response of structural metals;
  - theory of microstructure evolution and its effect on fatigue and ductility.
5. Develop and deploy “The Materials Commons,” a knowledge repository and virtual collaboration space for curating, archiving and disseminating information from experiments and computations as well as providing a collaborative platform for development of open-source code with active involvement of a broader PRISMS open source community.

The center will establish systematic protocols for extension of this integrated multi-scale computational capability to the development of predictive capabilities for other structural materials and to incorporate emerging modeling and experimental methods.

The faculty involved in the PRISMS Center are: John Allison, Center Director and professor of materials science and engineering, Samantha Daly, assistant professor of mechanical engineering; Krishna Garikipati, professor of mechanical engineering; Vikram Gavini, assistant professor of mechanical engineering; Margaret Hedstrom, professor and associate dean for academic programs at the School of Information; H. V. Jagadish, the Bernard A. Galler Collegiate Professor of electrical engineering and computer science; J. Wayne Jones, professor

of materials science and engineering; Emmanuelle Marquis, assistant professor of materials science and engineering; Veera Sundararaghavan, assistant professor of aerospace engineering; Katsuyo Thornton, associate professor of materials science and engineering; and Anton Van der Ven, associate professor of materials science and engineering.

### **PROGRAM MOTIVATION:**

The materials field has benefited significantly from major advances in the understanding of materials behavior enabled by the development and application of computational methods. However these advances have not translated into a reduction in the time required to develop new materials. The Materials Genome Initiative (MGI) has established the acceleration of the process of materials discovery and development as a major national need. Progress toward the goal of accelerating new product development has been made by practitioners of the new field of Integrated Computational Materials Engineering (ICME), however, this progress has been limited to ad-hoc, “brute force” efforts conducted by large industrial teams [Allison 2006, Backman 2006]. These efforts have produced significant economic value by accelerating the pace of new product development and new materials development [Pollock 2008]. While the long range goal of making the materials field more computationally oriented and holistic has been well articulated [Pollock 2008], to date, there is no coherent, generally accepted framework or protocol for capturing materials information to make it available to scientists for developing new theoretical understandings or to engineers for use in engineering design. A key motivation of the PRISMS Center is the establishment of PRISMS as a core and widely adopted scientific software (and associated experiments and protocols) that forms a common basis for rapid insertion of science into the growing field of ICME.

The planned PRISMS computational tools will be general in nature and applicable to prediction of a wide-range of phenomena in structural metals, complex ceramics and semiconductor compounds. In this program, to provide focus, we will specifically target two major scientific challenges, namely predicting the role of alloy composition and microstructure on a) ductility and b) fatigue. The materials field abounds with long-standing scientific and technological challenges such as these that are characterized by phenomenology and qualitative understanding and limited predictive theory. Our bold goal is to provide a step change in the predictive and quantitative understanding of ductility and fatigue and a solid and systematic framework for future advances. We will do this by focusing the attention of this large integrated team with the required theoretical, computational and experimental expertise, coupled with the integrated multi-scale modeling capability. To achieve this goal, we must also significantly improve the predictive and quantitative understanding of microstructural evolution, in particular recrystallization, grain growth and precipitate evolution and the influence of microstructure on monotonic stress-strain response. While these phenomena have better established theoretical frameworks, quantitative prediction of these processes is lacking and requires significant and non-systematic empirical “calibration”. In this program we will develop systematic methods for replacing these empirical calibrations with the results of the multi-scale models and targeted

quantitative experiments. We will develop and validate our integrated predictive capability for magnesium and its alloys, which will serve as a prototype materials system for demonstrating the capability of PRISMS and the scientific advances it will enable.

Magnesium presents an important test case for accelerated material development. Relative to other structural metals, the development of commercial magnesium alloys and our understanding of magnesium alloy physical metallurgy are relatively immature. While modern alloys of aluminum and nickel can have five to ten alloying elements, Mg alloys have remained simple and are typically based on only two or three alloying additions, such as Al and Zn or Al and Mn. Magnesium alloys also have significant potential for reducing the weight of automobiles and other transportation systems – and thus for improving fuel economy and reducing emissions. Many of the potential applications for magnesium require significant improvements in strength, ductility and fatigue resistance. Adoption of an ICME or "Materials by Design" approach for rapid development and insertion of new magnesium alloys into the transportation industry is a major Materials Genome Initiative opportunity. However it is one that will require quantitative predictive theories and models for these key properties. This will become a central focus of the PRISMS Center.

A critical challenge for the materials community continues to be the integration of knowledge from a wide variety of sources into knowledge repositories that are open to the broad technical community. Such knowledge repositories are becoming increasingly essential for disseminating, validating and archiving the results of scientific investigations – and, importantly, for collaborating and expanding our scientific horizons. While fields as far ranging as biology, astronomy, climate change and earthquake science have embraced this concept, the materials field has lagged behind. This limits the ready access to the latest results of scientific endeavors, including details of experiments and models and leads to the costly and time consuming development of redundant information. We suggest that this shortcoming has limited scientific advances in the materials field. Thus we seek to develop and deploy “The Materials Commons” as a site that not only provides the software and results of this investigation, but also, importantly, establishes a broader collaborative community for open source code development and data sharing for the structural materials community. A key metric of success will be the degree to which other researchers access and utilize the software tools and digital data, both experimental and computational, developed in this program.

### **2012-2013 HIGHLIGHTS**

The program was awarded in September 2012. Since that time, the Center has fired four senior staff members and we are well along in hiring a five junior staff member. Six graduate students and two post-docs have recently joined the program. The faculty and senior staff meet weekly to refine the scientific and software development program plan, as well as define initial use cases. Initial use cases for the PRISMS computational/experimental tools have been defined and developments are underway. High performance computation and knowledge repository facilities

have been procured and installed. A new scanning electron microscopy facility for in-situ tensile and high cycle fatigue studies has been ordered.

## REFERENCES

- Allison 2006. Allison, J. E., Li, M., Wolverton, C. and Su, X-M, "Virtual Aluminum Castings: An Industrial Application of ICME," JOM, The Mineral, Metals and Materials Society, Warrendale, PA, November 2006, p 28.
- Backman 2006 Backman, D. G., Wei, D. Y., Whitis, D. D., Buczek, M. B., Finnigan, P. M. and Gao, D., "ICME at GE: Accelerating the Insertion of New Materials and Processes," JOM, 58, 2006, p. 36.
- Pollock 2008 Pollock, T. M., Allison, J. E., Backman, D. G., Boyce, M. C., Gersh, M., Holm, E. A., LeSar, R., Long, M., Powell, IV, A. C., Schirra, J. J., Whitis, D. D., Woodward, C., "Integrated Computational Materials Engineering: A Transformational Discipline for Improved Competitiveness and National Security," The National Academies Press, 500 Fifth Street, N.W. Washington, DC 20001, 2008.

# Deformation of Nanostructured Two-Phase B2/L2<sub>1</sub> FeNiMnAl Alloys

I. Baker,

Thayer School of Engineering, Dartmouth College, Hanover, NH 03755-8000, USA

[ian.baker@dartmouth.edu](mailto:ian.baker@dartmouth.edu)

## Program Scope

There were four parts to the proposed work. First, we produced different microstructures in Fe<sub>30</sub>Ni<sub>20</sub>Mn<sub>20</sub>Al<sub>30</sub>: an initial as-cast, ultrafine, B2/L2<sub>1</sub> microstructure, and then a variety of coarser microstructures produced by annealing.

Second, we characterized the resulting microstructures. Some specific questions that we were attempting to answer are: do the phases lose coherency upon ageing as the size of the particles increases? How does the matrix/particle interface dislocation structure depend on the particle size? How does the degree of order of the two phases vary with temperature? Do the compositions of the particles and matrix change upon coarsening?

Third, we determined how the strength depends on both temperature and strain rate for each of different microstructures.

Fourth, we determined the deformation mechanisms for a variety of temperatures and strain rates for different microstructures. In particular, we determined the slip systems that operate in the B2 and in the L2<sub>1</sub> phase, including determining if these depend on temperature and strain rate. We will also determine how the interface dislocation structure depends on the testing temperature and strain rate.

## Recent Progress

The microstructures of Fe<sub>30</sub>Ni<sub>20</sub>Mn<sub>20</sub>Al<sub>30</sub> in both the as-cast condition and after annealing at 823 K for various times up to 72 h were characterized using a transmission electron microscope (TEM) (**Figure 1**), a scanning transmission electron microscope equipped with a high angle annular dark field detector and an energy dispersive spectrometer, synchrotron-based X-ray diffraction, and atom probe tomography (**Figure 2**). The microstructures exhibited a basket weave morphology of (Mn, Fe)-rich B2-ordered (ordered b.c.c.) and (Ni, Al)-rich L2<sub>1</sub>-ordered (Heusler-type) phases with a lattice misfit of only 0.85% and interfaces roughly, but not exactly, aligned along <100>. The phase width increased from 5 nm for the as-cast alloy to 25 nm for material annealed for 72 h at 823 K, with no change in the elemental partitioning between the phases. Interestingly, no interfacial dislocations were produced as the phase width increased and a very low exponent (0.19) for the time dependence of the coarsening was observed. Using both differential scanning calorimetry and *in-situ* heating in a TEM, an L2<sub>1</sub>-to-B2 was found at 750 ± 25 K. The mechanical properties of the alloy were characterized in various annealed states. Surprisingly, it was found that the room temperature hardness was largely independent of the phase width (**Figure 3**).

The temperature dependence of the compressive strength of Fe<sub>30</sub>Ni<sub>20</sub>Mn<sub>20</sub>Al<sub>30</sub> showed three distinct regions (**Figure 4a**): 1) brittle fracture at low temperature, 2) plastic flow with a rapid decline in yield strength from 1500 MPa to 250 MPa from the brittle-to-ductile transition temperature (BDTT) to 873 K, and 3) a slight decrease in yield strength to ~150 MPa from 873 K to 1073 K. Interestingly, the BDTT (573 K) exhibited by the coarser microstructure in the 72 h annealed material was lower than that of the as-cast alloy (623 K). Interestingly, wear tests showed that the coarser alloy showed less wear than the fine as-cast alloy. A mixture of intergranular fracture and transgranular cleavage was observed after room temperature compression while only cleavage was found at 673 K. All the specimens deformed extensively without fracture when tested at temperatures higher than 673 K. The strain rate had little effect on the strength at 573 K and a moderate effect at 873 K with a strain-rate sensitivity exponent value of 0.1 (**Figure 4b**).

Dislocation analyses showed that deformation was by <100> slip (**Figure 5**), which provides only three independent slip systems, hence explaining the poor low temperature ductility.

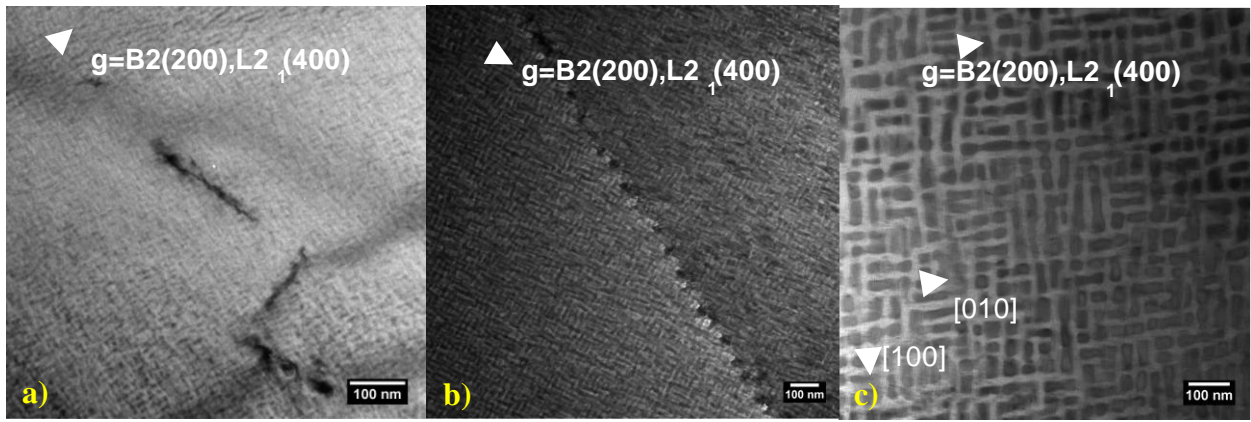


Figure 1. BF TEM images of  $Fe_{30}Ni_{20}Mn_{20}Al_{30}$ : (a) as-cast, (b) after a 30 min anneal at 823 K, and (c) after a 72 h anneal at 823 K.

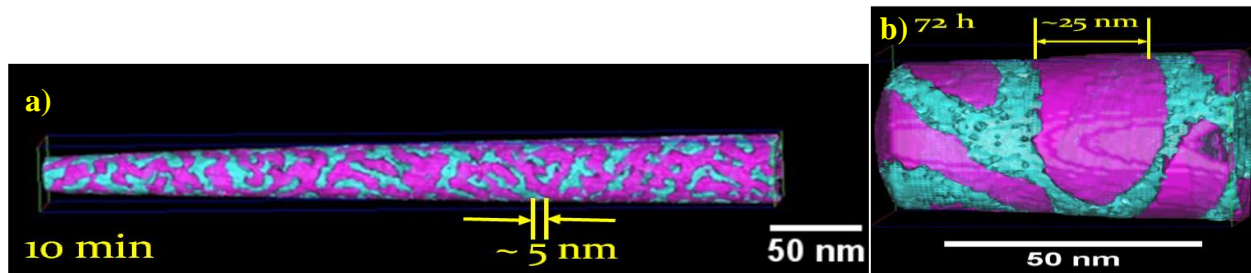


Figure 2. LEAP iso-concentration surfaces of  $Fe_{30}Ni_{20}Mn_{20}Al_{30}$  annealed for (a) 10 min and (b) 72 h at 823 K. The mauve phase has >30 at. % Fe, while the blue phase has >30 at. % Al.

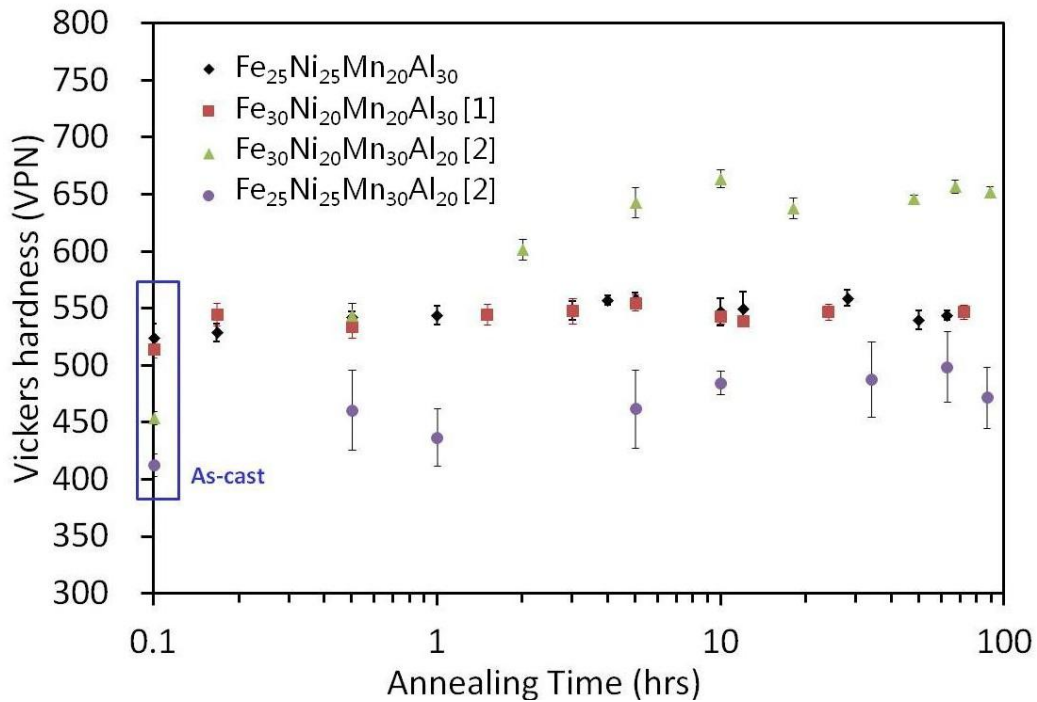


Figure 3. Room temperature hardness as a function of annealing time (log. scale) at 823 K for  $Fe_{25}Ni_{25}Mn_{20}Al_{30}$ ,  $Fe_{30}Ni_{20}Mn_{20}Al_{30}$  [1],  $Fe_{30}Ni_{20}Mn_{30}Al_{20}$  [2] and  $Fe_{25}Ni_{25}Mn_{30}Al_{20}$  [2].

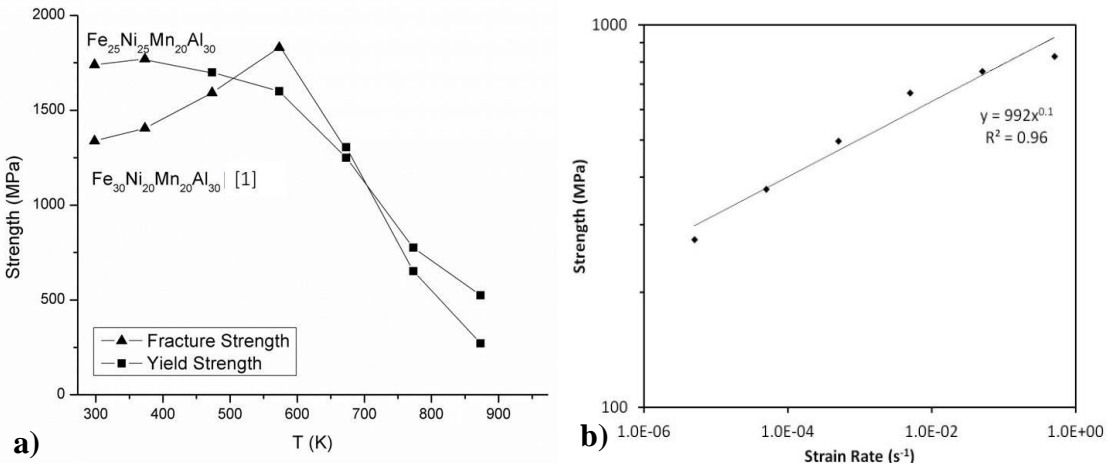


Figure 4. (a) Strength vs. temperature for  $Fe_{25}Ni_{25}Mn_{20}Al_{30}$  and  $Fe_{30}Ni_{20}Mn_{20}Al_{30}$  [1], (b) strain rate dependence of  $Fe_{30}Ni_{20}Mn_{20}Al_{30}$  at 873 K, showing that the strain-rate sensitivity is  $\sim 0.1$ .

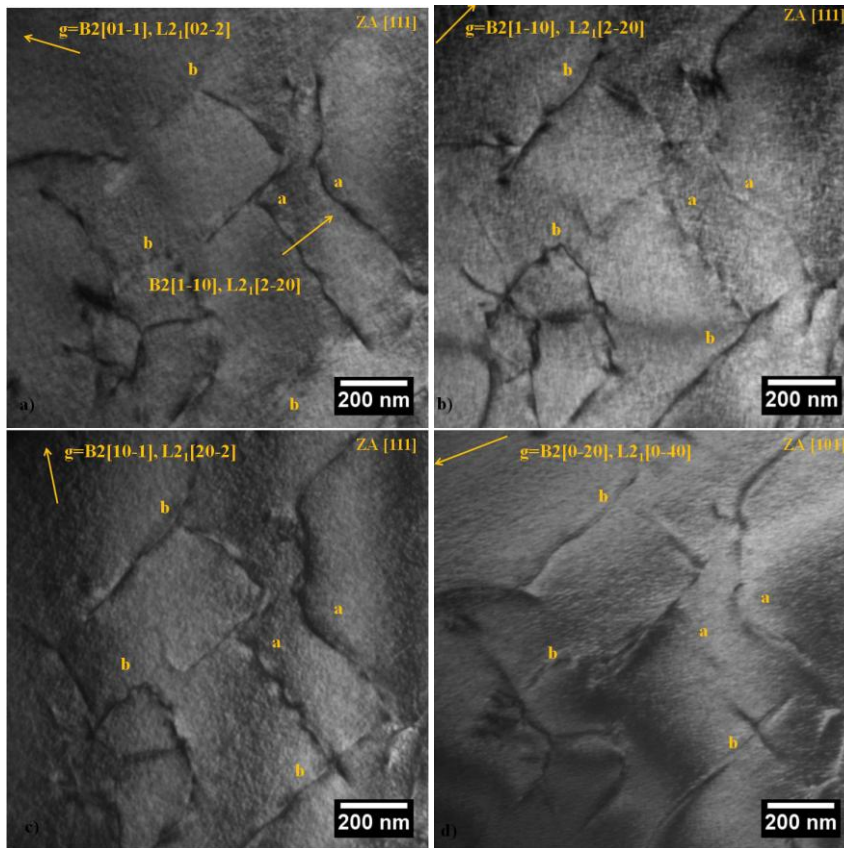


Figure 5. BF TEM micrographs of  $Fe_{30}Ni_{20}Mn_{20}Al_{30}$  annealed for 72 h at 823 K and subsequently strained at 873 K showing dislocations under different two-beam conditions. Details of the analysis are given in the text. The Burgers vectors are all  $\langle 001 \rangle$ .

### Future Plans

1) The greater ductility observed in the coarser  $Fe_{30}Ni_{20}Mn_{20}Al_{30}$  is being investigated further using micropillar compression tests on material with a 5 nm phase width and material with a 25 nm phase width. 2) We have determined the lattice mismatch between the B2 and  $L2_1$  phases in  $Fe_{30}Ni_{20}Mn_{20}Al_{30}$  using synchrotron-based X-ray diffraction. We are performing similar X-ray diffraction measurements to determine the lattice mismatch between the B2 and  $L2_1$  phases in the related alloys  $Fe_{25}Ni_{25}Mn_{20}Al_{30}$  and  $Fe_{35}Ni_{15}Mn_{25}Al_{25}$  and between the B2 and b.c.c. phases in  $Fe_{30}Ni_{20}Mn_{25}Al_{25}$ . 3) In earlier work, we determined the slip dislocations in B2/b.c.c.  $Fe_{30}Ni_{20}Mn_{25}Al_{25}$  ( $a/2\langle 110 \rangle$  pairs) and in the work described here we determined the slip

dislocations in B2/L2<sub>1</sub>-structured Fe<sub>30</sub>Ni<sub>20</sub>Mn<sub>20</sub>Al<sub>30</sub> (a<100>). We are currently determining the slip vectors of the gliding dislocations in B2/L2<sub>1</sub>-structured Fe<sub>25</sub>Ni<sub>25</sub>Mn<sub>20</sub>Al<sub>30</sub> and Fe<sub>35</sub>Ni<sub>15</sub>Mn<sub>25</sub>Al<sub>25</sub>. We are also performing TEM in-situ straining studies on these alloys. 4) We are also performing TEM in situ annealing studies on Fe<sub>30</sub>Ni<sub>20</sub>Mn<sub>20</sub>Al<sub>30</sub> in an attempt to discover the origin of the low time dependence exponent (0.19) observed during the coarsening of the phases in this alloy.

### Participants/Collaborators

X. Wu, *Dartmouth College*

H. Wu, Y. Liu, J. Qiu; *State Key Laboratory of Powder Metallurgy, Central South University, Changsha 410083, P.R.C.*

M. K. Miller, K. L. More; *Materials Science and Technology Division, Oak Ridge National Laboratory, Oak Ridge, TN 37831, USA*

P.R. Munroe; *Electron Microscope Unit, University of New South Wales, Sydney, NSW 2052, Australia*

Z. Cai, S. Chen; *X-ray Science Division, Advanced Photon Source, Argonne National Laboratory, Argonne, IL 60439, USA*

### Publications

1. I. Baker, Y. Liao, X. Wu, H. Wu, M. K. Miller, K. F. Russell and P.R. Munroe, "An Overview of the Microstructures of High-Strength Two-Phase Near-Equiatomic FeNiMnAl Alloys", Proc. 139<sup>th</sup> Annual Meeting & Exhibition, Supplemental Proceedings, Volume 3, 2010.
2. I. Baker, H. Wu, X. Wu, M. K. Miller and P. R. Munroe, "The Microstructure of Near-Equiatomic B2/f.c.c. FeNiMnAl Alloys", *Materials Characterization*, 62 (2011) 952-958.
3. I. M. Robertson, C.A. Schuh, J.S. Vetrano, N. D. Browning, D. P. Field, D. Juul Jensen, M. K. Miller, I. Baker, D. C. Dunand, R. Dunin-Borkowski, B. Kabius, T. Kelly, S. Lozano-Perez, A. Misra, G.S. Rohrer, A.D. Rollett, M. Taheri, G. B. Thompson, M. Uchic, X.-L. Wang, G. Was, "Towards an Integrated Materials Characterization Toolbox", *Journal of Materials Research*, 26 (2011) 1341-1383.
4. I. Baker, "Some Unusual Aspects of the deformation of FeAl", proceedings of the David Pope Honorary Symposium on Fundamentals of deformation and Fracture of Advanced Metallic Materials, 2011 TMS Annual Meeting, Feb. 27<sup>th</sup> - March 3<sup>rd</sup>, 2011, San Diego, CA.
5. X. Wu, I. Baker and P. R. Munroe, "Dry sliding wear of nanostructured Fe<sub>30</sub>Ni<sub>20</sub>Mn<sub>20</sub>Al<sub>30</sub>", *Intermetallics*, 23 (2012) 116-127.
6. H. Wu, I. Baker, Y. Liu and X. Wu, "Dry sliding tribological behavior of a Zr-based bulk metallic glass", *Transactions of Nonferrous Metals Society of China*, 22 (2012) 585-589.
7. X. Wu, I. Baker, H. Wu, M. K. Miller, K. L. More and H. Bei, "Microstructure and Mechanical Behavior of Directionally-Solidified Fe<sub>35</sub>Ni<sub>15</sub>Mn<sub>25</sub>Al<sub>25</sub>" *Intermetallics*, 32 (2013) 413-422.
8. H. Wu, I. Baker, Y. Liu, X. Wu and P. R. Munroe, "Effects of environment on the sliding tribological behaviors of Zr-based bulk metallic glass", *Intermetallics*, 25 (2012) 115-25.
9. H. Wu, I. Baker, Y. Liu, X. Wu, P. R. Munroe and J. Zhang, "Tribological Studies of Zr-based Bulk Metallic Glass", *Intermetallics*, 35 (2013) 25-32.
10. X. Wu and I. Baker, "Dislocations in Nanostructured Two-Phase Fe<sub>30</sub>Ni<sub>20</sub>Mn<sub>20</sub>Al<sub>30</sub>", *Microscopy Research and Technique*, in press. DOI: 10.1002/jemt.22162
11. X. Wu, F. Meng, I. Baker and P. R. Munroe, "A Comparison of Dry Sliding Wear in Two FeNiMnAl Alloys", *Proceedings of the Materials Research Society*, in press.
12. X. Wu, I. Baker and H Wu, "The Mechanical Properties of Near-equiatomic B2/f.c.c. FeNiMnAl Alloys", *Proceedings of the Materials Research Society*, in press.
13. X. Wu, I. Baker, H. Wu and P. R. Munroe, "Mechanical Milling of B2/L2<sub>1</sub> Two-Phase Fe<sub>30</sub>Ni<sub>20</sub>Mn<sub>20</sub>Al<sub>30</sub>", *Journal of Alloys and Compounds*, in press.
14. X. Wu, I. Baker, H. Wu, M. K. Miller, K. L. More, Z. Cai and S. Chen, "Microstructure and Mechanical Properties of Two-Phase Fe<sub>30</sub>Ni<sub>20</sub>Mn<sub>20</sub>Al<sub>30</sub> Alloy", submitted to *Journal of Materials Science*.

# Materials for Extreme Irradiation Environments

Pascal Bellon, Robert Averback, Shen Dillon, William King, Dallas Trinkle

Frederick Seitz Materials Research Laboratory, University of Illinois  
104 S. Goodwin Av. Urbana, IL 61801

Phone: (217) 265-0284, e-mail: bellon@illinois.edu

## Program Scope

It has long been recognized that nanostructured materials should be highly resistant to radiation damage owing to a large density of interfaces that trap point defects and He atoms. The problem with this approach, however, has been that these materials are not usually stable under irradiation, thus limiting their overall viability for general application. In this cluster we are exploring a novel approach to overcome this problem by investigating nanostructures that are induced by the irradiation itself, and thus stable by design. As illustrated below, through appropriate alloying with one or several solute elements, we gain control of the phase stability of these nanostructures, and can begin exploring strategies for improving their properties, such as dimensional stability, ductility and strength. A vital part of this research is the development of novel experimental methods for characterizing nanostructured materials and performing *in situ* mechanical properties tests on miniaturized specimens during elevated temperature irradiation. These experiments are employed to validate and guide our multiscale modeling efforts.

## Recent Progress

### A. Irradiation-induced nanostructuring in Cu-base alloy systems

We have continued our studies on Cu-base model alloy systems since Cu forms many immiscible alloys with varying degrees of miscibility and solute diffusivity. This affords us great flexibility in controlling driving forces and kinetics of nanoprecipitation under irradiation.

#### *A.1. Nanoscale characterization of irradiation-induced nanostructuring in Cu-Fe and Cu-V*

**Averback** and **Bellon** have nearly completed a systematic study of the evolution of Cu-Fe and Cu-V thin films under irradiation [1]. The results confirm that in these moderately immiscible systems, stationary nanostructured states can be achieved by irradiation. Furthermore, using atom probe tomography, a novel precipitation morphology has been identified in these alloys under irradiation, where solute-rich precipitates enclose Cu-rich inner precipitates, resulting in a “cherry-pit” structure, as shown in Fig. 1a. This novel morphology, which we have succeeded in reproducing in atomistic computer simulations, is a

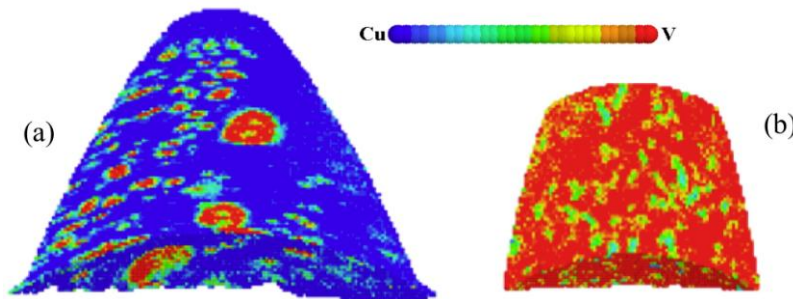


Fig. 1: Atom probe reconstruction maps of patterning induced by 1.8 MeV Kr irradiated with  $3 \times 10^{16}$  ions/cm<sup>2</sup> at 450°C in Cu-V: (a) Cu<sub>90</sub>V<sub>10</sub> (note pits inside some precipitates); (b) Cu<sub>10</sub>V<sub>90</sub>. Diameter of left tip base is 80 nm.

clear signature of the nonequilibrium character of the nanostructuring induced by irradiation, and it is consistent with the fact that irradiation induces patterning for dilute compositions on the Cu poor, as well Cu rich, side of that phase diagram, e.g. for Cu<sub>90</sub>V<sub>10</sub> and Cu<sub>10</sub>V<sub>90</sub> as illustrated in Fig. 1b.

#### *A.2. Nanostructuring in Cu-base ternary alloys*

**Averback** and **Bellon** have also explored nanostructuring in ternary alloys such as Cu-Nb-W. This work reveals that the interplay between precipitation driving force and kinetics can lead to a bimodal precipitate

size distribution. Analysis of these nanostructures combined with atomistic kinetic Monte Carlo simulations suggest that the larger, Nb-rich precipitates formed first, and then undergo partial dissolution when W later precipitates [2]. This precipitation sequence leads to remarkable stability during annealing at temperatures as high as  $0.8 T/T_M$ , and during irradiation to doses as high as  $\approx 100$  dpa.

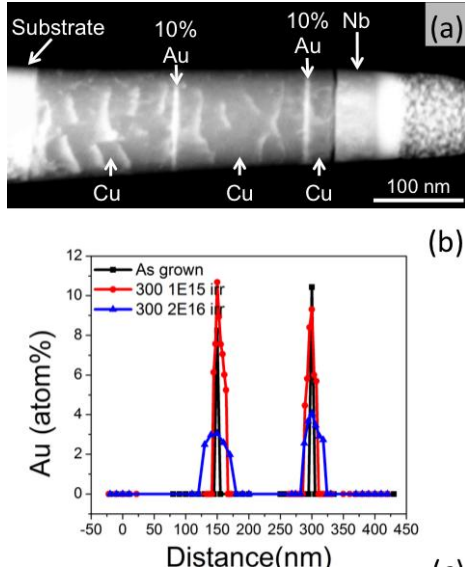


Fig. 2: (a) a DF-STEM image of a Cu-Nb multilayer sample with Au markers in the Cu, and complimentary EDS line scans associated with (b) the broadening of the Au marker.

### A.3. Quantitative evaluation of interface sink strength

A critical element in designing radiation-resistant materials via nanostructuring is the efficiency of interfaces for absorbing point defects. Evaluations of sink strengths, however, has remained qualitative, for instance based on the presence or absence of dislocation loops in the grains. **Dillon** and **Averback** have designed experiments that will enable a quantitative assessment of interface sink strength via diffusion measurements.

In this first experiment, tailored thin film samples are grown by PVD, with a 10 at.% Au marker layer embedded in Cu, and positioned at a variable distance from one or two Cu/Nb interfaces. The experiments track the broadening of the marker layer, as well as the evolution of the Cu/Nb interface after ion irradiations. The rate of broadening of the marker at a particular temperature and dose correlates with the local vacancy concentration. By sampling multiple positions, the vacancy gradient perpendicular to the interface may be deduced and fit by appropriate models. This work is ongoing. Fig. 2a depicts the model microstructure after  $1 \times 10^{15}$   $\text{cm}^2/\text{s}$  irradiation with 1.8 MeV  $\text{Kr}^+$  as observed by dark-field scanning transmission electron microscopy (DF-STEM). By

alloying the Nb layers with miscible BCC elements of different lattice parameter, we intend to extend this approach to characterizing the role of interfacial strain in affecting vacancy sink efficiency.

## B. Radiation-induced creep and hardness of Cu-W, Cu-Nb, and Cu-Fe nanostructures

### B.1. In-situ investigation of radiation-induced creep

**Averback** and **Bellon** have started to investigate the mechanical properties of the model nanostructures presented in Section A, with an emphasis on developing techniques allowing for in-situ measurements. Of particular importance is the creep resistance of these materials, owing to their small grain size. Current understanding suggests that dislocations are unstable in nanocrystalline materials, and therefore irradiation-induced creep (IIC) should be negligible in these materials. We modified a bulge test technique on free-standing thin films to measure creep in nanograined and nanostructured Cu-W alloys during irradiation at elevated temperature [3,4]. Some of the results of these studies are shown in Fig 3. First we observe that the steady state creep rate increases linearly with applied stress, suggesting that the creep is, in fact, due to grain boundary mechanisms, not dislocations. We found that the creep becomes constant above  $200^\circ\text{C}$ . Analysis shows that the nanocrystalline alloy enters the sink-limited regime at this temperature and all defects annihilate in the grain boundaries. These results thus indicate that contrary to current understanding IIC can indeed occur by GB diffusion mechanisms. The creep rate, however, is notably smaller than in polycrystalline alloys where dislocation processes dominate.

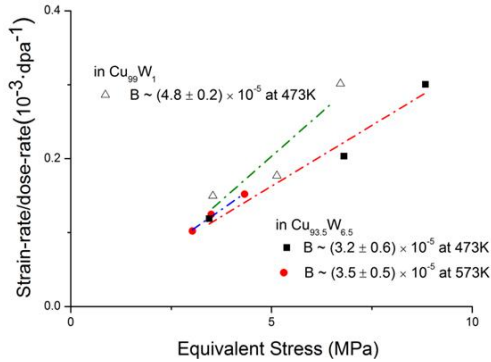


Fig. 3 Dependence of strain rate/dose rate on the (von Mises) equivalent uniaxial stress in  $\text{Cu}_{93.5}\text{W}_{6.5}$  and  $\text{Cu}_{99}\text{W}_1$ . Creep compliance,  $B$ , is provided [3].

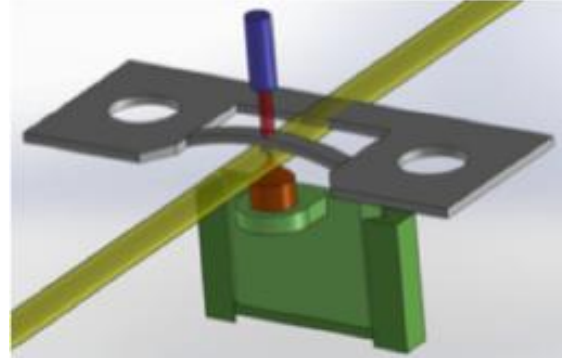


Fig. 4. Design for a novel in-situ nanomechanical testing, during irradiation of nanopillars at variable temperatures.

A limitation of the present bulge test is its requirement of thin-film specimens, thus precluding studies on bulk alloys. **King** and **Averback** plan to overcome this significant limitation by developing a novel in-situ apparatus that will measure creep of nano-pillars, as a function of temperature and radiation dose. Such samples can be cut from bulk alloys (for example prepared by severe plastic deformation) using established focused ion beam methods. Fig. 4 shows our design of the test apparatus.

### B.2 Modeling Radiation-induced creep in nanocrystalline Cu.

A new mechanism of irradiation-enhanced creep was revealed for nanocrystalline materials that explains the experimental results described in the previous section. The creep mechanism derives from local relaxations within the grain boundaries as they absorb point defects produced by irradiation. Calculated creep compliances are found in good agreement with those measured. The simulations, moreover, provide a direct link between irradiation-induced creep in nanocrystalline materials with radiation-induced viscous flow in amorphous materials, suggesting that grain boundaries in these materials can be treated as an amorphous phase [5].

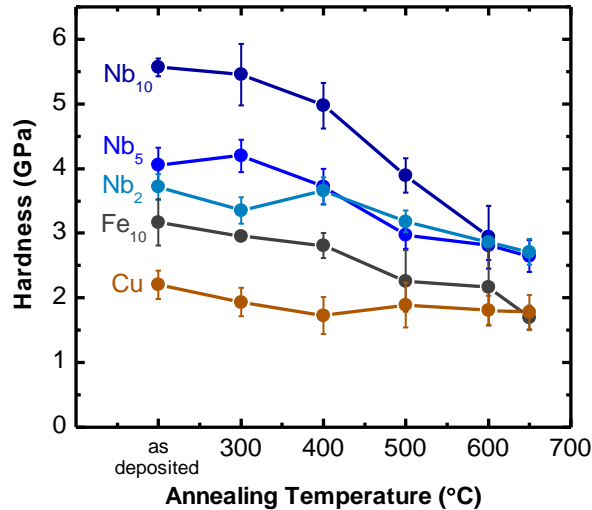


Fig. 5. Evolution of hardness with annealing for Cu-Nb and Cu-Fe thin films [7].

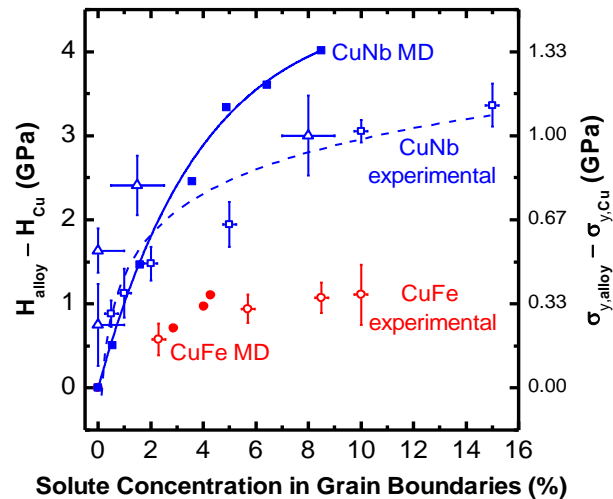


Fig. 6. Comparison of experimental data and molecular dynamics simulations [7].

### B.3 Hardness of nanostructured Cu-Nb and Cu-Fe alloys

To complement the creep study, **King**, **Averback**, and **Bellon** have investigated the effect of solute distribution on strength in nanocrystalline alloys. Indeed recent molecular dynamics (MD) simulations [6] suggested that increasing the solute concentration at the grain boundaries leads to significant

strengthening in nanocrystalline Cu alloys. We experimentally investigated this prediction by measuring the hardness of thin films of Cu-Nb and Cu-Fe annealed at temperatures ranging between 300°C and 600°C. Cu-Nb hardness decreases dramatically with increasing annealing temperature as shown in Figure 5. X-ray diffraction and transmission electron microscopy analyses showed that grain growth itself cannot explain the significant softening. EDS analyses showed that Nb concentration in the grain boundaries decreases with annealing. MD simulations predict that decreasing grain boundary Nb composition increases the grain boundary energy, and with it, a decrease in the resistance to plastic deformation. Figure 6, in fact, shows good agreement between the simulations and our experimental data in terms the variation of hardness enhancement ( $H_{\text{CuNb}} - H_{\text{Cu}}$ ) as a function of the solute concentration at the grain boundaries. Cu-Fe results in less hardness enhancement when compared to Cu-Nb due to the fact that the strengthening effect diminishes when the solute size mismatch becomes smaller [7].

### C. Modeling of diffusion and microstructural evolutions in alloys under irradiation

Development of radiation-resistant structural materials requires the understanding of transport mechanisms of point defects, their coupling to solute atoms and their interaction with sinks (e.g. dislocations). Point defect transport can be biased by the local stress originating from sinks, as well as by applied stress as in the case of creep. The effect of stress is, however, poorly understood. **Trinkle and Bellon** are combining *ab initio* calculations of defect formation and migration energies with continuum transport theory. Our first model system is Ni-Si alloy, for which extensive experimental data on radiation-induced segregation is available [8].

One important finding is that non-hydrostatic stress modifies the various barriers in different ways depending on the directionality, and it greatly influences the temperature for the onset of solute drag. Even qualitatively predicting these effects is complex, as the traditional “five-frequency model” for vacancy-mediated solute diffusion no longer applies. In collaboration with Dr. **Nastar** (CEA-Saclay, France), we have used the newly developed self-consistent mean-field model to compute phenomenological coefficients from our first principles data. There are temperature regimes where, under stress, solute drag is predicted to take place in certain diffusion directions but not in others. This should have profound effects on the migration of solute near dislocations and boundaries, and it may explain why precipitation does not take place on all sinks. **Trinkle**, and **Bellon** will integrate these results into continuum transport models, including phase field models.

### **References**

- [<sup>1</sup>] B. Stumphy, N. Vo, S. Chee, **R.S. Averbach** and **P. Bellon**, “Compositional patterning in dilute  $\text{Cu}_{1-x}\text{Fe}_x$  alloys during ion irradiation”, (manuscript in preparation).
- [<sup>2</sup>] X. Zhang, N.Q. Vo, **P. Bellon**, and **R.S. Averbach**, “Microstructural stability of nanostructured Cu-Nb-W alloys during high-temperature annealing and irradiation”, *Acta Materialia*, **59**, 5332-5341 (2011).
- [<sup>3</sup>] K-P Tai, **R.S. Averbach**, **P. Bellon**, and Y. Ashkenazy, “Irradiation-Induced Creep in Nanostructured Cu Alloys,” *Scripta Materialia*. **65**, 163-166 (2011).
- [<sup>4</sup>] K-P Tai, **R.S. Averbach**, **P. Bellon**, and Y. Ashkenazy, and B. Stumphy. Temperature dependence of irradiation-induced creep in dilute nanostructured Cu-W alloys,” *J. Nucl. Mater.* **422**, 8 (2012).
- [<sup>5</sup>] Y. Ashkenazy, R. S. Averbach, “Radiation induced grain boundary flow – a new creep mechanism at the nanoscale,” *Nano Letters* **12** 4084-4089 (2012).
- [<sup>6</sup>] N.Q. Vo, J. Schaefer, **R.S. Averbach**, K. Albe, Y. Ashkenazy, **P. Bellon**, “Reaching theoretical strengths in nanocrystalline Cu by grain boundary doping,” *Scripta Materialia*, **65**, 660-663 (2011).
- [<sup>7</sup>] S. Z. Ozerinc, K. Tai, N. Q. Vo, **P. Bellon**, **R. S. Averbach**, **W. P. King**, “Grain boundary doping strengthens nanocrystalline Copper Alloys,” *Scripta Materialia*, **67**, 720-723 (2012).
- [<sup>8</sup>] **R.S. Averbach**, L.E. Rehn, W. Wagner, H. Wiedersich, and P.R. Okamoto, *Phys. Rev. B*, **28**, 3100 (1983).

**Program Title: Characterization & Modeling of Deformation Induced Damage in Titanium Alloys**  
**Principal investigators: Carl J. Boehlert, Thomas R. Bieler, and Martin A. Crimp**  
**Michigan State University, CHEMS, 428 S. Shaw Lane, Rm 2527, East Lansing, Michigan 48824**  
**Emails: boehlert@egr.msu.edu, bieler@egr.msu.edu, crimp@egr.msu.edu**

### **Program scope**

We are using a synergistic experimental and computational approach to identify and examine processes that cause damage nucleation at interfaces in two-phase  $\alpha+\beta$  titanium (Ti) alloys. We have systematically studied a near- $\alpha$  phase Ti alloy (Ti-5Al-2.5Sn (wt.%), henceforth referred to as Ti525) and compared the results with work on commercially pure (CP) Ti in order to determine how differences in composition and microstructure affect the processes that cause damage nucleation at interfaces at ambient and elevated temperature. We have successfully characterized the deformation behavior and the preferential slip systems, as well as instances of slip transfer and grain boundary deformation behavior of this alloy, under a variety of loading rates and temperature and compared the results to single-phase  $\alpha$  CP Ti. Using this knowledge to examine the deformation behavior in more complex and commercially important two-phase  $\alpha+\beta$  Ti-alloy systems is the next objective. Future work will accomplish this objective using our unique combination of experimental techniques that allow the details of the deformation and fracture initiation mechanisms to be characterized in the context of the larger microstructure. The deformation in selected microstructure patches that are large enough to identify how neighboring grains influence stress shielding and strain incompatibilities will also be simulated using state-of-the-art polycrystalline plasticity-based finite element models. Successful completion of this research program will establish a paradigm by which the fundamental processes responsible for damage nucleation in polycrystals can be identified. The Ti alloys that will be examined are currently used in a wide range of aerospace structural applications, as well as within the energy generation, automotive, and biomedical industries, thereby making the program outcomes of broad practical interest.

### **Recent Progress**

Four half-time PhD graduate students have been conducting the bulk of this research. Mr. James Seal has focused on the role of the  $\beta$  phase and  $\alpha/\beta$  slip transfer. Ms. Hongmei Li has performed *in-situ* mechanical deformation tests, including tension and tension-creep experiments on CP Ti, Ti525, and Ti-3Al-2.5V(wt.%). Mr. Chen Zhang has focused on modeling the deformation, and in particular microstructural patches of Ti525, using CPFEM methods. Indraroop Dastidar started in January 2013 and he will focus on the deformation behavior of Ti-6Al-4V(wt.%). Together, we have characterized the deformation behavior during ambient and elevated-temperature *in-situ* SEM tensile and tensile-creep experiments on a Ti525 forging donated to us by Pratt and Whitney Rocketdyne. For most of the experiments, EBSD maps were acquired within the gage section of the samples before the experiments. Combined with the SEM images of the deformed grains, we have identified the active slip systems. The elevated-temperature tests focused around 455°C so that the deformation behavior of this alloy can be compared with data from other Ti alloys, including Ti-6Al-4V(wt.%). The following summarizes our findings to date.

#### **1 Slip transfer between the $\alpha$ and $\beta$ phases**

The mechanisms of slip transfer between the  $\alpha$  and  $\beta$  phases in Ti alloys have been examined systematically in lamellar microstructures in Ti-6Al-4V [96,97], but there has been no comparable study of how slip in the  $\alpha$  phase interacts with the  $\beta$  phase in near- $\alpha$  alloys such as Ti525, or when the  $\beta$  phase is globular. As shown in Figure 1a, the minority  $\beta$  phase in Ti525 resides at  $\alpha$  grain boundaries and triple points as grains that are a few microns in diameter. The orientation relationships between these  $\beta$  grains and their  $\alpha$  neighbors, as determined through EBSD (see Figure 1b), were assessed to determine if the Burgers relationship  $\{0001\}_\alpha \parallel \{01\bar{1}\}_\beta$  with  $\langle 11\bar{2}0 \rangle_\alpha \parallel \langle 111 \rangle_\beta$ , which is well known to exist in lamellar  $\alpha/\beta$  exists with one of the adjacent  $\alpha$  grains. Only 16% of these boundaries were found to be close to this relationship.

After deformation, basal, prismatic, and pyramidal slip systems were identified in the  $\alpha$  phase based upon slip trace analysis using EBSD data. Of 94  $\alpha/\beta$  interfaces studied, there were visible slip traces in the  $\alpha$  phase at the interface in only 36 (38%) of the boundaries. Of these interfaces, correlated slip transfer at the  $\alpha/\beta$  interface was only observed at 15 (42%) of these interfaces. All 15 instances of observed prism, basal, and pyramidal slip transfer to  $\beta$  occurred by  $\langle a \rangle$  slip. This is likely due to the fact that the  $\langle a \rangle$  slip vector in  $\alpha$  is only 4.2% greater than the  $\frac{1}{2}\langle 111 \rangle$  in  $\beta$ . Regardless, some degree of the residual Burgers vector must be absorbed into the  $\alpha/\beta$  boundary for this slip transfer to occur. While  $\langle c+a \rangle$  slip was active in the  $\alpha$  phase at 3  $\alpha/\beta$  interfaces, no  $\langle c+a \rangle$  slip was ever

observed to be involved in slip transfer (Figure 2), possibly due to its Burgers vector being 64% greater in the  $\alpha$  than the  $\frac{1}{2}\langle 111 \rangle$  Burgers vector in the  $\beta$ .

Slip transfer was also analyzed using the slip transfer parameter  $m'$  in the 36 instances where slip bands were observed ( $m' = 1$  if both the slip planes and slip directions are parallel). Comparing the 15 instances of slip transfer and the 21 instances without, there is a 98% confidence that the slip plane alignment favors slip transfer, but only an 80% confidence that the slip direction is correlated. Combining the two into the  $m'$  measurement indicated only a 30% confidence that the combination of the slip plane and the direction favors slip transfer. This low confidence in  $m'$  differs from observations in CP Ti and TiAl grain boundaries where  $m'$  combined with a high Schmid factor is effective in predicting conditions that lead to slip transfer.

Furthermore, slip traces in the  $\beta$  phase were always correlated with slip traces in the  $\alpha$  phase, suggesting that slip in the  $\beta$  phase cannot be stimulated without slip in  $\alpha$ . This suggests that the  $\beta$  phase is shielded by the deformation in the  $\alpha$  phase, and may serve as a means of accommodation of strain incompatibilities between neighboring  $\alpha$  grains. However, slip bands are not the only indication of slip activity, as slip can occur in less concentrated ways. Thus, the coplanarity of favored slip systems with high Schmid factors may be the best predictor for slip transfer across a phase boundary in this alloy and microstructural condition evaluated. This contrasts with observations of slip transfer in semi-coherent lamellar microstructures, where the alignment of the slip vector was the most important parameter for accommodating slip transfer [Savage *et al.*, Phil Mag 2004].

## 2 Heterogeneous strain and cracking in Ti525 and CP Ti at different T and strain rates

Using methods similar to those described above, the slip behavior of Ti525 samples with a moderate texture was examined systematically after ambient and elevated-temperature tensile and tensile-creep deformation. Both strain rate and temperature significantly affected the relative activity of the deformation systems, and these slip characteristics were nearly independent of strain. At ambient temperature, the fraction of grains exhibiting obvious slip traces was over 90%, whereas less than 10% of the grains exhibited surface slip traces during creep at 200-250MPa. Furthermore, under creep conditions grain boundary sliding is apparent. Figure 3 shows two micrographs that illustrate the extremes in deformation microstructures. Table I shows the relative fraction of grains with obvious slip bands for the Ti525 alloy tested at a number of different conditions in comparison with CP Ti, showing this slip activation varies considerably with alloy content, temperature, and strain rate. Prismatic slip was the most prevalent deformation mode in both CP Ti and Ti525, but basal slip activity in Ti525 was significantly greater than CP Ti, as expected based on similar results from Williams *et al.* [Met. Trans., 2002]. Although twinning was active in CP Ti, it was almost completely suppressed in Ti525.

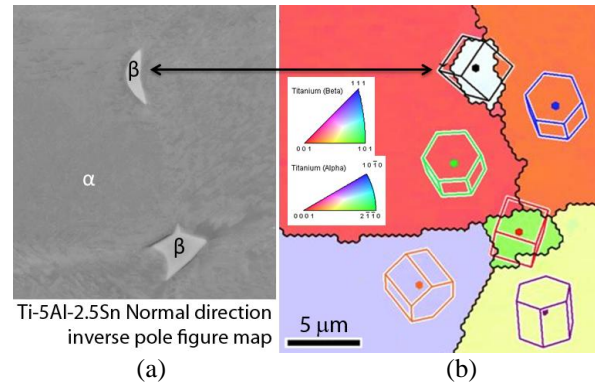


Figure 1. a) Backscattered electron SEM image of globular  $\beta$  grains surrounded by larger  $\alpha$  grains in Ti525. b) EBSD inverse pole figure map showing the orientation of  $\beta$  grains at  $\alpha$  boundaries.

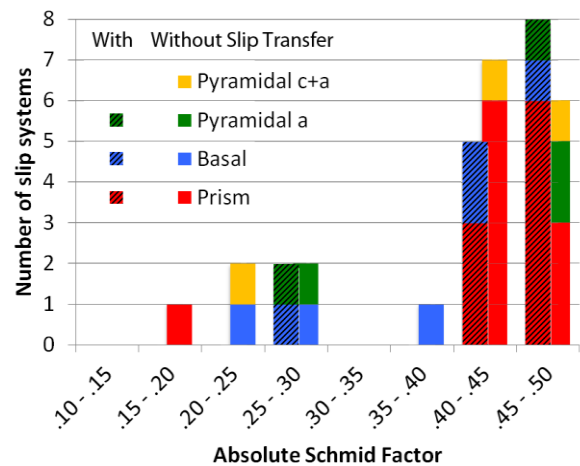


Figure 2. Histogram showing Schmid factors based upon global uniaxial tension, for the observed slip systems in the  $\alpha$  phase that were involved and not involved in  $\alpha/\beta$  slip transfer for Ti525 deformed to 3% tensile strain.

Grain boundary sliding can cause cracks or pores to develop, as illustrated in Figure 4, which shows one region with a triple point crack and grain boundary crack. An orientation map is shown to illustrate that there are relatively hard orientations (c-axis within 30° of the tensile axis) among at least one of the grains adjacent to each of the

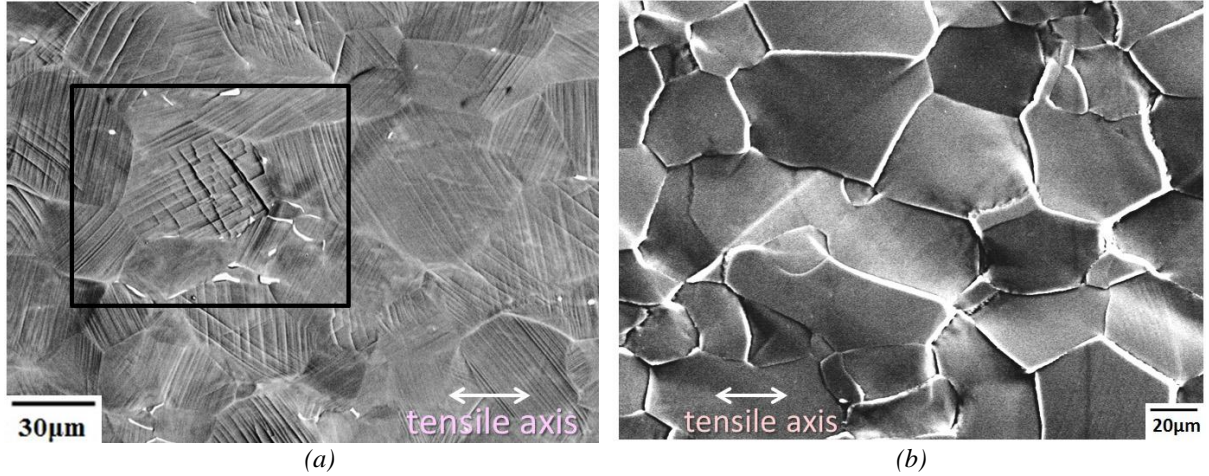


Figure 3. SEM images providing examples of a deformed Ti525 microstructures showing extensive slip bands after low tensile strain ((a) 23 °C) and only a few slip bands after large creep strain ((b) 455 °C 250 MPa).

cracks. In hard oriented grains, only  $\langle c+a \rangle$  slip has high Schmid factors, and the lack of more easily operated slip systems leads to the inability of hard orientations to accommodate shape changes that occur in neighboring grains.

### 3 Crystal Plasticity Finite Element (CPFE) simulation of dislocation slip

A 3D CPFE model of the black boxed area in Figure 3 was constructed with combined geometrical and crystallographic information from both EBSD and 3D-XRD data collected at Beamline 34-ID-E in APS, Argonne National Lab. The 3D CPFE model was computationally deformed with MSC®Marc/Mentat, using a phenomenological power law module from DAMASK (The Düsseldorf Advanced Material Simulation Kit, [damask.mpie.de](http://damask.mpie.de)), under development at Max-Planck-Institut für Eisenforschung (Düsseldorf). The hardening parameters and initial slip resistance values were based on those reported in the literature [Salem et al., Acta Met., 2003] to simulate activity observed in Table 1. Post FEM analysis was conducted with our own python scripts as well as the post processing module from DAMASK. The simulated accumulated shear maps show that both basal and prism slip systems are highly active in the central grain where ledges were observed, consistent with surface trace analysis that shows two slip systems were active in this region. Both simulation and experiment indicate that deformation is more active in the right side of the grain than the left side. This can be partially explained by the more complicated simulated stress state in the right side of the grain. To gain a better understanding of complex processes of polycrystalline deformation, we are developing better 3D models with more complete geometrical information.

Table I Frequency of instances of active slip systems in Ti-5Al-2.5Sn and CP Ti

Percentage of instances of → Test mode, material, (approx. strain)	Basal <a>	Prism <a>	Pyram <a>	Pyram <c+a>	Twin
23°C tension Ti525(3.5%)	41.3%	50.2%	3.5%	4.5%	1%
455°C tension Ti525(4.4%)	47.6%	41.3%	4.8%	6.3%	0
455°C tension Ti525(9%)	42.4%	47.1%	4.2%	6.3%	0
455°C-250MPa creep Ti525(16.5%)	77.8%	15.6%	2.2%	4.4%	0
23°C tension CP Ti(4%)	10%	63.3%	5.6%	10%	11%
23°C tension CP Ti(8.4%)	10.8%	61.5%	4.8%	13.5%	9.6%
455°C tension CP Ti(4.3%)	11.0%	59.0%	6.0%	14.0%	10%
455°C tension CP Ti(11.2%)	10%	60%	5.8%	14.2%	10%

## Future Plans

The momentum of this research program will continue in order to have sufficient data for statistical confidence in identification of deformation mechanism interactions with grain boundaries. The items listed below summarize important research accomplishments. Some of these outcomes have inspired new focus areas that are also described below.

i. Rules for slip transfer and damage nucleation across  $\alpha/\beta$  boundaries have been investigated for the first time, and indicate that the  $\beta$  phase deformation is strongly influenced by activated slip in the neighboring  $\alpha$  phase.

ii. Effects of chemistry, temperature, and strain rate on slip heterogeneity have been identified (some quantitatively) from novel *in-situ* experimental methods.

iii. CPFÉ simulation suggests significant correlations with observed complex strains in a real sample. This use of the local stress tensor, which is not experimentally measurable, and 3-D geometrical information will accelerate understanding of the driving forces for observed slip.

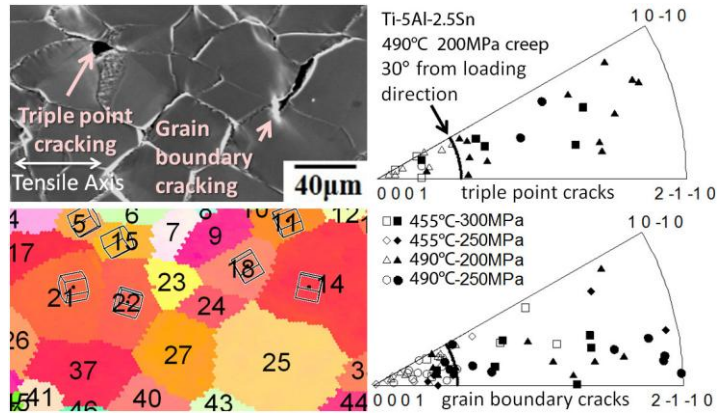


Figure 4. Upper left is a secondary electron SEM image of Ti525 after tensile creep deformation to ~16% strain at 490 °C and 200 MPa. Lower left is the EBSD inverse pole figure map of the corresponding microstructural patch before deformation. The right hand side shows inverse pole figures highlighting the grain orientations associated with cracks; open symbols represent the hardest orientations of grain pairs or triples.

## Publications that have appeared in 2010-2012:

C.J. Boehlert, H. Li, L. Wang, B. Bartha, “Slip System Characterization of INCONEL alloy 718 using *In-Situ* Scanning Electron Microscopy”, *Advanced Materials and Processes*, November-December (2010) 41-45.

H. Li, C.J. Boehlert, T.R. Bieler, M.A. Crimp, “Analysis of the tension and creep behavior of Ti525(wt.%) using *in-situ* SEM Experiments”, Proceedings of the 12th World Conference on Titanium (Ti-2011), Beijing, China. vol. 2 (2012) 937-941.

M.A. Crimp, Y. Yang, L. Wang, P. Eisenlohr, and T.R. Bieler, “Grain boundary strain transfer and anisotropic polycrystalline deformation in commercial purity titanium”, *Proc. 12th World Conference on Titanium (Ti-2011)*, Beijing, China. vol. 2 (2012) 1061-1065.

H. Li, C.J. Boehlert, T.R. Bieler, M.A. Crimp, “Analysis of Slip Activity and Heterogeneous Deformation in Tension and Tension-Creep of Ti525(wt.%) Using *In-Situ* SEM Experiments”, *Philosophical Magazine*, Vol. 92 No. 23 (2012) 2923-2946.

J.R. Seal, T.B. Britton, A.J. Wilkinson, T.R. Bieler, M.A. Crimp, “Characterizing Slip Transfer In Commercially Pure Titanium Using High Resolution Electron Back Scatter Diffraction (HR-EBSD) and Electron Channeling Contrast Imaging (ECCI)”, *Proc. Microscopy & Microanalysis 2012*, Phoenix, AZ, paper 67.

J. Seal, M.A. Crimp, C.J. Boehlert, and T.R. Bieler, “Analysis of the Beta-to-Alpha Phase Slip transfer Behavior in Ti525(wt.%)”, *Materials Science and Engineering A*, Vol. 552 (2012) 61-68.

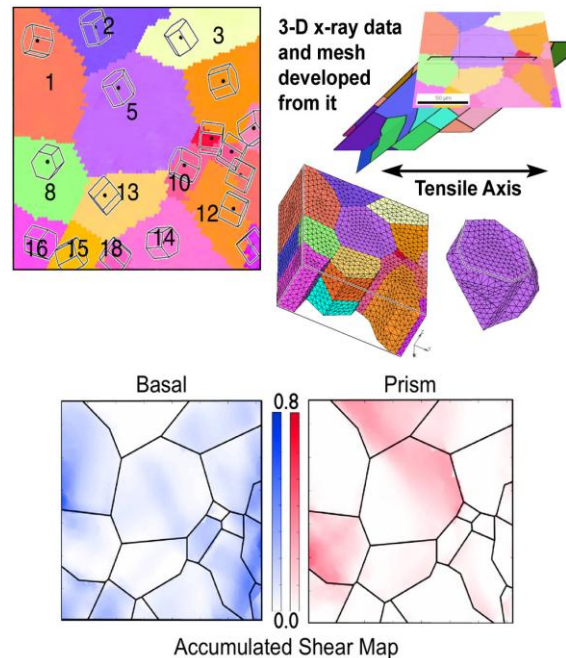


Figure 5. OIM and 3-D orientation data of Ti5Al-2.5Sn patch in Figure 3 with CPFÉ mesh computationally deformed. Patterns of accumulated shear match observed surface topography better than quasi-3D columnar grain mesh.

## NANOMECHANICS AND NANOMETALLURGY OF BOUNDARIES

**B.L. Boyce<sup>1</sup>, S.M. Foiles<sup>1</sup>, E.A. Holm<sup>1</sup>, B.G. Clark<sup>1</sup>, K.M. Hattar<sup>1</sup>, and J.A. Sharon<sup>1</sup>**

<sup>1</sup>Sandia National Laboratories,  
PO Box 5800, MS 0889,  
Albuquerque, NM 87185, USA

*Abstract* Nanostructured metals are not only susceptible to mechanically-induced grain growth, but this grain growth process manifests itself in unusual mechanical properties, ranging from anomalous fatigue behavior to outstanding wear resistance under some conditions. Through this program, we have uncovered behaviors in nanostructured metals that seem to contradict basic tenants of metallurgy. Specifically, while the driving force for mechanically-induced grain growth is understood to be associated with elastic and plastic strain energy minimization, the exceedingly low mobility of metal grain boundaries at low homologous temperatures ( $T \ll 0.3T_{mp}$ ) was previously thought to be insurmountable. New concepts of detwinning and dislocation-analogue boundary motion help to explain this diffusionless or diffusion-limited behavior. We have come to realize that in the absence of traditional dislocation plasticity, the well-known grain boundary sliding process for tangential motion of the grain boundaries is complimented by perpendicular motion of the grain boundary resulting in grain growth. In the coming three years, the goal of the program is to take advantage of this new class of boundary-mediated deformation processes as a means to dissipate energy. Nanostructured alloys are well known for their exceptional strength, but they often suffer from limited ductility, a classic materials paradox. A few exceptions from our own work and from the literature suggest that there is a pathway to enable both enhanced strength and improved ductility. Our core hypothesis for this program is that the ductility, toughness, and flaw tolerance of nanostructured alloys can be dramatically enhanced by enabling mechanically-induced boundary motion. To explore this hypothesis, our project will continue to rely on an ICME-inspired balance of computational modeling and experimentation at multiple length scales from the atomistic to the macroscale.

Sandia is a multiprogram laboratory operated by Sandia Corporation, a Lockheed Martin Company, for the United States Department of Energy's National Nuclear Security Administration under contract DE-AC04-94AL85000.

# Crack-Tip Mechanisms During Environmental Degradation

Stephen M. Bruemmer

Pacific Northwest National Laboratory, P.O. Box 999, Richland, WA 99352  
[stephen.bruemmer@pnnl.gov](mailto:stephen.bruemmer@pnnl.gov)

Kevin M. Rosso, Matthew J. Olszta, Daniel K. Schreiber and Chongmin Wang  
Pacific Northwest National Laboratory

Gary S. Was, University of Michigan

## Program Scope

First-of-a-kind, discovery-based research is being conducted to explicate environmental degradation mechanisms through atomistic measurement and modeling of interfacial reactions occurring at buried crack tips. Oxidation at liquid-solid, gas-solid and solid-solid interfaces is being evaluated to establish basic processes leading to grain boundary degradation. This research builds on recent analytical transmission electron microscopy (ATEM) measurements revealing unexpected nanometer-scale crack opening and oxidation reactions driving intergranular (IG) cracking of light-water-reactor structural alloys in service. ATEM measurements have also shown dramatic compositional changes and eventual nanoporosity at the metal grain boundary leading the crack tip. Kinetic development of such features can only be explained by oxidation-induced vacancy injection. Collective evidence and analyses have suggested that IG penetrative degradation can advance in many corrosion-resistant alloys by selective grain-boundary oxidation even at low temperatures. Direct mechanistic links have been made among degradation of corrosion-resistant structural alloys in water, supercritical-water, steam and high-temperature gaseous environments. These measurements and observations are generally inconsistent with continuum mechanics and electrochemical models of environmental degradation and point toward the need for atomic and molecular level understanding of the processes.

## Recent Progress

Research activities focus on the ex-situ and in-situ measurement of discrete atomistic, molecular and solid-state reactions integrated with atomistic modeling of chemo-mechanical processes at crack tips. Four primary task areas are being pursued in the first year of the project: (1) quantitative environmental degradation experiments; (2) ex situ atomistic-scale examination of crack tips; (3) in situ studies of selective oxidation and vacancy generation processes, and (4) atomistic modeling to elucidate selective oxidation mechanisms relevant to environment-induced degradation processes at crack tips. A brief description of recent results in all four areas is provided in the following section.

### *(1) Quantitative Environmental Degradation Experiments*

Corrosion and stress corrosion crack-growth-rate experiments are being conducted to produce well-defined grain boundary degradation that will be examined ex situ for structure, composition and chemistry using ATEM and three-dimensional, atom-probe tomography (APT). Construction of a second stress-corrosion test system was recently completed along with two corrosion cells. The stress corrosion system enables the simultaneous testing of three compact-tension samples in high-temperature water with interactive control of loading/environmental conditions and the in-situ,  $\mu\text{m}$ -resolution measurement of crack extension using direct current potential drop. Corrosion and stress corrosion tests have been conducted in hydrogenated water on the high-purity binary Ni alloys with controlled additions of Cr, Fe, Al, Si or Cu (selected based on differing oxidation characteristics). Grain boundary corrosion was found to extremely rapid for the Ni-Si binary alloy, followed by slower IG degradation rates for the Ni-Cr and Ni-Al alloys and no attack for the Ni, Ni-Cu or Ni-Fe alloys. Stress corrosion response for these low-strength, high-purity alloys was influenced by creep processes, but tests confirmed the unique susceptibility for the Ni-Si alloy and high stress-corrosion rates for Ni-Cr and Ni-Al. Crack-growth response has been mapped as a function of temperature, hydrogen concentration and electrochemical potential assessing behavior in both the Ni-metal

and NiO stable regimes. Crack-tip stress intensity and environmental conditions were held constant during the final experimental stage, thereby generating significant crack extension under a controlled environmental condition for ex-situ characterizations.

### (2) Ex Situ Atomistic-Scale Examination of Crack Tips

Unexpected solid-state internal oxidation or sulfidation has been discovered in commercial Ni-Cr alloys during exposure in hydrogenated, high-temperature water environments using high-resolution ATEM and APT. Selective oxidation of Cr was found<sup>5,11</sup> to drive penetrative degradation along dislocations at crack walls and surfaces, preventing formation of a protective oxide layer in high Cr, Ni alloys. Internal sulfidation was identified<sup>6,14</sup> leading grain boundary oxidation during localized IG corrosion of lower Cr, nickel alloys. The source of S was determined to surface contamination and its removal before water exposure resulted in only grain boundary oxidation. New research is focused on selective oxidation experiments isolating effects of Cr and Al on IG corrosion and cracking in binary Ni alloys. ATEM and APT examinations reveal quite different IG oxidation structures and composition changes in the leading grain boundaries. Narrow, porous attack containing  $\text{Cr}_2\text{O}_3$  is observed in the Ni-Cr alloy, while  $\text{NiAl}_2\text{O}_4$  forms in the Ni-Al alloy during IG corrosion. A striking difference in the structure and composition of the grain boundary ahead of the oxidation front is seen for the two materials. Extensive grain boundary Cr depletion is measured out to distances of  $>10\ \mu\text{m}$  for the Ni-Cr alloy along with evidence for significant boundary migration as illustrated in Fig 1. These results suggest that vacancy injection at the oxidation front enhances grain boundary diffusivities and promotes the long-range Cr depletion and boundary migration. Very limited interfacial Al depletion is detected for the corroded Ni-Al alloy without any apparent boundary migration. However, ATEM and APT have identified discrete  $\text{NiAl}_2\text{O}_4$  nanoparticles in the metallic grain boundary beyond the continuous oxidation front. Directly correlated ATEM and APT examinations have been critical to resolve the oxide crystal structure, clarify the 3D oxide morphology and measure the local composition for the oxide and the grain boundary. Although O enrichment has not been detected in the metallic grain boundaries, the presence of discrete oxides indicates that grain boundary O diffusion has occurred prompting internal oxidation.

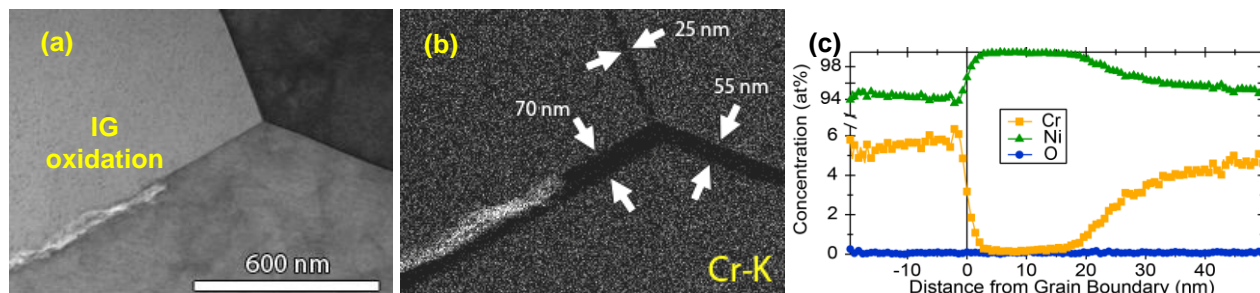


Fig 1. TEM and APT analyses of IG oxidation in Ni-5at%Cr: (a) TEM brightfield image of grain boundary oxidation front; (b) TEM - energy dispersive X-ray spectroscopy Cr elemental map showing extensive grain boundary depletion and (c) APT composition profile across a metallic grain boundary ahead of the oxidation front.

### (3) In Situ Studies of Selective Oxidation

To gain fundamental information about selective oxidation and vacancy generation processes, nanoparticles with model binary alloy compositions are being characterized<sup>3</sup> by in-situ high-resolution TEM during controlled surface oxidation. Recent work has focused on in-situ TEM oxidation experiment using an aberration-corrected environmental TEM (ETEM). These experiments provide the opportunity for direct visualization of the dynamic structural evolution of the nanoparticle during oxidation. In combination with high spatial resolution scanning TEM and electron energy loss spectroscopy (EELS) analysis, unprecedented information has been gained regarding the chemistry and vacancy injection characteristics during the oxidation process of Ni and Ni doped with 5 at% Cr. The in-situ TEM experiment was carried at 375°C in an  $\text{Ar}/\text{O}_2$  gas mixture at  $\sim 1$  mbar pressure in the ETEM column.

Multi-site nucleation of oxides was discovered on the metal nanoparticle surface. Growth of the oxide nanoparticles leads to the impingement of the oxides and the formation of a polycrystalline surface oxide layer. Most dramatically, clustering of injected vacancies is observed within the metal nanoparticles during the oxidation process leading to the nucleation of an internal cavity. As soon as a stable cavity forms, it becomes an effective sink for subsequent injected vacancies promoting cavity growth until the remaining metal is oxidized. EELS mapping indicates that for the oxide film formed on Ni doped with 5 at% Cr, the Cr oxide is present with a size of ~1-2 nm as indicated in Fig 2. The formation of local Cr oxide demonstrates the clustering of Cr during the oxidation process, however the Cr concentration is too low for a continuous Cr oxide layer to form under the exposure conditions. In-situ TEM oxidation experiments are continuing on the Ni-Cr alloys under different gaseous environments to help isolate selective oxidation processes.

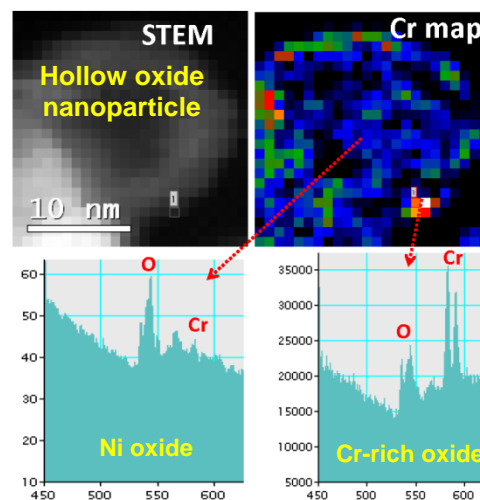


Fig. 2 STEM-HAADF image and EELS results showing the structure and chemistry of the oxide nanoparticle.

#### (4) Atomistic Modeling to Elucidate Selective Oxidation Mechanisms

Towards building a multi-scale atomistic model for the internal oxidation process, a combined theory development and quantum mechanical simulation approach is being employed. Classical analytical models of metal oxidation kinetics were first evaluated and generalized into a mathematical framework that incorporates transport processes consistent with the observations, with mechanistic detail that can extend their applicability to grain boundary oxidation in binary alloys. The target analytical framework will help guide computational molecular simulation for elementary transport processes to be computed in detail at the density functional theory (DFT) level. For example, a generalized mathematical model for growth kinetics of oxide films was presented<sup>2</sup> for oxygen diffusion limitation at the oxide-metal interface. The theory of Deal-Grove was shown to be the lower order approximation of the proposed model. A model was also developed<sup>12</sup> for metal diffusion limitation to the gas-oxide interface. Theory presented unifies Cabrera-Mott's and Wagner's models and provides a complete description of oxidation including the transition from thin to thick films. Our analytical models are being adapted from pure metal oxidation to the case of binary alloys and for geometries relevant to grain boundary oxidation, where in tandem DFT simulations are underway to compute transport rate constants to populate the analytical models. For example, electronic and ionic transport properties of bulk NiO were calculated<sup>4</sup> from first principles with the GGA+U formalism. This included ab initio prediction of energy barriers for diffusion of interstitial Ni, O and their corresponding vacancy partners, and explicit calculation of electron and hole small polaron hopping rates. Quantum mechanical approaches are now being used to compute coupled oxygen/vacancy diffusion rates in Ni, starting with the bulk material and progressing to model grain boundary structures focusing the analytical framework to account for observed vacancy injection and oxygen diffusion in grain boundaries ahead of the continuous oxide front. The modeling activity ultimately will help parameterize large scale numerical simulations, such as by kinetic Monte Carlo methods, which should be a useful mechanistic tool for predicting corrosion kinetics at buried crack tips based in part on elementary transport processes.

#### Future Plans

Corrosion and stress-corrosion testing in high-temperature water will continue to focus on the Ni binary alloys evaluating grain boundary degradation under environmental conditions crossing key phase stability regions. The high-purity, solution-annealed materials have now been cold forged to increase strength, thereby enhancing stress corrosion susceptibility at lower temperatures and minimizing creep-dominated effects at higher temperatures. Selective oxidation behavior of Cr, Fe, Al and Si will be investigated relative to response for pure Ni and Ni-Cu alloys. Crack-tip characterizations by ATEM and APT will document structural and chemical modifications at leading grain boundaries due to oxidation processes. In-situ TEM oxidation experiments will assess vacancy injection for Ni-Cr binary nanoparticles and evaluate

higher Cr alloys along with the Ni-Al binary. In addition, oxidation experiments will be attempted in APT focused on identifying atomistic clustering of Cr-O and Al-O as a precursor to oxide formation. Development of the molecular simulation tool for understanding the dynamics of selective oxidation will move into the Ni-Cr and Ni-Al binary systems. Work on activation energies for transport processes will continue and a Monte Carlo based dynamics code will be developed for coupled collective processes capable of reaching into long length and time scales. A key focus will be to address oxidation-induced vacancy injection processes and their influence on grain boundaries ahead of the oxidation front.

#### References: 2010-2012

1. S. M. Bruemmer and L. E. Thomas, "Insights into Stress Corrosion Cracking Mechanisms from High-Resolution Measurements of Crack-Tip Structures and Compositions," *Proc. 2010 MRS Spring Meeting, Volume 1264: Materials for Nuclear Applications and Extreme Environments*, Materials Research Society, Paper 1264-BB01-09.
2. Zhijie Xu, K. M. Rosso and S. M. Bruemmer, "A Generalized Mathematical Framework for Thermal Oxidation Kinetics," *J. Chemical Physics*, 135 (2011) 024108.
3. C. Wang, D. R. Baer, S. M. Bruemmer, M. H. Engelhard, J. A. Sundarajan and Y. Qiang, "Microstructure of the Native Oxide Layer on Ni and Cr-doped Ni Nanoparticles," *J. Nanoscience and Nanotechnology*, 11-10 (2011) 8488.
4. Jianguo Yu, K. M. Rosso and S. M. Bruemmer, "Charge and Ion Transport in NiO and Aspects of Ni Oxidation from First Principles," *J. Physical Chemistry C*, 116 (2011) 1948.
5. M. J. Olszta, D. K. Schreiber, L. E. Thomas and S. M. Bruemmer, "Penetrative Internal Oxidation from Alloy 690 Surfaces and Stress Corrosion Crack Walls during Exposure to PWR Primary Water," *Proc. 15th Int. Conf. Environmental Degradation of Materials in Nuclear Power Systems – Water Reactors*, "The Minerals, Metals and Materials Society, 2011, p. 331.
6. M. J. Olszta, D. K. Schreiber, L. E. Thomas and S. M. Bruemmer, "Electron Microscopy Characterizations and Atom Probe Tomography of Intergranular Attack in Alloy 600 Exposed to PWR Primary Water," *Proc. 15th Int. Conf. Environmental Degradation of Materials in Nuclear Power Systems – Water Reactors*, "The Minerals, Metals and Materials Society, 2011, p.1503.
7. S. M. Bruemmer, M. J. Olszta, M. B. Toloczko and L. E. Thomas, "High-Resolution Characterization of Grain Boundary Damage and Stress Corrosion Cracks in Cold-Rolled Alloy 690," *Proc. 15th Int. Conf. Environmental Degradation of Materials in Nuclear Power Systems – Water Reactors*, "The Minerals, Metals and Materials Society, 2011, p. 301.
8. T. Moss, M. J. Olszta, W. Grant and G. S. Was, "Grain Boundary Oxidation and Stress Corrosion Cracking in Nickel-Base Alloys Strained in Supercritical Water," *Proc. 15th Int. Conf. Environmental Degradation of Materials in Nuclear Power Systems – Water Reactors*, "The Minerals, Metals and Materials Society, 2011, p. 1519.
9. J. A. Sundararajan, T. Schimel, M. Kaur, Y. Qiang, C. Wang, D. R. Baer and S. M. Bruemmer, "Heat Treatment on Ni and Cr Doped Ni Core-Shell Nanoparticle Granular Films," *Proceedings of IEEE NANO 2011 Conference*, Institute of Electrical and Electronics Engineers, 2011, p. 657.
10. Sung-Il Baik, M. J. Olszta, S. M. Bruemmer and D. N. Seidman, "Grain Boundary Structure and Segregation Behavior in a Nickel-Base Stainless Alloy," *Scripta Materialia*, 66 (2012) 809.
11. M. J. Olszta, D. K. Schreiber, L. E. Thomas and S. M. Bruemmer, "High Resolution Crack Imaging Reveals Degradation Processes in Nuclear Reactor Structural Materials," *Advanced Materials and Processes*, American Society for Materials, April (2012) 17.
12. Zhijie Xu, K. M. Rosso and S. M. Bruemmer, "Metal Oxidation Kinetics and the Transition from Thin to Thick Films," *Physical Chemistry Chemical Physics*, 14-42 (2012) 14534.
13. S. M. Bruemmer, M. J. Olszta, M. B. Toloczko, and L. E. Thomas, "Linking Grain Boundary Microstructure to Stress Corrosion Cracking of Cold Rolled Alloy 690 in PWR Primary Water," *Corrosion*, 2012, accepted, in press.
14. D. K. Schreiber, M. J. Olszta, D. W. Saxey, K. Kruska, K. Moore, S. Lozano-Perez and S. M. Bruemmer, Examinations of Oxidation and Sulfidation of Grain Boundaries in Alloy 600 Exposed to PWR Primary Water,' *Microscopy and Microanalysis*, 2012, accepted, in press.

**Energetics of Radiation Tolerant Nanoceramics**  
Early Career Program Award

Dr. Ricardo Castro, Associate Professor  
Chemical Engineering and Materials Science Department & NEAT ORU  
University of California, Davis  
Davis, CA 95616

**Program Scope or Definition**

Nanomaterials emerged as strong candidates to enable a new generation of radiation barriers with nanoceramic coatings, nanoparticles dispersed in metallic matrices, or even monolithic nanoceramics parts. Nanocrystalline materials (typically below ~100 nm) were initially expected to show generally enhanced radiation resistance [1]. This would be attributed to the increased interface areas in the form of grain boundaries that could act as effective sinks for radiation-induced defects, significantly hindering the accumulation of point defects. The mechanisms behind this effect were described by molecular dynamics for nanocrystalline copper [2], and it was shown that, under irradiation, the interstitial defects created during the damage events primarily move into the grain boundary. These interstitials could then return to the bulk material, annihilating vacancies (healing effect) and promoting radiation tolerance (Figure 1 shows a schematic representation of the mechanism by Ackland [1]). Therefore, one could expect that the higher the amount of interfaces, the lower the radiation damage. This would explain the enhanced radiation tolerance observed, for instance, in nanocrystalline partially inverted spinel  $MgGa_2O_4$ , that can tolerate doses up to 96 displacements per atom (dpa), while its bulk counterpart was amorphized by a dose of just 12 dpa [3].

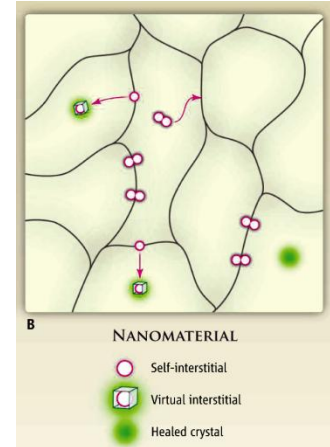


**Figure 1.** Schematic representation of self-healing mechanism in nanomaterials.

Interestingly, this effect is not always experimentally observed. For instance,  $ZrO_2$  or  $Si$  nanocrystals (3-6 nm) embedded in an amorphous  $SiO_2$  matrix were observed to be more susceptible to radiation-induced amorphization than their micro-grained counterparts [4-6]. A thermodynamic explanation for the opposite effects of a higher interface area on the radiation tolerance of different materials has been proposed based on the balance between the grain boundary energy and point defects energy [7]. Thermodynamics shows that the phase-transition ( $\Delta G_{pt}$ ) (e.g. amorphization or crystalline structure change) resistance in irradiated nanocrystalline material is dependent on both total grain boundary energy ( $\Delta G_{gb}$ ) and irradiation-induced point defects ( $\Delta G_{pd}$ ), such that, to show a significant radiation resistance, the sum of these contributions must be smaller than  $\Delta G_{pt}$ :

$$\Delta G_{gb} + \Delta G_{pd} < \Delta G_{pt} \quad (1)$$

As both terms on the left of equation (1) are distinctly dependent on the grain size, depending on the relative energies of the system, one may observe critical size ranges where the phase-transition may be avoided. That is, the interface term is directly proportional to the interface area, i.e.  $\Delta G_{gb} = S_{gb}\gamma_{gb}$  (where  $S_{gb}$  is the interface area and  $\gamma_{gb}$  is the interface energy), indicating that  $\Delta G_{gb}$  is inversely proportional to the grain size. Shen [7] has shown that  $\Delta G_{pd}$  depends on the concentration of point defects and, by assuming that the thermal vacancy creation is negligible and the defect annihilation is dominated by grain boundary sink during irradiation,  $\Delta G_{pd}$  would be proportional to the square of grain size (as confirmed by experimental data from Rose et al. [8]). Thus, a decrease in the grain size leads to an increase of  $\Delta G_{gb}$  but a decrease of  $\Delta G_{pd}$ , as schematically shown in Figure 2.

The diagram shows a grain size range (as indicated in the plot) where the phase-transition is thermodynamically unfavorable because equation (1) is respected. Moreover, it suggests that nanocrystalline materials with relatively low interface energy are expected to show higher radiation tolerance. This would be particularly true for very small sizes, where the free energy of the point defect contribution is smaller. This is consistent with the literature reporting that gold nanocrystals, that have relatively low grain boundary energy (0.4 J.m<sup>-2</sup> [9]), show enhanced radiation

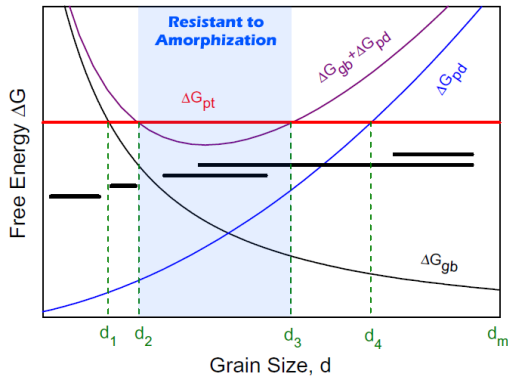


**Figure 2.** Free energy as a function of the grain size showing the balance between grain boundary and point defect energy to improve resistance to amorphization

tolerance, and that  $\text{MgGa}_2\text{O}_4$ , which has no data available on its grain boundary energy but is also expected to have low interface energy as recently suggested [10], also shows the improved radiation tolerance.

The lack of reliable data on the interface energy of ceramic materials makes it extremely difficult to test this thermodynamic hypothesis and enable the prediction and tuning of nanoceramics performance as radiation shields to exploit their full potential. In this project, we systematically evaluate this concept by measuring the interface energies of series of nanoceramics with potential interest for nuclear components, and establish the relationship between composition (and distribution of components), interface energies, and radiation resistance, aiming to enable a fine selection of nanomaterials with enhanced performance.

### Recent Progress

At this stage of the project (second year), we have concentrated the efforts on (1) the fabrication of surface- and grain boundary-clean nanograined ceramics and (2) on the measurement unprecedented data on the surface and grain boundary energies of those samples using highly sensitive calorimetric techniques. The selected materials were YSZ and  $\text{MAl}_2\text{O}_4$  spinels ( $M = \text{Zn}, \text{Mg}$  or  $\text{Ni}$ ).

#### 1. Yttria Stabilized Zirconia (YSZ)

Extensive research has been carried out on the radiation damage of pure zirconia, partially and fully stabilized zirconia [11-15]. Zirconia displays impressive resistance to radiation damage, and amorphization could not be observed upon high doses of irradiation (680 dpa with up to 400 keV  $\text{Xe}^+$  irradiation) in cubic fully stabilized  $\text{ZrO}_2$ . Some reports have suggested that nanosized zirconia shows a completely different response to irradiation. Meldrum et al. have [4, 5] shown that  $\text{ZrO}_2$  crystalline nanoparticles (<5 nm) can be fully amorphized after irradiation at doses as low as 1 dpa. From a thermodynamics perspective, one may attribute this different response to irradiation of the nanoparticles to their interface energies. That is, it's known that the polymorphic stability at the nanoscale is controlled by the relative interface energies of the polymorphs, as the interface term becomes a significant fraction of the total free energy.

In fact, there was not enough data on the interface energy of zirconia in the literature to back up a systematic correlation between grain boundary energy and radiation tolerance. We started our research by synthesizing 10YSZ (10 mol%) using a co-precipitation method, and obtaining nanograined samples using the technique called Spark Plasma Sintering (high heating rates associated with high pressures to allow densification of the compact while retaining the grain size). Nanograined samples with grain sizes as low as 25 nm were fabricated free of contaminations [16].

The nanograined sample was then subjected to a heating cycle inside a differential scanning calorimeter. The heat released during the process of grain growth was then associated with the microstructural changes, such that the grain boundary energy for 10YSZ could be calculated. Figure 3 shows the DSC curve indicating states before and after the exothermic peak associated with grain growth. SEM images are also shown at those stages and were used to estimate the grain size in each step.

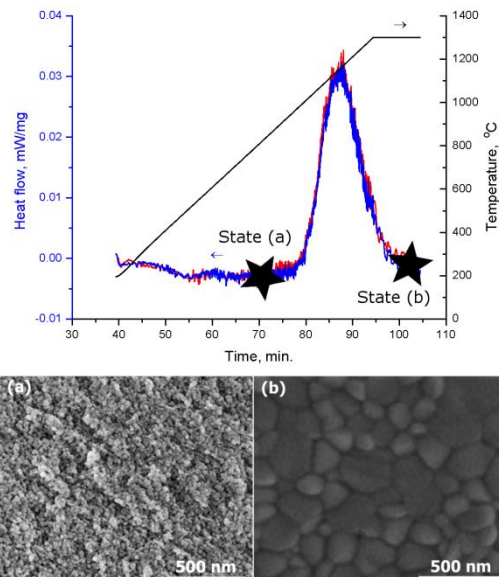


**Figure 3.** (top) DSC curve for grain growth of 10YSZ revealing distinguishable exothermic effect. (bottom) SEM showing grain sizes for the samples at state (a) and (b) as indicated in the figure.

The grain boundary energy for this composition was determined to be  $1.00 \pm 0.29 \text{ J.m}^{-2}$ . With this data in our hands we have then synthesized and sintered 3 different sets of samples: (1) fully dense 10YSZ with grain size of 25 nm, (2) fully dense 10YSZ with grain size of 38 nm, (3) fully dense bulk 10YSZ. The goal is to generate samples with different excess energies and then subject it to irradiation at the Los Alamos National Laboratory with 400 keV  $\text{Kr}^+$  to check if the nanoscale samples are more radiation tolerant to amorphization than the bulk sample and correlate with the proposed theory. Grain growth will also be studied during irradiation.

Mg and Ca-doped zirconia are also under study in our laboratories, and we are concentrated on getting nanosized samples that are fully stabilized cubic zirconia. This is to facilitate the future works on irradiation, as the presence of second phases (monoclinic and tetragonal) would complicate the analysis of the data. We have used the co-precipitation method to obtain both of them at the required condition (a paper is being prepared on those unprecedented syntheses), and we will next access both surface and grain boundary energies, followed by SPS to produce fully dense nanograined cubic zirconia.

## 2. Zinc Aluminate ( $\text{ZnAl}_2\text{O}_4$ )

Spinel structures have been considered of special interest for inert matrix materials to dispose radioactive materials due to their usual stability against ballistic displacements caused by neutron or low energy dose when in the bulk form [17]. This resistance has been attributed to several factors [18]: (1) the spinels' chemistry causes an enlargement of the critical size for the dislocation loop nucleation; (2) their structure generates constraints prohibiting dislocation loops from unfauling (faulted interstitial loops remain poor sinks for interstitial absorption when compared to unfaulted ones); and (3) spinels can readily accommodate disordering defects within their structures, such that cation sublattices can be completely disordered by irradiation. These features turn the interstitial-vacancy recombination a highly efficient point defect annihilation mechanism in spinel structures.

There is limited literature on the effect of radiation on nanocrystalline spinels. Shen et al. have reported on the radiation tolerance on nanocrystalline partially inversed spinel  $\text{MgGa}_2\text{O}_4$  [3]. By using irradiation with 300 keV  $\text{Kr}^{++}$  ions and estimating the radiation damage by Monte Carlo, it was observed that the nanocrystalline. Though there is not much data on the interface energies of spinel structures, the thermodynamic hypothesis described above seems to perfectly fit the observed data as interface energies of spinels are expected to be lower than that for other structure types. That is, based on a careful review of available data on surface energy of spinel and other structures, Navrotsky et al. [10] have recently reported that spinels commonly have lower surface energies than metals, rocksalt oxides, and trivalent oxides of the same metal. Though there is not a direct correlation between surface and grain boundary energy, it is reasonable to assume that the grain boundary energies of spinel structures are also relatively low.

In this work, we started with  $\text{ZnAl}_2\text{O}_4$  for testing the hypothesis. Nanosized particles of the aluminate were prepared by the polymeric precursor method, and both surface and grain boundary energies measured by calorimetry. Though surface energies have not direct influence in our hypothesis, it does have effects on the thermodynamic stability of the nanoparticles [19]. So, if nanoparticles are dispersed in polymeric matrixes, for instance, for shielding of radiation, this is key information. The surface energy was studied by using a water adsorption microcalorimetry methodology specially designed during this project to measure surface energy of virtually any oxide composition. The method is based on the thermodynamics of water adsorption on the oxide surface, and both anhydrous and hydrated surface energies (at different water coverage) can be determined (Figure 4). Using nanoparticles with 25 nm, we determined the surface energy of  $\text{ZnAl}_2\text{O}_4$  to be  $1.36 \pm 0.08 \text{ J.m}^{-2}$ . This is within the range for reported data for spinels but is the first time it was directly measured. We also used high temperature oxide melt solution calorimetry to measure the surface energy and got essentially the same result but with larger error bar  $1.29 \pm 0.33 \text{ J.m}^{-2}$ . Using the same methodology, we have assessed the contribution of the solid-solid interfaces to the *powder*, and showed that its energy is relatively low. This is because these boundaries were formed during calcination (not sintering), which typically leads to low energy (when compared to grain boundaries formed during sintering) agglomerations. As a

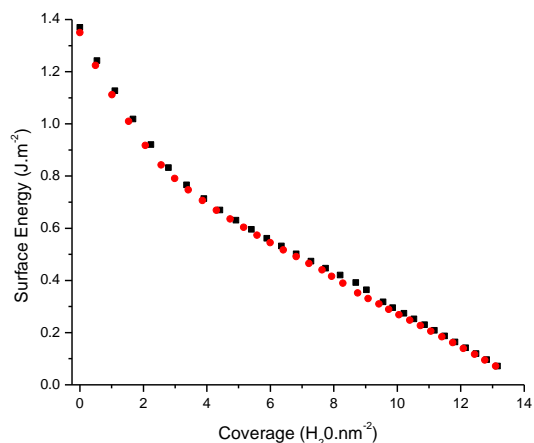


Figure 4. Surface energy for zinc aluminate at different water coverages determined by water adsorption microcalorimetry.

next step, we are prepared SPS sintered zinc aluminate to both measure the enthalpy of grain boundary and expose to irradiation to evaluate the tolerance to amorphization.

Other spinels are also under preparation, such as  $\text{MgAl}_2\text{O}_4$  and  $\text{NiAl}_2\text{O}_4$ . The first has been synthesized using both co-precipitation and polymeric precursor method and we discovered a strong influence of the synthesis method on the sintering behavior, as reported [20]. The nickel aluminate was also synthesized by both methods, but only co-precipitation was observed to produce small particle sizes suitable for sintering and calorimetry. Nickel deficiency was a constant during the synthesis, which is a common behavior for spinels, but we fixed this by using chemical strategies. A paper is also under preparation regarding the synthesis topic.

## References

- [1] Ackland G. Controlling Radiation Damage. *Science*. 2010;327:1587-8.
- [2] Bai XM, Voter AF, Hoagland RG, Nastasi M, Uberuaga BP. Efficient Annealing of Radiation Damage Near Grain Boundaries via Interstitial Emission. *Science*. 2010;327:1631-4.
- [3] Shen TD, Feng S, Tang M, Valdez JA, Wang Y, Sickafus KE. Enhanced radiation tolerance in nanocrystalline  $\text{MgGa}_2\text{O}_4$ . *Applied Physics Letters*. 2007;90.
- [4] Meldrum A, Boatner LA, Ewing RC. Size effects in the irradiation-induced crystalline-to-amorphous transformation. *Nucl Instrum Methods Phys Res Sect B-Beam Interact Mater Atoms*. 2003;207:28-35.
- [5] Meldrum A, Boatner LA, Ewing RC. Nanocrystalline zirconia can be amorphized by ion irradiation. *Phys Rev Lett*. 2002;88:4.
- [6] Kachurin GA, Ruault MO, Gutakovskiy AK, Kaitasov O, Yanovskaya SG, Zhuravlev KS, et al. Light particle irradiation effects in Si nanocrystals. *Nucl Instrum Methods Phys Res Sect B-Beam Interact Mater Atoms*. 1999;147:356-60.
- [7] Shen TD. Radiation tolerance in a nanostructure: Is smaller better? *Nucl Instrum Methods Phys Res Sect B-Beam Interact Mater Atoms*. 2008;266:921-5.
- [8] Rose M, Balogh AG, Hahn H. Instability of irradiation induced defects in nanostructured materials. *Nucl Instrum Methods Phys Res Sect B-Beam Interact Mater Atoms*. 1997;127:119-22.
- [9] Jiang Q, Lu HM. Size dependent interface energy and its applications. *Surface Science Reports*. 2008;63:427-64.
- [10] Navrotsky A, Ma CC, Lilova K, Birkner N. Nanophase Transition Metal Oxides Show Large Thermodynamically Driven Shifts in Oxidation-Reduction Equilibria. *Science*. 2010;330:199-201.
- [11] Debelle A, Moll S, Decamps B, Declémy A, Thome L, Sattonnay G, et al. Ability of cubic zirconia to accommodate radiation damage. *Scripta Materialia*. 2010;63:665-8.
- [12] Moll S, Thome L, Sattonnay G, Debelle A, Garrido F, Vincent L, et al. Multistep damage evolution process in cubic zirconia irradiated with MeV ions. *Journal of Applied Physics*. 2009;106.
- [13] Thome L, Moll S, Sattonnay G, Vincent L, Garrido F, Jagielski J. Radiation effects in cubic zirconia: A model system for ceramic oxides. *Journal of Nuclear Materials*. 2009;389:297-302.
- [14] Moll S, Thome L, Garrido F, Vincent L, Sattonnay G, Costantini JM, et al. Radiation effects in yttria-stabilized zirconia: Comparison between nuclear and electronic processes. *Nucl Instrum Methods Phys Res Sect B-Beam Interact Mater Atoms*. 2008;266:3048-51.
- [15] Sickafus KE, Matzke H, Hartmann T, Yasuda K, Valdez JA, Chodak P, et al. Radiation damage effects in zirconia. *Journal of Nuclear Materials*. 1999;274:66-77.
- [16] Quach DV, Castro RHR. Direct measurement of grain boundary enthalpy of cubic yttria-stabilized zirconia by differential scanning calorimetry. *Journal of Applied Physics*. 2012;112:083527 (5 pp.)- (5 pp.).
- [17] Wang LM, Gong WL, Wang SX, Ewing RC. Comparison of ion-beam irradiation effects in  $\text{X}_2\text{YO}_4$  compounds. *Journal of the American Ceramic Society*. 1999;82:3321-9.
- [18] Sickafus KE, Minervini L, Grimes RW, Valdez JA, Ishimaru M, Li F, et al. Radiation tolerance of complex oxides. *Science*. 2000;289:748-51.
- [19] Castro RHR. On the thermodynamic stability of nanocrystalline ceramics. *Materials Letters*. 2013;96:45-56.
- [20] Rufner J, Anderson D, Van Benthem K, Castro RHR. Synthesis and sintering behavior of ultrafine (< 10 nm) magnesium aluminate spinel nanoparticles. *Journal of the American Ceramic Society*. Submitted.

## **Deformation and Failure Mechanisms of Shape Memory Alloys (DOE Grant DE--SC0003996, 4/15/2010--4/15/2015)**

Principal Investigator: Samantha Daly (samdaly@umich.edu)  
Department of Mechanical Engineering  
Department of Materials Science and Engineering  
2350 Hayward Street, The University of Michigan, Ann Arbor, Michigan 41809

### **Program Scope**

We are exploring the fundamental mechanics that drive the deformation and failure of shape memory alloys (SMAs). SMAs are difficult materials to characterize because of the complex solid-to-solid phase transformations that give rise to their unique properties, including shape memory and superelasticity. These phase transformations occur across multiple length scales and result in a large hysteresis loop, which allows these materials to store or dissipate substantial amounts of energy. Our current efforts focus on new methodologies that will provide the first quantitative, full-field characterizations of phase transformation across multiple length scales. We are working on utilizing new combinations of microscopy, diffraction, optical metrologies, and custom testing equipment to study phase transformation processes at a wide range of length scales, including very small length scales with fields of view on the order of tens of microns.

We have chosen to examine Nickel-Titanium as a representative shape memory alloy. In addition to being the most widely used SMA, it is also a very good example of the fact that nearly all materials are dependent on multi-scale interactions; thus the lessons that we are learning are representative of, and applicable to, a wide class of materials. Here, atomic interactions, sub-granular transformation, intra-granular interactions, localized strain banding, and macroscopic behavior are all closely linked. We expect that the quantitative information from our experiments will be especially useful to the numerous theoretical and computational studies of shape memory alloys that are currently underway. In addition, the new experimental methodologies that we are developing are applicable to a wide range of future investigations into the mechanics of strain localization and small-scale deformations.

### **Recent Progress**

#### *Structural Deformation Modes*

We recently finished a study of bending on superelastic shape memory alloys tubes. Bending is a fundamental deformation mode of practical importance for SMAs, but there are few pure bending experiments in the literature and none that are compared to pure tension and compression responses on the same material. We performed isothermal experiments on superelastic NiTi tubes in tension, compression, and large rotation pure bending using custom-designed fixturing. We found that due to strain localizations from transformation, plane sections did not remain plane locally, causing Euler-Bernoulli beam theory to under/over predict the local strain by as much as 2x. However, if one averages the later strain profile over a few diameters of tube length, the Euler-Bernoulli assumptions can be used as a reasonable approximation in this (averaged) sense. Using the uniaxial tension/compression data as inputs, Euler-Bernoulli beam theory successfully captured the measured moment-average curvature response and neutral axis evolution during loading up to the end of the moment plateau, provided tension-compression asymmetry was included. Thus, despite the existence

of strain localization and the local highly non-linear strain profiles in bending, reasonable global moment-curvature predictions could still be achieved by suitable homogenization of the strain fields along the axial direction. These observations have several implications for further research and device applications as detailed in (Reedlunn et al. 2013).

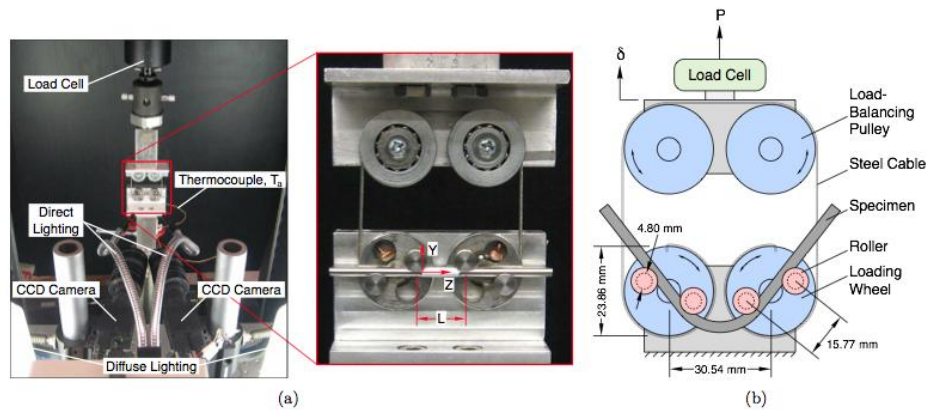


**Figure 1: Macroscopic (bending) setup; custom apparatus.**

### Fatigue

We have made substantial progress towards understanding the low-cycle fatigue behavior of stress-induced martensitic phase transformation at the meso- and macro- scales, focusing on the effects of strain rate and texture. The rich local thermo-mechanical interactions that underlie transformation were examined through the use of simultaneous three-dimensional Digital Image Correlation (strain fields) and infrared imaging (thermal fields). Digital Image Correlation, or DIC, is an *in situ* method that measures displacements (and thus Lagrangian strain) on the surface of an object by tracking and correlating a random pattern on the sample surface. This non-contact approach to material characterization is somewhat analogous to putting tens of thousands of contiguous strain gages over the entire specimen surface, except that by using digital image correlation we can calculate the full-field strain as a “snapshot” in time and with much higher resolution than through the use of strain gages (which are locally averaged).

Through macroscopic experiments, we quantified the complex local interactions between latent heat and the extent of transformation, and explored the characteristics of the phase fronts and the evolution of phase volume fraction. We discovered and quantified, for the first time, a remarkable amount of strain memory in the martensite phase that forms in the wake of the phase transformation front and most interestingly, persists in the martensite from cycle to cycle. This memory indicates that the local elastic stress fields in the martensite are driven by a dislocation structure and martensitic nuclei that largely stabilize during the first loading cycle. In a practical sense, it means that the manner in which martensite transforms in the first cycle will very strongly dictate how it transforms in later cycles; i.e., there seems to be little adjustment in transformation possible after cycling has started, and the initial microstructure is a critical factor in long-term fatigue performance. We have also found that the extent of this transformation similarity in the martensite – while strong for all textures – becomes particularly strong in textures that are unfavorable for transformation. In order to understand the reasons for this similarity in martensitic transformation, we needed to examine the microstructural length scale.

### Small-Scale Behavior

In order to examine small-scale phase transformation behavior, we developed a combined technique utilizing deformation tracking under Scanning Electron Microscopy. This methodology was first conceived by Sutton's group from USC in 2007; we took his approach as an initial baseline and

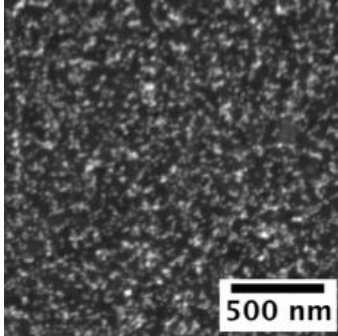


**Figure 2: New pattern deposition method using chemically functionalized nanoparticles for unprecedented spatial resolution.**

have spent significant effort to redevelop it for increased accuracy and for the functionality we needed. In order for this to work successfully at the small fields of view that we require, we first needed to create a method for applying a random, isotropic pattern of “tracking markers” approximately 1-50 nanometers in size. We developed a reliable, inexpensive, and widely applicable method to do this by using functionalized nanoparticles (Kammers et al., 2013a), which to our knowledge enables unprecedented pattern resolution. We have also

developed an extensive set of corrections for the complex spatial and temporal distortions that occur in SEM images. Details and validation of our methodology can be found in (Kammers et al., Exp Mech, 2013b).

We are now using this approach to examine phase transformation at the microstructural length scale and its relation to underlying crystallography (Kimiecik et al, Materials Letters, 2013). These experiments represent the first full-field, quantitative studies of phase transformation at the microstructural length scale. As such they have yielded a wealth of information even in these initial stages. From our early measurements, we have determined that martensitic transformation is extremely heterogeneous at the microstructural length scale. Transformation does not proceed in a grain-to-grain domino effect as has been postulated, but rather will skip over entire grains or portions of grains as it proceeds. It also proceeds by a transformation front that, when viewed on the microstructural length scale, appears to be quite diffuse. One question of interest is what drives the diffusivity of this transformation front, and how microstructure can affect energetic barriers to transformation. A representative image of the transformation front proceeding at the grain level is shown in Figure 3, where the white lines represent grain boundaries (obtained from aligned and concurrent EBSD). Currently, we are investigating the effect of texture and are focusing on point-by-point sub-grain analysis of these measurements, including examining the effect of (Euclidean) distance from the grain boundaries, grain size, grain boundary misorientation (inclusive of martensite variants), residual plastic deformation, and other microstructural markers.

### **Future Plans**

There are two main areas for the future work funded by this award – small-scale aspects of phase transformation (with a focus on the effect of crystallographic texture) and the fracture properties of SMAs (both macroscale and microscale).

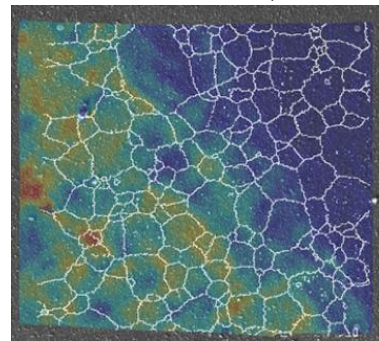


**Figure 3: Phase transformation at the microstructural length scale. White are grain boundaries; phase transformation is advancing from the bottom left with yellow/red representing primarily martensitic regions. Please see abstract pdf for color.**

A current focus is to characterize the micromechanics of phase transformation during superelastic deformation and provide insights into, and validation benchmarks for, the microstructural evolution (particularly intergranular interactions) that are central to constitutive theories of phase transformation. We are now able to characterize a local cluster of grains – including local deformation behavior and degree of martensitic transformation – and also know the displacement boundary conditions from the intragranular constraints on the outer edges of this cluster. A main aim of these experiments is to characterize the effect of microstructure, relative grain size, and boundary conditions on the ability of these alloys to store/dissipate energy on the small scale, and to provide experimental knowledge that we can directly tie into current theoretical and numerical modeling. We know that crystallographic texture plays a large role in transformation – from our earlier macroscale experiments, textures that are unfavorable for transformation lead to greater fidelity in the martensitic transformation from cycle to cycle. We plan to investigate, using small-scale approaches, exactly why this occurs. We also plan to investigate the interactions between favorable textures for slip and favorable textures for transformation at the microscale, and quantify their impact on transformation and superelastic behavior.

In terms of fracture, we will examine the interplay between fracture mechanisms and phase transformation at both the macroscopic and microscopic length scales. An experimental setup capable of measuring and quantifying phase transformation during macroscopic, dynamic fracture has been constructed and tested on brittle alumina. One aim is to examine the contribution of phase transformation towards shielding the crack tip. Another aim is to examine microstructural influences on fracture (using controlled crack growth) via a world-unique combination of ultrasonic fatigue and scanning electron microscopy, which has been designed and is currently in the build stage, with plans for implementation in Spring 2013. We are also mid-way through the creation of a computer code that will analyze local values of fracture toughness from micro-scale measures of deformation, to be used for analysis of the resulting information.

#### **Journal Publications (April 2010-current, accepted or in print):**

1. A. Kammers, S. Daly. Sub-Micron Patterning for Digital Image Correlation under Scanning Electron Microscopy, *Experimental Mechanics*, *Accepted*, 2013a.
2. A. Kammers, S. Daly. Digital Image Correlation under Scanning Electron Microscopy: Methodology and Validation. *Experimental Mechanics*, *Submitted*, 2013b.
3. B. Reedlunn, C. Churchill, E. Nelson, J. Shaw, S. Daly. Tension, Compression, and Bending of Superelastic Shape Memory Alloy Tubes. *JMPS*, *Accepted*, 2013.
4. K. Kim, S. Daly. The Effect of Texture on Stress-Induced Martensite Formation in Nickel-Titanium. *Smart Materials and Structures*, *Submitted*, 2013.
5. M. Kimiecik, J.W. Jones, S. Daly. A New Methodology for Tracking Phase Transformation in SMAs at the Microstructural Length Scale. *Materials Letters*, 95: 25-29, 2013.
6. A. Kammers, S. Daly. Small-Scale Patterning Methods for Digital Image Correlation Under Scanning Electron Microscopy. *Meas. Sci. Technol.* 22(12) 125501, 2012.
7. K. Kim, S. Daly. Martensite Strain Memory in the Shape Memory Alloy NiTi under Mechanical Cycling. *Invited publication: Experimental Mechanics* 51(4): 641-652, 2011. **(M. Hetényi Award for the best paper published in Experimental Mechanics in 2011).**

## Molecular-Reinforced Hybrid Glass Films with Superior Thermo-Mechanical Properties

Reinhold H. Dauskardt  
Department of Materials Science and Engineering  
Stanford University  
Stanford, CA 94305 – 4034  
dauskardt@stanford.edu

### Program Scope

Our DoE-BES supported research addresses fundamental questions related to the mechanical and fracture properties of nanostructured hybrid glass films that have application for emerging nanoscience and energy technologies. *The hybrid films can be processed from a range of organo-silane and selected metal-alkoxide precursors and exhibit unique electro-optical properties while maintaining excellent chemical and thermal stability, in some compositions to 400°C.* The resulting amorphous molecular networks contain organic and inorganic components. Applications include antireflective and ultra-barrier layers in photovoltaics and display technologies, microelectronic interlayer dielectrics, optical waveguides, and high-performance coupling layers in laminates.

Hybrids are limited primarily by their inherently mechanically fragile nature which remains a fundamental challenge for their integration and application. Mechanical and fracture properties are controlled by the molecular structure and connectivity of the molecular precursors and how they form an extended molecular network. Their inherently fragile nature derives from the brittle inorganic glass component and the incorporation of *univalent* (terminal) groups which dramatically reduce glass network connectivity. We have made significant progress on our DoE-BES program to develop a fundamental understanding of how these variables govern even such basic mechanical properties as elastic stiffness and cohesive fracture.

Our research also involves the complex interaction of reactive chemical and photon environments with the hybrid film which leads to unexpected mechanical and fracture behavior. Hybrids represent a rich area for future fundamental materials discovery with significant technological impact.

### Recent Progress

We report recent progress in several areas toward our goal of understanding the fundamental connection between hybrid molecular structure and mechanical behavior.

**Network Connectivity and Plasticity in a-SiC:H:** Amorphous hydrogenated a-SiC:H hybrids exhibit excellent thermal, chemical stability and resistance to moisture-assisted cracking. We investigated the cohesive fracture energies of a-SiC:H thin films as a function of the average molecular coordination number, a measure of network connectivity characterized by both NMR and RBS. a-SiC:H thin films with stoichiometric compositions (C/Si ~1) exhibited decreasing cohesive energies with coordination numbers (**Fig. 1**) similar to the trend in other hybrid glasses. However, a-SiC:H films with non-stoichiometric compositions (C/Si~5) showed greater cohesive fracture energies regardless of their low average coordination numbers than those of stoichiometric thin films with higher values. In particular, one of the non-stoichiometric films exhibited markedly increased cohesive fracture energy (~9.5J/m<sup>2</sup>), even greater than that of

dense silica glasses (**Fig. 1**). The increased fracture energy was due to crack-tip plasticity as evidenced by a) significant pileup formation during nanoindentation, b) fracture energy dependence on film thickness, and c) a NMR peak corresponding to  $sp^3$  polymeric  $CH_x$  chains. We showed further that the amount of crack-tip plasticity contribution to cohesive fracture energy can be tailored by controlling the fraction of  $sp^3$   $CH_x$  chains to network Si-C bonds. This offers a promising approach to toughen hybrids, particularly if the network connectivity can be increased at the same time.

**Toughening Thin-Film Structures with Amorphous Silicon Carbide Hybrids:** Crack tip plasticity plays a crucial role in the fracture behavior of materials. The same is true for the adhesion of interfaces in thin-film structures, where *absent* plasticity, fracture occurs at low fracture energy. Plasticity can be conferred to weak interfaces from embedded adjacent ductile metal films. However, toughening is often fundamentally limited because of the strong size-dependent plasticity in metal films. Alternatively, polymer thin films exhibit little size-dependent plasticity but are mechanically weak and have low thermal stability.

We recently demonstrated that the amorphous silicon carbide (a-SiC:H) hybrids described above with carbon-rich non-stoichiometric compositions and plastic properties can overcome these limitations and markedly toughen weak interfaces (**Fig. 2**). We showed that by embedding the elastic-plastic a-SiC:H films in structures that contain weak interfaces (in this case the weak interface between SiCN and another nanoporous organosilicate hybrid layer), the interface adhesion could be increased by a factor of 3 to 7 (**Figs. 3**). At these film thicknesses, metal films would not have been effective as toughening layers. The far more effective toughening from the a-SiC:H hybrid films is due to their unique deformation behavior.

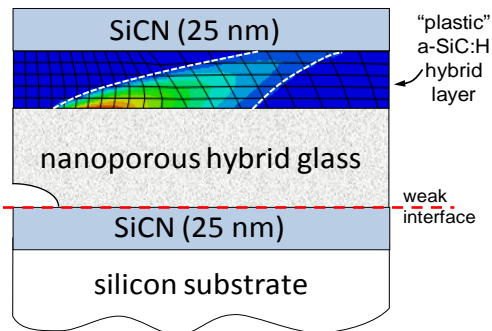


**Fig. 2:** Thin-film structure showing how an embedded a-SiC:H hybrid film that exhibits plastic deformation (FEA results showing plastic strains) can toughen another nearby interface.

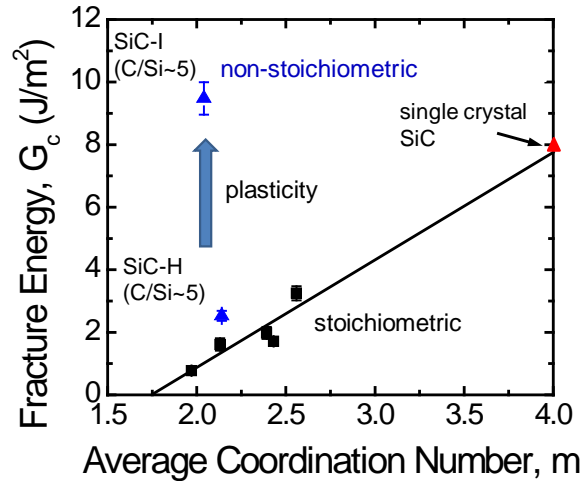


**Fig. 1:** Cohesive fracture energy a-SiC:H thin films as a function of average coordination number. A non-stoichiometric film exhibits significantly increased fracture energy due to crack tip plasticity.

To our knowledge, this is the first time that such **significant toughening** by adjacent plasticity has been achieved at such small nanometer sized dimensions. The multi-functionality of the ceramic-like a-SiC:H hybrid films together with their excellent thermal stability and chemical resistance open new avenues to improved mechanical durability of nanoscale device structures capable of surviving harsh processing/operating environments.

**Hybrid Glasses on Plastic Substrates:** Silica based hybrid glasses were deposited by atmospheric plasma using a newly developed high temperature precursor delivery system for depositing high boiling point organosilicate precursors, to our knowledge, for the first time. The coating deposition rate, molecular

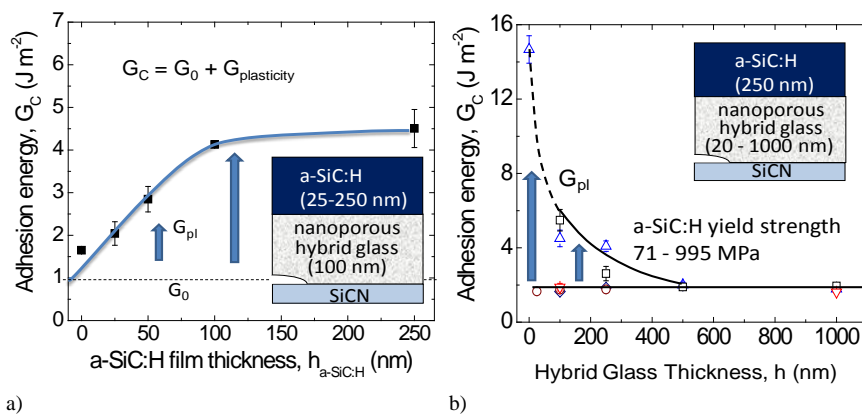


**Fig. 3:** Toughening film structures with embedded "plastic" hybrid a-SiC:H layers showing the effect of a) the a-SiC:H film thickness, and b) the adjacent hybrid glass layer thickness and the yield strength of the a-SiC:H film itself.

calculation), together with a large variation of the mechanical properties. The Young's modulus of the SiOC coatings ranged from 6 to 34 GPa, depending strongly on the coating density (**Fig. 4**). The adhesion of the coatings on plastics was affected by chemical structure of the precursor and the extent of exposure of the plastic substrate to the plasma during the initial stage of deposition.

**Cross-Linked Polycarbosilane (CLPCS) Hybrid Films:** CLPCS thin films are siloxane-free hybrids and we have been interested to understand their mechanical properties and particularly their sensitivity to moisture-assisted cracking. We found that the elastic constant (9.2 GPa) and cohesive fracture resistance ( $3.8 \text{ J/m}^2$ ) of the films substantially exceed those of traditional lower density sol-gel organosilicate hybrids (e.g. 4.8 GPa,  $2.1 \text{ J/m}^2$ ) and even higher density CVD produced films (8.1 GPa,  $3.2 \text{ J/m}^2$ ). We described the behavior in terms of the unique molecular structure of the films that consists of both stiff Si-C bonds and flexible  $\text{sp}^3$  C-C bonds. Perhaps most notably, we showed that the films show a remarkable insensitivity to moisture-assisted cracking, which could never be achieved by traditional organosilicate glasses containing siloxane bonds susceptible to moisture-attack. CLPCS hybrid films are potential novel materials for emerging nanoscience and energy applications that need protection from moisture and harsh environments.

### Future Plans

Specific objectives of our future research include the possibility of creating hybrid glasses with *hyper-connected* molecular structures for enhanced mechanical stiffness and fracture properties, attempting to confer plasticity to higher-coordinated hybrids to produce elastically stiff *and* ductile hybrid glasses, controlling the moisture-sensitive and insensitive bonds in hybrids to disproportionately effect moisture-assisted cohesive cracking behavior, grading the through-thickness hybrid film molecular structure and composition to enhance cohesive fracture

network structure, density, Young's modulus and adhesion to plastics exhibited a strong dependence on the precursor delivery temperature and rate, and the functionality and number of silicon atoms in the precursor molecules. The carbon content of the coatings could be tuned from zero to 85 atomic percent (excluding H in the

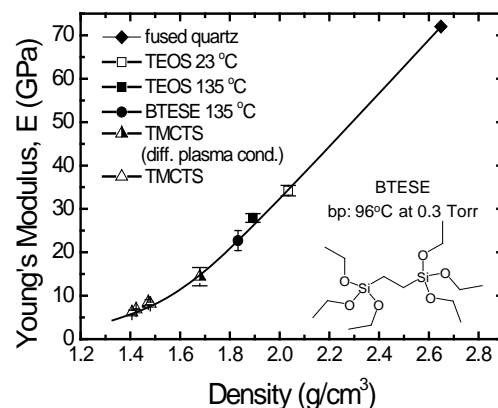


**Fig. 4:** Atmospheric plasma deposited organosilicate transparent hybrids from high and low boiling point precursors showing the effect of hybrid glass density on resulting Young's modulus.

properties, and finally to explore the effects of UV radiation and chemically active environments on the fundamental mechanisms of bond rupture and fracture resistance with the ultimate goal of designing mechanically robust hybrid glass films.

### DoE Program Publications

1. Y. Matsuda, S.W. King, R.H. Dauskardt, "Tailored Amorphous Silicon Carbide Barrier Dielectrics by Nitrogen and Oxygen Doping," **Thin Solid Films**, 2013. In press.
2. Y. Matsuda, S.W. King, M. Oliver, R.H. Dauskardt, "Moisture-Assisted Cracking and Atomistic Crack Path Meandering in Oxidized Hydrogenated Amorphous Silicon Carbide Films," **J. Applied Physics**, 2013. In press.
3. L. Cui, A.N. Ranade, M.A. Matos, L.S. Pingree, T.J. Frot, G. Dubois, R.H. Dauskardt, "Atmospheric Plasma Deposited Dense Silica Coatings on Plastics," **ACS Applied Materials and Interfaces**, 4, 6587–6598, 2012.
4. Y. Matsuda, J Rathore, L. Interrante, R. H. Dauskardt, G. Dubois, "Moisture-Insensitive Polycarbosilane Films with Superior Mechanical Properties", **Applied Materials and Interfaces**, 4, 2659–2663, 2012.
5. Vitali Brand, Kemal Levi, M. McGehee and Reinhold H. Dauskardt, "Film Stresses and Metal Electrode Buckling in Organic Bulk Heterojunction Solar Cells," **Solar Energy Materials and Solar Cells**, 103, 80–85, 2012.
6. R. Jia, S. Dong, T. Hasegawa, J. Ye, R.H. Dauskardt, "Contamination and moisture absorption effects on the mechanical properties of catalyst coated membranes in PEM fuel cells", **International Journal of Hydrogen Energy**, 37, 6790-6797, 2012.
7. V. Brand, C. Bruner, R.H. Dauskardt, "Cohesion and Device Reliability in Organic Bulk Heterojunction Photovoltaic Cells," **Solar Energy Mat. and Solar Cells**, 99, 182–189, 2012.
8. Y. Matsuda, S.W. King, J. Bielefeld, J. Xu, R. H. Dauskardt, "Fracture Properties of Hydrogenated Amorphous Silicon Carbide Dielectric Thin Films", **Acta Materialia** 60, 682-691, 2012.
9. R. Jia, B. Han, K. Levi, T. Hasegawa, J. Ye, R.H. Dauskardt, "Mechanical durability of proton exchange membranes with catalyst platinum dispersion", **Journal of Power Sources**, 196(20), 8234-8240, 2011. (Note: incomplete acknowledgement. It should read "This work was supported by the Director, Office of Energy Research, Office of Basic Energy Sciences, Materials Sciences Division of the U.S. Department of Energy, under contract no. DE-FG02-07ER46391.)
10. M.S. Oliver, G. Dubois, M. Sherwood, D.M. Gage, R.H. Dauskardt "Molecular origins of the mechanical behavior of hybrid glasses," **Advanced Functional Materials** 20 [17], 2884-2892, 2010.
11. MS Oliver, Dubois G, Dauskardt RH, "Molecular Design of Ultra-Low-k Hybrid Glasses", **Proceeding of the IEEE International Interconnect Technology Conference**, Burlingame, CA, June 7-9 2010. (Note: incomplete acknowledgement. It should read "This work was supported by the Director, Office of Energy Research, Office of Basic Energy Sciences, Materials Sciences Division of the U.S. Department of Energy, under contract no. DE-FG02-07ER46391.)
12. Y. Matsuda, S. W. King, J. Bieffield and R.H. Dauskardt, "High Toughness and Moisture Insensitive Hydrogenated Amorphous Silicon Carbide Films for MEMS/NEMS", **ECS Transactions**, 33 (8), 257-261, Las Vegas, Nevada, 2010.
13. Y. Matsuda, S. W. King, J. Bieffield and R.H. Dauskardt, "Mechanical Properties of Hydrogenated Amorphous Silicon Carbide Thin Films", **Proceeding of the IEEE International Interconnect Technology Conference**, Burlingame, CA, June 7-9, 2010.
14. T. Kim and R. H. Dauskardt, "Molecular Mobility under Nanometer Scale Confinement," **Nano Letters**, 10(5), 1955-1959, 2010.
15. D. M. Gage, L. M. Peng, J. Stebbins, K. S. Yim, A. Al-Bayati, A. Demos, and R. H. Dauskardt, "Effects of e-beam curing on glass structure and mechanical properties of nanoporous organosilicate thin films," **International Journal of Materials Research**, 101, 228-235, 2010.

**Program title: Inferring grain boundary properties from heterogeneous data**

PI: Michael J. Demkowicz

<demkowicz@mit.gov>

Department of Materials Science and Engineering, Massachusetts Institute of Technology  
Cambridge, MA 02139

The goal of this project is to build analysis tools that infer accurate and general grain boundary (GB) crystallography-property relations with rigorously quantified uncertainty by assembling partial but complementary data readily obtainable with existing experimental and modeling methods. Currently available techniques for studying GB properties, whether through experiments or modeling, are incomplete and uncertain. The novel contribution of this project is to integrate these techniques—within the framework of Bayesian inference—into an analysis tool that infers accurate and general GB crystallography-property relations with rigorously quantified uncertainty from a heterogeneous database of partial but complementary data. This tool may be used address questions such as:

- What is the incremental utility of specific new measurements or simulations for improving a GB crystallography-property relation? Which ones should be prioritized?
- What investigation strategy arrives at a desired level of accuracy in representing GB crystallography-property relations with least expenditure of resources?
- How can the efforts of an entire research community be evaluated, integrated, and guided to achieve maximum improvement in GB crystallography-property relations?

This project inherently confronts very large and diverse data sets spanning all the time- and length-scales accessible to experimental and modeling investigations of GBs. It therefore draws on the expertise of principal investigator Michael Demkowicz as well as co-PIs Christopher Schuh (MIT Department of Materials Science and Engineering) and Youssef Marzouk (MIT Department of Aeronautics and Astronautics). Modeling of GBs at scales ranging from atoms to polycrystals is conducted by postdocs Akbar Bagri and Lin Li and PhD student Oliver Johnson, Bayesian analysis is conducted by PhD student Raghav Aggarwal, and experiments are performed by postdoc Matteo Seita.

This project began in September of 2012. Accomplishments to date are summarized below.

1) *Initiation of work on model problem: Ga penetration into polycrystalline Al.* We have selected gallium penetration into GB networks in fiber-textured polycrystalline aluminum as a model problem because of the abundance of both modeling and experimental data available on it. This problem is therefore a convenient starting point for developing the analysis tools we envisioned. Our goal is for these tools to be applicable to other classes of GB-controlled properties as well.

2) *Completed project staffing:* The project supports three postdocs and two PhD students.

Collaborations:

We envision extensive use of BES user facilities, specifically x-ray sources such as the Advanced Photon Source (APL) and the National Synchrotron Light Source (NSLS and NSLS-II). This work will build on existing collaborations with P. Kenesei (ANL), R. Suter (CMU), and S. Gill (BNL) initiated through other programs.

## **Designing Nanoscale Precipitates in Novel Cobalt-based Superalloys to Improve Creep Resistance and Operating Temperature**

Principal Investigator: Prof. David C. Dunand  
Institution: Northwestern University  
Postal Address: Northwestern University, 2220 Campus Drive, Cook Hall  
Telephone Number: (847) 491-5370  
Email: [dunand@northwestern.edu](mailto:dunand@northwestern.edu)

Co-Principal Investigator: Prof. David N. Seidman  
Institution: Northwestern University  
Postal Address: Northwestern University, 2220 Campus Drive, Cook Hall  
Telephone Number: (847) 491-4391  
Email: [d-seidman@northwestern.edu](mailto:d-seidman@northwestern.edu)

Co-Principal Investigator: Prof. Chris Wolverton  
Institution: Northwestern University  
Postal Address: Northwestern University, 2220 Campus Drive, Cook Hall  
Telephone Number: (847) 467-0593  
Email: [c-wolverton@northwestern.edu](mailto:c-wolverton@northwestern.edu)

### **Program Scope**

Ni-base superalloys are the material of choice for high-temperature structural applications. Ni alloys are especially prevalent in the aeronautics industry for use as single crystal turbine blades as well as turbine disks. The favorable high-temperature properties of Ni-based superalloys are the result of a two-phase microstructure consisting of ordered  $L1_2$  precipitates ( $\gamma'$ -phase) embedded in a disordered f.c.c. matrix ( $\gamma$ -phase). Conventional cobalt-base superalloys have long been utilized in mid-level temperature ranges for jet-engine turbine applications but do not approach the operating temperatures of Ni alloys. Cobalt alloys do not exhibit high-temperature due to their lack of a two-phase microstructure such as Ni and thus are strengthened through solid solution and the addition of carbides.

A recent advancement in Co alloys occurred in 2006, when it was discovered that a  $\gamma + \gamma'$  two-phase structure analogous to Ni alloys could be formed in the Co-Al-W system (Sato et al. Science; 2006 March;312(5770): 90-91.). The goal of this project is to further advance the new Co-superalloy by studying the microstructure, kinetics, and mechanical properties of various Co-base superalloy systems. These goals are being achieved through collaboration with the National Institute of Standards and Technology (NIST), NASA, and Lawrence Livermore National Lab (LLNL).

### **Recent Progress**

#### *Experimental:*

An initial atom-probe tomographic (APT) study was conducted on a high volume fraction Co-9.7Al-10.8W alloy aged at 900°C for 1,006 h. SEM micrograph and atom-probe reconstructions of this alloy are shown in Figure 1. Compositional measurements of the  $\gamma$  and  $\gamma'$ -phases and interfacial excess were measured from these reconstructions. The compositional measurements for both Al and W in the  $\gamma$ -phase agreed well with the proposed phase diagram found in the literature (Sato et al. Science; 2006 March;312(5770): 90-91.), whereas the  $\gamma'$  was found to be ~0.5 at. % more rich in W than shown in the literature. This work has recently been accepted for publication in *Scripta Materialia*.

APT has also been used to study ternary alloy more dilute in Al and W: A Co-8.8Al-7.3W alloy has been aged at 650°C from 10 min to 4,096 h as well as at 900 °C (up to 256 h). APT measurements conducted on samples aged at 650°C for 4-4,096 h demonstrate that the  $\gamma$ -phase composition of a Co alloy aged at 650°C is much more depleted in Al and W than the  $\gamma$ -phase composition from samples aged at 900°C: the Al and W concentrations of samples aged at 650°C were measured at 6.7 and 0.5 at. % respectively, compared with 8.9 and 5.7 at.% respectively, for samples aged at 900°C. The change in phase composition over time from 4 to 4,096 h in the 650°C sample also demonstrates that the slow diffusing W, with an initial composition of ~1.5 at% at 4 hours, continuously partitions to the  $\gamma$ '-phase, suggesting that precipitation is kinetically limited. Future work will include characterizing the composition and microstructure at earlier aging times.

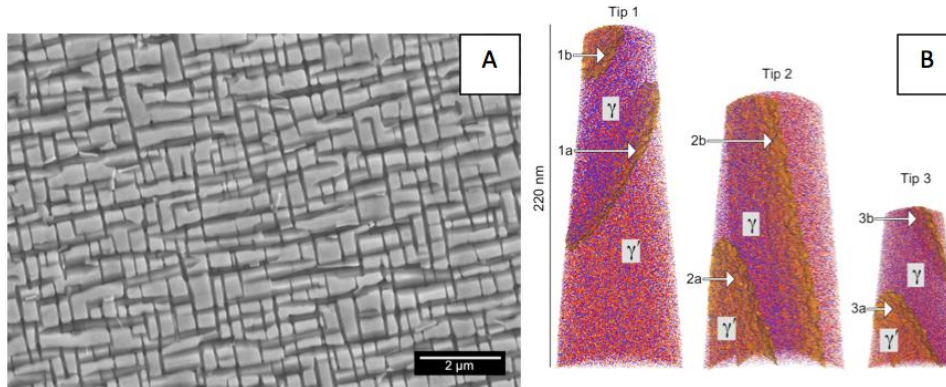


**Figure 1:** A) Secondary electron SEM micrograph of etched Co-9.7Al-10.8W aged at 900 °C for 1,006 h.  $\gamma'$  is indicated by the lighter cuboid shapes whereas the  $\gamma$ -phase is indicated by the darker channels. B) 3-D APT reconstruction of 3 microtips, where the  $\gamma/\gamma'$  interfaces are represented by an isoconcentration surface of 8.6 at. % W. Arrows refer to each interface Co, Al and W are represented in blue, red, and orange respectively.

#### *DFT Calculations:*

The anti-phase boundary (APB) energy is an important thermodynamic quantity in the study of  $\gamma/\gamma'$  strength in Ni-based superalloys. We had previously calculated APB energies for  $\text{Co}_3\text{W}$  and  $\text{Co}_3\text{Al}$  L1<sub>2</sub> for 001 and 111 APB's as an approximation for those in  $\text{Co}_3(\text{Al}_{0.5}\text{W}_{0.5})$ , which are given in Table 1;  $\text{Ni}_3\text{Al}$ 's APB energies are shown for comparison. We have now completed calculations for the 001 APB energy in  $\text{Co}_3(\text{Al}_{0.5}\text{W}_{0.5})$  itself, also given in Table 1, using a super-cell approach to describe the Al/W solid solution present at the APB. The 111  $\text{Co}_3(\text{Al}_{0.5}\text{W}_{0.5})$  APB energy appears to be near the average of the 111 APB energies of  $\text{Co}_3\text{W}$  and  $\text{Co}_3\text{Al}$ . The 001  $\text{Co}_3(\text{Al}_{0.5}\text{W}_{0.5})$  APB energy, on the other hand, is more positive than either those of  $\text{Co}_3\text{W}$  and  $\text{Co}_3\text{Al}$ , suggesting there are some critical interactions between W and Al giving rise to unique APB energetics in this particular direction. Future work will focus on studying the effect of quaternary alloying elements on the  $\text{Co}_3(\text{Al}_{0.5}\text{W}_{0.5})$  APB energy.

**Table 1: 001 and 111 APB energies in  $\text{mJ/m}^2$ . The anisotropy ratio is defined as 111/001.**

	$\text{Co}_3\text{W}$	$\text{Co}_3\text{Al}$	$\text{Co}_3(\text{Al}_{0.5}\text{W}_{0.5})$	$\text{Ni}_3\text{Al}^*$
<b>001</b>	72	-72	153	82
<b>111</b>	412	-18	253	177
<b>An. Ratio</b>	5.72	0.25	1.65	2.16

- Manga et al. *J. Appl. Phys.* 2010;108:103509.

The stability of the  $\gamma/\gamma'$  two-phase field is of critical importance in the application of Co-superalloys, as  $\gamma'$  precipitates are primarily responsible for the mechanical strength of the alloy. The thermodynamic stability of the ternary  $\text{Co}_3(\text{Al}_{0.5}\text{W}_{0.5}) \gamma'$  has been questioned after diffusion couple and bulk annealing experiments have observed the decomposition of  $\gamma'$  into HCP Co, B2 CoAl, and  $\text{D0}_{19} \text{Co}_3\text{W}$  (Kobayashi et al. *Intermetallics*; 2009 Dec;17(12):1085–9., Tsukamoto et al. *Materials Science Forum*. 2010 Jun;654-656:448–51.). From DFT using a special quasi-random (SQS) approach to describe the Al/W disordered solid solution, we had previously predicted the stability of  $\text{Co}_3(\text{Al}_{0.5}\text{W}_{0.5}) \gamma'$  at 0K ( $\Delta E_{\text{Stab}}$ ), lying 66 meV/atom above the three phase mixture of HCP Co, B2 CoAl, and  $\text{D0}_{19} \text{Co}_3\text{W}$ .

Since then, we have extended this work beyond 0K to include finite-temperature effects to the free energy to explore the possibility that  $\text{Co}_3(\text{Al}_{0.5}\text{W}_{0.5}) \gamma'$  is stabilized at higher temperatures where it is commonly observed. Specifically, at 1200 K, we have predicted contribution to the free energy of stability from lattice vibrations ( $\Delta F_{\text{vib}} = -27$  meV/atom) with the frozen-phonon supercell approach, from configurational entropy of Al/W mixing ( $\Delta F_{\text{Config}} = -27$  meV/atom), and from thermal electronic excitations ( $\Delta F_{\text{el}} = -10$  meV/atom) with the one-electron and temperature-independent bands approximations. These contributions are all predicted to enhance the stability of  $\gamma'$ . Given values for the free energy of stability ( $\Delta E_{\text{Stab}} = 66$  meV/atom) and free energy of defects ( $\Delta E_{\text{Defect}} = -7$  meV/atom), the total free energy for  $\text{Co}_3(\text{Al}_{0.5}\text{W}_{0.5}) \gamma'$  is -5 meV/atom. This value is almost positive, meaning that, although  $\text{Co}_3(\text{Al}_{0.5}\text{W}_{0.5}) \gamma'$  is very close to being stable at 1200 K.

### *Dislocation Dynamics Modeling*

Dislocation dynamics simulations were run for edge, screw, super-edge, and super-screw dislocation types for precipitate radii of 12.5, 31.5, and 63.0 nm at volume fractions of  $f = 5, 10, 20, 40, 60, 70, 80 \%$ , using material properties from the Ni-base superalloy Nimonic PE16. An example of a simulation is shown in Figure 2, and the results of all simulations are shown in Figure 3, where the increase in the critical resolved shear stress (CRSS) is plotted vs. the average edge-to-edge precipitate distance. The results indicate that a superalloy is more likely to shear from a pair of super-dislocations, consistent with experimental observations.

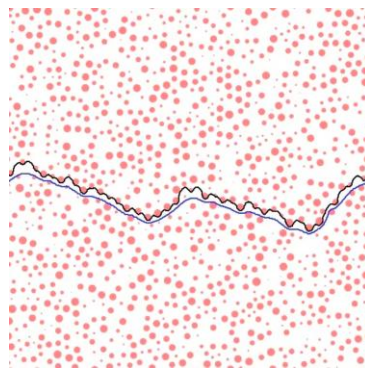


**Figure 2: Simulation of a superdislocation moving through a precipitate field with a volume fraction of 40%.**

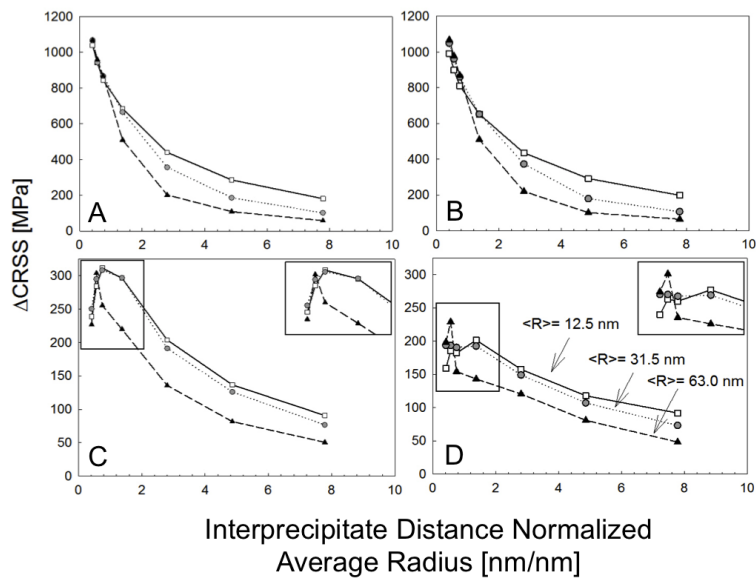


**Figure 3: Increase in CRSS of A) single edge B) single screw C) super edge and D) super screw dislocations due to precipitation strengthening from Nimonic PE16 as a function of average interprecipitate distance normalized to  $\langle R \rangle$ .**

### Future Work

Future experimental work will focus on examining the mechanical and microstructural properties of Co-Ni-Al-W, Co-Al-W-B-Zr, Co-Ni-Al-W-Ti, and Co-Al-W-Ti-B alloys through atom-probe tomography, SEM, differential thermal analysis (DTA), microhardness, and compression creep testing which will be compared with results obtained through dislocation dynamics simulations. Each of these alloys, which has already been cast, was designed to improve upon the Co-Al-W ternary system through either grain boundary strengthening in the case of B and Zr additions, elevating the solvus temperature in the case of Ti, and increasing  $\gamma'$  stability in the case of Ni.

Density functional theory will be further implemented to predict the effect of alloying elements on the  $\text{Co}_3(\text{Al}_{0.5}\text{W}_{0.5}) \gamma'$  APB energies as well as to predict potential  $\text{Co}_3(\text{Al}_{0.5}\text{W}_{0.5}) \gamma'$  stabilizing alloying elements from high-throughput DFT.

Dislocation dynamics modeling will be improved in two major ways. The first will be to start implementing 3-D microstructures obtained from APT to simulate experimentally informed microstructure. The second advancement will be to begin using the 3-D dislocation dynamics simulation ParaDIS code in collaboration with Lawrence Livermore National Lab (LLNL).

### Publications

Saal JE, Wolverson C., Thermodynamic Stability of Co-Al-W L1<sub>2</sub> gamma prime, *Acta Materialia* 2013; 61(7): 2330-2338.

Bocchini PJ, Lass EA, Moon KW, Williams ME, Campbell CE, Kattner UR, Dunand DC, Seidman DN, Atom-probe tomographic study of gamma/gamma prime interfaces and compositions in an aged Co-Al-W superalloy. *Scripta Materialia* 2013; 68(8):563-566.

# Response of Simple, Model Systems to Extreme Conditions

GRANT #DE-FG02-97ER45656

Rodney C. Ewing<sup>1,2,3</sup> (Principal Investigator, [rodewing@umich.edu](mailto:rodewing@umich.edu))  
Maik Lang<sup>1</sup> (Co-Investigator, [mklang@umich.edu](mailto:mklang@umich.edu))

<sup>1</sup>Department of Earth & Environmental Sciences

<sup>2</sup>Department of Materials Science & Engineering

<sup>3</sup>Department of Nuclear Engineering & Radiological Sciences

The University of Michigan

1100 N. University Avenue

Ann Arbor, Michigan 48109-1005

## PROGRAM SCOPE

The emphasis of the proposed research is on the application of high-pressure/high-temperature techniques, together with intense energetic ion beams, to the study of the behavior of simple oxide systems (e.g.,  $\text{SiO}_2$ ,  $\text{GeO}_2$ , and  $\text{Ln}_2\text{O}_3$ ) under extreme conditions. The structural response of solids to pressures of up to 1 Mbar, temperatures of up to several thousand Kelvin, and the extreme energy density generated by energetic heavy ions (tens of keV/atom) is in general complex and depends on material-specific properties, such as chemical composition, structure, bond-type and electronic properties. This program will focus on the response of simple stoichiometries as unique model systems with multiple structural “outcomes”, establishing the basic knowledge required for the prediction of the response of more complex structures to extreme conditions. Key to the research program is a recently developed method, allowing the simultaneous coupling of irradiation, pressure and temperature by injecting relativistic heavy ions through mm-thick anvils of diamond-pressure cells (Fig. 1). The experimental approach includes additional high-pressure techniques, for example, multi-anvil apparatuses, for the synthesis of high-pressure polymorphs, and intense heating lasers, for temperature application to pressurized samples. Structural modifications induced by different extreme conditions will be characterized by a number of complementary advanced analytical techniques. The transparency of the diamond windows to x-rays, infrared and visible light allow for *in situ* (i.e., at high pressure and high temperature) spectroscopic and diffraction measurements. After pressure release, materials will be investigated by a variety of *ex situ* microbeam methods (e.g., high-resolution transmission electron microscopy and high-angle annular dark field imaging).

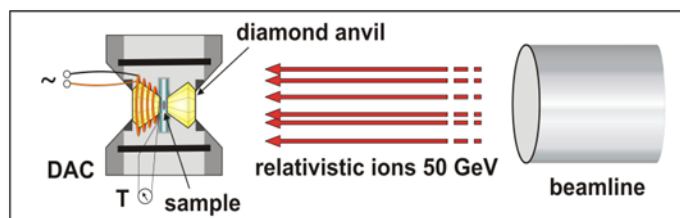


**Fig. 1:** Scheme of high-pressure irradiation experiments with relativistic heavy ions. In order to reach the sample (size  $\sim 100 \mu\text{m}$ ) pressurized between two diamond anvils, the initial beam energy must be  $\sim 50 \text{ GeV}$ . Temperature can be controlled by heating wires or intense heating lasers (not shown).

## RESEARCH PROGRESS

A range of rare earth sesquioxides samples,  $\text{Ln}_2\text{O}_3$ , has been used to study systematically the effect of structure and chemistry on a materials' response to energetic heavy ion irradiation. This class of simple oxides is characterized by a pronounced polymorphism of different high-pressure and high-temperature phases. Hexagonal ( $\text{La}_2\text{O}_3$  and  $\text{Nd}_2\text{O}_3$ ) and cubic ( $\text{Sm}_2\text{O}_3$ ,  $\text{Gd}_2\text{O}_3$ ,  $\text{Ho}_2\text{O}_3$ ,  $\text{Tm}_2\text{O}_3$ , and  $\text{Lu}_2\text{O}_3$ ) starting materials have been irradiated with 185-MeV Xe and 2.2-GeV Au ions and analyzed by means of synchrotron X-ray diffraction (XRD). Radiation-induced crystalline-to-crystalline transformations have been observed for most of the oxide samples concurrent with amorphization. Transmission electron microscopy (TEM) is ongoing; however, it is evident that the observed damage morphology and structural modifications are linked to the phase and chemistry of the starting material. Ion-induced crystalline-to-crystalline phase transitions have been reported previously only for a limited number of materials, such as  $\text{ZrO}_2$  and  $\text{HfO}_2$ . Simple oxides appear to be particularly sensitive to this type of radiation response, which opens interesting possibilities to the use of ion beams for nanoscale modifications, in particular, in rare earth sesquioxides with important technologically applications owing to their unique physical and chemical properties.

To investigate the effect of temperature on ion-track formation in simple oxides,  $\text{SiO}_2$  samples have been irradiated over a temperature range of 200 and 640 °C using 2.2 GeV Au ions. The quartz was cut parallel to the c-axis, leading to a track alignment perpendicular to the crystal's c-axis. Reference samples, irradiated at room temperature, underwent the same heat cycles as the samples irradiated at elevated temperatures. For characterization of the track radii, Small Angle X-Ray Scattering (SAXS) measurements were carried out at the Australian Synchrotron. The track radius increases as a function of irradiation temperature with 0.1 nm/100 K (Fig. 2). The reference samples also exhibit an increase in track radii, although about one order of magnitude lower than samples irradiated at high temperature. This small increase is possibly a result of heat-induced stress relaxation. The increase in track radii for the high temperature irradiated samples is predominately attributed to the conditions during track formation, which has been confirmed by thermal spike calculations as well as molecular dynamics simulations. At elevated temperatures, the energy required for the melting of  $\text{SiO}_2$  is lowered and thus the melting radius or equivalently the ion track radius is increased. Additional high-temperature experiments have been completed by using a novel sample-preparation technique, together with advanced TEM. Latent tracks created by 80 MeV-Xe ions in apatite have been successfully imaged along their entire length. *In situ* thermal annealing experiments within the TEM revealed that damage recovery significantly increases as the track diameter decreases along the ion trajectory from an initial diameter of 8.9 nm to ~1.5 nm at the track end (track length ~8.1  $\mu\text{m}$ ).

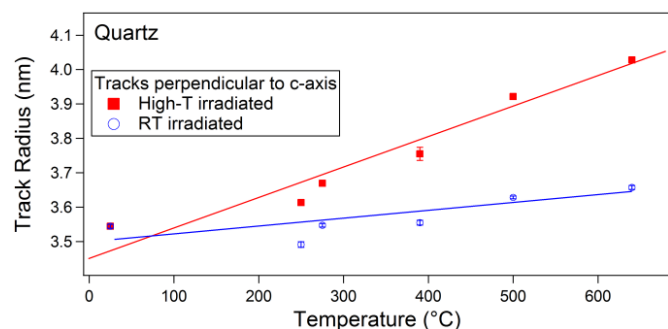


**Fig. 2:** Track radii of 2.2-GeV Au ions in  $\text{SiO}_2$  deduced from SAXS data of samples irradiated at room temperature (blue circles) and at high temperatures (red squares).

The slowing down of energetic ions in matter is characterized by electronic excitation and ionization. The deposited energy in the electronic subsystem is converted into atomic motion *via* electron-phonon coupling. Doped perovskite samples have been irradiated with energetic Au and U ions to investigate track-formation and its dependence on the electronic properties of a material, specifically electric resistivity. The resistivity in SrTiO<sub>3</sub> dramatically decreases with the addition of low concentrations of Nb (0, 0.1 and 1 wt %), covering the entire electronic regime from an insulating to a conducting material. SAXS and TEM demonstrated independently that track-formation is insensitive to changes in the electric resistivity in this perovskite over at least seven orders of magnitude (Fig. 3). Hence, other electronic material properties, such as bond type (metallic *vs.* covalent or ionic) or electron density, may be responsible for the observed radiation-resistance increase from insulators to metals. The electron density did not change significantly in SrTiO<sub>3</sub> after doping with Nb, and was with  $\sim 10^{20}$  cm<sup>-3</sup> for 1% Nb still low compared with the number of excited electrons within a track core ( $\sim 10^{22}$  cm<sup>-3</sup>). Within this research program, high-pressure irradiations are an important alternative for the study of track formation within a solids modified electronic landscape. *In situ* TEM studies of low-energy (1-MeV Kr) ion irradiations show that the doping with Nb of up to 1% has only a minor influence on radiation-induced amorphization as a result of subtle structural variations of incorporated impurity atoms.

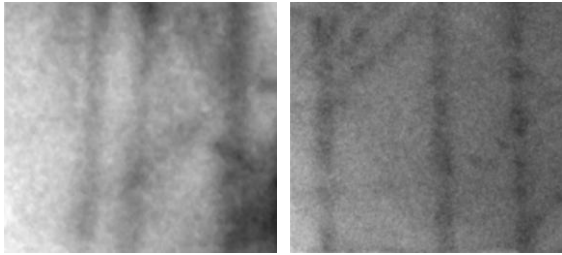


**Fig. 3:** Bright-field TEM images of SrTiO<sub>3</sub> (left) un-doped and (right) doped with 1% Nb after irradiation with 2.0-GeV uranium ions at room temperature. Tracks of about 6 nm in diameter were observed independently of the doping with Nb ions. The TEM micrographs are 100 x 100 nm<sup>2</sup>.

## FUTURE RESEARCH PLANS

The coupling of high-pressure techniques and high-energy ion beams is in general complex and involves beamtimes at several user facilities. We have preliminary results on the interplay of irradiation and high pressure revealing dramatic effects in simple oxides. Synchrotron XRD experiments confirmed that highly densified vitreous GeO<sub>2</sub> irradiated with relativistic heavy ions at a pressure of 50 GPa was transformed into a crystalline, disordered hexagonal phase. We plan to further investigate such structural modifications by exposing other simple oxides (*e.g.*, SiO<sub>2</sub>) at extreme pressures to the enormous energy deposition of energetic heavy ions. The role of the starting phase, amorphous *vs.* crystalline, will be an important aspect of the future research program. The synthesis of the GeO<sub>2</sub> high-pressure phase with the NiAs-structure is in general difficult to obtain by conventional high-pressure\ temperature experiments. It is therefore interesting to evaluate the utilization of ion beams at high pressure as a new means to synthesize metastable simple-oxide phases. The rare earth sesquioxides with preliminary results of ion-induced phase transitions at ambient pressure are interesting target materials for such studies.

The radiation response of single oxides will be investigated with respect to their initial structure by exposing a range of SiO<sub>2</sub> and GeO<sub>2</sub> polymorphs to swift heavy ions. Coesite and stishovite have been already successfully synthesized from fused silica glass in a multi-anvil press at high-pressure and high-temperature conditions. We plan to irradiate both polymorphs together with quartz, amorphous SiO<sub>2</sub>, and the high-temperature phase tridymite. This approach provides with different structure types by keeping the chemical composition unchanged.

Irradiation experiments at high pressure will be used to study additionally the effect of thermodynamic boundary conditions on ion-matter interactions. For example, if stishovite is less radiation resistant than quartz at 1 bar, irradiation experiments at 10 GPa (within the stability field of stishovite) will identify the influence of structure and thermodynamic constraints. It will be of particular interest to test whether crystalline-to-crystalline phase transformations among different polymorphs can be triggered within the tracks of energetic heavy ions. All material modifications will be characterized by complimentary analytical techniques, such as synchrotron XRD and Raman spectroscopy.

## REFERENCES WITHIN RESEARCH PROGRAM

- [1] W.X. Li, L.M. Wang, K. Sun, M. Lang, C. Trautmann, and R.C. Ewing: *Porous fission fragment tracks in fluorapatite*, Phys. Rev. B **82** (2010) 144109.
- [2] J.M. Zhang, J. Lian, F. Namavar, J.W. Wang, H. Haider, K. Garvin, and R.C. Ewing: *Nanosized rutile TiO<sub>2</sub> thin film upon ion irradiation and thermal annealing*, J. Phys. Chem. C **115** (2011) 22755-22760.
- [3] J.W. Wang, Z. Rak, F.X. Zhang, R.C. Ewing, and U. Becker: *Electronic structure and energetics of tetragonal SrCuO<sub>2</sub> and its high-pressure superstructure phase*, J. Phys.: Condens. Matter **23** (2011) 465503.
- [4] B. Afra, M. Lang, M.D. Rodriguez, J.M. Zhang, R. Giulian, N. Kirby, R.C. Ewing, C. Trautmann, M. Toulemonde, and P. Kluth: *Annealing kinetics of latent particle tracks in Durango apatite*, Phys. Rev. B **83** (2011) 064116.
- [5] W.X. Li, L.M. Wang, M. Lang, C. Trautmann, and R.C. Ewing: *Thermal annealing mechanisms of latent fission tracks: Apatite vs. zircon*, Earth Planet Sci. Lett. **302** (2011) 227-235.
- [6] W.X. Li, Y.B. Chen, J.M. Zhang, L.M. Wang, and R.C. Ewing: *Controlling the structure and size of Au-nanocrystals by annealing and ion sputtering*, Langmuir **28** (2012) 51-55.
- [7] A. Bengtson, R.C. Ewing and Udo Becker: *He diffusion and closure temperatures: A density functional theory investigation*, Geochimica et Cosmochimica Acta **86** (2012) 228-238.
- [8] F.X. Zhang, M. Lang, J.M. Zhang, Z.Q. Cheng, Z.X. Liu, J. Lian and R.C. Ewing: *Phase transition and abnormal compressibility of lanthanide silicate with the apatite structure*, Physical Review B **85** (2012) 214116 (6 pages).
- [9] W.X. Li, M. Rodriguez, P. Kluth, M. Lang, N. Medvedev, M. Sorokin, J.M. Zhang, B. Afra, and R.C. Ewing: *Effect of doping on the radiation response of conductive Nb-SrTiO<sub>3</sub>*, submitted to Nucl. Instrum. and Methods B (2013).
- [10] D. Schauries, M. Lang, B. Afra, M.D. Rodriguez, O.H. Pakarinen, K. Nordlund, C. Trautmann, M. Toulemonde, R.C. Ewing, N. Kirby, and P. Kluth: *Temperature dependent formation of ion tracks in natural quartz and apatite*, (2013) in preparation.
- [11] J.M. Zhang, M. Lang, M. Toulemonde, M. Costantini, and R.C. Ewing: *Radiation effects in TiO<sub>2</sub> and ZrO<sub>2</sub> induced by C<sub>60</sub>-clusters ions*, (2013) in preparation.
- [12] M. Lang, F.X. Zhang, J.M. Zhang, D. Severin, C. Trautmann, and R.C. Ewing: *Structural modifications in Ln<sub>2</sub>O<sub>3</sub> induced by swift heavy ions*, (2013) in preparation.

# Multiscale Mechanical Properties and Alloy Design

## Principal Investigators

E. P. George, H. Bei, Y. F. Gao, J. R. Morris, Y. N. Osetskiy, G. M. Pharr

Materials Science and Technology Division, Oak Ridge National Laboratory, Oak Ridge, TN 37831.

[georgeep@ornl.gov](mailto:georgeep@ornl.gov), [beih@ornl.gov](mailto:beih@ornl.gov), [gaoy@ornl.gov](mailto:gaoy@ornl.gov), [morrisj@ornl.gov](mailto:morrisj@ornl.gov), [osetskiyyn@ornl.gov](mailto:osetskiyyn@ornl.gov), [pharrgm@ornl.gov](mailto:pharrgm@ornl.gov)

## Program Scope

This program aims to develop fundamental understanding of mechanical behavior across multiple length scales in metals. Of special interest are new mechanical phenomena, including size effects on mechanical properties and mechanical responses of multi-element (high-entropy) alloys that challenge conventional notions of solid solubility. Interesting size effects occur at several different length scales, but our near-term focus is on small-scale mechanical behavior. Over the long term, our goal is to understand the physical mechanisms of interaction across multiple length scales in multicomponent alloy systems. The observed relationships between mechanical properties and microstructural features (controlled, as needed, by innovative processing techniques and characterized by state-of-the-art microanalytical tools) are used to model and develop fundamental understanding of deformation and fracture processes. This understanding will lead to the formulation of broad scientific principles for the design of advanced metallic materials for use in a variety of next-generation energy conversion and structural applications.

## Recent Progress

A few highlights of our research since the last PI Meeting in 2010 are provided below. A partial list of publications resulting from this project is provided at the end of this abstract.

### *Understanding the compression behavior of micropillars in terms of their dislocation structures*

Our earlier compression tests on Mo-alloy micropillars produced by directional solidification of NiAl-Mo eutectic composites had shown that as-grown pillars yielded at the theoretical stress whereas pre-strained pillars yielded at much lower stresses. In addition, the yield and flow behaviors changed from stochastic to deterministic with increasing pre-strain. To gain microstructural insight into this behavior, scanning transmission electron microscopy was performed on Mo-alloy fibers extracted from the NiAl matrix, both in the as-grown state and after different amounts of pre-strain. As shown in Fig. 1a, the as-grown fibers were largely dislocation-free. However, four isolated regions containing a few (2-5) dislocations in each region were observed over a total fiber length of 186  $\mu\text{m}$ . The mean spacing between such regions was determined to be 37  $\mu\text{m}$  (linear density of defects,  $\sim 3 \times 10^4 \text{ m}^{-1}$ ). Since the as-grown micropillars used for the compression experiments had much smaller gage lengths (1-3  $\mu\text{m}$ ) and diameters (360-1000 nm), they would be expected to contain no dislocations. This explains why they all yielded (deterministically) at the theoretical stress.

At the other extreme, pillars that were pre-strained to 11% and tested in compression also exhibited deterministic stress-strain curves (Fig. 1b). The main differences between these pillars and the as-grown ones were (i) their much lower yield strengths, and (ii) their ability to work harden. Figure 1b includes a representative STEM image showing a relatively high dislocation density,  $\sim 2.7 \times 10^{13} \text{ m}^{-2}$ , in a fiber subjected to 16% pre-strain. Examination of other regions indicated that this high defect density was uniformly distributed throughout. These microstructural observations explain why (i) fibers with high pre-strains (11-16%) have lower yield strengths than the as-grown fibers (many pre-existing dislocations so no need to nucleate new ones) and (ii) their stress-strain curves are very reproducible (because of the uniform distribution of dislocations).

At intermediate pre-strains (4%), the stress-strain curves are stochastic (Fig. 1c). Consistent with this, the STEM images shown alongside indicate that a

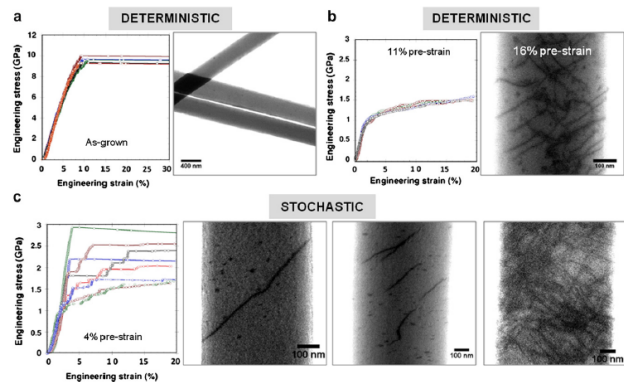


**Fig. 1** Dislocation structures and corresponding compressive stress-strain curves showing deterministic behavior for (a) 0% pre-strain (as-grown fibers), (b) 11/16% pre-strain, and (c) stochastic behavior for 4% pre-strain [1].

variety of dislocation distributions and densities are present in different fibers. In some cases, the fibers are practically dislocation-free (similar to the as-grown fibers) whereas in others the dislocation densities are very high (similar to those in the 16% pre-strained fibers). There are also many fibers with an intermediate dislocation density ( $\sim 3.9 \times 10^{12} \text{ m}^{-2}$ ). This inhomogeneous distribution of dislocations naturally leads to the stochastic stress-strain curves in Fig. 1c, where some are reminiscent of the as-grown fibers that yield at high stresses followed by large unstable pop-ins (Fig. 1a), others are reminiscent of fibers subjected to large pre-strains that yield at low stresses followed by stable work hardening (Fig. 1b), while the remainder exhibit a variety of stochastic responses in between these two extremes. Thus, the spatial inhomogeneities in the starting dislocation distributions determine the deformation behavior of micropillars in compression.

### Tensile stress-strain response of Mo-alloy fibers

In pure single-phase, single crystals, there are two inter-related length scales that affect size-dependent strengthening behavior: (i) the average spacing between dislocations ( $\lambda$ ), which is a material length scale set by the dislocation density ( $\lambda \sim \rho^{-0.5}$ ), and (ii) the specimen dimensions (diameter  $d$  and length  $l$ ). When  $d$  and  $l \ll \lambda$ , the probability of encountering a dislocation in the sample volume is small and the specimens yield at the theoretical stress as described above. Since  $\lambda \approx 37 \mu\text{m}$  in our as-grown fibers, as the specimen dimensions start approaching this value, one would expect to see an effect of the pre-existing dislocations on the stress-strain curves. Unfortunately, in compression, it is difficult for  $l$  to exceed  $\sim 10\%$  of this value since the maximum diameters of our fibers are in the range 1.0-1.5  $\mu\text{m}$ , which means that the maximum lengths that can be tested without the specimens buckling are on the order of 3-4  $\mu\text{m}$ . To overcome this limitation, we decided to test fibers in tension, which allows much longer lengths to be tested. The Mo-alloy fibers in directionally solidified NiAl-Mo eutectics were extracted by etching away the matrix and tested in the as-grown state, as well as after 4 and 16% pre-strain. The cross-sectional dimensions of the fibers ranged from 360-550 nm and the gage lengths ranged from 9-41  $\mu\text{m}$ .

Unlike the compression pillars which were only 1-3  $\mu\text{m}$  long, the tensile gage lengths (9-41  $\mu\text{m}$ ) were significant fractions of, or comparable to, the mean spacing between dislocations in the as-grown state (37  $\mu\text{m}$ ). Therefore, there was a high probability of dislocations being present in the as-grown tensile specimens. Consistent with this, Fig. 2 shows that there is considerable scatter in the yield strength, with one specimen yielding at close to the theoretical strength, some specimens yielding at close to the bulk strength and others at a variety of stresses in between. This is in sharp contrast to the case of micropillar compression where all the specimens yielded at the theoretical strength (Fig. 1a). With increasing pre-strain, the scatter decreases, until at 16% pre-strain, the tensile yield strengths are all clustered together, similar to the compressive yield strengths (Fig. 1b).

### Weak-link model of stochastic yielding

The simplest case to consider is a random spatial distribution of dislocations in one dimension. In material containing a limited number of dislocations, some specimens will be dislocation-free and yielding will require the nucleation of dislocations at the theoretical stress. Others will contain dislocations and yield at lower stresses.

The reduction in strength of specimens containing dislocations will depend on the (random) stresses needed to activate the different pre-existing dislocations. This randomness in the activation stresses can be modeled in a number of ways. Our approach is to assign random Schmid factors to each dislocation but the model can easily accommodate other types of randomness. First consider the case where all the dislocations have the maximum Schmid factor of 0.5. In this case, it is useful to think of the material as having two limiting strengths: a high theoretical strength,  $\sigma_0$  of  $\sim 10 \text{ GPa}$  (for dislocation-free specimens) and a lower bulk strength,  $\sigma_b$  of  $\sim 1 \text{ GPa}$  (for dislocation-containing specimens). Then, in the limit of a large number of tests, the average stress,  $\sigma_{\text{avg}}$ , is the weighted average of  $\sigma_0$  and  $\sigma_b$  where the weighting factors are, respectively, the probability of not finding a dislocation in the test specimen ( $p_0$ ) and the probability that there is at least one dislocation in the specimen ( $1-p_0$ ). That is,  $\sigma_{\text{avg}} = \sigma_0 p_0 + \sigma_b(1-p_0)$  and it can be shown that  $p_0 = e^{-\rho l}$ , where  $\rho$  is the dislocation density (which is related

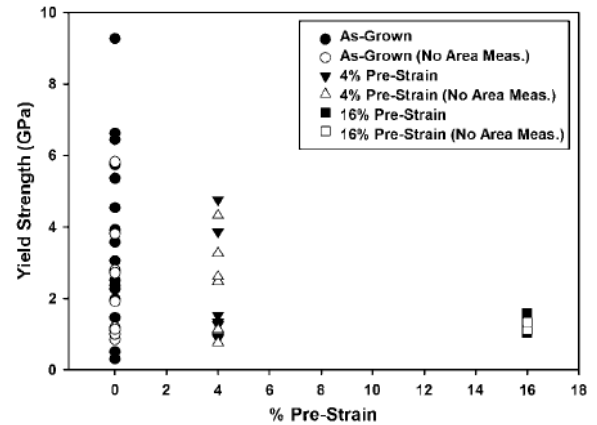


Fig. 2 Tensile yield strengths of Mo-alloy fibers as a function of pre-strain [2].

to the average spacing between dislocations,  $\lambda$ ) and  $l$  is the specimen length. This approach can be generalized to the case of yielding in the presence of dislocations with random Schmid factors between 0 and 0.5 by using the weak-link assumption and finding the dislocation with the highest Schmid factor. If the maximum Schmid factor in a given test specimen is so low that the yield strength calculated by our model is higher than the theoretical strength, then the yield strength is assumed to be the theoretical strength since it would be easier to nucleate a new dislocation than to move an existing one. Because of the two sources of randomness in our model, namely the random spatial distribution of dislocations and the random activation stresses, there is a continuous strength variation from the theoretical to the bulk, and the calculated yield strengths exhibit scatter at intermediate values of normalized specimen lengths,  $0.1 < l/\lambda < 10$  (or, equivalently,  $0.1 < \rho l < 10$ ). This scatter was treated analytically and a closed-form solution obtained for the 90% scatter bounds. The scatter can also be visualized using Monte Carlo simulations and, as shown in Fig. 3 (top), the two approaches yield very similar results. The distribution of strengths for a given value of  $l/\lambda$  is not Gaussian but is skewed to extremes of strengths depending on the value of  $l/\lambda$ . While this is an expected result for both small and large values of  $l/\lambda$  where the strengths skew towards the theoretical and bulk strengths, respectively, it is also surprisingly true at intermediate values of  $l/\lambda$  where, despite the considerable scatter, intermediate strengths are much less likely than high or low strengths. This is a consequence of yielding being a weak-link phenomenon, which requires that, in order to obtain intermediate strengths, all the dislocations in the specimen should have low Schmid factors, which is a low-probability event.

The above 1D model was extended to 2D by replacing the linear density of dislocations with an areal density and specimens of length  $l$  with those of area  $A$ . As before, we assumed a random spatial distribution of dislocations and orientations (Schmid factors) and determined the relevant dislocation and Schmid factor probabilities. The predictions of the 2D model can be directly compared with our experimentally determined yield strengths. The only parameters needed in the model are the theoretical and bulk strengths (which we assumed to be 10 and 1 GPa, respectively) and the dislocation densities in our materials, which were determined using STEM as described earlier. Figure 3 (bottom) shows the excellent agreement between our model and experimental data.

### ***Nanoindentation pop-in investigations of dislocation nucleation and activation***

Analogous to yielding in uniaxial tension and compression, elastic-plastic transitions occur during nanoindentation (at small scales) and are marked by sudden discontinuities (“pop-ins”) on the load-displacement curves. In single crystals with low dislocation densities indented with small spherical tips, incipient plasticity occurs when dislocations are homogeneously nucleated at stresses near the theoretical strength. However, when the indented volumes contain defects, pop-ins denote their activation at relatively low stresses, rather than dislocation nucleation. We developed a statistical model for pop-ins resulting from the activation of pre-existing dislocations [4] which predicted that pop-in stresses depend on the indenter radius for a given dislocation density. To verify this prediction, experiments were performed on single-crystal Mo utilizing indenter radii that varied over three orders of magnitude. The pop-in stresses ranged from the theoretical strength at small radii to one order of magnitude lower at large radii. At intermediate radii, the pop-in stresses exhibited wide stochastic variability which was accurately described by the model.

Our recent studies [5] have shown that pop-ins are extraordinarily sensitive to the polishing conditions employed prior to indentation. On an electropolished surface, pop-in was consistently observed for each indentation at the theoretical strength of the material. However, the pop-ins vanished completely when the surface was subsequently polished with 0.05  $\mu\text{m}$  alumina, a fine polishing medium that is often used to obtain mirror-finish on

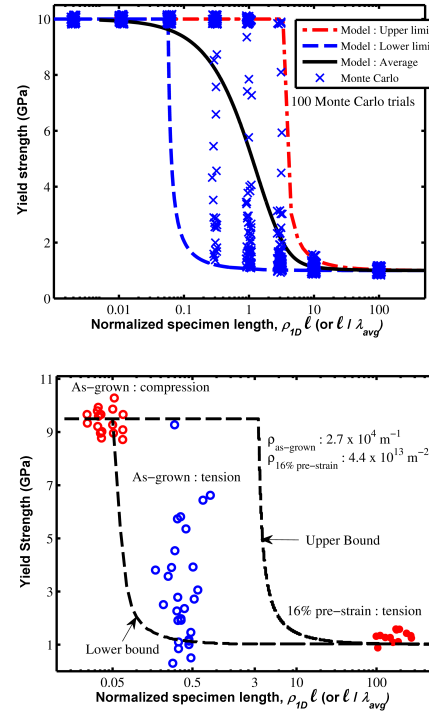


**Fig. 3** Comparison of the scatter in strength predicted by the model and Monte Carlo simulations (top), and comparison of the model predictions with experimental yield strengths of Mo-alloy fibers [3].

metals but introduces enough damage (surface steps and/or sub-surface dislocations) that plasticity occurs right from the start of indentation, at the smallest measurable loads and displacement. Thus, pop-in experiments used to measure quantities such as the stress for homogeneous dislocation nucleation must be performed with utmost care.

To investigate the effects of crystallography on the statistics of pop-in, nanoindentation was performed on nine differently oriented single crystals of NiAl within the [001] unit triangle [6]. This material was chosen because its {110}<001> slip avoids the complications of partial dislocation nucleation. In general, pop-in loads were lowest for indentation directions close to [111] and highest for those close to [001]. To understand this dependence, we analytically derived the stress fields in elastically anisotropic NiAl under Hertzian contact using the Stroh formalism coupled with a 2D Fourier transformation. This allowed us to determine an “indentation Schmid factor” which we defined as the maximum resolved shear stress under the indenter normalized by the maximum contact pressure, analogous to the conventional Schmid factor for uniaxial deformation. Good agreement was obtained between the experimental data and the theoretically predicted orientation dependence obtained from the indentation Schmid factor suggesting that homogeneous dislocation nucleation during spherical indentation is dominated by the maximum resolved shear stress.

### Future Plans

Effects of crystal structure on small-scale mechanical behavior will be studied by investigating the tensile properties of HCP and FCC fibers. In addition to the two length scales discussed above (specimen size and dislocation spacing) nanoscale precipitation in BCC fibers will be used to study the influence of another internal length scale on nano-mechanical behavior. Effects of processing and microstructure on the mechanical behavior of single-phase, FCC-structured, high-entropy alloys will be investigated.

### Partial list of DOE Sponsored Publications in 2010-2012

1. P. Sudarshan Phani, K. E. Johanns, G. Duscher, A. Gali, E. P. George, and G. M. Pharr, “Scanning Transmission Electron Microscope Observations of Defects in As-Grown and Pre-strained Mo Alloy Fibers,” *Acta Mater.* **59** (5) 2172-2179 (2011).
2. K. E. Johanns, A. Sedlmayr, P. Sudharshan Phani, R. Mönig, O. Kraft, E. P. George, and G. M. Pharr, “In-Situ Tensile Testing of Single Crystal Molybdenum Alloy Fibers with Various Dislocation Densities in a Scanning Electron Microscope,” *Journal of Materials Research* **27** (3) 508-520 (2012).
3. P. Sudarshan Phani, K. E. Johanns, E. P. George, and G. M. Pharr, “A simple stochastic model for yielding in specimens with limited number of dislocations,” *Acta Mater.* **61** (7) 2489-2499 (2013).
4. J. R. Morris, H. Bei, G. M. Pharr, and E. P. George, “Size Effects and Stochastic Behavior of Nanoindentation Pop-in,” *Phys. Rev. Lett.* **106**, 165502:1-4 (2011).
5. Z. G. Wang, H. Bei, E. P. George, G. M. Pharr, “Influences of surface preparation on nanoindentation pop-in in single-crystal Mo”, *Scr. Mater.* **65** 469-472 (2011).
6. T. L. Li, Y. F. Gao, H. Bei, and E. P. George, “Indentation Schmid Factor and Orientation Dependence of Nanoindentation Pop-in Behavior of NiAl Single Crystals.” *J. Mech. Phys. Solids*, **59**, 1147-1162 (2011).
7. C. Begau, A. Hartmaier, E. P. George, and G. M. Pharr, “Atomistic Processes of Dislocation Generation and Plastic Deformation During Nanoindentation,” *Acta Mater.* **59** (3) 934-942 (2011).
8. L. Wang, H. Bei, T. Li, Y. F. Gao, E. P. George, T.G. Nieh, “Determining the Activation Energies and Slip Systems for Dislocation Nucleation in Body-centered Cubic Mo and Face-Centered Cubic Ni Single Crystals,” *Scripta Mater.* **65** 179-182 (2011).
9. R. I. Barabash, H. Bei, Y. F. Gao, G. E. Ice, “Interface strength in NiAl-Mo composites from 3-D X-ray microdiffraction” *Scripta Mater.* **64**, 900-903 (2011).
10. L. Wang, H. Bei, T. L. Li, Y. F. Gao, E. P. George, T. G. Nieh, “Determining the activation energies and slip systems for dislocation nucleation in body-centered cubic Mo and face-centered cubic Ni single crystals”, *Scr. Mater.* **65** 179-182 (2011).
11. T.-H. Ahn, C.-S. Oh, K. Lee, E. P. George, and H. N. Han, “Relationship between Yield Point Phenomena and the Nanoindentation Pop-in Behavior of Steel,” *J. Mater. Res.* **27** (1) 39-44 (2012).
12. C. Chisholm, H. Bei, M. Lowry, J. Oh, S. A. Syed Asif, O. L. Warren, Z. W. Shan, E. P. George, and A. M. Minor, “Dislocation Starvation and Exhaustion Hardening in Mo alloy Nanofibers,” *Acta Mater.* **60** (5) 2258-2264 (2012).
13. Yue Fan, Yuri N. Osetsky, Sidney Yip, and Bilge Yildiz, “Onset mechanism of strain rate induced flow stress up-turn,” *Phys. Rev. Lett.* **109**, 135503 (2012).

**Modulating Thermal Transport Phenomena in Nanostructures via Elastic Strain at Extreme Limits of Strength (DE-SC0008135, Project period 8/2012 – 8/2017)**

**Daniel S. Gianola**

*Department of Materials Science and Engineering  
University of Pennsylvania  
Philadelphia, PA 19104*

**PROGRAM SCOPE**

Nanoscale materials fabricated with nearly pristine crystal structure are often endowed with ultra-strength behavior, where material failure occurs at a significant fraction of its ideal limit. The thermal conductivity exhibited by such materials is also uniquely affected by the high surface-to-volume ratio at the nanoscale. The juxtaposition of the vastly increased dynamic range of elastic strain available in ultra-strength nanomaterials and altered thermal transport shows promise for tunable thermal properties. This project aims to exploit these properties of high-strength nanostructures to elucidate the coupling between large mechanical strains and thermal conductivity (both electron and phonon) leading to better understanding and control of the thermal performance in these materials. Unique fabrication methods to produce nanosized quasi-defect free single crystals and modern nanomechanical testing will be used to identify the size-dependent dynamic range of elastic strain and understand deformation mechanisms near the ideal limit. Identifying and quantifying thermal transport phenomena as a function of mechanical strain in these nanostructures will open the door to using elastic strain engineering in high-strength nanomaterials to tune thermal transport. The results of these investigations will be used to improve the performance, efficiency, and versatility of advanced thermal management and energy conversion devices with tunable response.

**RECENT PROGRESS**

We have recently developed a novel non-contact *in situ* approach for measuring thermal conductivity of a single suspended nanowire subjected to varied strain levels, which we name *in situ*  $\mu$ -Raman optomechanothermography. We employ a microelectromechanical (MEMS) device to apply uniaxial tensile stress to individual silicon nanowires under a confocal  $\mu$ -Raman spectroscope. Heating from the input laser polarized along the nanowire axis provides a controlled heat flux, while the Raman spectra provide quantitative determination of temperature and stress. Modeling the experimental results allow for calculation of strain-dependent nanowire thermal resistances. Preliminary results on  $\langle 111 \rangle$  and  $\langle 100 \rangle$  Si nanowires have been obtained to validate the method, as described below. Full realization of this method will enable determination of strain-modified thermal conductivity in single nanostructures and elucidation of the influence of strain on thermal transport phenomena.

*Experimental Methods*

Images of the MEMS device used to strain an individual nanowire are shown in Figure 1. The device consists of a suspended thermal actuator, which is electrically and thermally isolated from the grip region, and a suspended compound flexure load cell. Vapor-liquid-solid-grown  $\langle 111 \rangle$  intrinsic silicon nanowires approximately 175 nm in diameter are drop cast onto a lacey carbon TEM grid and a single

nanowire is harvested and mounted to the MEMS devices using a nanomanipulator inside a scanning electron microscope (SEM).

The MEMS device with a clamped silicon nanowire is placed under the objective (NA=0.9) of a confocal  $\mu$ -Raman system equipped with a 532 nm laser, at ambient temperature and pressure, as shown schematically in Figure 2. A series of images are obtained during actuation with an optical camera, and the additional load applied

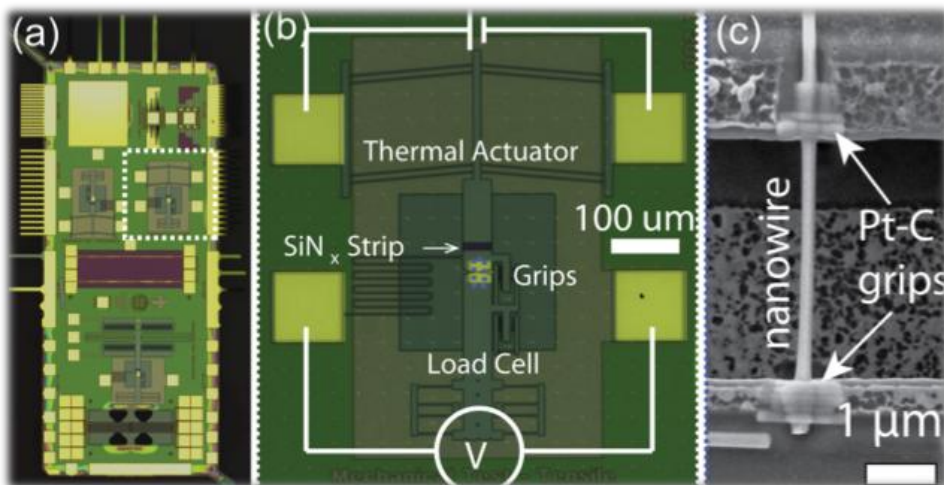


**Figure 1: MEMS device used for *in situ* nanowire tensile testing. (a) Low-mag image of chip, (b) tensile testing device consisting of thermal actuator and flexure-based load cell, and (c) mounted Si nanowire suspended between grips.**

between each stress increment is determined via digital image correlation. Spectra are obtained for all testing conditions using a 1800 lines/mm grating along the nanowire with a 100 nm step size. The laser intensity is precisely controlled with a neutral density filter, and at least seven different intensities in the range of 10 to 300  $\mu$ W are used. Increments of tensile stress are applied and the corresponding series of spectra are acquired. Following the maximum load, the specimen is unloaded incrementally to ensure that thermal conductivity measurements are consistent upon loading and unloading and the material remains elastic.

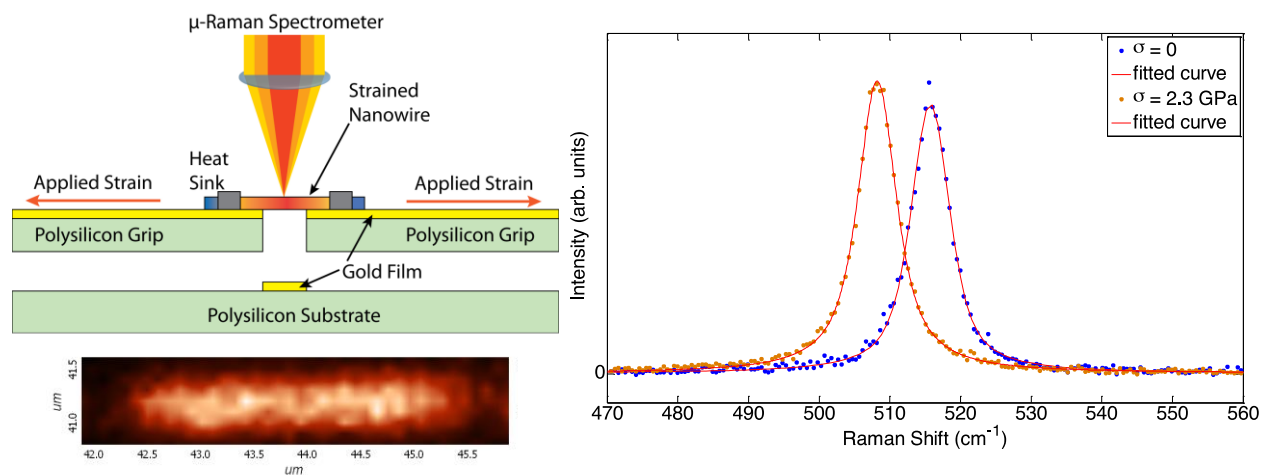


**Figure 2: (left) Schematic of *in situ*  $\mu$ -Raman optomechanothermography and an experimental Raman map showing location of an individual Si nanowire. (right) LO Raman peaks in Si for unstressed and stressed nanowire showing peak shifting owing to changing phonon frequency.**

The LO Stokes peak corresponding to the Raman active optical phonon mode in Si is sensitive to both temperature and stress, and shows shifts in frequency as shown in Figure 2. Collected spectra are fit to a superposed Gaussian and Lorentzian line profile to determine the Stokes shift, integrated intensity, and peak breadth. Furthermore, scanning the laser along the length and collecting Raman spectra as a

function of position (with respect to the heat sinks at the two grips) allows for a mapping of the temperature distribution along the wire at various laser intensities.

### Determination of Temperature

Plotting peak shift as a function of input laser intensity for varying stress shows the evolution of the Raman spectra with both stress and temperature, as shown in Figure 3. The zero-intensity intercept of the fit shown in Figure 3 is taken to be the room temperature peak position, which allows for the decoupling of the temperature and stress effects on the Raman spectrum: the difference between the unstrained room temperature peak and the strained room temperature peaks indicates the stress, and the difference between the room temperature peak at a given stress and the measured peaks give temperature. Temperature can then be calculated as

$$\Delta T = \frac{W - W_{RT}}{C}, \quad (\text{Eq. 1})$$

where  $\chi = d\omega/dT = -0.022 \text{ cm}^{-1}/\text{K}$  for silicon nanowires (Doerk *et al.*, Physical Review B, 2009),  $\omega$  is the measured peak position and  $\omega_{RT}$  is the room temperature peak position. The value of  $\chi$  for a strained nanowire here is assumed to be the same as  $\chi$  for the bulk and for unstrained nanowires. Additionally, the temperature excursions here are sufficiently small so that changes to the elastic moduli would be expected to be negligible (Varshni, Physical Review B, 1970).

### Thermal Conductivity Calculation

The temperature profile corresponding to the shifts in the Raman frequencies is plotted in Figure 4 together with quadratic fits in the gage section of the wire. This temperature profile is used to calculate thermal conductivity as follows. For a doubly clamped system of length  $L$  and cross-sectional area  $A$  heated from some point in the interior at a distance  $x$  from the left end, the relation between temperature rise at the point source and absorbed power from the point source can be written as

$$\Delta T = R_{system} \Delta P = \left( \frac{1}{\frac{x}{A\kappa} + R_{cl}} + \frac{1}{\frac{L-x}{A\kappa} + R_{cr}} \right)^{-1} \Delta P,$$

(Eq. 2)

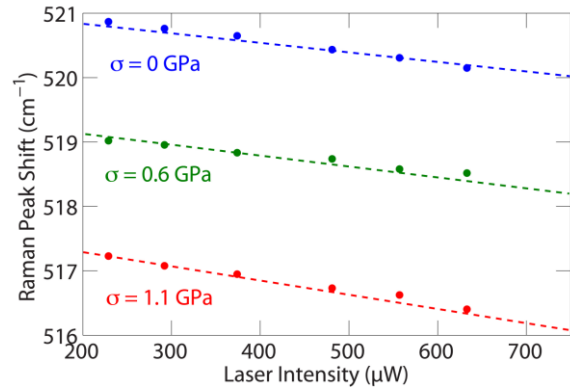


Figure 3: Raman peak shift vs. laser intensity for unstrained and stressed Si nanowire. Thermal resistance is calculated from the fits of each curve, with the room temperature reference as the zero-intensity intercept.

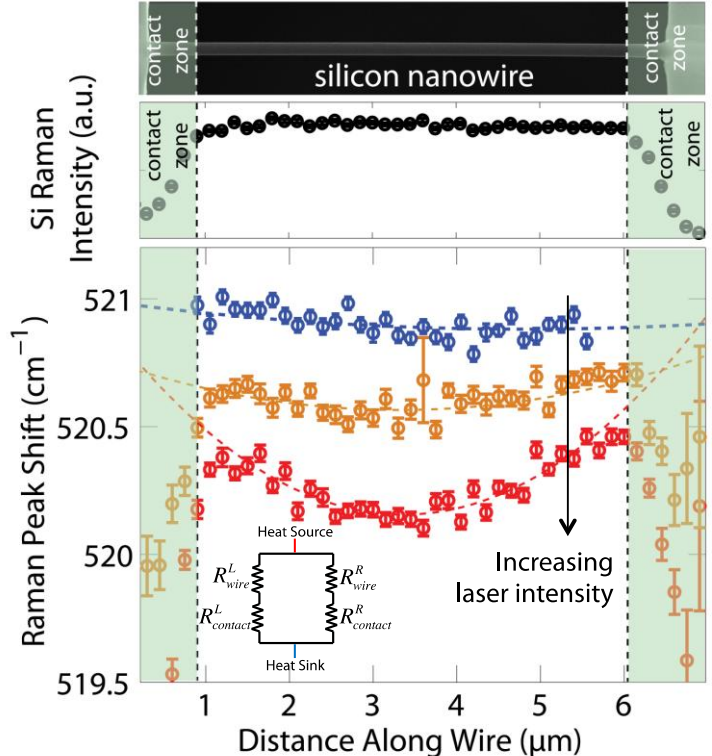


Figure 4: (top) SEM image of individual Si nanowire, (middle) LO phonon peak intensity from Raman scan along nanowire, showing gage section region, and (bottom) Raman peak shifts vs. position, with dashed curves represent quadratic fits used to calculate thermal resistance.

where  $\Delta T$  is temperature rise,  $\Delta P$  is the power absorbed,  $R_{system}$  is the thermal resistance of the entire system,  $\kappa$  is the thermal conductivity, and  $R_{cl}$  and  $R_{cr}$  are the thermal resistances of the left and right contacts, respectively. Rearranging this expression yields temperature as a quadratic function of  $x$ , and such that fitting the temperature profile along the wire gives  $\kappa$  corrected for contact resistance if one can accurately determine  $\Delta P$ . In this case,  $\Delta P$  is calculated as  $lfQ_a$  where  $l$  is laser intensity,  $f$  is the fraction of the laser spot which is incident on the nanowire, and  $Q_a$  is the diameter- and wavelength-dependent absorption efficiency, determined by numerically solving Maxwell's equations for the appropriate nanowire geometry. We assume radiative and convective losses to be negligible compared with conduction due to the small sample size and temperature excursions.

A second, self-consistent, method of determining  $\kappa$  uses the slope of the plot of Stokes shift vs. laser intensity, as shown in Figure 3 and used to determine the room temperature peak position. Eq. 2 can be rewritten as  $R_{system} = (\chi Q_a f)^{-1} d\omega/dI$ . Thus, the slope of the plot of peak position vs. laser intensity shown in Figure 3 gives the thermal resistance of the system. The ratios between the thermal resistances of the left and right contacts and that of the nanowire,  $r_l$  and  $r_r$ , respectively, are found from the quadratic fit to the temperature profile following the method of Hsu *et al.* and the thermal conductivity of the wire is given by

$$\kappa = \frac{L}{A} \left( \frac{1 + r_l + r_r}{(r_l + 1/2)(r_r + 1/2)} R_{system} \right)^{-1}. \quad (\text{Eq. 3})$$

Our preliminary results of thermal conductivity using both self-consistent methods are in good agreement and suggest that thermal conductivity can be tuned in nanostructures offering a large dynamic range of elastic strain.

## FUTURE PLANS

Preliminary results of thermal conductivity as a function of stress for Si nanowires have been obtained and are being analyzed in the context of changes to phonon group velocities and relaxation lifetimes. Our immediate goal is to apply our newly developed *in situ*  $\mu$ -Raman optomechanothermography to a systematic study of single crystalline semiconductor nanowires to determine the underlying physics of stress-augmented thermal transport and the efficacy of strain engineering in such materials.

Additional efforts are underway to fabricate and test novel strained nanomesh thin film geometries to amplify the effects of remote stress on local thermal transport around periodically patterned nanoscale features. A full microfabrication scheme has been implemented, allowing for full control of mesh and array geometry and length scales. A testing device will be designed, allowing for thin film testing *in situ* in the  $\mu$ -Raman spectroscopy.

## ACKNOWLEDGEMENTS

This research was supported by the U.S. Department of Energy, Office of Basic Energy Sciences, Division of Materials Science and Engineering under Award #DE-SC0008135. We thank J.P. Sullivan (Sandia National Laboratories) for providing the MEMS testing devices.

## Abstract

---

Program Title: **Investigation of radiation damage tolerance in interface-containing metallic nano structures**

Principal Investigator: **Greer, Julia**

Mailing Address **1200 E. California Blvd. MC 309-81 Pasadena, CA 91125**

E-mail: **jrgreer@caltech.edu**

### PROGRAM SCOPE

The proposed work seeks to conduct a basic study by applying experimental and computational methods to obtain quantitative influence of helium sink strength and proximity on He bubble nucleation and growth in He-irradiated nano-scale metallic structures, and the ensuing deformation mechanisms and mechanical properties. The proposed work utilizes a combination of **nano-scale *in-situ* tension and compression** experiments on low-energy He-irradiated samples combined with site-specific **microstructural characterization** and **modeling efforts**. This systematic approach will provide us with critical information for identifying key factors that govern He bubble nucleation and growth upon irradiation as a function of both *sink strength and sink proximity* through an experimentally-confirmed physical understanding. So far, the attention has been focused on studying individual bcc/fcc interfaces within a single nano structure: a single **Fe (bcc)-Cu (fcc)** boundary per pillar oriented perpendicular to the pillar axes, as well as pure bcc and fcc nano structures. Additional interfaces of interest include bcc/bcc and metal/metallic glass all within a single nano-structure volume. The model material systems are: (1) pure single crystalline **Fe and Cu**, (2) a single **Fe (bcc)-Cu (fcc)** boundary per nano structure (3) a single **metal-metallic glass**, all oriented non-parallel to the loading direction so that their fracture strength can be tested.

A nano-fabrication approach, which involves e-beam lithography and templated electroplating, is utilized, which enables precise control of the initial microstructure control. Experimentally determined stress-strain relationships are enhanced by *in-situ* SEM observations coupled with TEM microstructural characterization of the same samples before and after deformation (irradiated and as-fabricated) and atomistic (MD) modeling. A comprehensive suite of experiments is being conducted to quantitatively assess the key parameters for He bubble nucleation and growth by independently varying the sink strength, sink proximity, and He implantation temperature and dose. The implantations have been conducted at Sandia and Los Alamos National Labs. Nano structures containing He-enriched interfaces are tested under *uniaxial tension* to assess embrittlement, resulting boundary strength, and deformation mechanisms. Successful execution of this work will help identify which types of interfaces are particularly resilient against radiation damage.

### RECENT PROGRESS

- 1. He-irradiated fcc-bcc nano bi-crystals.** We developed a nano-fabrication methodology to produce nano-tensile Cu-Fe specimens with diameters of 100nm, each containing a single Cu grain in the bottom half and a single Fe grain in the top half. These samples were implanted directly into the interface region, with He at 200keV to a dose of  $10^{14}$  ion/cm<sup>2</sup>. Nanomechanical experiments revealed that the Irradiated Cu-Fe nano bi-crystals exhibited greater than 60% higher yield and ultimate tensile strengths than the as-fabricated ones for all samples tested, while retaining comparable ductility. No brittle fracture was observed; tensile failure always occurred gradually, along the interfaces, with no noticeable localization (Landau, Guo, Hattar, & Greer, 2012). High-resolution, site-specific transmission electron microscopy (TEM) and through-focus analysis revealed that the interfaces were non-planar and contained several He bubbles with diameters of 1-2nm, spaced  $\sim$ 12-15nm apart. This is supported by the reasonable agreement between the mean He bubble spacing calculated by the weak obstacle hardening relation and TEM analysis. We attribute such an absence of brittle failure, in part, to the wavy topology of the fcc-bcc interface, which led to the gradual detachment of localities subjected to normal stress, with the remaining intact interfacial regions carrying plastic deformation until fracture. The absence of brittle failure in He-irradiated metals is likely due to the inability of the small He bubbles to serve as sufficient stress concentrators for cracking. These results shed light on the mechanical response and fracture behavior of a single interface and its role in absorbing He. Further examination of a controlled number of interfaces can determine the contribution of each interface to the improvement in radiation tolerance and resolve the effect of sink proximity on absorbing He.
- 2. He-irradiated fcc nano crystals.** We also developed a fabrication methodology of 120 nm-diameter, 500–600 nm-tall,  $\langle 111 \rangle$ -oriented single crystalline Cu and Fe nanopillars, which were uniformly implanted with 0.35  $\pm$  0.05 at% of He at Los Alamos National Lab (P. Hosemann and Y. Wang). Uniaxial nanocompression experiments revealed that their yield strengths were  $\sim$  1.2 GPa,  $\sim$  30% higher than the yield strengths of the unimplanted, asfabricated pillars with the same dimensions. The stress-strain data of the implanted pillars exhibited shorter and more frequent strain bursts, as well as notable strain hardening with a hardening slope of 3.52 $\pm$ 0.82 GPa (Guo, Landau, Hosemann, Wang, & Greer, 2012). The substantial irradiation hardening effect at  $\sim$  100 nm scale is in stark contrast with a previous report on proton-irradiated Cu nanopillars. Such a discrepancy can be rationalized in terms of the difference in the interplay between the type of irradiation-induced defects and the spacing between the single-arm dislocation sources. In contrast with previous studies on the compressive properties of irradiated metallic nanocrystals, samples in our work were made without the use of FIB, and hence were free from the FIB-induced damage, which facilitated a much cleaner experiment. This study sheds light on the fundamental understanding of the deformation mechanism of irradiated metallic nanocrystals, and has important implications for the interplay between irradiation-induced defects and the external sample dimensions at the nanoscale.
- 3. He-irradiated bcc nano crystals.** We studied the effects of He-implantation on the compressive and tensile responses of  $\langle 110 \rangle$ -oriented single crystalline 100nm-diameter Fe nano-pillars. The 0.36 $\pm$ 0.06 at. % uniformly implanted He caused  $\sim$ 0.4GPa increase in the yield strengths and flow stresses at 10% strain for pillars tested by uniaxial compression, and  $\sim$ 0.5GPa increase in UTS for pillars tested in tension, without significantly affecting the pillars' compressive strain hardening behavior. This strengthening effect can be rationalized in terms of the obstruction of mobile dislocations by the implantation-induced defects, and is consistent with literature values under similar He implantation doses, indicating that the results obtained from these nano-scaled test specimens may be used to extract bulk properties of irradiated materials. The compressive stress-strain behavior of both as-fabricated and implanted pillars was shown to have three distinct regimes, starting from elastic loading up to  $\sim$ 2% strain, followed by notable strain hardening between 2% and 10% strains, and

eventually reaching a steady state for strains over 10% where the flow stress remained a constant. Such a phenomenon was explained by the competition between a dislocation generation and multiplication mechanism, and a dislocation starvation mechanism (Guo, Landau, Hosemann, Wang, & Greer, 2013).

## COLLABORATORS

A. Misra, P. Hosemann, Y. Wang (LANL)

K. Hattar (SNL)

## FUTURE PLANS

The next steps will involve

- (1) Fabrication of Ni-{Ni-based metallic glass} nano-structures, which contain a single metal-metallic glass interface and testing these samples in tension. This will allow us to quantify the role of free volume within the metallic glass and the boundary on the ability of He bubbles to be accommodated within the boundaries.
- (2) Implantation of He into the existing Cu, Fe, and Cu-Fe nano-tensile samples at higher temperatures (400°C) and doses to attain greater bubbles sizes (~10nm) and closer bubble spacing. This will allow us to test the ability of the larger bubbles to serve as sufficient stress concentrators for embrittlement (if at all).
- (3) Training a new graduate student (R. Liontas) and a new post-doc (to be hired) because the previous two post-docs who worked on this project, P. Landau and Q. Guo both got faculty positions and moved on. Certain ramp-up learning time is anticipated.

## REFERENCES

- Guo, Q., Landau, P., Hosemann, P., Wang, Y., & Greer, J. R. (2012). Helium Implantation Effects on the Compressive Response of Cu Nanopillars. *Small*, DOI: 10.10, 1–6. doi:10.1002/smll.201201614
- Guo, Q., Landau, P., Hosemann, P., Wang, Y., & Greer, J. R. (2013). Compressive and Tensile Response of Helium-Implanted Single Crystalline Fe Nano-Pillars. *submitted*.
- Landau, P., Guo, Q., Hattar, K., & Greer, J. R. (2012). The Effect of He Implantation on the Tensile Properties and Microstructure of Cu/Fe Nano-bicrystals. *Advanced Functional Materials*, 10.1002/adf. doi:10.1002/adfm.201201776

## **In situ characterization of stress-coupled grain boundary migration**

**Kevin Hemker**

hemker@jhu.edu  
223 Latrobe Hall  
3400 N Charles St  
Baltimore MD 21218

### **PROGRAM SCOPE**

Stress-coupled grain boundary migration has been shown to be an active deformation mechanism in a number of nanocrystalline materials. While a fundamental understanding of this mechanism would allow for increased utilization of nanocrystalline materials for many thin film and MEMS applications, very few quantitative experimental studies are available to guide and corroborate predictions obtained from simulations. In particular, the ability to understand and model a material's propensity to facilitate stress-coupled grain boundary migration as a function of grain boundary character and grain size distribution would increase our ability to understand the microstructural stability and attendant mechanical behavior of nanocrystalline materials. Ex situ tensile tests have proven to be a valuable tool in identifying materials that exhibit stress-coupled grain boundary migration but cannot by itself provide detailed information about the microstructure as it evolves. The focus of this research program is to develop capabilities to test and characterize nanocrystalline materials in situ, allowing for characterization of individual grains and grain boundaries as the material deforms. By conducting mechanical tests in conjunction with orientation imaging microscopy, information about how grain boundaries respond to stress can be obtained and compared with simulated predictions. Key topics of interest are how the coupling factor (amount of shear strain imposed on the grains as the grain boundary migrates) and grain boundary mobility are affected by the grain boundary character and grain size and shape. Both SEM and TEM-based in situ tensile testing methods are being developed and employed to study these unique materials.

### **RECENT PROGRESS**

Previous thin film micro-tensile specimens were deposited on a single crystalline silicon bridge and released by etching away the underlying silicon with xenon difluoride. The xenon difluoride was found to attack many metallic thin films, and so a new thin film fabrication technique has been developed that precludes use of xenon difluoride and can produce tensile specimens of any material that can be vapor deposited with a low residual stresses (Figure 1). Use of this new methodology also facilitates fabrication of nanocrystalline thin films for in situ TEM experiments. In the past year, copper films with bimodal grain size distributions were deposited, transferred, pulled in tension (both ex situ

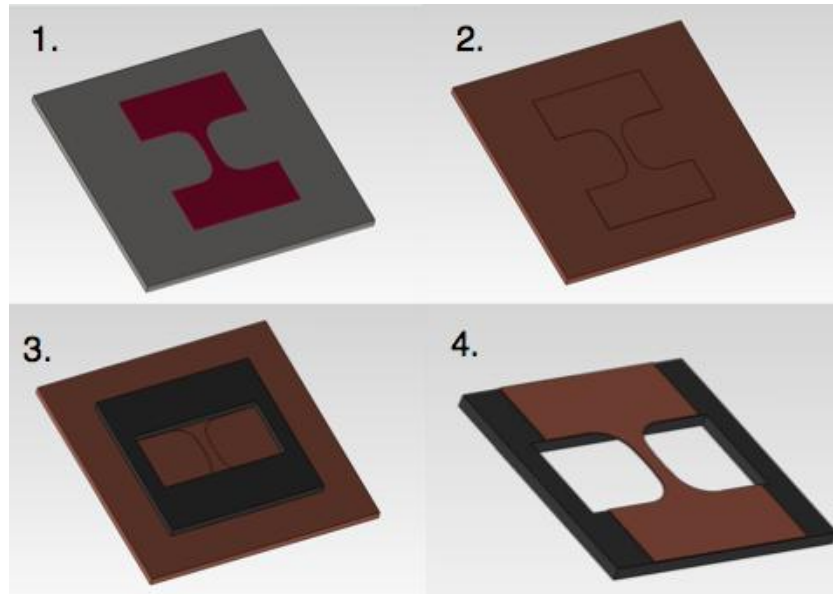


**Figure 1:** Procedure to fabricate freestanding nanocrystalline thin film micro-tensile specimens: 1) pattern specimen geometry into photoresist with photolithography, 2) vapor deposit metallic thin film, 3) attach load frame, and 4) lift-off in acetone to create freestanding gage.

and in situ), and found to exhibit enhanced strength and good tensile ductility as a result of stress-coupled grain boundary migration. The efficacy of using ASTAR orientation imaging to characterize microstructural evolution is illustrated in Figure 2. The grain size of the as-deposited and deformed microstructures have been color coded and plotted to illustrate the extent and spatial location of grain growth. Moreover, importing the ASTAR images into commercial EBSD software allows for statistical treatment and representation of the microstructure. Size distribution plots that would have taken hundreds of individual measurements and several days of work are now readily available. The distribution plot in Figure 2 not only evidences the grain growth but also shows that the growth occurs predominantly in the larger grains with the size of the smaller grains remaining constant.

Use of the ASTAR orientation maps and EBSD software also allow for identification of grain boundary character for the case of vertical grain boundaries in TEM thin films (Figure 3). In this example, the grain boundary characters of the grains that have undergone grain growth are compared with the average grain boundary character that was present in the undeformed films. If, as predicted by molecular dynamics simulations, certain boundaries were less mobile than others, one would expect an increase in boundaries of that character. The preliminary observations presented in Figure 3 indicate no such preference, but additional experiments involving a variety of materials are underway. Tensile tests are also being conducted in situ in a TEM using ASTAR orientation imaging microscopy. These in situ observations allow direct measurement of the influence of grain size, shape and orientation, as well as grain boundary character, on coupled boundary migration.

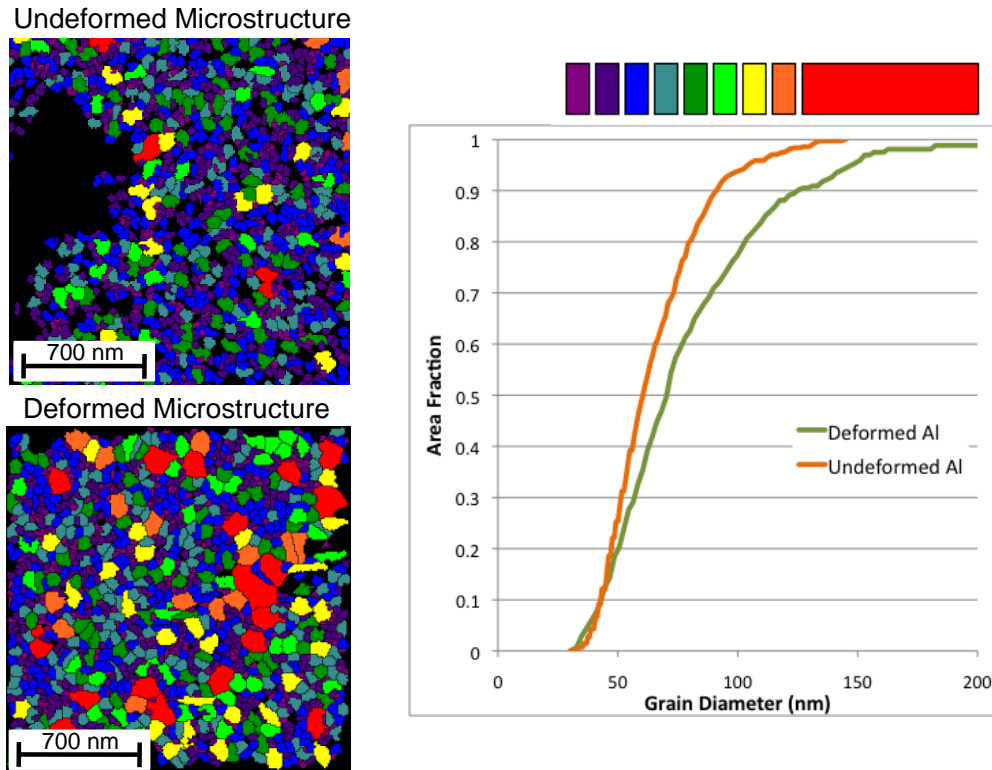


**Figure 2:** Grain size comparison between as-deposited and strained microstructures for nanocrystalline aluminum. Grain color represents grain diameter as shown on the plot and clear evidence of discontinuous grain growth is evident.

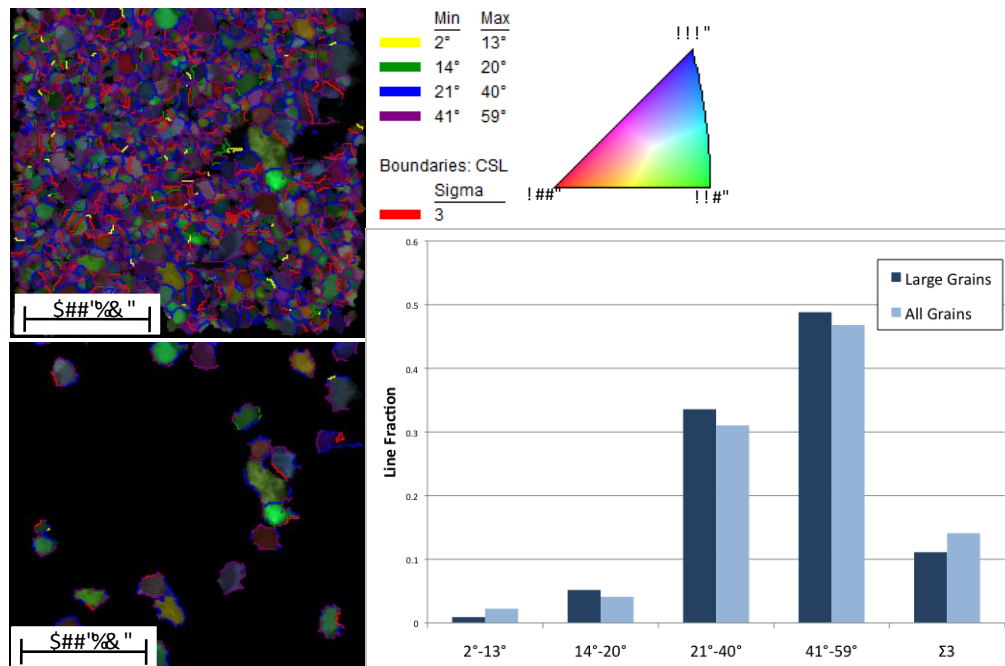


**Figure 3:** Comparison of grain boundary character for all grains (top) and large grains (bottom) in a strained nanocrystalline aluminum sample. Grain color represents orientation (see inverse pole figure) and grain boundary color represents misorientation angles between grains.

A main benefit of TEM-based in situ techniques is that nanometer-resolution orientation maps may be collected at a high speed. However, due to the spatial constraints in a TEM it is very difficult to obtain full stress-strain information of the specimen as it is being tested. We have developed and fabricated a tensile testing stage that can be used within an SEM to provide stress-strain information. The resolution required for observing nanocrystalline grains has not been attainable using conventional electron backscatter diffraction (EBSD) techniques. We are currently developing and utilizing a relatively new technique, transmission Kikuchi diffraction (TKD), with which nanocrystalline grains can be oriented and mapped by collecting Kikuchi patterns in transmission. This technique provides the speed and resolution required to collect orientation maps throughout a tensile test. By utilizing TKD to obtain orientation maps that show how the grain structure evolves during testing and combining this information with the macroscopic stress being applied to the specimen, we can begin to understand in more detail how the local stress surrounding a grain boundary can drive its motion.

## **FUTURE PLANS**

In the near future our efforts will focus on utilizing the capabilities of ASTAR orientation mapping combined with mechanical tests to further understand the mechanism of stress-coupled grain boundary migration. We will implement parallel in situ tensile tests in the SEM using TKD to obtain orientation maps and thus enable a connection between microstructural observations with the overall stress-strain response of the film. We also plan to implement micro-bending ultra-high frequency fatigue testing to probe the effect of cyclic loading on stress-coupled boundary migration and grain growth.

## **LIST OF PAPERS SUPPORTED BY THIS WORK**

- TJ Rupert, DS Gianola, Y Gan, KJ Hemker, Experimental Observations of Stress-Driven Grain Boundary Migration, *Science*, **326** (2009) 1686-90.
- JA Sharon, P-C Su, FB Prinz, KJ Hemker, Stress Driven Grain Growth in Nanocrystalline Pt Thin Films, *Scripta Materialia*, **64** (2011) 25–28.
- HH Liu, S Schmidt, HF Poulsen, A Godfrey, ZQ Liu, JA Sharon, X Huang, Three dimensional orientation mapping in the transmission electron microscope, *Science*, **332** (2011) 833-834.
- F Momprou, M Legros, T Radetic, U Dahmen, DS Gianola, KJ Hemker, “In situ TEM observation of grain annihilation in tri-crystalline aluminum films, *Acta Materialia*, **60** (2012) 2209–2218.
- Y Zhang, JA Sharon, GL Hu, KT Ramesh, and KJ Hemker, Stress-driven grain growth in ultrafine-grained Mg thin film, *Scripta Materialia*, **68** (2013) 424-427.

## **PERSONNEL SUPPORTED BY THIS PROJECT**

Professor Kevin Hemker (PI), Dr. Jessica Krogstad (partial postdoctoral support), Mr. Paul Rottmann (PhD student stipend), Dr. Marc Legros (visiting scientist support).

# PLASTIC STRAIN RECOVERY IN NANOCRYSTALLINE MATERIALS

Marisol Koslowski

School of Mechanical Engineering, Purdue University

West Lafayette, IN 47907

*marisol@purdue.edu*

## PROGRAM SCOPE

Materials with engineered microstructures are able to achieve exceptional functionality and performance not possible with bulk materials. **Nanocrystalline materials** for example exhibit high yield and fracture strengths<sup>i</sup>, superior wear and radiation damage resistance.<sup>ii</sup> Grain boundaries act as obstacles to slip and sinks for radiation-induced defects rendering increased strength and radiation tolerance to materials with grain size in the nanometer scale due to the high density of grain boundaries compared to coarse-grained materials. Understanding the interaction of these interfaces with defects play a prominent role in achieving the desired properties.

The reduction of grain size to nanometer scales leads to these enhanced properties. This reduction in grain size is responsible for new deformation mechanisms that are not present in coarse grained crystalline materials. One of these mechanisms is plastic strain recovery.<sup>iii</sup> Even though, plastic deformation is not recoverable in coarse grained crystalline materials, very recent experiments in nanocrystalline aluminum, gold and nickel show that plastic strain recovers after unloading. This surprising effect remains unexplained but is believed to be the result of the interaction between complex processes driven by thermally activated motion of crystalline defects with different characteristic time and length scales, such as grain boundaries and dislocations. This recovery mechanism has a strong dependency on loading history, temperature, mean grain size and grain size distribution.<sup>iv</sup> Numerical simulation of plastic strain recovery in nanocrystalline metals is a particularly challenging case of multiscale modeling that requires resolution of the small length scales involved while capturing the long time scales inherent to the recovery process.

The scope of this program is to develop models and numerical tools to capture both short length scales and long time scales. This new approach incorporates thermally activated mechanisms, into large-scale numerical simulations of deformation of nanocrystalline materials with a phase field micro mechanics model (PFMM).<sup>v</sup> The model is informed from atomistic processes<sup>vi vii viii</sup> and includes crystal anisotropy, dislocations and its interactions with grain boundaries,<sup>ix</sup> voids<sup>x</sup> and interfaces<sup>xi</sup> and grain boundary mediated deformation.<sup>xii</sup> The theory and simulations proposed in this project provide insight regarding the interaction of crystalline defects at nanometer scales over time scales not accessible with atomistic simulations and will be a critical step toward new, more general and predictive approaches in multiscale modeling.

## RECENT PROGRESS

Phase field models have been used to simulate a wide range of mechanical systems and were developed specifically to model heterogeneous systems and phase transformations<sup>xiii, xiv</sup>. Some of these models are based on Eshelby's effective eigenstrain method<sup>xv</sup>. In this approach, a heterogeneous system is replaced by an equivalent homogeneous system in which eigenstrains are used to represent structural inhomogeneities of the original system. In the PFMM dislocations are described as eigenstrains that account for the amount of slip in each crystallographic slip system. That allows us to resolve length scales small enough such that individual dislocations can be followed during the simulations. Other defects such as grain boundaries, different phases and voids can be added in a similar way.

In the PFMM the evolution of dislocation and other defects as well as the interactions follows from the energetics of the system. We have used this approach to incorporate interaction of dislocations with voids<sup>x</sup>, grain boundary sliding<sup>xii</sup> and solid state phase transformations.<sup>xvi</sup> Figure 1 shows dislocation patterns close to a grain boundary and a void and solid-state transformations in molecular crystals.

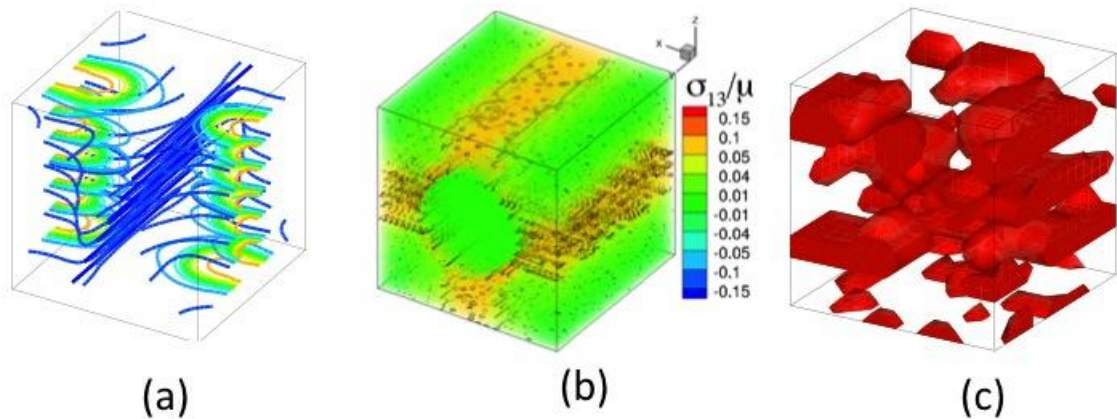


**Figure 1: (a) Dislocation pile-ups close to a grain boundary (b) dislocation patterns in the presence of voids, (c) amorphous regions in gamma-indomethacin.**

The PFMM is coupled to a Kinetic Monte Carlo (KMC) algorithm to analyze thermally activated evolution of dislocations and creep deformation of nanocrystalline materials. In simulations of single crystals under an externally applied stress we recover Andrade's creep behavior in which the strain follows  $\varepsilon \sim t^{1/3}$ .

We perform simulations on polycrystals with a grain distribution containing nano and micro meter size grains. The sample is loaded and unloaded until the average stress is zero. Figure 2(a) shows the loading and unloading curve for the sample and the local response of two representative small and large grains. These curves show that upon unloading the small grains remain in tension while the large grains are in compression. These local stresses drive creep deformation that leads to the plastic strain recovery observed in experiments. The dashed lines show the strain recovered on each grain and the total strain recovered ( $\gamma_r$ ).

After unloading a KMC algorithm evolves the dislocation ensemble at room temperature. Figure 2(b) shows the strain evolution of the polycrystalline sample simulated with KMC. Different maximum loads are applied resulting in different maximum strains ( $\gamma_{\max}$ ) from 2% to 6%. The results show that as the maximum strain is increased the percentage of strain recovered decreases. This is in agreement with our previous analytical results that indicate that plastic strain in the small grains limits the amount of plastic strain that can be recovered.

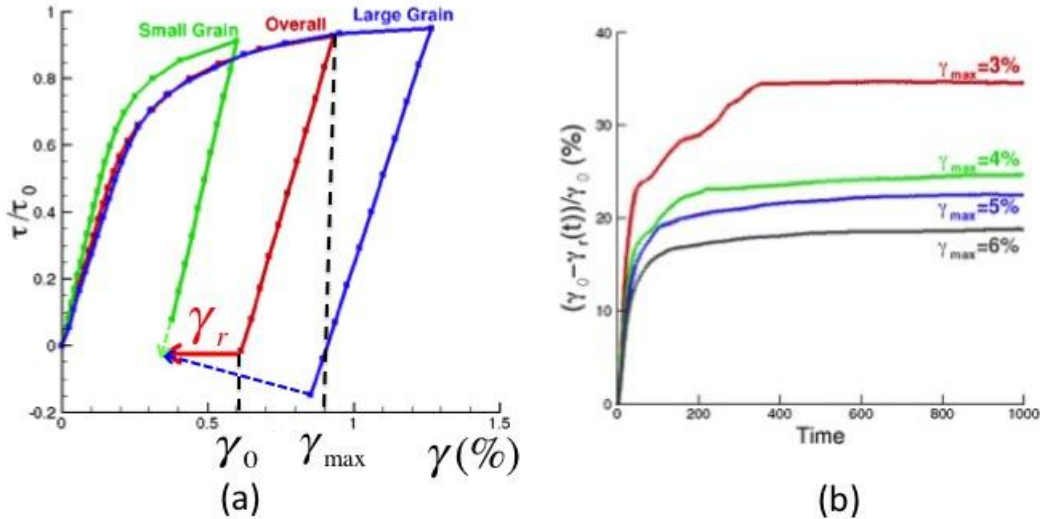


Figure 2: (a) Strain stress curve of the polycrystalline sample showing the local behavior of small and large grains. (b) Percentage of strain recovered,  $\gamma_r$  (%), for different maximum applied strains.

## FUTURE PLANS

We are currently performing simulations with the PFMM-KMC approach to predict creep stress exponents in a wide range of configurations (grain sizes and distributions). It is worth to notice that our simulations **do not use phenomenological creep laws with parameters fitted to experiments**. Instead the evolution follows from the energetic of the dislocation ensemble and the interaction of dislocations with other dislocations and grain boundaries.

The PFMM-KMC is a predictive tool that can investigate creep deformation response dependent on the microstructure. We plan to extend this methodology to investigate creep behavior of metal alloys based on numerical simulations at the microscopic scale with different microstructures and environmental conditions. The goal is to establish a framework to build continuum constitutive equations of creep deformation in nanocrystalline materials and alloys based on numerical simulations at the microscopic scale.

## REFERENCES\*

\* REFERENCES (IV) TO (XII) ACKNOWLEDGE SUPPORT FROM DOE-BES.

- 
- <sup>i</sup> N. A. Mara, D. Bhattacharyya, P. Dickerson, R. G. Hoagland, and A. Misra, Deformability of ultrahigh strength 5nm Cu/Nb nanolayered composites, *Applied Physics Letters* **92**, 231901, 2008.
- <sup>ii</sup> A. Misra, M. J. Demkowicz, X. Zhang and R. G. Hoagland, The radiation damage tolerance of ultra-high strength nanolayered composites *JOM Journal of the Minerals, Metals and Materials Society* , Volume 59, Number 9, 62-65, 2010.
- <sup>iii</sup> J. Rajagopalan, J. H. Han, and T. A. Saif, *Science* **315**, 1831, 2007.
- <sup>iv</sup> Marisol Koslowski, Effect of grain size distribution on plastic strain recovery, *Physical Review B* **82**, 054110, August 2010.
- <sup>v</sup> Abigail Hunter, Chin Le, Faisal Saied and Marisol Koslowski, Large scale phase field dislocation dynamics simulations on high performance architectures, *Journal of High Performance Computer Applications*, **25**(3) 223-235, 2011.
- <sup>vi</sup> DongWook Lee, Hojin Kim, Alejandro Strachan and Marisol Koslowski, Effect of core energy on mobility in a continuum dislocation model, *Physical Review B*, **83** (10) 104101, 2011.
- <sup>vii</sup> Hunter, Abigail; Zhang, Ruifeng; Beyerlein, Irene; Germann, Timothy; Koslowski, Marisol, Dependence of equilibrium stacking fault width in fcc metals on the  $\gamma$ -surface, *Modeling and Simulations in Materials Science and Engineering*, 21 025015-025034, 2013.
- <sup>viii</sup> Hunter, A., Beyerlein, I., Germann, T. and Koslowski, M. Influence of the stacking fault energy surface on extended partials with a 3D Phase Field Dislocations Model, *Physical Review B*, **84** 144108, 2011.
- <sup>ix</sup> Lei Cao and Marisol Koslowski, Effect of microstructural uncertainty on the yield stress of nanocrystalline nickel, *Acta Materialia*, 61 1413-1420, 2013.
- <sup>x</sup> Lei Lei, J. L. Marin and M. Koslowski, Phase field modeling of defect initiation and propagation, *Modeling and Simulations in Materials Science and Engineering*, 21 025009, 2013.
- <sup>xi</sup> Abigail Hunter, H. Kavuri and Marisol Koslowski, A continuum plasticity model that accounts for hardening and size effects in thin films, *Modeling and Simulations in Materials Science and Engineering*, **18** 45012-45023, April 2010.
- <sup>xii</sup> Marisol Koslowski, DongWook Lee and Lei Lei, Role of the grain boundary energetics on the maximum strength of nanocrystalline Nickel, *Journal of the Mechanics and Physics of Solids*, **59** 1427-1436, 2011.
- <sup>xiii</sup> M.R. Dorr, J. L. Fattebert, M. E. Wickett, J. F. Belak and P.E. A. Turchi, A numerical algorithm for the solution of phase-field model of polycrystalline materials, *Journal of Computational Physics*, 229, 626-641, 2010.
- <sup>xiv</sup> A. G. Khachaturyan, *Theory of Structural Transformations in Solids*, John Wiley & Sons, New York, 1983
- <sup>xv</sup> T. Mura, *Micromechanics of defects in solids*, 2nd Edition, Kluwer Academic (1987).
- <sup>xvi</sup> Lei Lei, T. Carvajal and M. Koslowski, Defect induced amorphization of molecular crystals, *Journal of Applied Physics*, **111**, 073505, 2012.

## Evolution of Grain Boundary Networks in Extreme Radiation Environments

Mukul Kumar, Joel Bernier, Vasily Bulatov, Thomas Lagrange, Shiu Fai Li (PD), Jeremy Mason (PD), Bryan Reed, and Ming Tang  
Lawrence Livermore National Laboratory  
7000 East Avenue, L-342  
Livermore, CA 94550  
E-mail: mukul@llnl.gov

### Project Definition:

Advanced nuclear energy systems will require materials to perform for extended periods under conditions of elevated temperatures and high radiation exposures. Conventional engineering materials lack the required microstructural stability and exhibit excessive coarsening, hardening, and swelling. It is considered that grain boundaries (GB) in nanocrystalline materials can substantially reduce this degradation by acting as highly effective sinks for point defects. Unfortunately, nanocrystalline materials can also be unstable with respect to thermal coarsening, so their long-term efficacy requires the microstructure to be stabilized. Our previous work shows that grain boundary networks (GBN) consisting of a high fraction of annealing twins and twin variant boundaries can be stabilized against thermal coarsening [Schwartz, King, and Kumar, *Scripta Mater.*, **54** (2006), 963] and interface-mediated degradation.

We are investigating whether such networks of GBs can also sustain microstructural stability under irradiation. The objective of the project is to develop the basic science needed to address the overarching question: What must the GBN look like if it is to act as an effective point defect sink, not only on initial deployment, but after months or years of severe irradiation? We envision a network in which high free volume, high-energy “random” boundaries act as point defect sinks while the more stable, low energy special boundaries anchor the network, and the entire ensemble is statistically stable over the lifetime of the material. To understand whether this is possible, we are studying (1) the coupled evolution of GB structure and point defects, using simulation, theory, and transmission electron microscopy (TEM) of irradiated materials, and (2) what this implies about the evolution of the GB network, using spatially-resolved diffraction coupled with mesoscale theory.

We have inter-related thrusts that represent a tightly coupled combination of theory (crystallography and defect dynamics), computations (molecular dynamics and phase field), and experiment (*in situ* transmission electron microscopy, electron backscatter diffraction, and three-dimensional X-ray diffraction microscopy) to explore the basic physics governing the evolution of microstructures under high-dose irradiation. Using a model system (copper), we are exploring the phase space of energy and intrinsic mobilities of interfaces commonly observed in GB engineered microstructures ( $\Sigma 3$ ,  $\Sigma 9$ , and  $\Sigma 27$ , and other random, using the notation of the Coincident Site Lattice model) and extending the analysis from perfect structures to vicinal character. These results are informing a crystallographically-sophisticated multiscale model of the interaction between radiation-induced point defects and grain boundaries in the context of a highly coordinated GB network. As a complement to the theory and simulations efforts, the experimental effort has focused on thermal coarsening and irradiation of a variety of microstructures in pure copper. A synopsis of this work in progress will be described below.

### Recent Progress and Future Plans:

To understand aspects of microstructures that influence their stability and evolution under particle radiation, we must first examine their thermal stability alone. For this purpose, we have chosen several varieties of nano-twinned copper (nt-Cu). One of these described below has a unique microstructure and topology, exhibiting strong  $\{111\}$  fiber textures and GBN consisting of high angle or low angle columnar boundaries interspersed with a high fraction of low-energy GBs that are mostly growth twins. Using a TEM-based orientation mapping system, we have statistically analyzed the GBN in as-deposited and

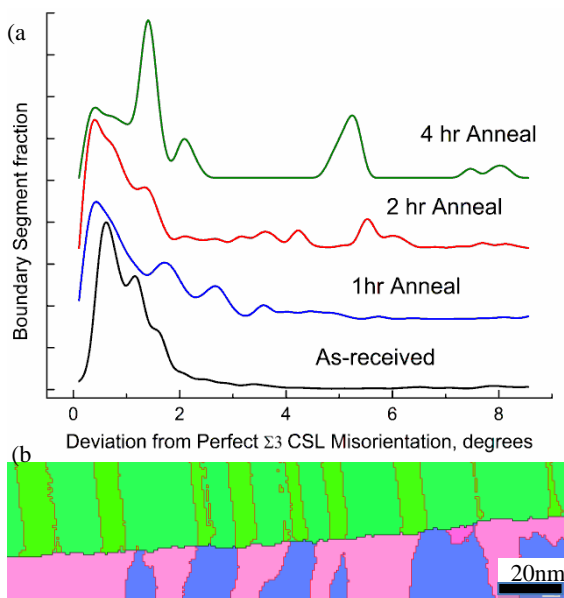


Figure 1. a) Plot showing the deviation from perfect  $\Sigma 3$  disorientation as a function of annealing time at 573 K. The increasing spread in deviation suggests that the defect content (incoherent segments) of remaining  $\Sigma 3$  boundaries increases with annealing, b) An IPFOM of a single columnar boundary (colored black) between two columnar grains showing the differences in  $\Sigma 3$  boundary morphologies.

migrate to minimize its overall curvature and the area of CTBs in neighboring columnar grains. This mechanism suggests that an initial content of incoherent twin segments in the as-deposited film is highly detrimental to the microstructural stability, particularly considering the elevated energy and mobility of incoherent twins relative to CTBs.

We have performed preliminary in-situ electron irradiation experiments on the nt-Cu foils in a 3 MeV transmission electron microscope. At room temperature, Frenkel defects formed by the high energy electron irradiation coalesce and evolve into stacking fault tetrahedra and vacancy type dislocation loops. However, at temperatures around 573K, voids form readily after 5 mins of irradiation at a dose of  $10^{24} \text{ e}^- \text{ m}^{-2}$ . Once formed and under further irradiation at 573K, the voids coarsen, coalesce and facet until they impinge on grain boundaries and the free surfaces of the TEM foils (see Figure 2a-c). Post-

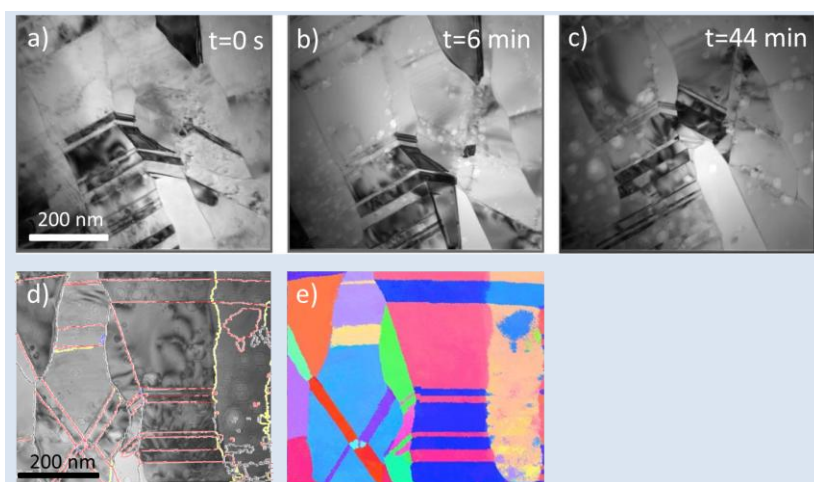


Figure 2. a-c) Bright-field TEM images of nt-Cu foil taken after various time intervals and electron irradiation dose at 573K that show void formation and evolution with time and dose. d) GB character map overlay on a bright-field TEM image of the irradiated zone (red-  $\Sigma 3$ , blue- $\Sigma 9$ , yellow-low-angle GBs, black-high-angle GBs). e) An IPFOM of the irradiated sample.

annealed nt-Cu foils. From the observed GB characteristics and network evolution during thermal annealing, we derive a better understanding of stability of these nanostructures. In particular, the character of the columnar GBs, triple junctions (TJ) and nanotwins controls the thermal stability of the nt-Cu. We infer that de-twinning via mobile incoherent twin segments followed by lateral motion of the high-angle columnar boundaries negates the pinning effect of the triple junctions.

Incoherent segments can occur from growth faults in the as-deposited nt-Cu foil, as illustrated by the IPOM in Figure 1. The incoherent  $\Sigma 3$  twin segments in the bottom columnar grain are quite visible; the  $\Sigma 3$  boundaries are highly curved and stepped, indicating a high content of Shockley partials. The incoherent segments could also form during annealing by nucleation of a set of partial dislocations at triple junctions joining coherent twin boundaries (CTBs) with the column boundaries. This would be consistent with the increasing deviation over time of twins from the perfect  $\Sigma 3$  misorientation that is observed in Figure 1. As observed *in-situ*, incoherent twin segments migrate by thermally activated motion to reduce the twin boundary area and eventually to de-twin the column. Being unpinned, the column boundary could then

irradiation analysis to obtain orientation and grain boundary character maps of the irradiated zone revealed a predominant trend in the void distribution. The voids tend to form around  $\Sigma 3$  type boundaries, as shown in Figure 2. Void formation is typically related to biased point defect diffusion kinetics. The crystallography and low free volume of  $\Sigma 3$  type boundaries leads to a local excess of vacancies to accumulate causing voids to form. For example, high-angle GBs may be adequate sinks for both vacancies and interstitials, whereas  $\Sigma 3$  CSLs are biased towards interstitial defects, leaving excess vacancies.

We are conducting MD simulations to further explain this biased defect kinetics and void formation. In addition, proton irradiated samples with various microstructures are also under investigation and the results will be reported in the coming months.

Our experimental observations of thermal coarsening suggest that twins, or more generally singular boundaries, enhance the stability of the microstructure. We contend that this is the result of an increased frequency of triple lines and quadruple nodes coordinated by boundaries that resist changes in inclination due to their being in a cusp in the energy landscape. These triple lines and quadruple nodes could then function as intrinsic pinning points, slowing or even arresting grain boundary migration. Simulations provide an ideal platform to investigate this hypothesis, but only provided that they accurately reflect variations in energy with boundary plane inclination.

In order to capture the anisotropy of grain boundary (GB) energy as a function of all five macroscopic degrees of freedom (misorientation + plane inclination), we utilized the extensive datasets of GB energies previously computed for four FCC metals [Olmsted *et al.*, *Acta Mater.* **57** (2009) p. 3694] to investigate the topography and topology of the functional space of grain boundary energies. We have explored various low-dimensional subsets of the 5-space and, based on this analysis, proposed that the global topology (connectivity) and topography of the GB energy in the 5-space are defined by grofs, *i.e.* special sub-sets of the 5-space where the energy is locally minimal with respect to variations locally orthogonal to the set. Based on this observation we developed a hierarchical interpolation approach in which a few selected low-dimensional GB subsets are used as scaffolding. Our novel hierarchical approach was then implemented into a closed-form function that quantitatively describes energy variations in the entire 5-space of macroscopic parameters in FCC metals Ni, Cu, Al and Au. The new function is observed to be universal for the crystallography class of face-centered cubic metals containing only two metal-specific parameters. The high accuracy of the new analytical GB energy function is illustrated in Figure 3.

With a complete description of GB energy variations in place, it is imperative to put this new knowledge to use for predicting GB network microstructure evolution under thermal and irradiation coarsening conditions. Having previously developed and implemented two different flavors of the phase-field method for polycrystals, we eventually determined that GB energy anisotropy and, specifically, the inclination dependence of the GB energy is difficult to include in the quaternion-based implementation while the same anisotropy induces numerical stiffness in the multi-field implementation.

Given that it is precisely the inclination-dependent energy variations that define the capillary force driving the GB network evolution, we decided to include Potts Monte Carlo in our arsenal of microstructure simulation methods. Potts MC is numerically robust but so far has not been adopted and used for simulations of grain coarsening with realistic (inclination-dependent) GB energy anisotropy. A notable shortcoming of

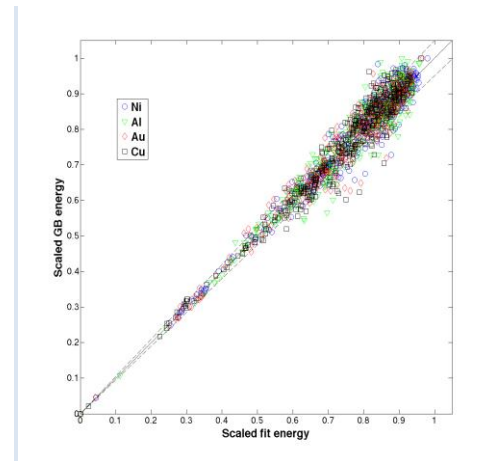


Figure 3. The atomistic energies of all 388 boundaries in all four elements reported by Olmsted *et al.* plotted against the energies of the same boundaries computed from the interpolation function. The solid line corresponds to a perfect fit, while the dashed lines indicate the assumed 5% error bounds. For each metal the energies are scaled by the maximum energy computed over all 388 boundaries for the same metal.

Potts MC that it shares with phase-field methods is that being grid-based they can suffer from unwanted effects of the underlying regular grid. In particular, being defined on a grid makes it difficult for the Potts model to resolve GB plane orientations with sufficient accuracy. Having served as a workhorse method for grain coarsening simulations since late 80's, further applications Potts MC to more realistic simulations with full GB energy anisotropy are severely limited by this and other discrete grid effects.

To address these limitations, we developed a novel implementation of the Potts MC method in which the interactions among lattice spins are non-local with their magnitude made to gradually decrease with increasing distance between the grid elements. Coupled with a novel non-local definition of the boundary plane, our extension mitigates the mentioned undesirable grid effects while preserving the simplicity and robustness of the original method. Although non-locality of spin-spin interactions results in an increased computational cost, the latter remains acceptable and will be further reduced once the method is implemented in an efficient parallel model such as one developed at SNL. Our non-local Potts MC has been implemented and carefully tested in 2D with 3D implementation currently in the works. Eventually, our intention is to provide a high-throughput method for the search for optimal microstructures, extending ideas from the Materials Genome Initiative to the level of microstructures and incorporating them into the current investigation.

### **Acknowledgments:**

This work was performed under the auspices of the U.S. Department of Energy by Lawrence Livermore National Laboratory under Contract DE-AC52-07NA27344, with support from the DOE Office of Science, Division of Materials Science & Engineering. JM would also like to thank the Lawrence Postdoctoral Fellowship Program at LLNL for support.

### **Publications:**

B. W. Reed, B. L. Adams, J. V. Bernier, C. M. Hefferan, A. Henrie, S. F. Li, J. Lind, R. M. Suter, and M. Kumar; "Experimental tests of stereological estimates of grain boundary populations," *Acta Materialia*, **60**, p. 2999 (2012)

M. Tang, B. W. Reed, and M. Kumar; "Coarsening kinetics of topologically correlated grain boundary networks," *Journal of Applied Physics*, **112**, Article 043505 (2012)

T. Lagrange, B. W. Reed, M. Wall, J. K. Mason, T. Barbee, and M. Kumar; "Topological view of the thermal stability of nanotwinned microstructures," *Applied Physics Letters*, **101**, Article 011905 (2013)

V. Bulatov, B. W. Reed, and M. Kumar; "Anisotropy of interfacial energy in 5 dimensions," in review (2013).

S. F. Li, J. K. Mason, M. Kumar, and J. F. Lind; "Quadruple nodes and grain boundary connectivity in three dimensions," submitted for review (2013)

J. K. Mason, O. K. Johnson, B. W. Reed, S. F. Li, J. S. Stolken, and M. Kumar; "Statistics of twin related domains and the grain boundary network," submitted for review (2013)

A. Stukowski, V. Bulatov, A. Arsenlis; "Automated identification and indexing of dislocations in crystal interfaces," *Modeling and Simulation in Materials Science and Engineering*, **20**, 085007 (2012). (partial support)

K. Kang, V. Bulatov, and W. Cai; "Singular orientations and faceted motion of dislocations in body-centered cubic crystals," *Proceedings of the National Academy of Sciences*, **109**, p. 15174 (2012). (partial support)

Title: Nanotwinned Materials for Energy Technologies

PI: Richard LeSar, Ames Laboratory and the Department of Materials Science and Engineering, Iowa State University, Ames, IA 50011; lesar@iastate.edu

Co-PIs: Alexander King, Matthew Kramer, Mikhail Mendeleev, Ryan Ott, and Krishna Rajan, Ames Lab; Anthony Rollett, Carnegie Mellon University

## PROGRAM SCOPE

Nanotwinned metals and alloys are emerging as a particular form of nanoscaled material that can exhibit high strength coupled with improved thermal stability, both of which are yet unexplained. We have developed an integrated experimental, modeling and simulation program to examine the underlying mechanisms of plasticity in nanotwinned samples. We employ a range of methods to create systems with differing twin morphologies and microstructures and characterize their structures using a range of techniques, from electron microscopy to synchrotron scattering to the use of an atom probe. Mechanical testing of these samples is carried out in a novel tensile strain stage that enables accurate measurements of stress-strain behavior with concurrent *in situ* transmission electron microscopy (TEM) observations of evolving microstructures. We will also use a temperature-controlled nanoindenter to characterize the thermal dependence of the mechanical properties. The experiments are coupled with a modeling and simulation program that includes atomistics, dislocation dynamics and polycrystal plasticity simulations. The experiments provide both realistic validation of models and a deeper understanding of fundamental mechanisms, enhancing the development of new understandings of deformation in nanotwinned materials. This program will not only shed new light on plasticity in nanotwinned materials by bridging the current gap between the experiments and modeling, but it will also greatly enhance our overall understanding of many collective and cooperative mechanisms of plasticity.

## RECENT PROGRESS

*Summary:* The first task of this program was to develop methods by which we can reliably fabricate materials with controlled nanotwin spacings. We have developed two systems, a magnetron sputtering system and one based on electrodeposition. Below we will discuss results based on the sputtering system. We have also put in place the capabilities to characterize the samples, using standard TEM measurements, coupled with synchrotron data from the APS at Argonne and the SSRL at Stanford. In addition to standard EBSD studies, we are also using Precession Electron Diffraction (PED) that uses an Astar system in the Microscopy Facility at Carnegie Mellon University. Mechanical properties are being carried out using both micro- and nano-indentation as well as bulk testing of the free-standing films. We have created new methods for analyzing local atom probe data, which will be used to examine the distribution of solutes in nanotwinned systems. The modeling program has made considerable progress as well, focusing to date on atomistic simulations of interfacial mobility and structure.

*Nanotwinned silver:* While we also have data on copper, we will use results on nanotwinned silver as an example of the work being done in the program

The magnetron sputtering system was used to create a series of nanotwinned structures in silver. The sputtering system deposits the material on liquid nitrogen-cooled wafers, with a deposition rate that varies radially across the wafer surface. What we have found is that low deposition rates (at the edges of the wafer) lead to randomly-oriented, equiaxed grain structures with twins spaced at 8-10 nm apart. High deposition rates (at the center of the wafer) lead to columnar growth with a {111}-type growth direction with 4-6 nm twin spacings. We contrast the two structures in Figure 1. Because of the dependence of the nanotwin structure on deposition rate, our system enables us to fabricate a wide variety of nanotwinned structures with tailored properties in one deposition run.

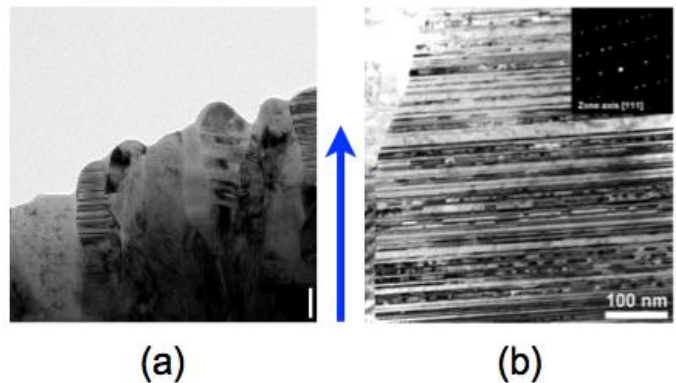


Figure 1: Nanotwinned silver films from the magnetron sputtering process. The growth direction is along the blue arrow. (a) Low rate deposition showing randomly-oriented grains and 8-10 nm nanotwin spacing. (b) High rate deposition showing columnar {111} growth and 4-6 nm spacing.

We have found regions in some samples with a second Ag phase, which has been tentatively identified as having a 4H hexagonal structure. Evidence for this phase comes from x-ray data taken at the APS as well as other experiments at Ames. There are, however, some inconsistencies between different types of data, so further work is being carried out to clarify the identity of this structure and its role in the mechanical behavior.

Work at CMU has focused on characterizing the nanostructured copper and silver materials. The main technique used has been Precession Electron Diffraction (PED) that uses an Astar system in the Microscopy Facility at CMU. The PED method generates orientation maps in thin foil samples that are equivalent to EBSD maps but with a resolution approaching 1 nm. In the case of the Cu samples, this permits stacking faults to be distinguished from true twins. In the case of the Ag samples, it is possible to verify the orientation relationship between the fcc matrix and the hexagonal second phase.

Using a tensile load frame with a laser extensometer that measures strains in the transverse and longitudinal directions for determining uniform tensile ductility, we have shown that free-standing nanotwinned films exhibit high flow stress for quasi-static uniaxial tension, with large strain-rate sensitivity. There is a strong correlation between microstructure and flow stress, showing a Hall-Petch like scaling of the form  $S = S_0 + kd^{-1/2}$ , where  $d$  is the twin lamellar spacing, with peak flow stresses on the order

of 600 MPa for 5 nm twin spacing. Recent measurements of resistivity on our samples show essentially no dependence on twin spacing, in marked contrast to nanocrystalline materials. We have also measured the thermal stability of the nanotwinned structures as a function of twin spacing using microhardness measurements. We find that the random films show grain growth and softening at about 200 °C, while the columnar {111} films show little change in mechanical behavior to about 600 °C.

*Atom probe tomography:* Understanding the impact of noise and incomplete data is a critical need for using atom probe tomography effectively, especially in the analysis of defects and interfaces such as nanotwins. Visualization of the raw data remains an important part of the analysis process. We made advances in two areas of visualizing data acquired through atom probe tomography: (1) we developed a rendering technique that enables the interactive rendering of large numbers (as large as 10 million plus) of pixel-perfect, lit spheres representing individual atoms and (2) we developed an interactive tool that allows the user to mask, filter, and colorize the data in real time to help them understand and visualize a precise subset and properties of the raw data.

*Molecular dynamics simulations:* Recent work by our group has helped clarify the most appropriate way to measure interfacial mobilities using molecular dynamics simulations. Specifically, we evaluated two commonly-used methods to model boundary mobility, finding that a commonly-used approach is unreliable. We have also used molecular dynamics simulations to identify a new mechanism for the adsorption of self-interstitials by a twin boundary, in which the self-interstitials are arranged as clusters in the twin boundary plane, with atoms in the middle of the cluster having hcp short range order rather than fcc. As a consequence of the formation of self-interstitial clusters inside each other, twin boundaries can be powerful, non-saturating sinks for self-interstitials. Finally, we have begun simulations of the properties of twinned structures. Detailed simulations of twin-boundary stability show that there are no stable asymmetric twin-boundaries in copper. Thus, there is no inclination dependence to their mobility.

#### FUTURE PLANS:

Future work will focus on synthesizing nanotwinned films (for example, Ag and Cu) with controlled twin boundary spacings and grain sizes. Our ability to tailor the nanostructure will be utilized to explore the underlying mechanisms that control the deformation behavior of nanotwinned materials. We will extend our work on the mechanical behavior to bridge the multiple length-scales inherent in nanotwinned materials. These will include pico-indentation to examine the plasticity mechanisms in individual grains, nano-indentation with temperature control to examine the thermal dependence of the mechanical response at the nanoscale, and bulk mechanical testing to explore the strain rate and temperature sensitivity of free-standing films.

The mechanical tests will be coupled with in situ characterization (TEM for pico- and nano-indentation and synchrotron X-ray for bulk mechanical testing) to examine the atomic-, nano-, and micro-scale structural changes associated with deformation. The PED work at Carnegie Mellon will continue, yielding information about small-scale orientational changes. We will continue our work to elucidate the structure, stability,

and mechanical behavior of the second phase (tentatively identified as a 4H hexagonal structure) formed during rapid quenching using the magnetron sputtering system. We can create samples of nanotwinned materials for atom probe tomography, which will be used to explore the structures of twin boundaries. The long-ranged goal is to use the atom probe to characterize the localization of solutes in nanotwinned materials.

Molecular dynamics activities will focus on the stability of nanotwinned systems. The proposed study includes (i) fixing problems with the artificial driving force method; (ii) studying the effect of point defects on coherent twin boundary migration; (iii) determining the twin boundary and stacking fault free energies; (iv) studying the kink propagation on the coherent twin boundary; (v) studying the twin boundary migration in the half-loop geometry and (vi) studying the effect of the twin boundaries on grain boundary migration. We will also examine how dislocations interact with the twin structures and how that affects their structure and mobility.

Modification to our basic dislocation dynamics code is underway to be able to apply it to thin films of nanotwinned materials. We developed the basic formalism to study polycrystalline thin films under a previous program. We are currently developing an approach by which we can directly include partial dislocations within the simulations, which are needed to examine how dislocations interact with twinned structures.

The PED results are being used to generate representative 3D digital microstructures that will be used to perform simulations of grain growth. Representative twins will be introduced into the individual grains to create uniformly spaced, large aspect ratio twinned structures. Twinned and equiaxed microstructures will be used as input structures to a Potts model for curvature-driven grain growth. Isotropic and anisotropic grain boundary properties will be used, where anisotropy will serve to apply low energy and mobility to the twin boundaries. Results from these simulations will play a large role in an investigation of what factors stabilize the nanotwinned material.

#### PUBLICATIONS:

- “Temperature-dependent competing deformation mechanisms in nanocrystalline metals,” Y. M. Wang, R. T. Ott, M. F. Besser, and A. V. Hamza, *Physical Review B* 85, 144122 (2012)
- “The Interactions of Self-Interstitials with Twin Boundaries,” M. I. Mendeleev and A. H. King, accepted for publication in *Philosophical Magazine*.
- “Understanding Noise in Atom Probe Tomography Data Through Visualization,” A. Bryden, S. Broderick, S. K Suram, K. Kaluskar, R. LeSar and K. Rajan, accepted for publication in *Ultramicroscopy*
- “The feedback loop between theory, simulation and experiment for plasticity and property modeling,” T. M. Pollock and R. LeSar, accepted for publication in *Current Opinion in Solid State and Material Sciences*.
- “Visualization in materials research: Rendering strategies of large data sets,” A. Bryden, K. Rajan and R. LeSar, in *Informatics for Materials Science and Engineering*, edited by K. Rajan, to be published by (Elsevier, Amsterdam, Netherlands).

**Program Title: Micro-mechanisms and Multiscale Modeling of Cyclic Plastic Deformation of Magnesium Single Crystals**

**PI:** Qizhen Li, Chemical and Materials Engineering  
University of Nevada, Reno  
1664 North Virginia Street, Mail Stop 388, Reno, NV 89557  
QIZHENL@UNR.EDU

**Program Scope or Definition**

The primary goal of this project is to explore the fundamental deformation and failure mechanisms for the materials with a hexagonal close packed (HCP) crystal structure. Magnesium based materials (magnesium single crystal, pure polycrystalline magnesium, and some magnesium alloys) are utilized in our investigations. These materials are chosen because they have HCP crystal structure, their excellent properties and broad structural applications in light-weight structural components, and their unclear deformation and failure mechanisms.

**Recent Progress**

The recent research activities were performed to understand the deformation mechanisms of magnesium (Mg) single crystals and polycrystalline Mg under different loading conditions. Research efforts were also devoted to study the effect of thermomechanical processing on the mechanical behavior of Mg. A list of performed research investigations is given in the following bullets.

I. Magnesium single crystals

The 0001 and  $\bar{1}014$  single crystal samples were tested under compression-compression cyclic loading for 50 cycles at room temperature. The tested samples were then studied using XRD, SEM, and HRTEM.

- It is clear that the samples with different orientations display quite different mechanical behavior and microstructural features.
- For 0001 single crystal, the strain range and ratcheting strain are constant and very small.
- The sample heavily strained and deformed for  $\bar{1}014$  single crystal, and the ratcheting strain is about ten times of that for 0001 single crystal.
- There is no cyclic hardening or softening for 0001 single crystal, while  $\bar{1}014$  single crystal experienced cyclic strain hardening.
- Microstructural observations and Schmid factor analysis show that the consistent deformation mechanisms for the samples. 0001 single crystal has twinning as the primary deformation mechanism and no basal slip operation. Tension twinning is not favorable at the beginning and becomes operable sparsely after the material experienced some rotation.  $\bar{1}014$  single crystal has basal slip, pyramidal slip, secondary pyramidal slip, and tension and compression twinning to operate. The basal slip results in the initial plastic deformation region for  $\bar{1}014$  single crystal.

## II. Polycrystalline magnesium

### a. High strain rate loading

- Polycrystalline magnesium samples were tested under quasi-static and dynamic compression loading to explore mechanical properties and microscopic deformation mechanisms. The strain rate for quasi-static testing is  $\sim 0.001 \text{ s}^{-1}$ , and those for dynamic testing is in the range of  $800 \sim 3600 \text{ s}^{-1}$ .
- The yield strength is slightly sensitive to strain rate (i.e. it barely varies with strain rate), and the ultimate strength, fracture strain, and work hardening rate are highly sensitive to strain rate (i.e. they vary significantly with strain rate).
- Three deformation regimes (I, II, and III) were observed on the quasi-static and dynamic stress-strain curves. These regimes show respectively increasing work hardening rate in the early stage of plastic deformation, constant work hardening rate in the intermediate plastic deformation region, and decreasing work hardening rate in the end region right before fracture.
- The ultimate strength and the maximum work hardening rate for dynamic loading is over twice of that for the quasi-static loading, while it does not change much in the employed dynamic strain rate range.
- Twinning/detwinning is the dominating deformation mechanism for the quasi-static loading, while the combination of dynamic recrystallization and twinning/detwinning is the dominating deformation mechanism for the dynamic loading.
- Theoretical modeling also provides predictions of the material behavior that match well with the experimental data. Different factors were in effect for different loading strain rates. The stress-strain relations are affected primarily by strain hardening for quasi-static testing; by strain hardening, strain rate hardening, and thermal softening for dynamic testing with  $\dot{\epsilon} \leq 2000 \text{ s}^{-1}$ ; and by strain hardening, damping, and thermal softening for dynamic testing with  $\dot{\epsilon} > 2000 \text{ s}^{-1}$ , respectively.

### b. Rolling and heat treatment

- Rolling increases yield strength significantly by about 100% to 130% and decreases ductility by about 55% to 66%.
- A rolling route with a lower thickness reduction strain per rolling pass corresponds to a higher strength increase.
- Annealing does not affect the magnitudes of yield strength and ductility, but largely increases ultimate tensile strength and strain hardening rate compared with the as-rolled material without experiencing annealing.

## Future Plans

The PI plans to further investigate the mechanical deformation behavior and the associated mechanisms in Mg under cyclic loading.

## References of Publications

- [1] "Effect of Strain Amplitude on Tension-Compression Fatigue Behavior of Extruded Mg6Al1ZnA Magnesium Alloy," *Scripta Materialia*, 62, 778-781 (2010).
- [2] "Multiaxial Fatigue of Extruded AZ61A Magnesium Alloy," International Conference on Fatigue Damage of Structural Materials VIII, Hyannis, MA, Sept.19-24, 2010.
- [3] "Cyclic Deformation and Multiaxial Fatigue of Extruded AZ61A Magnesium Alloy," International Conference on Mechanical Properties of Materials, May 24-28, 2010, Hangzhou, P.R. China.
- [4] "Microstructure and deformation mechanism of Mg6Al1ZnA alloy experienced tension-compression cyclic loading," *Scripta Materialia*, Vol. 64, pp. 233-236 (2011).
- [5] "Multiaxial Fatigue of Extruded AZ61A Magnesium Alloy," *International Journal of Fatigue*, Vol.33, pp. 437-447 (2011).
- [6] "An Experimental Study of Cyclic Deformation of Extruded AZ61A Magnesium Alloy," *International Journal of Plasticity*, 27 (5): 768-787, (2011).
- [7] "Deformation, Damage, and Fracture of Light Metals and Alloys", a conference symposium in TMS 2011 Annual Meeting & Exhibition, February 27 - March 3, 2011, San Diego, California.
- [8] "An Experimental Study on Cyclic Deformation and Fatigue of Extruded ZK60 Magnesium Alloy", TMS 2011 Annual Meeting & Exhibition, February 27 - March 3, 2011, San Diego, California.
- [9] "Effect of strain ratio on cyclic deformation and fatigue of extruded magnesium alloy AZ61A", TMS 2011 Annual Meeting & Exhibition, February 27 - March 3, 2011, San Diego, California.
- [10] "Cyclic Deformation of Extruded AZ61A Magnesium Alloy," *Proceedings of Plasticity'11*, *Plasticity'11*, Jan.2-8, 2011.
- [11] "Dynamic Mechanical Response of Magnesium Single Crystal under Compression Loading: Experiments and Simulations," *Journal of Applied Physics* 109, 103514 (2011).
- [12] "Direct observation of twinning-detwinning-retwinning on magnesium single crystal subjected to strain-controlled cyclic tension-compression in [0001] direction," *Philosophical Magazine Letters* 91, 757-765 (2011).
- [13] "Fatigue damage development in pure polycrystalline magnesium under cyclic tension-compression loading," *Materials Science and Engineering A* 528, 7816-7826 (2011).
- [14] "Deformation, Damage, and Fracture of Light Metals and Alloys," A conference symposium in 2012 TMS annual meeting, Orlando, FL, Mar. 11-15, 2012.
- [15] "Mechanical Behavior of Magnesium/Carbon Nanotube Composites," *Plasticity'12*, San Juan, PR, USA, Jan. 3-8, 2012.

- [16] “An Experimental Study on Cyclic Deformation and Fatigue of Extruded ZK60 Magnesium Alloy,” *International Journal of Fatigue* 36, 47-58 (2012).
- [17] “Mechanical properties and microstructure of pure polycrystalline magnesium rolled by different routes,” *Materials Letters* 67, 81–83 (2012).
- [18] “Mechanical Behavior of Metallic Nanostructured Materials,” A conference symposium in 2012 MRS Fall meeting, Boston, MA, Nov. 25-30, 2012.
- [19] “Mechanical Behavior of Magnesium/Carbon Nanotube Composites under Compression Tests,” MRS 2012 Fall meeting, Boston, Massachusetts, Nov. 25-30, 2012.
- [20] “Multiaxial fatigue of extruded AZ31B magnesium alloy,” *Materials Science and Engineering A* 546, p.119-128, 2012.
- [21] “An experimental study of fatigue crack propagation in extruded AZ31B magnesium alloy,” *International Journal of Fatigue* 47, p.174-183, 2013.
- [22] “Mechanical properties and microstructure of pure magnesium experienced rolling and annealing,” TMS 2013 Annual Meeting, San Antonio, Texas, Mar. 3-7, 2013.
- [23] “Dynamic mechanical response of magnesium single crystal under compression loading: Experiments, model, and simulations,” *Plasticity '13*, Sheraton, Nassau, Bahamas, Jan. 3-8, 2013.
- [24] “Effect of strain ratio on cyclic deformation and fatigue of extruded AZ61A magnesium alloy,” *International Journal of Fatigue* 44, p. 225-233, 2012.
- [25] “An Experimental Study on Cyclic Deformation and Fatigue of Extruded ZK60 Magnesium Alloy,” *International Journal of Fatigue* 36, p. 47-58, 2012.
- [26] “Mechanical Properties and Microscopic Deformation Mechanism of Polycrystalline Magnesium under High-Strain-Rate Compressive Loadings,” *Materials Science and Engineering A* 540, p. 130–134, 2012.
- [27] “Fatigue behavior and microstructure of 0001 and -1014 magnesium single crystals under compression-compression cyclic loading,” *Materials Science and Engineering A* 556, p. 301-308, 2012.

# Understanding microplasticity processes related to fatigue damage using high energy x-rays and a crystal-based modeling formulation

## (Presentation Abstract)

Matt Miller<sup>1</sup>, Paul Dawson<sup>1</sup>, Ulrich Lienert<sup>2</sup>, Jim Williams<sup>3</sup>, Jun-Sang Park<sup>1</sup>, Mark Obstalecki<sup>1</sup> and Su Leen Wong<sup>1</sup>

<sup>1</sup>Sibley School of Mechanical and Aerospace Engineering, Cornell University, Ithaca, NY

<sup>2</sup>Deutsches Elektronen-Synchrotron, Hamburg Germany

<sup>3</sup>Materials Science Department, The Ohio State University, Columbus, OH

## Scope

In this project, we proposed the creation of a hybrid experimental / computational capability for studying detailed subgrain scale elastic-plastic deformation processes in polycrystalline metals to build understanding of cyclic material evolution and eventually fatigue crack initiation. Our group has developed *in situ* mechanical loading / x-ray diffraction experiments that have enabled us to measure the deformation of individual grains within loaded polycrystalline aggregates. In this project, we would extend our mechanical loading capabilities to enable cyclic tests and create data reduction algorithms to examine diffracted intensities from each grain within the aggregate. Our group has also created finite element-based material models of elasto-viscoplastic deformation of metallic polycrystals formulated on the scale of the individual grain. We've modeled a wide range of processing and in-service conditions. We have also shown that the crystal stresses calculated from the *in situ* diffraction data compare well to those computed using the model. In this work we would extend the model to include the x-ray scattering phenomena to create virtual detector data that can be compared directly with that measured in the experiment. We build trust in the model by validation using the virtual diffractometer and comparing to hundreds of diffracted intensity "spots" for each crystal. We can then employ the model to explore hypotheses related to crystal scale elastic-plastic deformation during cyclic load and the eventual initiation of fatigue damage.

## Recent Progress

In our experiments, we quantify the distorted structure of each grain - the collection of diffracted intensities (spots) for each grain collectively define the distribution of orientations and strain within the grain. The model, corroborated with the experimental intensities, can then provide detailed information about crystal stress, strain hardening, shearing rates and intragrain misorientation distributions. During the first three years of this project, we created the new framework and demonstrated its feasibility. We conducted studies on OMC copper under monotonic and cyclic loading conditions.

In this talk we describe experimental and modeling results from the first 3 years of the grant from monotonic and cyclic loading of the Cu-Zr-Cr alloy, OMC Copper. As described in a recently accepted article, we used the monotonic experimental data from one crystal within the deforming OMC sample to construct a prototype Virtual Diffractometer [1]. Figure 1 depicts the macroscopic stress-strain curve from the monotonic experiment and the finite element model of the OMC specimen. Figure 2 depicts the measured and simulated diffraction spots from the target grain within the deforming OMC polycrystalline aggregate taken at the loads listed in Figure 1. The intensity distributions are initially very sharp – consistent with the crystal lattice within the grain being at a single orientation. As the material yields (load steps 3, 4 and 5) the diffracted intensity spreads - consistent with the spread of orientation and strain within the crystal. The close visual comparison in Figure 2 is consistent with the moments of the distributions given in Figure 3. Here we see general agreement in the radial spread (given by full width half maximum, FWHM, of the peak) that is associated with strain. The azimuthal FWHM, generally consistent with spread in orientation, increases in the bottom two rows (at larger macroscopic strains).

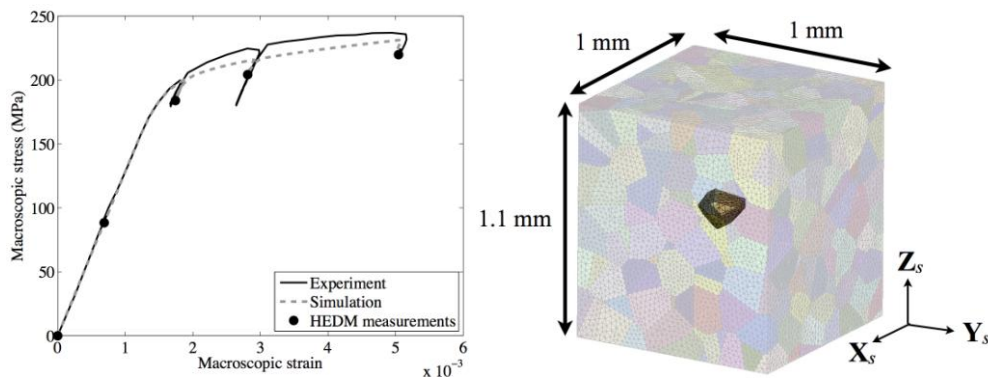


**Figure 1** (Left) Macroscopic stress-strain curve of the OMC copper sample depicting the points where High Energy Diffraction Microscopy (HEDM) experiments were conducted. The model prediction is also given. (Right) Finite element model of the OMC specimen. The target grain is highlighted.

In Figure 4, we have extracted the lattice strains from the experimental data and calculated a crystal-averaged value of stress using the single crystal elastic moduli. We compare these values to the simulation results – averaged over all elements within the virtual target crystal. The enormous potential of the model is illustrated in Figures 4 and 5, which depict how the model predicts the way stress and orientation are distributed over the grain. This is information that we cannot determine directly from the experiment. The spots themselves contain limited spatial information.

In the talk, we will also present results from cyclic tests on the OMC, which show the evolution of the internal structure of several grains within the aggregate with accumulated fatigue cycles and the associated simulation results.

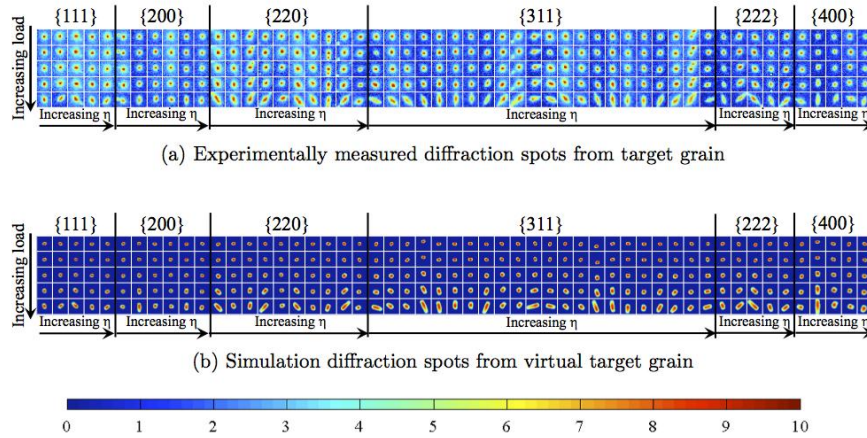


**Figure 2** Comparison between 53 experimental and simulated diffraction spots for the target grain at five macroscopic load levels. Experiment and simulation diffraction spot intensities are shown using the same logarithmic intensity scale.

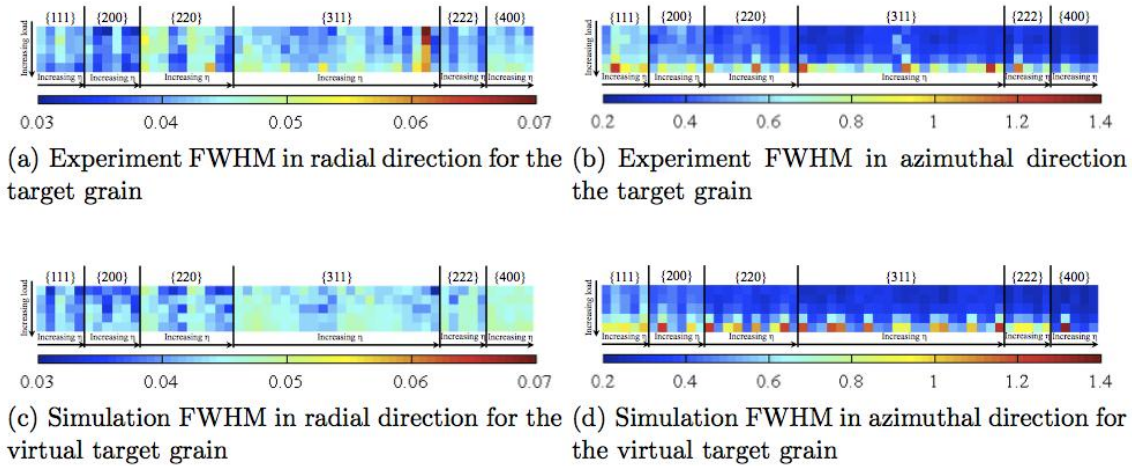


**Figure 3** Full width at half maximum (FWHM) in the radial and azimuthal directions for the experiment and simulation diffraction spots shown in Fig. 1. All values are given in degrees.

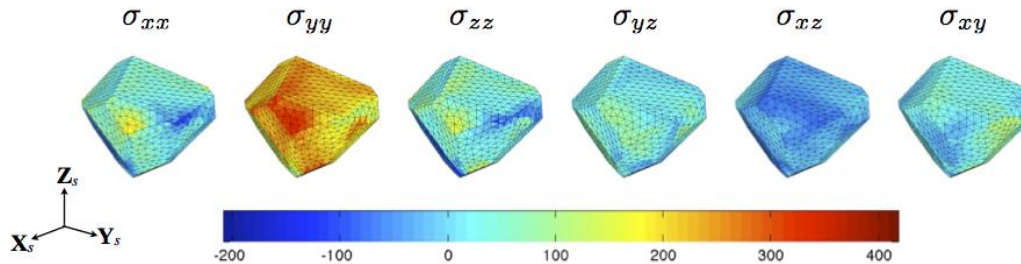


**Figure 4** Spatial distribution of the stress components within the target crystal at the fifth macroscopic load step (219 MPa) as predicted by the model. The macroscopic loading direction was  $y$ . The scale is given in MPa.

## Future work

In the next phase of the project, we will investigate pure, OFHC copper and investigate the following questions:

(1) Can we observe the cycle by cycle plasticity-driven structural evolution that occurs inside individual crystals within a deforming polycrystalline copper aggregate, identifying differences related to crystal orientation, crystallographic neighborhood and proximity to the sample surface?

(2) Can we understand the underlying physical conditions (stress, deformation character, strain hardening...) that drive the structure evolution we observe within each crystal?

(3) Can we link this cyclic-plasticity driven structure evolution to the initiation of fatigue microcracks?

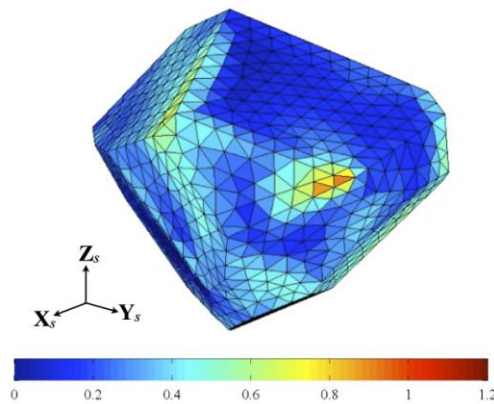


**Figure 5** Spatial distribution (in degrees) of lattice orientation within the target crystal at the fifth macroscopic load step (219 MPa).

Key quantities, such as the details of the distributions of stress, misorientation, and strain hardening rates within each crystal can be extracted from the simulations to understand the source of the structure evolution we observe and to ultimately formulate a theory for microcrack initiation in copper. In addition to impacting the existing understanding of fatigue crack initiation, this research can change the way we design structures to avoid fatigue failure. More importantly, the fundamental quantitative structure–property links that this project will create can eventually be used to design fatigue- resistance materials. Finally, the novel experimental / computational approach developed in this project can be employed for other important materials science - based questions.

## Publications

[1] Wong, S.L., Park, J-S., Miller, M.P., and Dawson, P.R., “A Framework for Generating Synthetic Diffraction Images from Deforming Polycrystals Using Crystal-Based Finite Element Formulations, Computational Materials Science, Accepted with minor revisions, 2013

## Formation and Stability of Nanoclusters in a Nanostructured Ferritic Alloy

M. K. Miller, C. M. Parish, C.L. Fu, L. Yao, X.-L. Wang, Z.W. Zhang,  
G. B. Viswanathan, and M. J. Mills

### Program Title: Stability of Nanoclusters in Metal Matrices under Extreme Environments

#### Principal Investigator:

Michael K. Miller  
Corporate Fellow  
Materials Science and Technology Division  
Oak Ridge National Laboratory  
P. O. Box 2008, Oak Ridge, TN 37831-6139  
Phone: 865/574-4719  
E-mail: [millermk@ornl.gov](mailto:millermk@ornl.gov)

#### Co-Investigators:

Chong Long Fu  
Distinguished R&D Staff  
Phone: 865/574-5161  
E-mail: [fucl@ornl.gov](mailto:fucl@ornl.gov)

#### Co-Investigators:

Chad M Parish  
Research & Development Staff  
Phone: 865/574-0092  
E-mail: [parishcm@ornl.gov](mailto:parishcm@ornl.gov)

Dong Ma  
Instrument scientist  
Phone: 865/574-6080  
E-mail: [dongma@ornl.gov](mailto:dongma@ornl.gov)

Yanwen Zhang  
Senior Research Staff  
Phone: 865/574-8518  
E-mail: [zhangyl@ornl.gov](mailto:zhangyl@ornl.gov)

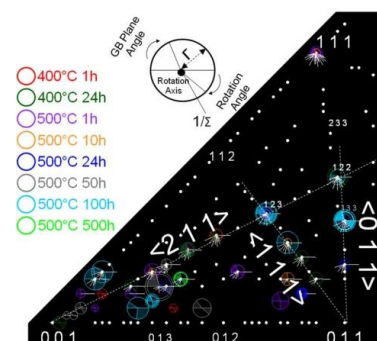
The goal of this project is to understand the formation mechanism, energetics, and fundamental hardening behavior associated with stable nanoclusters (NCs) in metallic alloys, and to establish a fundamental understanding of the mechanisms that control their response to intense irradiation and other extremes. The specific aims of the proposed research are to establish the mechanisms for homogenous and heterogeneous nucleation that occur during the earliest stages of NC and He bubble formation in materials far from equilibrium, to understand the mechanisms that enable radiation tolerant behavior in structural steels exposed to high doses of irradiation, and to understand the interaction of dislocations with the NCs and other microstructural features in an ultra-fine grain nanostructured ferritic alloy (NFA), and hence, understand their outstanding mechanical properties. This basic research is ultimately aimed at developing the understanding needed to enable fundamental discoveries regarding nucleation and defect mechanisms in nanostructured materials. The scientific principles developed are expected to have a broad applicability in the synthesis of new-generation nanostructured materials with high-temperature capability for use in advanced energy production and conversion systems under extreme environments.

A specific aim of this research is to establish the mechanisms for homogenous and heterogeneous nucleation that occur during the earliest stages of formation of NCs and He bubbles in materials far from equilibrium. First Principal (FP) calculations indicate that there is a strong interaction between vacancies and O, Ti, and Y atoms in  $\alpha$ -Fe, and that solute-vacancy clusters are a key component for controlling solute diffusion and the stability of the NCs, precipitates, and grain boundaries (GBs) of NFAs. Previous investigations have shown that atom probe tomography (APT) and neutron scattering can detect clusters with as few as three atoms; however, simulations indicate that the effectiveness of the APT estimates is strongly influenced by the detection efficiency (DE) of the single atom detector and that DEs greater than 90% are required for accurate analysis of solute clusters and NCs for matrix solute levels  $>\sim 1\%$ .

The mechanisms and kinetics of NC nucleation and growth have been studied in isothermally aged, mechanically alloyed (MA) 14YWT flakes. NCs were detected by APT after aging for only 1 h, 1 h, and 2 min., for samples aged at 400, 500, and 850 °C, respectively. An in-situ neutron scattering experiment of the evolution of the NC radius at 500°C suggested an incubation period indicative of a nucleation and growth process. The sizes of the NCs were evaluated from APT data from the same series of thermally aged MA 14YWT flakes. The finest size-scale (2-4 nm) NCs were characterized by high angle annular

dark field (HAADF)-STEM imaging techniques. Through-focus-series imaging indicated that the NCs could be highly disordered and amorphous, in agreement with FP calculations. A new Titan with ChemiSTEM technology and Super-X energy dispersive spectroscopy (EDS) system at Ohio State University was used to obtain compositional information from NCs and the surrounding matrix after creep at 900°C. Initial results indicate that this approach can be used to obtain the size and distribution of NCs with greatly improved statistics, and that, in agreement with APT results, the NCs appear larger when mapped with Ti and Cr compared to that for Y. These results indicate that, at least for this creep condition, Ti is found throughout the NCs, Y is present in larger concentrations at the center of the NCs, and Cr may be enriched at the exterior. In future research, the exact nature of the size-class, structure, and chemistry of NCs and the coarser precipitates will be investigated with the ChemiSTEM Titan using HAADF- and BF-STEM imaging modes, as well as APT.

The excellent creep response of NFAs has been shown to be related to the pinning of the GBs by solute segregation of Cr and W, and by precipitation of NCs and other coarser precipitates on the GBs. Therefore, the evolution of Cr and W segregation after a series of isothermal heat treatments at 400, 500, and 850 °C on MA flakes has been determined. A 3D-Hough-transformation-based method was used to define the five-parameter orientation relationship, and the extent of GB segregation has been refined to clearly reveal the trends. As the stability of the GBs is critical in maintaining good mechanical properties during high dose irradiation, similar GB characterizations are underway on high temperature, high dose ion irradiated conditions.



A specific aim of the research is to understand the interaction of dislocations with NCs and other nanometer-scale features. This interaction will be studied through in-situ deformation studies at elevated temperatures in a STEM and the unique neutron scattering facilities at the Spallation Neutron Source (SNS), together with interrupted deformation and creep tests. Dislocation-NC interactions have been studied using low-angle angular dark field (LAADF) STEM, which contains diffraction contrast (strain field) information. These investigations have shown that the dislocation contrast is reduced, and in some cases disappears, indicating that the dislocation strain field is relieved at the NCs. The dislocation structures following high temperature creep at 950°C are less heavily pinned than those after lower temperature creep, suggesting that the structure/chemistry of the NCs has been altered. Building on our steady-state creep Kocks-Argon-Ashby-based model, an improved model will be developed that incorporates transient creep effects using a cellular automata approach. The new image aberration-corrected Titan ChemiSTEM microscope will enable quantification of the strain field around dislocations and NCs to distinguish characteristics of NCs experiencing aging/creep at lower and higher temperatures.

A specific aim of this project is to understand the mechanisms that enable radiation tolerant behavior in structural steels exposed to high dose irradiation. The stability of solute-vacancy clusters and NCs in the presence of excess defects and highly supersaturated solute environments, such as those produced by displacement cascades during high dose radiation damage by neutrons, ions, and MA, are key components to understand this behavior. High-resolution STEM-EDS mapping of the as-extruded and high dose (30 and 300 dpa) ion irradiated conditions indicates significant microstructural evolution at high temperatures. In addition to Ti(N,C,O) precipitates, small numbers of Al-enriched precipitates are observed, and at a dose of 300 dpa, the Al is redistributed into the Ti-Y enriched GB features. As the ability of the NCs to trap He and vacancies is a strong function of the NC composition (including vacancy content), this result indicates that it is important to model these trapping effects. Irradiation at 750°C causes significant growth of the Ti-Y enriched GB and intragranular precipitates, indicating a coarsening mode not observed by thermal aging. The Cr-W GB segregation decreases with irradiation at 750°C, which is in contrast to APT and TEM results for -100°C irradiation, where little GB segregation or NCs

remain due to ballistic redistribution of the solute. These data indicate a thermodynamic driving force effect for re-establishment of the Cr-W GB segregation, which may help explain the excellent creep strength of NFAs. Creep in ultra-fine grained (UFG) materials is dominated by GBs, and the combination of segregation and precipitation at the GBs likely suppresses creep kinetics, so the driving force to retain segregation despite irradiation is likely beneficial. This research indicates that ion-irradiation-induced mixing of the Ti(N,O,C) precipitates into the matrix occurs when high dose irradiations were performed at -100°C to 100->300 dpa. The quantitative changes in the chemistry of the NCs and GB segregation under various irradiation conditions and temperatures will be studied with a combination of APT and STEM. Planned research will compare and contrast differences between ion and neutron irradiations.

Another specific aim includes establishing the interaction of He atoms with solutes, the mechanisms of He bubble formation, and the mechanisms to minimize or eliminate deleterious He embrittlement due to the presence of He bubbles at GBs. In our previous research, the hypothesis that the surfaces of the NCs and the larger Ti(N,O,C) precipitates are preferential nucleation sites for He bubble formation was verified by direct observation in the APT data and TEM images, respectively. Current research has revealed that NCs capture a significant fraction (~48%) of the He bubbles in the as-implanted specimens. However, service under irradiation at reactor temperatures will result in prolonged aging of the He bubbles. To simulate this, and to understand aging effects, a  $6.75 \times 10^{16}$  He/cm<sup>2</sup> He specimens was annealed for 10 and 100 h at 650°C. TEM images indicate coarsening of the bubbles, and a quantitative analysis of intragranular and GB bubbles shows coarsening of the bubble sizes. Intragranular bubbles grew slightly from  $2.4 \pm 1.0$  nm as-implanted to  $2.7 \pm 1.6$  nm after 100 h; GB bubbles grew much more significantly, from  $1.5 \pm 0.3$  nm as-implanted to  $4.7 \pm 2.1$  nm after 100 h aging. This indicates there are limits to the ability of the NCs to sequester He away from the boundaries. Future research will investigate 1) if lower He concentrations, such as in in-reactor service, become more sequestered by the NCs, 2) whether the GB He bubbles are trapped at the GB surface itself or at NCs and precipitates co-located with the GB, and 3) the effects of higher levels of damage at constant He concentration on the microstructure.

Previous work has shown the strong influence of NCs on dislocation motion and creep deformation. Preliminary work has indicated the ability of simultaneous BF- and HAADF-STEM imaging to image dislocations, NCs, and He bubbles. He-ion irradiations will be used to determine the effects of glissile dislocations on He bubble nucleation. It is hypothesized that varying the dislocation density will affect He sequestration at NCs vs. precipitates along dislocations.

This research was sponsored by the Materials Sciences and Engineering Division, Office of Basic Energy Sciences, US Department of Energy, and performed in part at ORNL's Shared Research Equipment (ShaRE) user facility, which is sponsored by the Scientific User Facilities Division, Office of Basic Energy Sciences, US Department of Energy. Heavy ion irradiations were performed at the Environmental Molecular Sciences Laboratory, a national scientific user facility sponsored by the US Department of Energy's Office of Biological and Environmental Research and located at Pacific Northwest National Laboratory.

Paper published from this research project (2010 – present)

1. M. K. Miller, D. T. Hoelzer, and K. F. Russell, "Towards Radiation Tolerant Nanostructured Ferritic Alloys," *Materials Science Forum* **654-656**, 23-28 (2010), invited.
2. A.G. Certain, K.G. Field, T. R. Allen, M. K. Miller, J. Bentley, and J. T. Busby, "Response of Nanoclusters in a 9Cr ODS Steel to 1 dpa, 525°C Proton Irradiation," *J. Nucl. Mater.* **407**, 2-9 (2010).
3. J. Bentley and D. T. Hoelzer, "In Situ Ion Irradiation of Nanostructured Ferritic Alloys," *Microscopy and Microanalysis* **16** (suppl 2), 1610-1611 (2010), invited
4. M. K. Miller, D. T. Hoelzer, and K. F. Russell, "Radiation Response of a 12YWT Nanostructured Ferritic Steel," *Proc. MRS 2009 Fall Meeting, Materials Research Needs to Advance Nuclear Energy*, eds., G. Baldinozzi, K.L. Smith, K. Yasuda, and Y. Zhang, vol. 1215-V06-02 (2010).

5. M. K. Miller, "Effects of Extreme Conditions on the Microstructures of Nanostructured Ferritic Steels," *Proc. International Microscopy, Congress, IMC17*, Rio de Janeiro, Brazil, Sept. 19-24, 2010, I14.7 on CD.
6. M. K. Miller, K. F. Russell, D. T. Hoelzer, L. Kovarik, M. J. Mills, A. G. Certain, and T. R. Allen, "Atom Probe Tomography as a Tool for Characterizing Irradiated Materials," *Microscopy and Microanalysis* **16** (suppl. 2), 1602-1603 (2010).
7. P. D. Edmondson, C. M. Parish, Y. Zhang, A. Hallén, and M. K. Miller, "Helium Entrapment in a Nanostructured Ferritic Alloy," *Scripta Mater.* **65**, 731-734 (2011).
8. M. K. Miller and C. M. Parish, "The Role of Alloying Elements in Nanostructured Ferritic Steels," *Mater. Sci. Technol.* **27**, 729-734 (2011).
9. M. K. Miller and Y. Zhang, "Fabrication and Characterization of APT Specimens from High Dose Heavy Ion Irradiated Materials," *Ultramicroscopy* **111**, 672-675 (2011).
10. C. M. Parish, P. D. Edmondson, Y. Zhang, and M. K. Miller, "Direct observation of ion-irradiation-induced chemical mixing," *J. Nucl. Mater.* **418**, 106-109 (2011).
11. C. M. Parish, P. D. Edmondson, and M. K. Miller, "Multivariate Statistical Analysis of STEM-EDS at the Noise Floor," *Microscopy and Microanalysis*, **17** (suppl. 2), 595-596 (2011)
12. M. K. Miller and D. T. Hoelzer, Effect of Neutron Irradiation on Nanoclusters in MA957 Ferritic Alloys, *J. Nucl. Mater.* **418** (2011) 307-310.
13. H. Zhao, C. L. Fu, M. Krcmar, and M. K. Miller, "Effect of strain on the stabilization of oxygen-enriched nanoclusters in Fe-based alloys," *Phys. Rev B*, **84**, 144115 (2011).
14. M. C. Brandes, L. Kovarik, M. K. Miller, G. S. Daehn, and M. J. Mills, "Creep Behavior and Deformation Mechanisms in a Nanocluster Strengthened Ferritic Steel," *Acta Mater.* **60**, 1827-1839 (2011).
15. M. C. Brandes, L. Kovarik, M. K. Miller, M. J. Mills, "Morphology, Structure, and Chemistry of Nanoclusters in a Mechanically-Alloyed Nanostructured Ferritic Steel," *J. Mater. Sci.* **47**, 3913-3923 (2012).
16. M. K. Miller, T. F. Kelly, K. Rajan and S. P. Ringer, "The Future of Atom Probe Tomography," *Materials Today* **15**(4) 158-165 (2012), invited.
17. X.-L. Wang, C. T. Liu, U. Keiderling, A. D. Stoica, L. Yang, M. K. Miller, C. L. Fu, D. Ma, and K. An, "Unusual Thermal Stability of Nano-structured Ferritic alloys," *Journal of Alloys and Compounds* **529** (2012) 96- 101.
18. Z. W. Zhang, C. T. Liu, X.-L. Wang, M. K. Miller, D. Ma, G. Chen, J. R. Williams, B. A. Chin, "Effects of proton irradiation on nanocluster precipitation in ferritic steel containing fcc alloying additions," *Acta Mater.*, **60**, 3034-3046 (2012).
19. M. K. Miller, "Atom Probe Tomography of Phase Transformations in Steels," Book chapter in Phase transformations in steels: Diffusionless transformations, high strength steels, modelling and advanced analytical technique, Eds. E. Pereloma, and D. V. Edmonds, Chapter 17, vol. 2, (2012) pub. Woodhead Pub., Cambridge, UK, pp. 532-556; ISBN 1 84569 971 8; ISBN-13: 978 1 84569 971 0.
20. C. M. Parish, L. Yao, Y. Zhang, P. D. Edmondson, A. Hallén, and M. K. Miller, "A multi-technique approach to understand radiation-tolerant nanostructures," *Microscopy and Microanalysis* **18** (suppl. 2), 1430-1 (2012).
21. P. D. Edmondson, C. M. Parish, Y. Zhang, A. Hallen and M. K. Miller, "Helium bubble distributions in a nanostructured ferritic alloy," *J. Nucl. Mater.* **434**, 210-216 (2013).
22. M.K. Miller, C. M. Parish, and Q. Li, "Advanced Oxide Dispersion Strengthened and Nanostructured Ferritic Alloys," *Material Science and Technology*, in press, Jan 2013, invited.

## Transformation and Deformation Mechanisms in High Temperature Shape Memory Alloys With Nanoprecipitates

**Principle Investigators:** Y. Wang (wang.363@osu.edu), P. M. Anderson (anderson.1@osu.edu)  
M. J. Mills ([mills.108@osu.edu](mailto:mills.108@osu.edu))

**Students:** F. Yang, D. Coughlin, L. Casalena, H. Paranjape, Y. Gao  
Department of Materials Science and Engineering, The Ohio State University  
Columbus, OH 43210

The focus of this program is on an emerging class of high temperature shape memory alloys (HTSMAs) that are exciting candidates for actuators and adaptive components in a wide range of energy and transportation applications. These HTSMAs offer the possibility of high reliability, lighter weight and increased capability while lowering space and power consumption. However, at present there is only elementary understanding of the important microstructure-property relationships. The goals of this effort therefore are to (1) develop a fundamental understanding of the inherent microstructure-property behavior of high temperature shape memory alloys and (2) develop computational models that capture these structure-property relationships and provide novel insights into the important transformation and plasticity mechanisms that govern their behavior. Two “Ni-rich” HTSMA alloy systems are at the core of the effort: (Ni,Pt)Ti and Ni(Ti,Hf) alloys can exhibit high transformation temperatures, large transformation strain and small permanent strain. These beneficial properties can be strongly influenced by the formation of nanoscale precipitates. Spearheaded by advanced characterization techniques, and aided by insights from first principles modeling, the unusual and novel atomic structure and composition of these precipitates is being determined, along with their coherency with the matrix. Interaction of precipitates with martensite at lower temperature and dislocation activity at higher temperature are key mechanistic insights being sought through in situ electron microscopy studies, and being understood through new phase field modeling approaches to particle/defect interactions. These insights are being incorporated into a microstructural finite element framework in order to capture how phase transformations, crystal plasticity, and time-dependent creep interact to determine the response of single crystal micropillar experiments under isothermal and load biased thermal cycling conditions.

### Recent Progress

In this joint experiment/modeling effort we are seeking to understand the fundamental microstructure-property relationships in high temperature shape memory alloys (HTSMAs) that are based on the NiTi-X alloy system. Our previous work on the TiNiPt system has demonstrated that P-phase precipitates form during aging could improve mechanical and shape memory properties significantly. Our efforts in the past year have been focused on Ni rich NiTiHf systems. Similarly, a novel precipitate phase (H-phase) forms after aging between 500~600°C. The structure of these novel precipitates was characterized by electron diffraction and high-resolution high angle annular dark field (HAADF) scanning transmission electron microscopy (STEM). Structural analysis confirmed that the H-phase has a face centered orthorhombic unit cell. The composition of the H-phase was investigated by both TEM-energy dispersive spectroscopy (EDS), as well as 3D atom probe tomography (APT). The latter study was enabled by a facility grant through the EMSL at Pacific Northwest Laboratory. Compared to the matrix, the H-phase is very Hf rich, Ti lean and very slightly Ni rich.

Mechanical properties were investigated for the alloys containing 20(at.%) Hf with varying Ti concentrations (29(at.%) , 29.7(at.%) , 30(at.%) , and 30.5(at.%) ). To determine the effect of aging on the behavior of these alloys, isothermal constant strain rate compression testing was performed at temperatures above the austenite finish temperature ( $A_f+10\text{C}$ ,  $A_f+30\text{C}$ ,  $A_f+50\text{C}$ ,  $A_f+70\text{C}$ ,  $A_f+90\text{C}$  for each alloy). This revealed that the alloy strength and the temperature range for pseudoelasticity versus austenite plasticity was strongly influenced by aging for the Ni-rich alloys. Additionally, the isothermal compression tests of  $\text{Ni}_{50.3}\text{Ti}_{29.7}\text{Hf}_{20}$  show that the 3 h/550°C heat treatment, that creates a dense distribution of H-phase precipitates with an average diameter of 16 nm, is an optimum aging condition

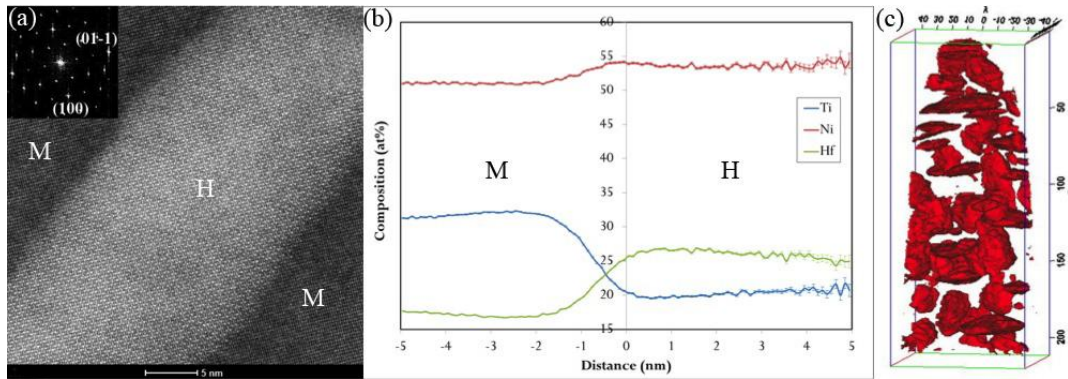


Fig. 1: (a) HAADF STEM image of the H-phase on zone  $[010]_H$ ; (b) proximity histogram composition profile across the H-phase and martensite matrix; (c) Hf iso-composition surface showing the distribution of the H-phase precipitates.

with the combination of highest strength at highest temperatures for that alloy (at 250°C the 0.2% yield strength is 1278 MPa). Strength levels for  $Ni_{51}Ti_{29}Hf_{20}$  are even higher for a sample subjected to a 3 h/500°C heat treatment (at 150°C the 0.2% yield strength is 2115 MPa). Also, the  $Ni_{51}Ti_{29}Hf_{20}$  alloy had high strength levels while maintaining pseudoelasticity.

In order to understand the effect of nano precipitates in Ni-Ti-Hf system, a phase field model of H-phase precipitation has been developed. The model predicts the shape and spatial distribution of the precipitates and coherency stress fields around them. The model also allows for quantitative investigation of effects of these nanoscale coherent precipitates on the subsequent martensitic transformation of the matrix.

Taking advantage of our characterization work combined with *ab initio* calculations, crystal structure and lattice parameters of H-phase ( $a=1.2635nm$ ,  $b=0.8824nm$ ,  $c=2.6093nm$ ) have been determined, which are used as input in the phase field simulations. The principal values of the stress-free transformation strain (SFTS) are determined to be 2.24%, 0.96% and -0.48%. Because of the symmetry reduction during precipitation, there are twelve crystallographically equivalent orientation variants (ORs). In the phase field simulations, contributions of both elastic strain energy and interfacial energy to precipitate morphology have been taken into account simultaneously, and the interplay between the two determine the shapes of and stress fields around the H-phase particles. It has been found that the H-phase particles have disk-like or lenticular shapes with  $\{311\}$  type habit planes (Fig. 2(a)), which agrees well with the experimental observations (Fig. 2(b)).

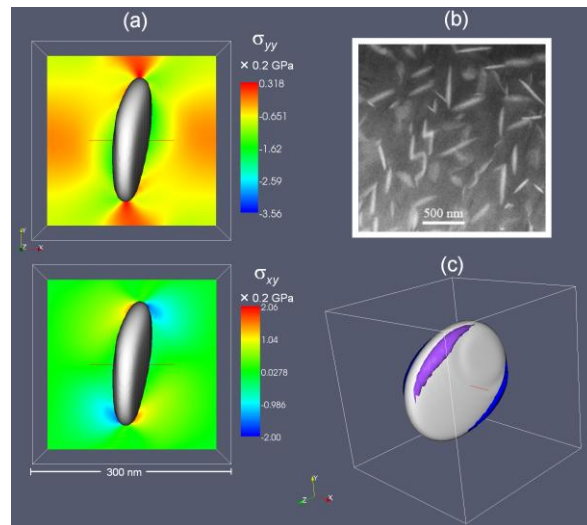


Fig. 2. (a) Stress Field around an H-phase precipitate; (b) HAADF STEM image of the 50.3Ni-29.7Ti-20Hf alloy aged at 600°C for 815 hours; (c) Calculated elastic interaction energy isosurface between the H-phase precipitate and a martensitic nucleus.

In order to investigate the effect of the presence of H-phase particles on the martensitic transformations, the stress field around an H-phase particle has been calculated, and it is found that different stress components (especially the shear components) are mostly concentrated near the rim of the disk, the magnitude of which is  $\sim 0.4GPa$  (Fig. 2(a)). The elastic interaction energy between the H-phase precipitate and a nucleating martensitic particle can be calculated through the equation  $E_{int} = -\sigma_{ij}\epsilon_{ij}^M$ , where  $\sigma_{ij}$  is the stress field associated with the H-phase particles and  $\epsilon_{ij}^M$  is the SFTS of the martensite. It can be found that the rim of an H-phase disk is the most preferred location for martensite to nucleate, and

the extra driving force caused by the elastic interaction can be as large as  $0.04\text{J}/\text{mm}^3$  ( $0.71\text{kJ}/\text{mol}$ ). In Fig. XX(c), the most favored locations for martensite nucleation have been identified on the both sides of the rim, with different martensitic variants indicated by different colors. Considering the thermodynamic parameters for martensitic transformation without the presence of the H-phase precipitates,  $T_0 \sim 415\text{K}$  (DSC result) and  $\Delta H \sim 6\text{kJ}/\text{mol}$  (*ab initio* result for NiTiPt, data for NiTiHf is yet to be calculated), an  $M_s$  increase of  $49\text{K}$  could be expected, which is close to the DSC measurement of  $M_s$  increase ( $\sim 50\text{K}$ ) after aging at  $600^\circ\text{C}$ . However, the H-phase precipitation will also change the chemistry of the B2 matrix and affect the  $M_s$  temperature, which is currently under investigation. Please also note that the elastic and chemical effects of H-phase precipitates on the martensitic transformation will depend strongly on the size, volume fraction and spatial distribution of the precipitates and parametric study is being carried out to document these effects.

Microstructural finite element (MFE) simulations have been developed to study the effect of H-phase precipitates on the thermo-mechanical response. These simulations incorporate discrete H-phase precipitates into a surrounding B2 crystal matrix that upon cooling or stressing, can transform into any of 24 correspondence variant pairs (CVPs) and/or plastically yield. The simulations also include anisotropic elasticity and thermal expansion mismatch between the precipitate and matrix.

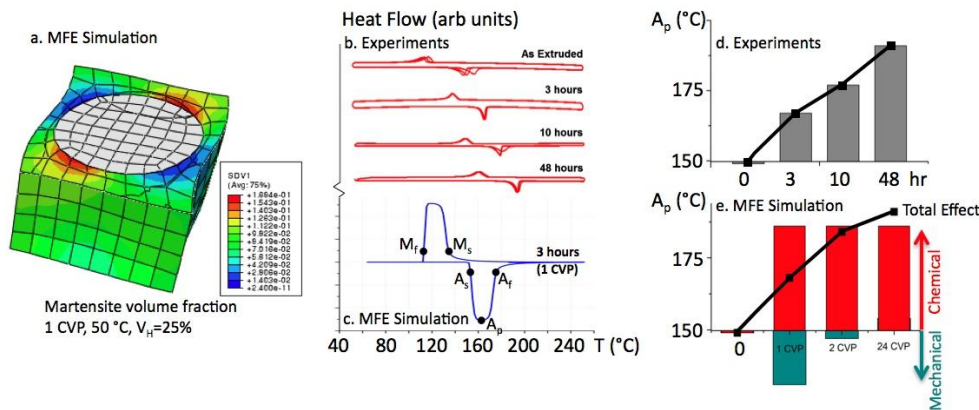


Figure 3. Microstructural finite element (MFE) predictions vs. experiment for a Ni<sub>50.3</sub>Ti<sub>29.7</sub>Hf<sub>20</sub> alloy showing (a) MFE martensite distrib. at an H-precipitate; (b,c) DSC data; (d,e) A<sub>p</sub> vs. aging.

Fig. 3a shows a MFE prediction of the martensite volume fraction distribution around an H-phase precipitate after cooling to  $50^\circ\text{C}$ . Only a single (most favored) CVP is permitted to form, consistent with transmission electron micrographs showing that single CVPs engulf numerous H-phase precipitates in alloys with short aging treatments. The skewed deformed shape and the inhomogeneous distribution of martensite underscores the large constraint imposed by the precipitate. Fig. 3b shows experimental differential scanning calorimetry (DSC) measurements (courtesy Haluk Karaca, Univ. Kentucky) for Ni<sub>x</sub>Ti<sub>29.7</sub>Hf<sub>20</sub> under different aging conditions to form H precipitates. MFE predictions in Fig. 3c of a  $\sim 25^\circ\text{C}$  decrease in critical temperature (e.g., austenite peak temperature  $A_p$ ) at short aging times. Figs. 3d and e compare the experimental versus simulated shift in  $A_p$  for different aging times at  $550^\circ\text{C}$  (solid black lines). The overall trend consists of chemical (red bars) and mechanical (blue bars) contributions. The former shifts  $A_p$  upward due to Ni and Hf depletion in the matrix caused by H-phase precipitation. The latter shifts  $A_p$  downward, especially at short aging time. The MFE simulations are informed by microscopy studies showing that aging does not increase precipitate area fraction but it relaxes constraint, by allowing an increasing number of CVPs to form in the interprecipitate regions.

Key findings from this simulation-experiment approach include: 1) A decrease in number of CVPs, which corresponds to shorter aging time, results in lower  $M_f$  and  $A_s$  but does not affect  $M_s$  and  $A_f$ ; 2) Increasing the precipitate misfit strain or volume fraction increases  $M_s$  and  $A_f$ , but has little effect on  $M_f$  and  $A_s$ ; 3) Precipitation depletes the matrix of both Ni and Hf, increasing the average transformation temperature  $T_c$  (average of  $M_s$  and  $M_f$ ) by  $\sim 40^\circ\text{C}$ .

## Future Plans

Future work has begun on the NiTiAu alloy system, which potentially has an even higher transformation temperature than the Hf- or Pt-alloys. Initial electron diffraction patterns have shown evidence of yet another unidentified precipitate phase in the system under aging. Characterization work will pursue a combined approach using diffraction, atomic-scale imaging, and VASP calculations in order to determine the precipitate structure, coherency and its effect on shape memory and mechanical properties. The Nonmechanics high temperature indentation system is now operational and will be used to probe isothermal behavior in individual grains of the in the NiTiHf system, providing orientation-dependence of the transformation and plasticity.

Effects of H-phase precipitation on martensitic transformation and shape memory properties will be further investigated through coupling between phase field simulations, microstructural finite element simulations, and experiments. The variables being considered include the size, shape, volume fraction and spatial distribution of precipitates, which could be controlled by changing aging conditions. Mechanical properties including dimensional stability and thermal fatigue will also be analyzed through the modeling of the transformation pathway and corresponding mechanism.

### **Papers published from this research project (2010 – present)**

1. L. Kovarik, F. Yang, A. Garg, D. Diercks, M. Kaufman, R.D. Noebe, and M.J. Mills, “Structural Analysis of a New Precipitate Phase in High-Temperature  $Ti_{50}Ni_{30}Pt_{20}$  Shape Memory Alloys,” *Acta Mater.*, **58** (2010) 4660-4673.
2. F. Yang, L. Kovarik, P.J. Phillips, R.D. Noebe, M.J. Mills, “Characterization of Precipitate Phases in a Ti-Ni-Pd alloy,” *Scripta Mater.*, **67** (2012) 145-148.
3. D. Coughlin, P.J. Phillips, G.S. Bigelow, A. Garg, R. D. Noebe, M.J. Mills, “Characterization of the microstructure and mechanical properties of a 50.3Ni-29.7Ti-20Hf shape memory alloy,” *Scripta Mater.*, **67** (2012) 112–115.
4. Y. Gao, N. Zhou, F. Yang, Y. Cui, L. Kovarik, N. Hatcher, R. Noebe, M.J. Mills, Y. Wang, “P-phase precipitation and its effect on martensitic transformation in (Ni,Pt)Ti shape memory alloys,” *Acta Mater.* **60** (2012) 1514-1527.
5. Y. Gao, H. Liu, R. Shi, N. Zhou, Z. Xu, J. Nie and Y. Wang, “Simulation Study of  $\square_1$  precipitation in Mg-Y-Nd Alloy” *Acta Mater.* **60** (2012) 4819-4832.
6. H. Liu, Y. Gao, J.Z. Liu, Y.M. Zhu, Y. Wang and J. F. Nie, “A Simulation Study of the Shape of  $\beta'$  Precipitates in Mg-Y and Mg-Gd Alloys,” *Acta Mater.* **61** (2013) 453-466.
7. F. Yang, D.R. Coughlin, P.J. Phillips, L. Yang, A. Devaraj, L. Kovarik, R.D. Noebe, M.J. Mills, “Structural analysis of a precipitate phase in Ni rich high temperature NiTiHf shape memory alloys,” accepted for publication in *Acta Mater.* (2013)
8. S Manchiraju , D. Gaydosh, R. Noebe, and P. Anderson, “Simulating Thermal Cycling and Isothermal Deformation Response of Polycrystalline NiTi,” MRS Symp. Proc. Vol. 1295 (B Bewlay, M Palm, S Kumar, K Yoshimi, eds), Cambridge University Press (2011). P. N01-11.
9. D. Norfleet, S. Manchiraju, M. Bowers, P. Anderson, M. Mills, P. Sarosi, and M. Uchic. “Observations and Modeling of Transformation-Induced Plasticity During Pseudo-Elastic Deformation in Ni-Ti Microcrystals,” SMST-2010 (D.S. Grummon, M.R. Mitchell, M. Mertmann, eds.), Springer (2011).
10. S. Manchiraju and P. M. Anderson, “Coupling Between Martensite Phase Transformations and Plasticity: A Microstructure-Based Finite Element Model,” *International J. Plasticity* 26 (2010) 1508-1526.
11. S. Manchiraju, D. Gaydosh, O. Benafan, R. Noebe, R. Vaidyanathan, P.M. Anderson, “Thermal Cycling and Isothermal Deformation Response of Polycrystalline NiTi: Simulations vs. Experiment,” *Acta Materialia* 59 (2011) 5238-5249.

**Program title: Deformation Physics of Ultra-fine Scale Materials**

PI: Amit Misra

<amisra@lanl.gov>

Los Alamos National Laboratory, MS K771,  
Los Alamos, NM 87545.

The focus of this research is to integrate cutting-edge experimental techniques and characterization tools with state-of-the-art multi-scale modeling to extend the fundamental knowledge of deformation physics and strength-limiting mechanisms in ultra-fine scale materials, with emphasis on behavior at nanometer length scales. The focus is on developing entirely new levels of understanding of the deformation and fracture behaviors of materials near their theoretical strength limit. The applicability of this knowledge should impact a broad range of engineering materials from load-bearing structural components in transportation, construction and power generation to thin films and coatings.

This proposal seeks to address a set of questions covering a broad area of deformation physics, and it is therefore appropriate that the program be able to draw upon a range of resources and capabilities. The current principal investigator is *Amit Misra* at LANL with *Jian Wang* as co-PI. *Richard G. Hoagland* (co-PI until April 2009) is now involved in the program as a LANL Lab Associate, along with *John P. Hirth* as a consultant. In the modeling task, the program currently involves *Jian Wang*, X.Y. "Ben" *Liu* and *Tim C. Germann* (staff scientists at LANL), *Christian Brandl* (post-doc, 50%), *Satyesh Yadav* (GRA, U-Conn; post-doc at LANL starting June 2013, 50%) and *Shuai Shao* (post-doc, 50%). Besides the PI, other experimentalists on the program include *J. Kevin Baldwin* (technologist, 50%), *Nan Li* (50%, post-doc; limited-term staff scientist starting February 2013), *William Mook* (post-doc, 50%) and *Sid Pathak* (LANL Director's post-doc fellow). We also collaborate extensively with the Electron Microscopy Lab at LANL: *Rob Dickerson* and *Pat Dickerson*, and access the nanomechanical testing and *in situ* indentation in a TEM in the CINT user facility through approved user projects with *Nathan A. Mara*. The program has significant current collaborations with *Johann Michler* (EMPA-Switzerland) in *in situ* nanomechanical testing, *Rampi Ramprasad* (U-Connecticut) in DFT calculations of Al-TiN interfaces, and *Peter M. Anderson* (Ohio State University) in dislocation theory.

Till 2010, the program focused on metallic multilayers (e.g., Cu-Nb, Cu-Ni, etc) and nano-twinned fcc metals (e.g. Cu). In the last 3 years, the focus in the program was directed towards brittle materials at the nanoscale such as nano-composites of ceramics (or glassy metals) and metals. The idea is to discover and understand unusual mechanisms that enable room temperature co-deformation of brittle ceramics with metals at the nanoscale in spite of the enormous difference in their respective flow properties in the bulk form.

Selected recent accomplishments are summarized as follows:

1) *Co-deformability and high work hardening in nanolayered metal-ceramic composites*

We discovered that at extremely small layer thicknesses (< 5 nm), the nano-scale Al-TiN multilayers exhibit high flow strengths (~4.5 GPa maximum) and high compressive deformability (5-7% plastic strain). These high strengths were accompanied by extraordinarily

high strain hardening rates in the Al nano-layers, which were of the order of 16-35 GPa ( $\sim E/4 - E/2$ ) in the 2-4 nm layered films. *In situ* indentation in a TEM shows cracking of the TiN layers in the 50 nm Al – 50 nm TiN composite but no evidence of cracking was observed in the 5 nm Al – 5 nm TiN composite. The high strengths and high work hardening rates were analyzed using the concepts of dislocation motion and interactions within the confined nanoscale Al layers (Fig. 1).

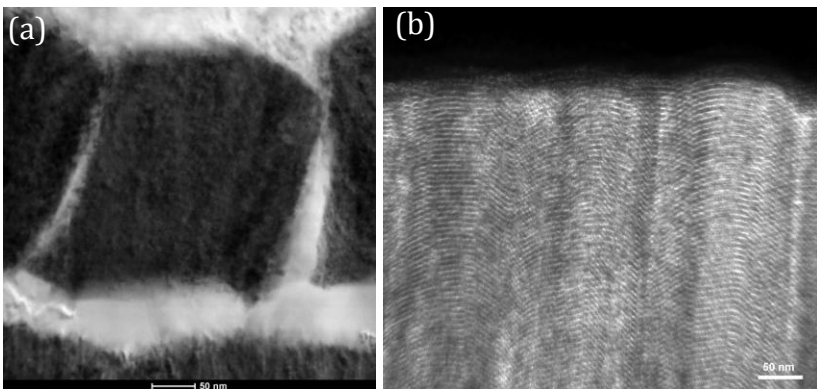


Fig. 1 Cross-section TEM images from below the nanoindents.

(a) 250 nm Al-250 nm TiN sample showing cracking of TiN, and thickness reduction of Al layers and plastic flow of Al into cracks in TiN. (b) No cracks or shear bands are observed in the 2 nm Al - 2 nm TiN sample.

## 2) Influence of interface chemistry on the shear behavior of metal-ceramic interfaces

We have used density functional theory (DFT) to calculate the ideal shear strengths of pure Al, pure TiN, a single Al/TiN interface and Al/TiN multilayers. The ideal shear strength of the Al/TiN interface was found to vary from very low (on the order of the ideal shear strength of Al) to very high (on the order of the ideal shear strength of TiN) depending on whether the TiN at the interface was Ti or N-terminated, respectively. For the Al/TiN multilayers with N-terminated interfaces, the ideal shear strength was limited by shear in the Al layer away from the interface, even when the individual layer thickness is less than a nanometer. The results suggest that the shear properties of Al/TiN depend strongly on the chemistry of the interface: Al:N (higher shear strength) vs Al:Ti (lower shear strength) terminations (Fig. 2).

DFT calculations were performed to compute the generalized stacking fault energies and Peierls barriers in TiN. For  $\langle 110 \rangle / \{111\}$  slip, a splitting of saddle point was observed, while for  $\langle 112 \rangle / \{111\}$  slip, a stable stacking fault at  $a_0/3 \langle 112 \rangle$  displacement was formed in TiN. The DFT calculations of the interface shear strengths and Peierls barriers provide inputs to the dislocation theory models for estimating the slip transmission stress across Al/TiN interfaces.

## 3) Calculation of the strength maximum in nanolayered composites

A theory was developed to interpret the maximum strength observed experimentally in nanolayered composites when the layer thickness is below approximately 5 nm. This theory builds upon the mechanism we discovered earlier in this program involving dislocation trapping at interfaces via core spreading along the plane of interface that is weak in shear. In recent work, we used “tunable” interatomic potentials to vary the interface shear strength for the same

interface crystallography. To reveal the transmission process and the associated energetics and mechanics we adopted the chain of states method to calculate the change in potential energy along the minimum energy path associated with nucleation and emission of a lattice dislocation from the interface. A virtual dislocation is introduced to describe the transmission process, corresponding to nucleation and emission of a lattice dislocation. The results show that the slip transmission barrier increases with decreasing shear strength of the interface and provide insight into tailoring the flow strength of nanocomposites via interface properties.

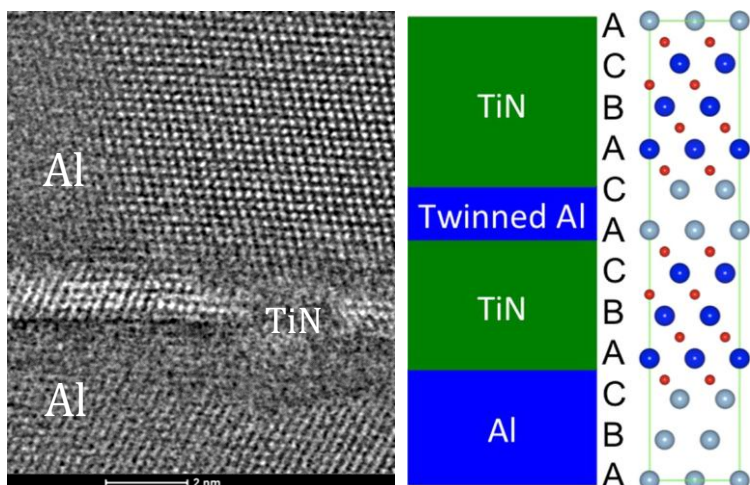


Fig. 2 High-resolution TEM of sputter deposited Al/TiN/Al multilayer showing a twin orientation between the Al above and below TiN, and the corresponding DFT unit cell used to calculate the interface energies.

Future work involves mechanistic understanding using both theory and *in situ* straining in TEM of slip transmission from metal to ceramic that enables co-deformation and room temperature plasticity in ceramics. Dislocation calculations will be done for Al/TiN/Al tri-layer structure using DFT, and results used as input in a micro-mechanical model for plastic flow stability of composite. Other systems of fcc metals and rock salt structure nitrides and carbides will be studied to develop a generalized framework for co-deformation in metal-ceramic composites.

### Selected Recent Publications

1. S. K. Yadav, R. Ramprasad, A. Misra, and X.-Y. Liu, *First-principles study of the shear behavior of Al, TiN, and coherent Al/TiN interfaces*, Journal of Applied Physics, **111** (2012) 083505.
2. S. K. Yadav, J. Wang, R. Ramprasad, A. Misra, and X.-Y. Liu, *Structural rotation of Al under uniaxial compression: a first-principles study*, Journal of Applied Physics, **112** (2012) 043513.
3. D. Bhattacharyya, N.A. Mara, P. Dickerson, R.G. Hoagland, A. Misra, *Compressive flow behavior of Al-TiN multilayers at nanometer scale layer thickness*, Acta Materialia, **59** (2011) 3804–3816.
4. D. Bhattacharyya, X.Y. Liu, A. Genc, H.L. Fraser, R.G. Hoagland and A. Misra, *Heterotwin*

- formation during growth of nanolayered Al-TiN composites*, Applied Physics Letters, **96** (2010) 093113.
5. D. Bhattacharyya, N. A. Mara, P. Dickerson, R. G. Hoagland, and A. Misra, *A transmission electron microscopy study of the deformation behavior underneath nanoindenters in nanoscale Al-TiN multilayered composites*, Philosophical Magazine, **90**:13, (2010) 1711 — 1724.
6. J. Wang, A. Misra, R. G. Hoagland, J. P. Hirth, *Slip transmission across fcc/bcc interfaces with varying interface shear strengths*, Acta Materialia **60** (2012) 1503–1513.
7. J. Wang and A. Misra, *An overview of interface-dominated deformation mechanisms in metallic multilayers*, Current Opinion in Solid State and Materials Science, **15** (2011) 20-28.
8. J. Wang, R. G. Hoagland, X. Y. Liu, A. Misra, *The Influence of Interface Shear Strength on the Glide Dislocation-Interface Interactions*, Acta Materialia **59** (2011) 3164-3173.
9. J. Wang, A. Misra, J.P. Hirth, *Shear response of  $\{112\}$  Twin Boundaries in Face Centered Cubic Metals*, Physical Review B **83**, (2011) 064106.
10. N. Li, J. Wang, J.Y. Huang, A. Misra, *Direct Observation of Dislocation Confined Layer Slip in Multilayer Films*, Microscopy & Microanalysis, **18** (2012) 1155-1162.
11. N. Li, J. Wang, N.A. Mara, J.Y. Huang, A. Misra, *Ex situ and In situ measurements of the shear strength of interfaces in metallic multilayers*, Scripta Materialia **67** (2012) 479-82.
12. N. Li, J. Wang, A. Misra and X. Zhang, J.Y. Huang, J. P. Hirth, *A new mechanism for dislocation multiplication at a coherent twin boundary*, Acta Materialia **59** (2011) 5989-5996.
13. Y. Kim, A. S. Budiman, J. K. Baldwin, N. A. Mara, A. Misra, S. M. Han, *Microcompression Testing of Al/Nb Nanoscale Multilayered Materials*, Journal of Materials Research, **27**, (2012) 592-598.
14. A. S. Budiman, S.M. Han, N. Li, Q.M. Wei, P. Dickerson, N. Tamura, M. Kunz, A. Misra, *Plasticity in the nanoscale Cu/Nb single crystal multilayers as revealed by synchrotron Laue x-ray microdiffraction*, Journal of Materials Research, **27** (2012) 599-611.
15. J.P. Hirth, R.C. Pond, R.G. Hoagland, X.-Y. Liu, and J. Wang, *Interface defects, reference spaces and the Frank-Bilby equation*, Progress in Materials Science, (2013), in press.

# Local morphing, magneto-mechanical fatigue and fracture of magnetic shape-memory alloys

Peter Müllner

Department of Materials Science and Engineering, Boise State University, 1910 University Dr., Boise, ID 83725

[petermullner@boisestate.edu](mailto:petermullner@boisestate.edu)

## Program Scope

Magnetic shape memory alloys (MSMAs) have great potential for small size, large stroke, highly energy efficient, high speed, high precision actuator applications. To enter this market, MSMAs must perform reliably over long life times, i.e. they must be fatigue resistant. This study will provide (i) a quantitative experimental and theoretical understanding of fracture mechanisms under dynamical loading and (ii) mechanism-based methods for improving fatigue resistance. The overarching hypothesis originates from the assumption that conjugate twins nucleate cracks which lead to fracture and failure during high-cycle actuation of MSMAs. To avoid fracture and failure, twins must not intersect. Furthermore, this project studies localized, reversible, magnetic-field-induced deformation as a morphing mechanism for micro-electromechanical systems.

## Recent Progress – Summary<sup>\*,\*\*</sup>

Local control of twinning via variable inhomogeneous magnetic fields initiates local reversible deformation. The material morphs into different shapes. We applied this concept to build a valve-less micropump consisting of a Ni-Mn-Ga single crystal, a casing, and a rod magnet. The reliable operation of the pump requires controlling the twin microstructure over millions of magneto-mechanical cycles. Here, we studied the impact of surface roughness on cracking and fracture under magneto-mechanical actuation. Polishing the surfaces with 1- $\mu\text{m}$ -diamond slurry reduced the twinning stress, increased twin mobility, and led to the formation of conjugate twins. Interacting conjugate twins mutually obstructed their motion, caused stress concentrations, and nucleated cracks. Cracks lead to a refinement of the twin microstructure near the fracture surface. Crystals polished with 1- $\mu\text{m}$ -diamond slurry showed significant cracking after 10,000 magneto-mechanical cycles and failed by fracture at 40,000 magneto-mechanical cycles. Introducing localized stresses near the crystal surface via grinding with 6- $\mu\text{m}$ -diamond slurry stabilized a microstructure with narrow, parallel twins without conjugate twins. Localized surface stresses increased the twinning stress and reduced twin mobility. Crystals polished with 6- $\mu\text{m}$ -diamond slurry did not develop cracks after 20,000 magneto-mechanical cycles.

## Introduction

Operating micro-electromechanical systems with classical designs such as wheels and gears is prone to fail due to adhesion and friction. Nature solved this problem with linear systems which operate by shape change: muscles. Engineers have adapted this concept with morphing materials such as piezoelectric ceramics, magnetostrictive materials, and shape memory alloys. In 1996, Ullakko et al. demonstrated 0.12% magnetic-field-induced strain (MFIS) in a Ni-Mn-Ga MSMA. By optimizing crystal composition and by improving crystal purity, MFIS was improved to 10% and the twinning stress was reduced to less than 0.1 MPa.

Compared with other functional materials, MSMAs have the largest stroke (10% strain), a high actuation frequency (2 kHz, possibly up to the megahertz regime), and a very high dynamical range (positioning accuracy a few nanometer at a stroke of several hundred micrometer).

To leverage these advantages, MSMAs must be fatigue resistant and deformation should be controlled locally. Here, we demonstrate local actuation quantitatively and qualitatively in form of a MSMA-based micropump. Furthermore, we demonstrate improvements of magneto-mechanical fatigue resistance via the modification of the crystal surface.

## Experimental

### Localized morphing

The working mechanism of the MSM micropump is the localized morphing of the magnetic shape memory (MSM) element. The MSM element was cut from a Ni-Mn-Ga single crystal so that the overall dimensions were 20mm x 2.5mm x 1mm. To relieve

---

\* Collaborators and students contributing to the project part on localized deformation: D. Kellis, N. Kucza, B. Muntiferling, K. Ullakko, A. Smith; Collaborators and students contributing to the project part on fatigue: S. Barker, M. Chmielus, T. Lawrence, P. Lindquist, K. Ullakko.

\*\* References are given in the publications listed at the end of this report.

surface stresses caused by cutting, the sample was then electropolished using a chilled solution consisting of 40 ml of ethanol and 20 ml of 16M nitric acid. After compressing the MSM element so that it was in a single martensite variant state, it was then again electropolished.

After the MSM element had been polished, it was carefully cleaned with ethanol and then compressed into a short, single phase and placed on a fixture with a rotating diametrically magnetized cylindrical permanent magnet beneath it. Using the perpendicular magnetic field from the diametrically magnetized cylindrical magnet, a second phase was introduced into the middle of the MSM element that was approximately 1 mm in length. Without this alternate phase in the MSM element, the micropump would be unable to transfer liquid from inlet to outlet. The MSM element was then attached to a glass plate with two holes, fixed in its length with epoxy, and sealed with elastomer.

The experiments were made with a cylindrical magnet of 6 mm in diameters. Rotation of the magnet produced a varying magnetic field distribution that changed the proportions of the two crystallographic variants.

### Fatigue

A diametrically magnetized, cylindrical permanent magnet with diameter and length of 5 cm was mounted to the rotor of a lathe (Fig. 1). A cylindrical sample holder with sixty sample chambers was mounted to the stator of the lathe. Each chamber could accommodate a disk-shaped sample with a diameter of 6 mm and a thickness between 1 and 3 mm. The sample holder was sled over the magnet such that when rotating, the magnet generated a variable field on each sample. Upon rotation, the magnetic field continuously changed from perpendicular to the disk face to parallel to the disk face. The maxima of the magnetic field for the central sample row were 0.30 and 0.54 T perpendicular and parallel to the disk face. For the outside rows, the maxima were 0.27 and 0.54 T. These field strength were sufficient for initiating twinning.

Six disk-shaped, cylindrical samples were cut from a Ni-Mn-Ga single crystal with composition varying between 25.9 and 26.6 at.-% Mn and 22.9 and 23.3 at.-% Ga (balance Ni) grown along  $\langle 100 \rangle$  and 10M martensite structure. The compositional variation was due to constitutional segregation.

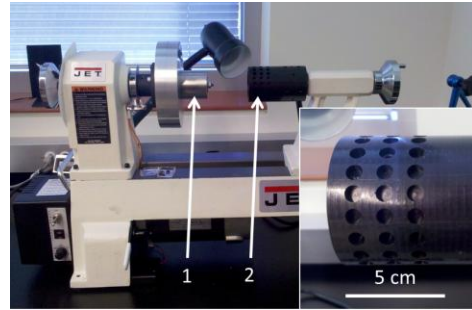


**Fig. 1:** Device for magneto-mechanical fatigue experiments; the magnet (1) was mounted to the rotor of the lathe while the sample holder (2) was mounted to the stator. The sample holder contained sixty sample chambers arranged in three rows of twenty chambers (inset).

The disk plane was (001) and the tangential direction was [100]. All samples were polished with 1- $\mu$ m-diamond slurry to a mirror finish and exposed to a 2T field perpendicular to the sample face prior to testing. Samples A, B, and C were additionally grinded with 6- $\mu$ m-diamond slurry. Samples D, E, and F were tested with mirror finish conditions.

## **Results**

### Localized morphing

The diametrically magnetized cylindrical permanent magnet, placed on one side of the MSM element, generated local magnetic fields in longitudinal and transversal directions in the MSM element. Those magnetic field components exhibited sufficiently high magnetic field energies with respect to the magnetocrystalline anisotropy energy of the MSM material for driving twin boundaries and generating MFIS. Fig. 2 shows the calculated magnetic field distribution in the MSM element made from a Ni-Mn-Ga alloy with a 10M martensite structure, produced by a diametrically magnetized cylindrical iron-boron-neodymium magnet.

Fig. 3 shows the surface of an MSM element placed on top of a magnet. The perpendicular field evoked twins with the short crystallographic  $c$  direction perpendicular to the bar axis as shown in the optical micrograph (Fig. 3a).

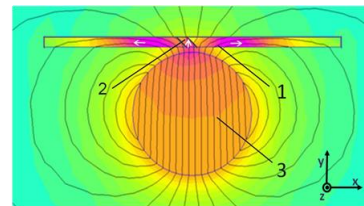


**Fig. 2:** Magnetic field lines in a Ni-Mn-Ga bar (1) with a twin (2) placed above a cylindrical magnet (3).

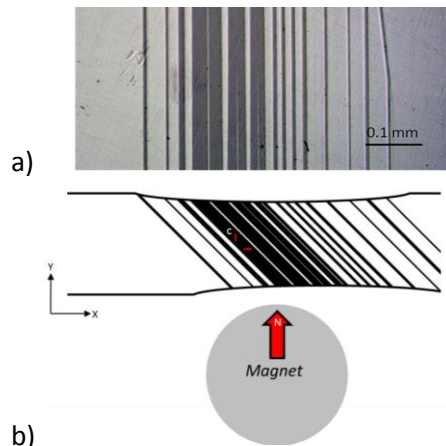


**Fig. 3:** Twins and shrinkage formed by a localized magnetic field; (a) Top view of an MSM element positioned on top of a magnet with twins (dark bands). (b) Schematic of the cross-section with twins producing a localized shrinkage.

The twins produced a localized shrinkage (Fig. 3b). The shrinkage was about 1 mm long. The volume of the shrinkage across an MSM element was calculated using measurements with an optical profilometer.

Fig. 4 shows the axial profiles of the MSM element when the magnet was rotated clockwise. In the micropump, the MSM element was covered by a glass plate. The shrinkage produced a cavity underneath this plate. Upon clockwise rotation of the magnet, the cavity moved from left to right. The volume of the cavity was 264, 331, and 260 nl (evaluated for the examples of Fig. 4). The volume of the cavity was the greatest when the magnetization direction of the cylindrical magnet was most perpendicular to the MSM element, i.e. in the intermediate profile in Fig. 4.

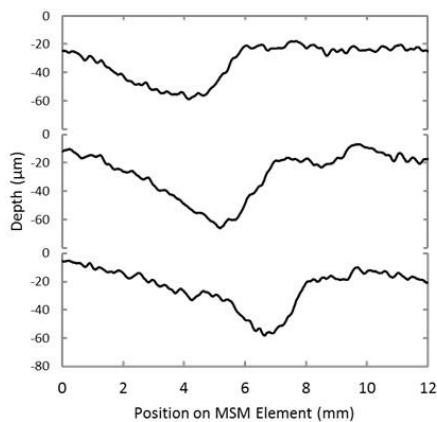


**Fig. 4:** Profiles along the MSM element as the magnet was rotated clockwise. The shrinkage moved from left (top profile) to right (bottom profile).

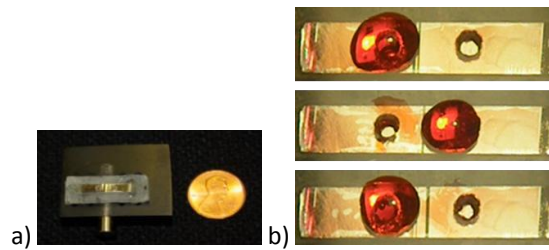


**Fig. 5:** Pump in operation; (a) The pump consisting of an MSM element, a glass plate, and a driving magnet; (b) a droplet of colored liquid was placed over the left hole, transported through the pump to the right whole, and back to the left hole by reversing the direction of magnet rotation.

The micropump (Fig. 5a) successfully pumped fluid in both directions when the magnet was turned at 1000 RPM by a drill clockwise and counter clockwise. The pumping precision was one discrete gulp, i.e. 260 nl. At 1000 rpm, the pump moved 16 gulps per second or 4.2  $\mu\text{l/s}$  with a precision of 0.26  $\mu\text{l}$  for any given volume.

#### Crack nucleation and fracture

Prior to testing, samples A, B, and C with a rough surface (grinded with 6- $\mu\text{m}$ -diamond slurry) contained no twins as seen with the differential interference contrast (DIC) image. Fig. 6 shows the evolution of the twin microstructure for sample B. After 10,000 revolutions of the magnet, some horizontal twins appeared which grew slightly in number and width by 20,000 revolutions. Thus, the variable magnetic field activated twinning. After 20,000 revolutions, cracks have not been formed.

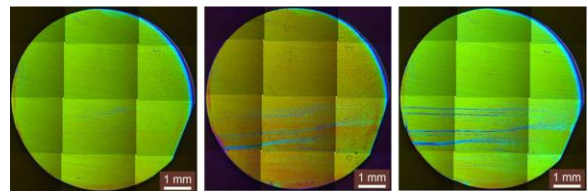


**Fig. 6:** Twinning in sample B with roughened surface. Left: no twins were present prior to fatigue testing; middle: some twins appeared after 10,000 magnet revolutions; right: more twins appeared after 20,000 revolutions.

Samples D, E, and F with a polished surface (1- $\mu\text{m}$ -diamond slurry), showed a few coarse twins DIC optical micrograph prior to testing. Figure 7 shows the evolution of the twin microstructure for sample E. After 10,000 revolutions of the magnet, some horizontal twins appeared together with a crack about 2 mm long. With increasing magneto-mechanical cycling, more cracks appeared

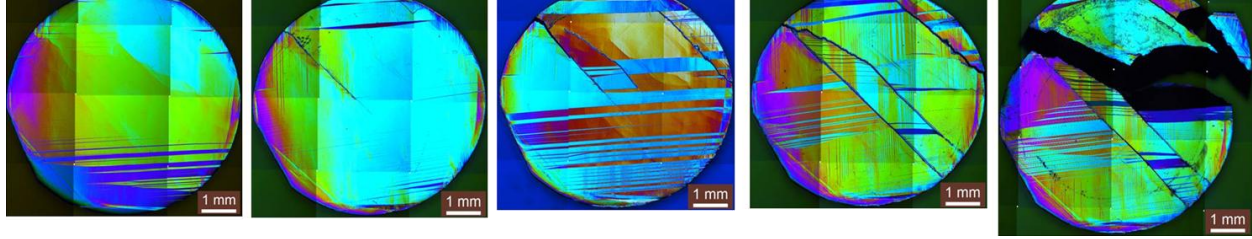


**Fig. 7:** Twinning in sample E with polished surface. First: few twins were present prior to fatigue testing; second: some twins and a crack appeared after 10,000 magnet revolutions; third and fourth: more cracks and twins appeared after 20,000 and 30,000 revolutions; fifth: the sample disintegrated after 40,000 revolutions.

and the twin microstructure became more complex. After 30,000 revolutions, the entire surface was covered with a dense, pattern of hierarchical twins. The sample disintegrated after 40,000 revolutions. Detail images show interactions of cracks with conjugate twins (Fig. 8) and branching twins (Fig. 9). On macroscopic scale, cracks grew on various planes. On microscopic scale, the fracture surface often followed a zigzag along  $\{110\}$  (Figs. 8 and 10).

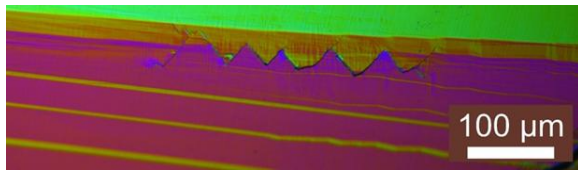


**Fig. 8:** A microcrack interacting with conjugate twins.

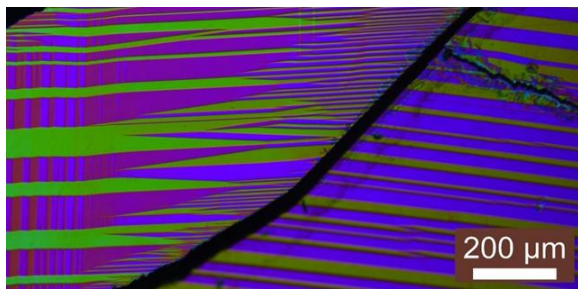


**Fig. 9:** Twin branching at a crack.

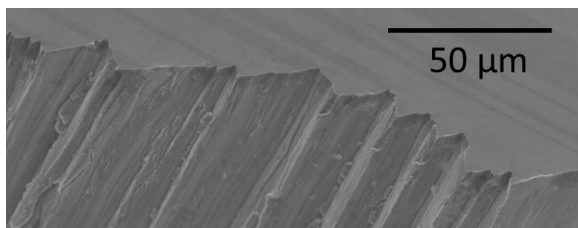


**Fig. 10:** SEM image demonstrating twin-crack interaction.

### Discussion and Future Plans

We demonstrated localized morphing of a Ni-Mn-Ga rod and utilized localized morphing for pumping liquids. We further demonstrated the nucleation of cracks and fracture under cyclic magneto-mechanical loading. We plan to study the impact of surface

roughness on twin stabilization and suppression of crack formation quantitatively by systematically measuring surface roughness, twinning stress, evolution of twin microstructure, crack formation, and crack propagation as a function of surface preparation and cyclic loading.

### Publications through this program in 2010-2012

- [1] K. Rolfs et al. "Double twinning in Ni-Mn-Ga-Co", *Acta Mater.* 58 (2010) 2646.
- [2] J. Guldbakke et al. "Magnetic, mechanical, and fatigue properties of a  $\text{Ni}_{45.4}\text{Mn}_{29.1}\text{Ga}_{21.6}\text{Fe}_{3.9}$  single crystal", *Scripta Mater.* 62 (2010) 875.
- [3] M. Chmielus et al. "Effects of surface roughness and training on the twinning stress of Ni-Mn-Ga magnetic shape-memory alloys", *Acta Mater.* 10 (2010) 3952.
- [4] P. Müllner and A. King, "Deformation of hierarchically twinned martensite", *Acta Mater.* 10 (2010) 5242.
- [5] M. Chmielus et al. "Influence of constraints and twinning stress on magnetic-field-induced strain of magnetic shape memory alloys", *Scripta Mater.* 64 (2011) 888.
- [6] M. Chmielus and P. Müllner, "Effects of surface pinning, locking, and adaption of twins on the performance of magnetic shape-memory alloys", *Mater. Sci. Forum* 684 (2011) 175.
- [7] M. Chmielus et al. "The role of constrained surfaces on magnetic-field-induced deformation", Extended abstract ICF SMA'11, Dresden, Germany, July 18-22, 2011, pp. 209.
- [8] M. Chmielus et al. "Effects of surface damage on twinning stress and the stability of twin microstructures of magnetic shape-memory alloys", *Acta Mater.* 59 (2011) 2948.
- [9] N. Kucza et al. "Grain growth and grain size distribution in polycrystalline Ni-Mn-Ga", Extended abstract ICF SMA'11, Dresden, Germany, July 18-22, 2011, pp. 161.
- [10] D. Kellis et al. "Oriented single crystals of Ni-Mn-Ga with very low switching field", *J. Cryst. Growth* 359 (2012) 64.
- [11] R. C. Pond et al. "Deformation twinning in  $\text{Ni}_2\text{MnGa}$ ", *Acta Mater.* 60 (2012) 3976.
- [12] K. Rolfs et al. "Key properties of Ni-Mn-Ga based single crystals grown with the SLARE technique", *Adv. Eng. Mater.* 14/8 (2012) 614.
- [13] K. Ullakko et al. "A magnetic shape memory micropump: contact-free, and compatible with PCR and human DNA profiling", *Smart Mater. Struct.* 21 (2012) 115020.

## Mechanical Properties of Materials with Nanometer Scale Microstructures

William D. Nix  
nix@stanford.edu

Department of Materials Science and Engineering  
Stanford University, Stanford CA 94305-4034

### Program Scope

We are currently engaged in a program of research on the mechanical properties of materials with micrometer and nanometer scale dimensions and microstructures. This includes work on the mechanical properties of crystalline materials in small volumes, as well as research on the emerging problem of mechanical properties of lithiated silicon nanostructures for lithium-ion batteries.

The research on small-scale plasticity focuses on understanding the dislocation processes responsible for the well known “smaller is stronger” effect on strength, which we, and others, discovered a few years ago, using the micropillar compression technique that we also introduced. Our work includes micropillar compression experiments, as well as computational modeling, using a dislocation dynamics code based on the ParaDis code developed at the Lawrence Livermore National Laboratory. The overall aim of this work is to determine the role that dislocations play in controlling strength at small scales. This work is being done in collaboration with Professor Wei Cai of the Division of Computational and Applied Mechanics in the Department of Mechanical Engineering at Stanford.

Our study of the mechanical properties of lithiated silicon nanostructures involves collaboration with Professor Yi Cui of our department and his research group. The work involves creating silicon nanostructures, subjecting them to various kinds of electrochemical lithiation and delithiation, studying the shape changes and fracture processes that may accompany these processes and modeling these events using both analytical and finite element methods. The work aims to develop a fundamental understanding of the decrepitation processes that currently limit the use of silicon as electrodes in lithium ion batteries.

### Recent Progress

We have developed and published a simple model that provides a rational account of why the size dependence of the strength of metallic micropillars varies from one metal to another and why BCC micropillars typically exhibit smaller size effects than comparable FCC metals [1]. The large size-independent friction stress contribution to the strength of BCC metals causes these metals to exhibit much smaller overall micropillar size effects than FCC metals with small friction stresses. By subtracting the different bulk strengths from the measured strengths of the micropillars we have shown (Fig. 1) that the size dependence of a wide variety of FCC and BCC metals can be brought together onto a common plot.

In another part of this work the size dependence of plasticity of BCC micropillars has been explored using dislocation dynamics (DD) simulations. We have formulated a three dimensional, DD model of dislocation plasticity in BCC micro-pillars and have used it to study size effects and the effects of initial dislocation density and strain rate on strength. The DD model is based on the molecular dynamics (MD) simulations of Weinberger and Cai [2] who discovered a surface-controlled cross-slip process leading to dislocation multiplication without the presence of artificial pinning points. As shown in Fig. 2, we find a “smaller is stronger” size effect that can be explained by the competition between the multiplication rate and depletion rate from the surface of the mobile dislocations. The predictions of an analytical model, which has been constructed to rationalize the behavior of the DD model, is also shown in Fig. 2.

Our work on the mechanical properties of Si nanostructures has focused on the fracture of silicon during lithiation [3]. Fig. 3 shows that nanopillars of crystalline Si fracture at the surface during lithiation, even though compression is expected there based on diffusion induced stresses. We, with others elsewhere, have solved the puzzle of why surface fracture occurs. By modeling the lithiation process as the growth of

an amorphous lithiated shell at the expense of a crystalline silicon core, we can account for the tensile stresses that develop at the surface during lithiation and cause fracture. Our analysis also gives a good account of the anisotropy of the lithiation of crystalline Si nanopillars, and shows that there is a critical size, below which fracture does not occur. Our analyses also explain why amorphous silicon nanopillars do not fracture on lithiation, as also shown in Fig. 3. Recent experiments have shown that amorphous Si micropillars several microns in diameter can be fully lithiated without fracture.

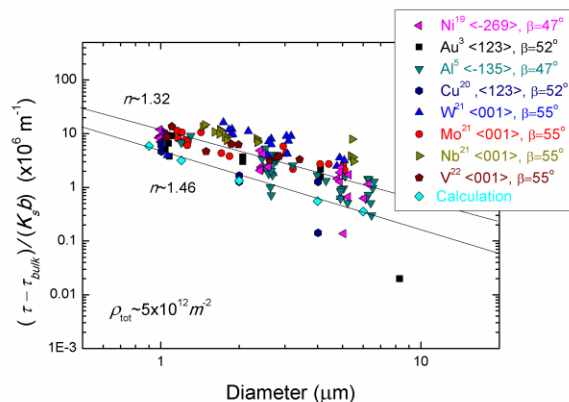


Fig. 1. Size dependence of strength of FCC and BCC metallic micropillars normalized primarily by subtracting the bulk strengths of these different metals from the measured strengths.

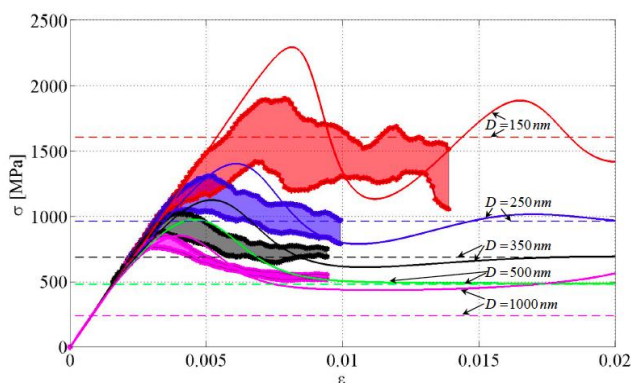


Fig. 2. Simulated stress-strain curves for micropillars of [001] Mo with diameters ranging from 150nm to 1000nm (room temperature and strain rate =  $10^5 \text{s}^{-1}$ ). Shaded regions are DD simulations; lines are analytical results; dashed lines are analytical steady states without strain hardening.

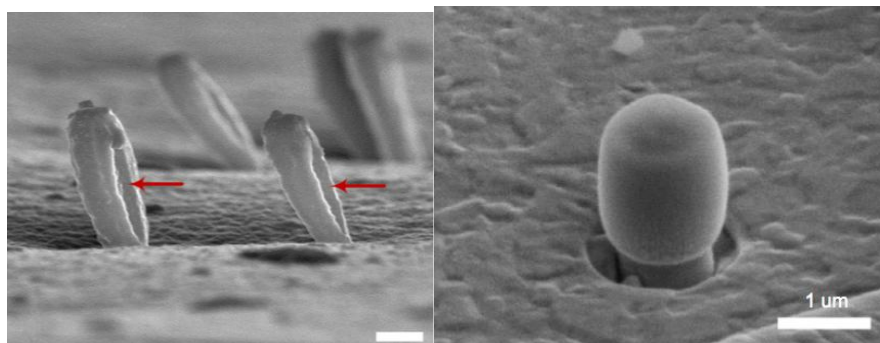


Fig. 3. Nanopillars of crystalline Si (left) and amorphous Si (right) after lithiation, showing surface fracture for crystalline Si and no fracture for amorphous Si.

## Future Plans

In our modeling of plasticity of BCC nanopillars using DD methods we see an opportunity to study strain gradient effects on strength by simulating torsion experiments. This kind of modeling is underway and will be continued.

Our work on the mechanical properties of lithiated Si is severely limited by the lack of knowledge of the mechanical properties of these materials. To address this need we plan to use both nanoindentation and micropillar compression techniques to determine the elastic and plastic properties of these materials. This will include ex-situ studies of the mechanical properties of both crystalline and amorphous silicon thin films on metallic substrates, in both lithiated and delithiated states. We have developed a procedure for testing these reactive materials under mineral oil and have some reliable results. The present experiments have been conducted using Ni substrates, which yield during nanoindentation of lithiated Si films with low Li concentrations and complicate the indentation data. Newly planed experiments with stronger Mo substrates should allow us to explore the mechanical properties of lithiated Si over a wider range of lithium content.

## References

1. S-W. Lee and W.D. Nix, "Geometrical analysis of 3D dislocation dynamics simulations of FCC micro-pillar plasticity," *Materials Science and Engineering A-Structural Materials Properties Microstructure and Processing*, **527**, 1903-1910 (2010).
2. C.R. Weinberger and W. Cai, "Surface-controlled dislocation multiplication in metal micropillars," *PNAS*, **105**, 14304-14307 (2008).
3. S-W. Lee, M.T. McDowell, L.A. Berla, W.D. Nix and Y. Cui, "Fracture of silicon nanopillars during electrochemical lithium insertion," *Proceedings of the National Academy of Sciences of the United States of America*, **109**, 4080-4085 (2012).

## Other DOE Sponsored Publications in 2010-2012

1. S-W. Lee and W.D. Nix, "Geometrical analysis of 3D dislocation dynamics simulations of FCC micro-pillar plasticity," *Materials Science and Engineering A-Structural Materials Properties Microstructure and Processing*, **527**, 1903-1910 (2010).
2. M.A. Hopcroft, W.D. Nix and T.W. Kenny, "What is Young's modulus of silicon," *Journal of Electromechanical Systems*, **19**, 229-238 (2010).
3. L.A. Berla, A. Allen, S.M. Han and W.D. Nix, "A Physically Based Model for Indenter Tip Shape Calibration for Nanoindentation," *Journal of Materials Research*, **24**, 735-745 (2010).
4. A.S. Budiman, C. S. Hau-Riege, W. C. Baek, C. Lor, A. Huang, H. S. Kim, G. Neubauer, J. Pak, P. R. Besser, and W. D. Nix, "Electromigration-Induced Plastic Deformation in Cu Interconnects: Effects on Current Density Exponent, n, and Implications for EM Reliability Assessment," *Journal of Electronic Materials*, **39**, 2483-2488 (2010).
5. S.M. Han, T. Bozorg-Grayeli, J.R. Groves, and W.D. Nix, "Size effects on strength and plasticity of vanadium nanopillars," *Scripta Materialia*, **63**, 1153-1156 (2010).
6. W.D. Nix and S.W. Lee, "Micro-pillar plasticity controlled by dislocation nucleation at surfaces," *Philosophical Magazine*, **91**, 1084-1096 (2011).

7. W.D. Nix, "Beyond the Lab Develop and Follow Your Own Passion," *MRS Bulletin*, **36**, 14-15 (2011).
8. S-W. Lee, S. Aubry, W.D. Nix, and W. Cai, "Dislocation junctions and jogs in a free-standing FCC thin film," *Modelling and Simulation in Materials Science and Engineering*, **19**, 025002 (2011).
9. S.M. Han, E.P. Guyer, and W.D. Nix, "Extracting thin film hardness of extremely compliant films on stiff substrates," *Thin Solid Films*, **519**, 3221-3224 (2011).
10. Y. Yao, M.T. McDowell, I. Ryu, H. Wu, N.A. Liu, L.B. Hu, W.D. Nix, and Y. Cui, "Interconnected Silicon Hollow Nanospheres for Lithium-Ion Battery Anodes with Long Cycle Life," *Nano Letters*, **11**, 2949-2954 (2011).
11. S-W. Lee, D. Mordehai, E. Rabkin, and W.D. Nix, "Effects of focused-ion-beam irradiation and prestraining on the mechanical properties of FCC Au microparticles on a sapphire substrate," *Journal of Materials Research*, **26**, 1653-1661 (2011).
12. D. Mordehai, S-W. Lee, B. Backes, D.J. Srolovitz, W.D. Nix, and E. Rabkin, "Size effect in compression of single-crystal gold microparticles," *Acta Materialia*, **59**, 5202-5215 (2011).
13. I. Ryu, J.W. Choi, Y. Cui, and W. D. Nix, "Size-dependent fracture of Si nanowire battery anodes," *Journal of the Mechanics and Physics of Solids*, **59**, 1717-1730 (2011).
14. M.T. McDowell, S-W. Lee, I. Ryu, H. Wu, W.D. Nix, J.W. Choi, and Y. Cui, "Novel Size and Surface Oxide Effects in Silicon Nanowires as Lithium Battery Anodes," *Nano Letters*, **11**, 4018-4025 (2011).
15. S-W. Lee and W.D. Nix, "Size dependence of the yield strength of fcc and bcc micropillars with diameters of a few micrometers," *Philosophical Magazine*, **92**, 1238-1260 (2012).
16. S-W. Lee, M.T. McDowell, L.A. Berla, W.D. Nix and Y. Cui, "Fracture of silicon nanopillars during electrochemical lithium insertion," *Proceedings of the National Academy of Sciences of the United States of America*, **109**, 4080-4085 (2012).
17. M.T. McDowell, I. Ryu, S-W. Lee, C.M. Wang, W.D. Nix and Y. Cui, "Studying the kinetics of crystalline silicon nanoparticle lithiation with in situ transmission electron microscopy," *Advanced Materials*, **24**, 6034 (2012) .
18. S-W. Lee, L.A. Berla, M.T. McDowell, W.D. Nix and Y. Cui, "Reaction front evolution during electrochemical lithiation of crystalline silicon nanopillars," *Israel Journal of Chemistry*, **52**, 1118-1123 (2012).
19. S.M. Han, G. Feng, J.Y. Jung, H.J. Jung, J.R. Groves, W.D. Nix and Y. Cui, "Critical-temperature/Peierls-stress dependent size effects in body centered cubic nanopillars," *Applied Physics Letters*, **102**, 041910 (2013).
20. M.T. McDowell, S-W. Lee, J.T. Harris, B.A. Korgel, W.D. Nix and Y.Cui, "In-situ TEM of two-phase lithiation in amorphous silicon nanospheres," (accepted for publication in *Nano Letters*)
21. I. Ryu, W.D. Nix and W.Cai, "Plasticity of BCC micro-pillars controlled by competition between dislocation multiplication and depletion," (accepted for publication in *Acta Materialia*).

# **The Coupling Between Interfacial Charge and Mechanical Deformation at High Temperatures in Ceramics**

Rishi Raj (Principal Investigator)

Department of Mechanical Engineering  
University of Colorado at Boulder  
Boulder, CO 80309-0427

Tel: (303)492-1029 Fax: (303)492-3498

[rishi.raj@colorado.edu](mailto:rishi.raj@colorado.edu)

February, 2013

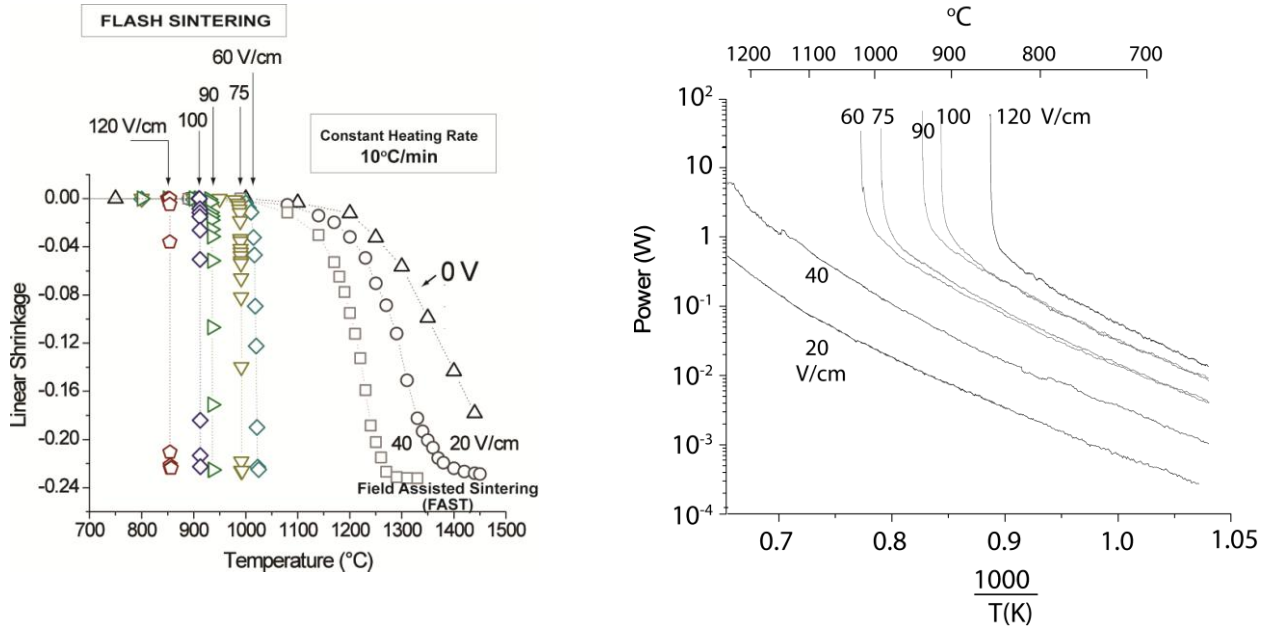
## **PROGRAM SCOPE**

The objective of this basic science project is to elucidate the mechanisms of the interactions between applied electric fields, fields generated within the polycrystals of oxides due to the segregation of charge at interfaces, physically applied mechanical stresses, and capillary pressures generated during the sintering process. The ongoing research has been spurred by a remarkable finding that many ceramics (oxides) can be sintered in just a few seconds at furnace temperatures (often less than 1000°C) that are several hundred degrees below the nominal sintering protocols. During these “flash events” a massive increase in self-diffusion is accompanied by an abrupt increase in the electrical conductivity of the specimens. We are investigating mechanisms that can explain why charge-neutral transport, which is controlled by the slowest moving charges species, is accompanied by electrical conduction which depends on the fast moving charged species. Surprisingly, the onset of the flash, which is characterized by a critical combination of applied electric field and temperature, is also influenced by the applied stress in sinterforging experiments. The stress lowers the temperature for the onset of plastic deformation in these experiments, in the same manner that a higher applied field affects the flash temperature, spelling equivalence between the electric field and the applied stress. The hypothesis driving this research is that the flash event is produced by the “nucleation” of a large number of defects in the form of vacancies and interstitials, as well as the generation of electron-hole pairs, with the point defects accelerating mass transport and the electron-hole pairs providing electron conduction.

## **RECENT PROGRESS**

The first result on flash sintering was published in November 2011 [1]. The experiment is carried out with a dog-bone shaped sample, with a gage length of 20mm, which is suspended within the hot zone of a furnace with platinum wires. A DC electric field is applied to the specimen by these wires, and current flowing through them, into the specimen is measured. The linear shrinkage in the specimen, which gives a measure of densification, is measured with a camera placed underneath the furnace. Two kinds of experiments are carried out. In one case the field is applied at ambient temperature, and the furnace is ramped up at a constant heating rate. In the other case the furnace is held at a constant temperature and the DC field is switched on as

a step-function. In the first instance the sintering occurs nearly instantaneously at a threshold value of the furnace temperature; a higher value of the applied field leads to a lower value of the flash temperature. In the isothermal experiments, there is an incubation period before the sudden onset of sintering; the incubation time increases as the applied field is lowered.



1. Sintering of 3YSZ under an electric field applied with a pair of electrodes as the specimen is heated at a constant rate in a conventional furnace. The two regimes of behavior are seen. At 40Vcm<sup>-1</sup> and below sintering is somewhat accelerated, but occurs abruptly at higher fields. This “flash” effect is accompanied by a sudden increase in electrical conductivity as shown on the right.

The first results [1], carried out with 3mol% yttria doped zirconia (3YSZ), at a constant heating rate of 10°Cmin<sup>-1</sup> are given in Fig. 1. The figure on the left shows the shrinkage strain as a function of the furnace temperature. At low values of the applied field, 20-40Vcm<sup>-1</sup>, there is some acceleration in the rate of sintering. However, at 60Vcm<sup>-1</sup> and above, the nature of the sintering behavior changes; sintering occurs abruptly in mere seconds, at a low temperature. As the applied field is increased the onset of flash sintering occurs at a lower temperature. Recent work from a different laboratory, which is to be published shortly (J. Am. Ceram. Soc., in press), shows that the flash temperature for 8YSZ can be as low as 400°C at higher fields.

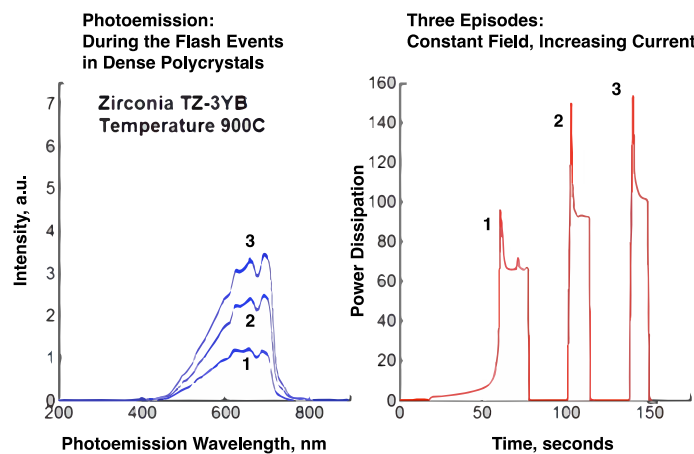
The graphs on the right in Fig. 1 show that flash sintering is accompanied by an equally abrupt increase in the conductivity of the specimen. Thus, mass transport, which controls sintering, and electronic conductivity occur simultaneously. The sudden increase in conductivity leads to Joule heating. The early speculation was that it was the Joule heating that was responsible for the ultrafast rates of sintering (however, this suggestion would still not answer the question why there is an abrupt increase in the conductivity of the specimen). A detailed study [2] has discounted Joule heating as the fundamental cause of the flash effect described in Fig. 1.

The phenomenon illustrated in Fig. 1 has been seen in several oxides ranging from Mg-doped alumina to cobalt-manganese oxide [3-6]. Some of these results have been published, and others are in the process of being prepared for submission.

We have also carried out experiments where a DC electric field is applied in addition to a compressive stress in a sinterforging experiment. These results have shown that modest stresses, in the range of 1.5MPa to 12MPa, not only leads to high rates of shear deformation at low temperatures, but they also influence the threshold temperature for the onset of the flash in the same way as a higher applied field lowers the flash temperature [7]. This apparent equivalence between applied stress and electrical field is novel, and urges the need for a unified theory of electro-chemo-mechanical potentials in ceramics science.

Indeed, the results presented in Fig. 1 open new scientific questions related to the interaction between electrical fields, defect chemistry, and self-diffusion in oxide-ceramics. These fundamental questions have implications in many different aspects of ceramic science including superplastic deformation and phase transformations as well as densification. It is possible that the defect avalanche mechanism that we are proposing to investigate has some degree of overlap with radiation damage where defects are created by energetic impingements instead of electrical fields. These are surely exciting new developments in the field of ceramic science.

The hypothesis we have proposed [8] to explain these findings is the nucleation of Frenkel pairs under the conditions of imposed field and temperature. The concept is that the vacancies and interstitials of these pairs, which have opposite charges on them (relative to the lattice), become ionized under the electric field, thereby creating neutral vacancies and interstitials, and electron-hole pairs. The abrupt increase in neutral defects increases self-diffusion, while the electron-hole pairs instigate electrical conductivity. While the quantitative analysis of this mechanism remains illusive, it at least qualitatively explains why mass-transport is coupled to electrical conductivity. The mechanism proposed above suggested that the electron-hole pairs may also act like excitons, that is, they may be able to recombine to emit photons. This prediction was confirmed by measurements of photoemission as shown in Fig. 2.



2. Photoemission from pre-sintered fully dense specimens, when repeatedly applying the power pulse of increasing intensity. The intensity of the photoemission, which lies in the visible range, increases with power level, but the fine structure, corresponding to absorption, remains steadfast. The experiments were done at constant field, with the power being raised by increasing the current setting (unpublished results).

Thus, we now discover that the mechanism to understand these new phenomena must explain the concurrence between, mass transport, electrical conductivity and photoemission.

## FUTURE PLANS

Future plans have three distinct threads: (i) to quantify the relationship between the electrical parameters in the experiments and the measurements of densification and shear deformation in oxide ceramics, (ii) to conduct experiments with spectroscopic methods and transmission electron microscopy to determine the presence of defects, and the nature of the defects produced during the flash events, and (iii) to develop quantitative models that quantitatively predict the onset of defect avalanche, and are able to explain the differences in the “flash temperature” in different oxides. Ultimately, *in-situ* experiments in transmission electron microscope on model materials are planned to visualize the defect avalanche and to validate the models that are developed to predict it.

Extensive use of the User Facilities at ORNL are planned to achieve the objectives outlined above. Discussions with Dr. L. Allard and Dr. S. Pennycook have occurred towards this goal.

## PUBLICATIONS (2010-2012)

1. COLOGNA, M., RASHKOVA, B. and RAJ, R., 2010. Flash Sintering of Nanograin Zirconia in < 5 s at 850 Degrees C. *Journal of the American Ceramic Society*, NOV, vol. 93, no. 11, pp. 3556-3559 ISSN 0002-7820. DOI 10.1111/j.1551-2916.2010.04089.x.
2. RAJ, R., 2012. Joule Heating during Flash-Sintering. *Journal of the European Ceramic Society*, AUG, vol. 32, no. 10, pp. 2293-2301 ISSN 0955-2219. DOI 10.1016/j.jeurceramsoc.2012.02.030.
3. COLOGNA, M., FRANCIS, J.S.C. and RAJ, R., 2011. Field Assisted and Flash Sintering of Alumina and its Relationship to Conductivity and MgO-Doping. *Journal of the European Ceramic Society*, DEC, vol. 31, no. 15, pp. 2827-2837 ISSN 0955-2219. DOI 10.1016/j.jeurceramsoc.2011.07.004.
4. KARAKUSCU, A., et al, 2012. Defect Structure of Flash-Sintered Strontium Titanate. *Journal of the American Ceramic Society*, AUG, vol. 95, no. 8, pp. 2531-2536 ISSN 0002-7820. DOI 10.1111/j.1551-2916.2012.05240.x.
5. PRETTE, A.L.G., COLOGNA, M., SGLAVO, V. and RAJ, R., 2011. Flash-Sintering of Co<sub>2</sub>MnO<sub>4</sub> Spinel for Solid Oxide Fuel Cell Applications. *Journal of Power Sources*, FEB 15, vol. 196, no. 4, pp. 2061-2065 ISSN 0378-7753. DOI 10.1016/j.jpowsour.2010.10.036.
6. COLOGNA, M., PRETTE, A.L.G. and RAJ, R., 2011. Flash-Sintering of Cubic Ytria-Stabilized Zirconia at 750 Degrees C for Possible use in SOFC Manufacturing. *Journal of the American Ceramic Society*, FEB, vol. 94, no. 2, pp. 316-319 ISSN 0002-7820. DOI 10.1111/j.1551-2916.2010.04267.x.
7. FRANCIS, J.S.C. and RAJ, R., 2012. Flash-Sinterforging of Nanograin Zirconia: Field Assisted Sintering and Superplasticity. *Journal of the American Ceramic Society*, JAN, vol. 95, no. 1, pp. 138-146 ISSN 0002-7820. DOI 10.1111/j.1551-2916.2011.04855.x.
8. RAJ, R., COLOGNA, M. and FRANCIS, J.S.C., 2011. Influence of Externally Imposed and Internally Generated Electrical Fields on Grain Growth, Diffusional Creep, Sintering and Related Phenomena in Ceramics. *Journal of the American Ceramic Society*, JUL, vol. 94, no. 7, pp. 1941-1965 ISSN 0002-7820. DOI 10.1111/j.1551-2916.2011.04652.x.
9. YANG, D., RAJ, R. and CONRAD, H., 2010. Enhanced Sintering Rate of Zirconia (3Y-TZP) through the Effect of a Weak Dc Electric Field on Grain Growth. *Journal of the American Ceramic Society*, OCT, vol. 93, no. 10, pp. 2935-2937 ISSN 0002-7820. DOI 10.1111/j.1551-2916.2010.03905.x.
10. FRANCIS, J.S.C., COLOGNA, M. and RAJ, R., 2012. Particle Size Effects in Flash Sintering. *Journal of the European Ceramic Society*, SEP, vol. 32, no. 12, pp. 3129-3136 ISSN 0955-2219. DOI 10.1016/j.jeurceramsoc.2012.04.028.
11. COLOGNA, M. and RAJ, R., 2011. Surface Diffusion-Controlled Neck Growth Kinetics in Early Stage Sintering of Zirconia, with and without Applied DC Electrical Field. *Journal of the American Ceramic Society*, FEB, vol. 94, no. 2, pp. 391-395 ISSN 0002-7820. DOI 10.1111/j.1551-2916.2010.04088.x.

## Mechanical Behavior in Ceramics with Unusual Thermal-Mechanical Properties

Ivar Reimanis\* and Cristian Ciobanu\*\*  
\*Metallurgical and Materials Engineering Department  
\*\*Mechanical Engineering Department  
Colorado School of Mines  
Golden, CO 80401

Email: [reimanis@mines.edu](mailto:reimanis@mines.edu)

### Program Scope

The study of ceramics with unusual properties offers new insight into structure-property relations as well as promise for the design of novel composites. In this spirit, the PIs seek to (1) develop a comprehensive understanding of mechanical phenomena in ceramics that exhibit pressure-induced phase transitions, negative coefficient of thermal expansion (CTE), and negative compressibility, and (2) explore the effect of these phenomena on the mechanical behavior of composites designed with such ceramics. The broad and long-term goal is to utilize this insight to obtain desired mechanical responses.

The present research impacts the design of ceramics for enhanced mechanical performance under challenging thermal or irradiation environments in a variety of applications including thermal shock resistant structures, battery materials, nanolithography, nuclear reactor materials. In particular, the use of phase transformations to modify mechanical behavior in ceramics is an unrealized potential. The overall approach embraces the concept that exceptional advances in mechanical behavior performance for ceramics will only occur if one understands and couples together phenomena at the nanoscale.

Much of our recent work has focused on  $\beta$ -eucryptite ( $\text{LiAlSiO}_4$ ), a lithium ion conductor that exhibits a negative CTE and a pressure-induced phase transformation. A combination of experiments and atomistic simulations has been used to understand property-structure relations in this fascinating ceramic. The specific objectives are to: (i) perform fundamental physical property measurements on silicates that exhibit unusual thermal-mechanical properties, with a focus on transformations in eucryptite. (ii) Develop atomistic level models that may be used to describe the above properties with the purpose of correlating structure and thermal and/or mechanical behavior. Models will be used to explore phase stability in eucryptite and other silicates. (iii) Utilize the above results to develop models that may be used to predict the response of ceramics under mechanical and thermal stimulus and under irradiation conditions. These models are inherently multi-scale and incorporate cooperative effects of individual phenomena. Specifically, a descriptive model for utilizing a pressure induced phase transformation for toughness enhancement in ceramics is sought. (iv) Verify experimentally the theoretical prediction that toughening is possible utilizing a pressure-induced phase transformation.

## Recent Progress Highlights

### ● Probing thermal and physical properties at the nanoscale

A nanoindentation technique was developed to probe the early stages of pressure-induced phase transformations in ceramics, and this was applied to  $\beta$ -eucryptite [1-3]. In ultra low load nanoindentation, deviations from linear elastic behavior (Figure 1) represent a thermally activated event in eucryptite which has been correlated to the pressure induced phase transformation. *It is the first time* that the present nanoindentation technique has been used to study the rate dependencies of a phase transformation. The activation volume for this event, calculated from the statistical compilation of numerous nanoindentation measurements (Figure 2), is about  $0.1 \text{ nm}^3$ , on the same order of size scale of the silica and alumina tetrahedra that comprise the  $\beta$ -quartz structure of  $\beta$ -eucryptite, indicating that the phase transformation is dictated by the rotation and distortion of these tetrahedra. It has previously been reported that the rotation and distortion of these tetrahedral, and the influence that has on structural ordering, control the thermal expansion behavior, and therefore, a bridge has been established between the thermal and mechanical properties. Additionally, this understanding about what controls the transformation at the nanoscale is a major step towards tailoring the characteristics of the transformation. The ability to make appropriate structural changes during synthesis [4] will enable tailoring of the thermal and physical properties. We have shown that small amounts of Zn dopant, believed to substitute for  $\text{Li}^+$  in  $\beta$ -eucryptite, lead to profound effects on the thermal expansion behavior [6] and also influence the pressure induced phase transformation [3]. Zn is believed to alter the temperature and pressure at which the  $\beta$ -eucryptite structure becomes disordered. Atomistic modeling is currently in progress to develop a more detailed picture. Also in progress are mechanical property studies to understand how to employ the transformation. An indentation strength technique was adapted to develop a new way to examine the strain rate dependence of subcritical crack growth, and this will be used to characterize crack growth in eucryptite composites [7].

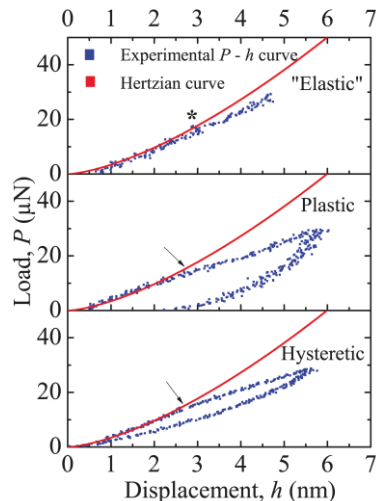


**Figure 1.** Nanoindentation load-displacement data taken from a specimen of  $\beta$ -eucryptite showing three types of behavior. The asterisk and arrows indicate the deviation from the Hertzian linear elastic prediction (red solid curve), thereby revealing the load at which the  $\beta - \epsilon$  phase transition occurs. The unloading portion of the elastic curve has been removed in the top curve to better visualize the deviation from linearity.

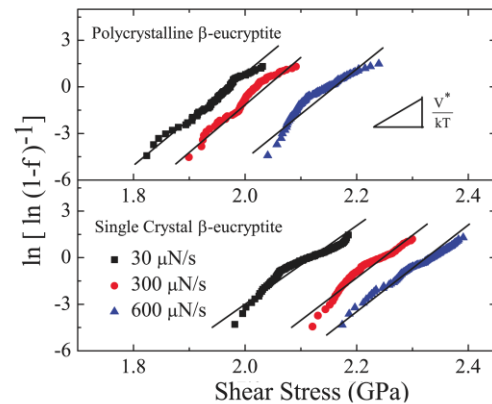


**Figure 2.** The Hertzian deviation load (see Figure 1) is plotted as a function of shear stress underneath the indenter in polycrystalline and single crystal  $\beta$ -eucryptite for three different loading rates. The loading rate dependence reveals that the transformation is thermally activated, and an activation volume on the order of  $0.1 \text{ nm}^3$  has been determined.

- *The origin of the negative bulk expansion coefficient*

We have computed the elastic stiffness constants of ordered  $\beta$ -eucryptite within the framework of generalized gradient approximation of density functional theory (DFT) [8]. The calculated elastic constants are in close agreement with the experimentally known values. The elastic constants were subsequently used to compute the linear compressibilities of  $\beta$ -eucryptite parallel and perpendicular to the  $c$  axis. The calculated compressibility values agree well with those calculated from experimentally known elastic constants as reported by others. The calculated values of compressibility are, however, in contradiction to those reported by Hortal et al., who measured the compressibilities using a direct three-terminal method (Hortal, et al., J. Am. Ceram. Soc. 58, 262, 1975). Our calculations showed that the compressibility parallel to the  $c$  axis is positive, as opposed to the negative value obtained from the direct three-terminal measurements [8]. Based on those calculations, it is shown that the negative bulk thermal expansion of  $\beta$ -eucryptite must be associated with a negative Grüneisen function parallel to the  $c$  axis rather than with a negative compressibility. The conclusion that the negative bulk thermal expansion coefficient occurs because of a negative Grüneisen function is consistent with the results of Lichtenstein, et al., who showed through the calculations of phonon density of states that the Grüneisen function parallel to the  $c$  axis strongly negative due to the bending modes of the Si-O and Al-O bonds (Lichtenstein, et al., Phys. Rev. B 62, 11487, 2000). Our results are also consistent with the neutron diffraction and X-ray synchrotron diffraction studies conducted by others. This study clearly indicates that the compressibilities must be positive, and that the negative bulk thermal expansion is due to cation disordering, rather than to elastic effects. These DFT-based results, along with the indirect measurements of elastic constants, should spark future developments in direct measurement techniques, which would be applicable for the study of a wide variety of ceramics.

- *Radiation tolerance mechanisms in  $\beta$ -eucryptite*

Previous studies on Li-silicates have shown that these materials could be resistant to radiation damage even in extreme physical and chemical environments, and are thus promising solid-state breeder materials in fusion reactors. Focusing on  $\beta$ -eucryptite as a member of Li-Al silicate class of ceramics with potential for nuclear applications, the PIs have studied the atomic-scale processes induced by radiation. Using molecular dynamics simulations based on ReaxFF [9,10], it was found that upon radiation dosage of 0.21 displacements-per-atom (dpa) or less, the structure largely retains its long-range order while exhibiting (a) disordering of the Li atoms, (b) distortion of the  $\text{SiO}_4$  and  $\text{AlO}_4$  tetrahedra defined as the change in their oxygen-coordination number, and (c) tilting of the  $\text{SiO}_4$  and  $\text{AlO}_4$  tetrahedra with respect to one another [11]. The  $\text{SiO}_4$  tetrahedra that distort to  $\text{SiO}_3$  during exposure to radiation recover significantly upon thermal relaxation, and provide the mechanism for this recovery. This mechanism (Figure 3) consists of the tilting of  $\text{AlO}_5$  polyhedra formed upon exposure so as to satisfy the oxygen-coordination of distorted  $\text{SiO}_4$  tetrahedra. A doubling of the dosage results in a significant increase of the concentration of Si-Al antisite defects, which renders the tolerance mechanism inefficient and leads to amorphization.

## **Future Plans**

Future research is designed to achieve a better understanding of how the structure of framework silicates is modified in the presence of doping (e.g,  $\text{Zn}^{2+}$  and  $\text{Mg}^{2+}$  doped into  $\beta$ -eucryptite) and how those modifications alter physical behavior such as the kinetics and thermodynamics of phase transformations. Atomistic modeling aided by metadynamics and several experimental characterization tools, such as nanoindentation and diamond anvil cell (DAC) Raman spectroscopy, will be employed. The goal is to modify the pressure at which the high pressure phase  $\epsilon$ -eucryptite forms so that it may be formed *in situ* in a composite with the purpose of activating a transformation toughening mechanism. A proposal has been submitted to Argonne National Laboratory to perform DAC studies with high energy x-rays. We also plan to examine orthopyroxenes, a class of chain silicates, with the goal of applying what is learned with  $\beta$ -eucryptite to a broader class of materials.

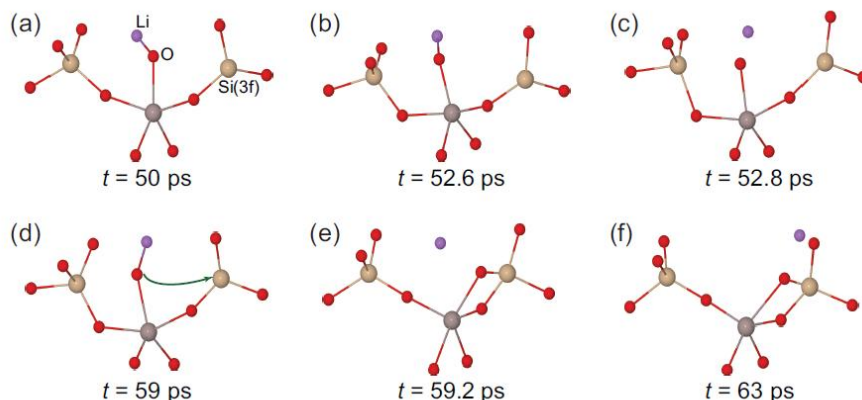


**Figure 3.** Mechanism for recovery of  $\text{SiO}_4$  from  $\text{SiO}_3$  in the radiated structure (a) during annealing at 900 K and 1 atm *via* intermediate steps (b)–(e) leading to the restoration of tetrahedral arrangement of silicon (f).

### References (DOE-Acknowledged Publications by the Authors 2010-2012)

1. S. Ramalingam, I. E. Reimanis, and C. Packard, "Determining Activation Volume for the Pressure-Induced Phase Transformation in  $\beta$ -eucryptite through Nanoindentation", *J. Amer. Ceram. Soc* 95[6] 2051-2058, (2012).
2. S. Ramalingam, C. Packard, and I. E. Reimanis, "In-situ Diamond Anvil Cell–Raman Spectroscopy and Nanoindentation Study of the Pressure-Induced Phase Transformation in Pure and Zinc-Doped  $\beta$ -eucryptite", in press in *J. Amer. Ceram. Soc.* (2013).
3. C. E. Packard, S. Ramalingam, I. E. Reimanis, "Indentation Study of the Pressure-Induced Phase Transformation in Beta-Eucryptite: a Candidate Material for New Transformation-Toughened Ceramics", International Symposium on Plasticity 2012 and its Current Applications Jan 3-8, 2012, San Juan, Puerto Rico.
4. T. Jochum and I. E. Reimanis, "Reactions in Eucryptite-Based Lithium Aluminum Silicates", *J. Amer. Ceram. Soc.*, 93[6] 1591-1596, (2010).
5. S. Ramalingam and I. E. Reimanis, "Effect of Doping on the Thermal Expansion of  $\beta$ -eucryptite Prepared by Sol-Gel Methods", *J. Am. Ceram. Soc.* 95[9] 2939-2943, (2012).
6. S. Ramalingam and I. Reimanis, Near Zero Coefficient of Thermal Expansion Beta-Eucryptite without Microcracking, Provisional patent filed by Colorado School of Mines, April 30, 2012
7. S. Ramalingam, I. E. Reimanis, E. R. Fuller, Jr., and J. Haftel, "Slow Crack Growth Behavior of Zirconia Toughened Alumina (ZTA) and Alumina using the Dynamic Fatigue Indentation Technique", *J. Amer. Ceram. Soc.*, 94[2] pp. 576-583 (2011).
8. B. Narayanan, I. E. Reimanis, E. R. Fuller and C. Ciobanu, "Elastic constants of  $\beta$ -eucryptite studied by density functional theory", *Phys. Rev. B* 81, 104106 (2010).
9. B. Narayanan, A. C. T. van Duin, B. B. Kappes, I. E. Reimanis and C. V. Ciobanu, "Reactive force field for lithium-aluminum silicates with applications to eucryptite phases", *Modelling and Simulation in Materials Science and Engineering*, 20, 1, 14 pages, (2012).
10. B. Narayanan, Y. Zhao, and C. V. Ciobanu, "Migration Mechanism for Atomic Hydrogen in Porous Materials", *Appl. Phys. Lett.* 100, 203901 (2012).
11. B. Narayanan, I. E. Reimanis, H. Huang, and C. V. Ciobanu, "Radiation Effects and Tolerance Mechanism in  $\beta$ -Eucryptite", in press in *J. Appl. Phys.* (2012).

# NanoMechanics: Elasticity and Friction in Nano-Objects

Elisa Riedo

School of Physics, 837 State St, Atlanta GA 30332-0430 Georgia Institute of Technology

[elisa.riedo@physics.gatech.edu](mailto:elisa.riedo@physics.gatech.edu)

The goal of this program is to understand, predict and manipulate the size, shape, chemistry and structure of different types of nanostructures, for producing nano-materials with tailored optimum mechanical, electro-mechanical and thermo-mechanical properties. At present this research program is focused on the study of the frictional properties and the radial deformation mechanisms of supported C- and BN-NTs as a function of their morphology, e.g. radius, number of layers, and length; structure, e.g. chirality and defects; substrate interaction, and chemical functionalization. Furthermore, we plan to initiate a new research program on the mechanical properties of epitaxial graphene oxide on SiC.

## Recent Progress

During the last funding round, 2010-2012, the PI has published 8 articles and 2 Book Chapters, listed at the end of this abstract, on the general topic of “Nanomechanics and Materials for Nanomechanics Applications”.

The PI and her collaborators have initiated a study of the **frictional properties of individual CNTs** using a nano-size atomic force microscope tip sliding on individual CNTs lying on a substrate. The PI *et al.* found a larger friction coefficient when the tip is sliding perpendicular to the CNT axis, as compared to sliding along the tube axis (see Fig. 1). This behavior is explained by a deformation, similar to a lateral swaying (or a “hindered rolling”) of the tube during the transverse sliding, which produces additional friction dissipation. This soft deformation mode is absent, or partially absent, when the tip slides along the CNT axis, thus, for the longitudinal sliding the friction force arises mostly from sliding the hard nano-contact between the tip and the tube. The AFM tip can slide along the tube axis, namely longitudinal sliding, or alternatively perpendicularly to the NT axis, namely transverse sliding. We call the ratio between transverse and longitudinal friction per unit area, friction anisotropy. Very recently, the PI and her collaborators have shown how structural defects, surface chemistry and possibly chirality can couple the transverse and longitudinal sliding, modulating nanotubes frictional properties. Specifically, the PI *et al.* studied the frictional

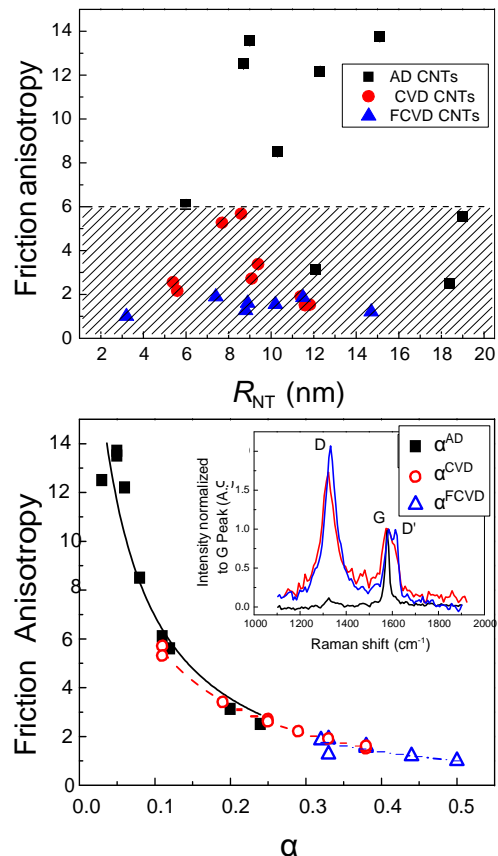
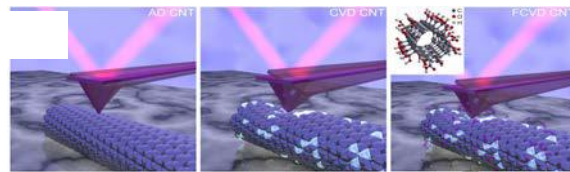


**Figure 1. Top.** Cartoon of the three types of NT investigated by the PI: AD NT, CVD NT, and Functionalized CVD NT. **Center.** Friction anisotropy vs NT radius, and **(Bottom)** vs. coupling coefficient  $\alpha$ . In the inset Raman Spectra of AD, CVD, and FCVD nanotubes.

properties of supported multiwalled CNTs produced by Arc Discharge (AD), and Chemical Vapor Deposition (CVD), as well as chemically functionalized CVD (FCVD) CNTs, see the results as reported in Fig. 1. A Raman Spectroscopy microscope (see Figure in the facilities document, purchased in part with DoE funds) was used to study the amount of structural defects in the NTs. The measurements were performed on the NTs solutions. In the future we plan to investigate by Raman individual NTs in situ with AFM mechanical measurements. It resulted that FCVD NTs are very rich of defects, CVD NTs slightly less, and AD NTs have a negligible amount of defects (see inset in Fig. 1). The friction anisotropy was found to decrease in the presence of defects (see Fig. 1). Isolated very high values of friction anisotropy, up to 14, for AD CNTs with no defects have been attributed to non-chiral CNTs. This anisotropy becomes less than 6 for CVD CNTs with defects and further reduced to less than 2 for FCVD CNTs with more defects and surface functionalization. Furthermore, the PI *et al.* have developed a simple analytical model to compute the amount of “coupling”  $\alpha$ , between the transverse and longitudinal sliding, the “intrinsic” hard contact sliding shear strength,  $\sigma^{\text{int}}$ , and the soft “hindered rolling” shear strength,  $\sigma^{\text{HR}}$ . From the model-experiments comparison  $\sigma^{\text{int-CVD}}$  is found to be 0.022 GPa, which is 4 times larger than  $\sigma^{\text{nt-AD}}$ . This increased  $\sigma^{\text{int-CVD}}$  can be related to the presence of defects, which are known to increase the shear strength during telescopic rotation of concentric CNTs. Furthermore, it is found that  $\sigma^{\text{HR-CVD}}$  varies between 0.29 GPa and 0.54 GPa, values up to one order of magnitude larger than  $\sigma^{\text{HR-AD}}$ . Also,  $\alpha^{\text{CVD}}$  varies in the range between 0.11 and 0.38, values much larger than  $\alpha^{\text{AD}}$ , as shown in Figure 1. This signifies that the coupling effect during tip sliding on CVD CNTs is indeed stronger than on AD CNTs owing to the structural disorder, which might also obscure any effect from CNT chirality. All these results clearly indicate that both the intrinsic friction and the “hindered rolling” dissipation are larger in nanotubes rich of structural defects and with a stronger interaction with the sliding silicon tip. Finally, Figure 1 (bottom) shows that this model captures very well the observed experimental behavior indicating for all the investigated CNTs a similar supralinear decrease of  $\alpha$  with increasing friction anisotropy.

The PI and her collaborators have also investigated the **frictional properties of individual multiwalled Boron Nitride nanotubes** synthesized by chemical vapor deposition (CVD) and deposited on a Silicon substrate. It was found that the friction anisotropy in BN-NTs increases with the nanotube-substrate contact area, estimated to be proportional to  $(L_{\text{NT}} \cdot R_{\text{NT}})^{1/2}$  where  $L_{\text{NT}}$  is the length on the NT and  $R_{\text{NT}}$  is the external radius. Larger contact area denotes stronger surface adhesion, resulting in a longitudinal friction coefficient closer to the value expected in absence of transverse deformations. Compared to Carbon nanotubes, BN-NTs display a friction coefficient in

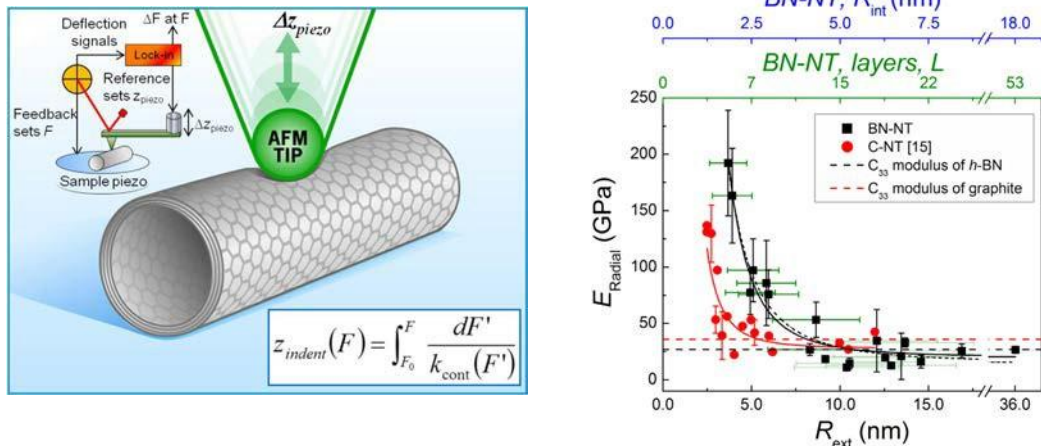


Figure 2. Left. Cartoon of the MoNI method. Right. Radial effective elastic modulus vs radius for BN and C- NTs.

each sliding direction with intermediate values between CVD and Arc Discharge CNTs. CVD BN-NTs with improved tribological properties and higher oxidation temperature might be a better candidate than CVD C-NTs for applications in extreme environments.

Regarding the **radial elastic properties of BN Nanotubes**, the PI and her collaborators have used the AFM based modulated nano-indentation (MoNI) technique developed in the PI's group (Fig. 2) to investigate the radial stiffness of individual CVD grown MW BN-NTs with radii ranging between 3.7 and 36 nm, and with a wall thickness approximately equal to 0.5 times the external radius,  $R_{\text{ext}}$ , as obtained by the statistical TEM analysis. The radial deformation is here always measured during the unloading regime for indentations below 10% of  $R_{\text{ext}}$  to insure the probing of the local radial elasticity of the nanotubes. It was found that  $E_{\text{Radial}}$  of MW BN-NTs decreases with increasing  $R_{\text{ext}}$  and the number of layers,  $L$ , from about  $192.2 \pm 46.8$  GPa for  $R_{\text{ext}} = 3.7 \pm 0.1$  nm and  $L = 5.4 \pm 1$ , to a plateau value of  $24 \pm 11$  GPa, a value very close to the elastic constant along the  $C_{33}$  axis of the corresponding bulk materials, i.e., 27 GPa for hexagonal Boron Nitride (*b*-BN). These elastic moduli are larger than previously reported values for MW BN-NTs because of the small indentation and large number of wall layers in the BN-NTs studied in this letter. When probing thick tubes the ovalization process at small indentations as in our experiments is minimal, instead, the localized radial compression creates a dimple in the tube's top layers and the elasticity depends on the layer-layer interaction and layer curvature. Here, the PI *et al.* found indications of the key role of the morphology in determining the radial rigidity of MW BN-NTs, in particular they found that the external and internal radii,  $R_{\text{ext}}$  and  $R_{\text{int}}$ , may have a stronger influence on the radial modulus than the thickness of nanotube,  $t$ .

**Graphene and graphene-based materials** hold great promise for the next generation of nanodevices. One of the most pressing issues for the technological use of graphene is the possibility to control physical and chemical properties by means of *ad hoc* functionalization. The PI and her collaborators demonstrated the ability to reduce graphene oxide at the nanoscale by using hot AFM tips (thermochemical nanolithography, TCNL). The resulting nanostructures have a conductivity that can be tune over 4 orders of magnitude. Graphene oxide (GO) is indeed a material of great interest for its potential applications in nanoelectronics, nanoelectromechanical system, sensors, polymer composites, catalysis, energy storage devices and optics. The PI and her collaborators have carried over a combined experimental and density functional theory study which shows that multilayer graphene oxide produced by oxidizing epitaxial graphene through the Hummers method is a metastable material whose structure and chemistry evolve at room temperature with a characteristic relaxation time of about one month. This study shows that the structural and chemical changes are driven by the availability of hydrogen in the oxidized graphitic sheets, which favors the reduction of epoxide groups and the formation of water molecules.

**Piezoelectric nanostructures.** The high piezoelectric response of ferroelectric perovskites (an order-of-magnitude higher than AlN and ZnO) makes these materials excellent candidates for nanoelectromechanical systems based sensors, actuators and energy harvesters. However, the high temperatures required for their synthesis are mostly incompatible with other on-chip components, and the properties of these materials can be easily affected during chemical and mechanical nanofabrication.

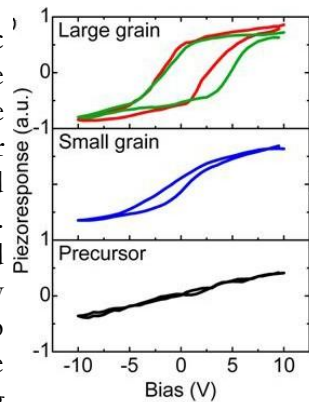


**Figure 3. Grain-size dependent piezoelectric hysteresis.** Typical piezoelectric hysteresis loops obtained from different locations of the pattern. The red (0.9 V, ~7 kHz) and the green (0.85 V, ~7 kHz) curves were obtained from the areas with large grains marked. The blue (0.6 V, ~7 kHz) hysteresis loop was obtained from the area composed of smaller grains in the range of 40-60 nm. The black curve represents the response from the untreated precursor film (0.8 V, ~7 kHz)

The PI and her collaborators have reported on a CMOS compatible method for the direct fabrication of arbitrary-shaped  $\text{Pb}(\text{Zr}_{0.52}\text{Ti}_{0.48})\text{O}_3$  and  $\text{PbTiO}_3$  piezoelectric nanostructures on a variety of substrates ranging from plastic (Kapton) to silicon and soda-lime glass. A heated nano-tip is used to induce nanoscale crystallization of sol-gel precursor films. Piezoelectric lines with widths  $\geq 30$  nm, spheres with diameter  $\geq 10$  nm and densities up to 213 Gb/in<sup>2</sup> are produced. A grain-size dependent piezoelectric response was also demonstrated (Fig. 3).

### References (2010-2012):

1. Hsiang-Chih Chiu, Sedat Dogan, Mirjam Volkmann, Christian Klinke, and Elisa Riedo “Adhesion and size dependent friction anisotropy in Boron Nitride nanotubes”, **Nanotechnology**, 23, 455706 (2012).
2. H.-C. Chiu, S. Kim, C. Klinke, and E. Riedo, “Morphology dependence of radial elasticity in multiwalled boron nitride nanotubes” , **Appl. Phys. Lett.** 101, 103109 (2012).
3. S. Kim, Si Zhou, Y. Hu, M. Acik, Y. J. Chabal, C. Berger , W.de Heer, A. Bongiorno, and E. Riedo “Room Temperature Metastability of Multilayer Epitaxial Graphene Oxide”, **Nature Materials**, 11, 544, (2012).
4. M. Lucas, and E. Riedo, Invited Review Article: “Combining scanning probe microscopy with optical spectroscopy for applications in biology and materials science”, **Rev. Sci. Instrum.** 83, 061101 (2012) **(Cover Article)**.
5. Hsian-Chih Chiu, Beate Ritz, Suenne Kim, Erio Tosatti, Christian Klinke, Elisa Riedo “Sliding on a Nanotube: Interplay of Friction, Deformations and Structure” **Adv. Mat.**, 24, 2879 (2012). **(Cover Article)**
6. Suenne Kim, Yaser Bastani, Haidong Lu, William P. King, Seth Marder, Kenneth H. Sandhage, Alexei Gruverman, Elisa Riedo, and Nazanin Bassiri-Gharb “Direct fabrication of arbitrary-shaped ferroelectric nanostructures on plastic, glass and silicon substrates”, **Adv. Mat.**, 23, 3786–3790, (2011). **(Cover Article)**
7. Z. Q. Wei, D. B. Wang, S. Kim, S. Y. Kim, Y. K. Hu, M. K. Yakes, A. R. Laracuente, Z. T. Dai, S. R. Marder, C. Berger, W. P. King, W. A. de Heer, P. E. Sheehan, and E. Riedo, "Nanoscale Tunable Reduction of Graphene Oxide for Graphene Electronics," **Science**, 328, 1373-1376, (2010).
8. M. Lucas, Z. L. Wang, and E. Riedo, “Growth direction and morphology of ZnO nanobelts revealed by combining in situ atomic force microscopy and polarized Raman spectroscopy” **Phys. Rev. B** 81, 045415 (2010).
9. D. Wang, V. Kodali, J. Curtis, E. Riedo, “Nanofabrication of Functional Nanostructures by Thermochemical Nanolithography” book chapter in *Tip Based Nanofabrication: Fundamentals and Applications*, Springer (2011).
10. D. Wang, R. Szoszkiewicz, V.K. Kodali, J.E. Curtis, S.R. Marder, E. Riedo, "A New-AFM Based Lithography Method: Thermochemical Nanolithography," *Applied Scanning Probe Methods, Volume 10: Biomimetics and Industrial Applications*, (2010).

# Damage-Tolerant Structural Materials

Robert O. Ritchie and Antoni P. Tomsia

Materials Sciences Division, Lawrence Berkeley National Laboratory, Berkeley, CA 94720

[roritchie@lbl.gov](mailto:roritchie@lbl.gov), [aptomsia@lbl.gov](mailto:aptomsia@lbl.gov)

## Program Scope

The attainment of strength and toughness is a vital requirement for structural materials; unfortunately these properties are generally mutually exclusive. It is the lower strength, and hence tougher, versions of materials that find use for most safety-critical applications where premature, or worse still catastrophic, fracture is unacceptable. Accordingly, the development of strong and tough materials has traditionally been a compromise between hardness *vs.* ductility. Using glasses, natural materials and biomimetic ceramics, we have examined strategies to solve this “conflict”. We focus on the interplay between the individual mechanisms that contribute to strength and toughness, that of plasticity and crack-tip shielding, noting that these phenomena originate at very different structural length-scales. The lessons from Nature are particularly relevant here, as natural materials such as bone and shells display unique combinations of mechanical properties that derive from architectures that span nano- to macro-scale dimensions with precisely engineered interfaces. Glasses can also display damage tolerance, but now in the absence of structure. By focusing on mechanisms that permit *stable* cracking, we examine how the strength *vs.* toughness conflict can be solved to achieve unprecedented levels of damage-tolerance.

## Introduction

Our research is focused on experimental/theoretical efforts to probe the mechanics and mechanisms of deformation and fracture (*damage tolerance*) at multiple dimensions in structural materials modeled on natural hierarchical designs. We also look at materials with no recognizable structure over most length-scales, specifically bulk metallic glasses. Our aim is to use ceramics, polymers and metals to create (with appropriate processing) new lightweight structural materials with unprecedented mechanical properties, specifically to achieve the often mutually exclusive properties of high toughness and strength.

An ability to undergo *limited* deformation is a crucial feature of toughness as this enables the local dissipation of stresses which would otherwise cause fracture; hard materials thus tend to be more brittle (Fig. 1a). The deformation mechanisms can be diverse; though dislocation plasticity in crystalline solids is most documented, inelastic deformation can occur via phase transformations, sliding of collagen fibrils in bone, frictional motion between mineral in seashells, and by potential fracture mechanisms such as microcracking in rocks and shear banding in glasses. The operative word here is *limited*; with too much deformability, toughness is lost. Toughness is thus a compromise, traditionally considered to be the combination of strength and ductility, two properties that also tend to be mutually exclusive.

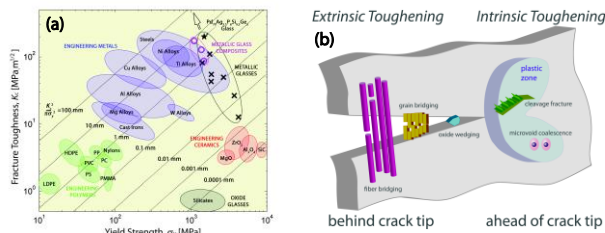


**Fig. 1.** (a) Ashby-plot showing strength-toughness relationships for various classes of materials. Diagonal lines show the plastic-zone size,  $K_c^2/\pi\sigma_y^2$ , where  $K_c$  is the fracture toughness,  $\sigma_y$  the yield strength. (b) Schematic illustration showing how strength and fracture behavior can be considered in terms of intrinsic (plasticity) *vs.* extrinsic (shielding) toughening mechanisms associated with crack extension.

However, toughness can be created without ductility, as in ceramics which cannot be toughened through plasticity. Here fracture is a mutual competition of intrinsic damage operating ahead of a crack tip to promote fracture and extrinsic “shielding” mechanisms mostly behind the tip to inhibit it (Fig. 1b). *Intrinsic toughening* involves plasticity, making damage more difficult. With *extrinsic toughening*, the material’s fracture resistance is unchanged; instead, mechanisms act principally in the crack wake to

reduce the crack tip stresses/strains, a consequence of which are R-curves, where the crack-driving force must increase to maintain crack extension (a key in designing strong and tough materials).

## Recent Progress

**Amorphous materials:** An unexpected example of damage tolerance is with bulk metallic glasses (BMGs). Being 100% amorphous, BMGs tend to have strengths that can easily be  $\sim 1\text{-}2$  GPa. Without dislocations, they deform by shear bands which can cause extreme brittleness; in tension, a single shear band can lead to failure at vanishingly small strains. Locally arresting shear bands before they can cavitate is thus key to making these BMGs tough, as this promotes multiple shear banding to relieve high stresses. This has been achieved by adding a crystalline dendritic phase implicitly to arrest shear bands (Fig. 2a,b); however, the spacing of this phase must be small enough to stop a shear band/crack before it can cause fracture, *i.e.*, by matching characteristic microstructural and mechanical length-scales. With Zr-based composite glasses, we have measured toughnesses of  $100\text{-}160$   $\text{MPa}\sqrt{\text{m}}$  at strengths of  $1.1\text{-}1.5$  GPa, representing one of the highest strength/toughness combinations (Fig. 1a). We have achieved even better strength/toughness properties in a monolithic Pd-based glass (Fig. 1a), although with a different approach; alloy composition was chosen for high bulk modulus but low shear modulus, the latter related to ease of shear band formation, the former to difficulty of cavitation. These alloys generate a proliferation of shear bands (mimicking large-scale plasticity - Fig. 2c), which are restrained from becoming cracks. They are the most damage-tolerant materials to date, with toughnesses of  $\sim 200$   $\text{MPa}\sqrt{\text{m}}$  (Fig. 2b) at strengths above 1.5 GPa.

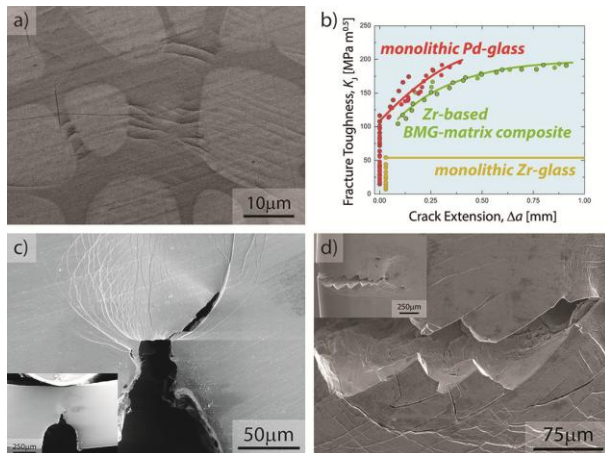


**Fig. 2.** Achieving high toughness and strength in BMGs involves preventing single shear bands from causing failure at near-zero strains. (a) An approach is to add a second-phase to arrest shear bands, *e.g.*, crystalline dendrites in a Zr-based glassy matrix, where the interdendritic spacing is less than the critical crack size; (b) compared to the matrix alloy (Vitreloy 1), this leads to a 3- to 4-fold toughness increase to  $\sim 150$   $\text{MPa}\sqrt{\text{m}}$ . (c) Another approach involves achieving a high bulk-to-shear modulus ratio; this makes shear-band formation easier but cavitation/fracture within the bands more difficult. The result, for a monolithic Pd-Ag-P-Si-Ge glass, is (c) multiple shear-band formation, exceptional strength ( $\sim 1.5$  GPa) and (b) a toughness  $>200$   $\text{MPa}\sqrt{\text{m}}$ . (d) Both materials also show exceptional fatigue strengths, in the case of the composite glass because incipient cracks are arrested at the second phase, and in the Pd-glass due to highly serrated (zig-zag) crack trajectories.

**Nature-inspired hierarchical materials:** Seashells are an example of Nature's design for damage-tolerance. Nacre, for example, has a brick-and-mortar structure, with sub-micron thick aragonite "bricks" separated by a biopolymer "mortar" (Fig. 3a). The mineral provides for strength; however, as it is inherently brittle, if the platelets were rigidly locked, the toughness would be low as local stresses could not be relieved. The organic "mortar" acts like a lubricant by allowing limited slip between the platelets, *i.e.*, intrinsic toughening via plasticity. The interplatelet sliding must be limited ( $\sim 1$   $\mu\text{m}$ ) though to retain strength, resulting in toughnesses far higher than its constituent phases. In our work,  $\text{Al}_2\text{O}_3$  powders mixed with water and frozen using an ice-templating technique were used to make ceramic scaffolds that can be processed with layer thicknesses of  $\sim 1\text{-}100$   $\mu\text{m}$  with interlayer motion controlled by grafting. After pressing and infiltrating with a polymer or metal, we made bulk "brick-and-mortar" hybrid materials in the image of nacre (Fig. 3b). When optimized for toughness, the resulting properties of these bioinspired ceramics are remarkable, with strengths comparable with alumina but toughnesses an order of magnitude larger (Fig. 3c). Indeed, our  $\text{Al}_2\text{O}_3/\text{PMMA}$  composites have  $K_{Ic}$  values exceeding  $30$   $\text{MPa}\sqrt{\text{m}}$  making these the highest toughness ceramics on record.

Whereas our  $\text{Al}_2\text{O}_3/\text{PMMA}$  and  $\text{Al}_2\text{O}_3/\text{Al-Si}$  materials are optimized for high toughness, we are also developing  $\text{Al}_2\text{O}_3/\text{Ni}$  and  $\text{SiC}/\text{PMMA}$  materials with structures tailored for higher strength, in both cases

guided by theoretical micro-mechanical modeling of the strengthening and toughening capacity of hybrid lamellar and brick-and-mortar structures. The biomimetic  $\text{Al}_2\text{O}_3/\text{Ni}$  material is being developed specifically for higher temperature applications; as metals do not wet ceramics, we are attempting to use high pressure infiltration of the metallic phase to make these structures. With respect to silicon carbide, as few ice-templated structures have been made with this ceramic, currently our work is focused on establishing the process parameters to identify optimal conditions for the achievement of nacre-like SiC-based composites. We have investigated the role of the cooling rate, solid content and organic additives in the starting ceramic slurry, since these are critical parameters which affect the ice nucleation and growth during freezing, and thus control the resulting structural features. We have related the process parameters to the scaffold morphology (Fig. 3d) where the influence of the average freezing front speed on the ceramic wall thickness can be defined. By varying these parameters, we have produced scaffolds with ~30-50 vol.% porosity, ceramic wall thicknesses of ~1-50  $\mu\text{m}$ , with highly differing morphologies. Selected SiC scaffolds, either before or after cold pressing, have been infiltrated with PMMA. The mechanical characterization of the lamellar and brick and mortar SiC-PMMA composite is in progress.

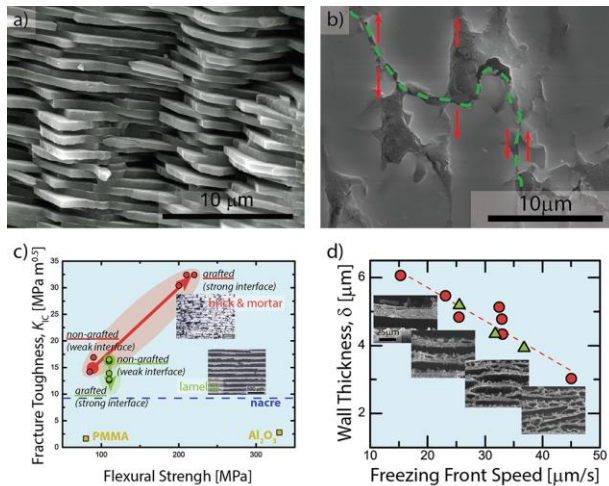


**Fig. 3.** Biomimetic ceramics are modeled on the structure of mollusk shells (nacre). (a) Nacre comprises aragonite mineral “bricks” separated by a biopolymeric “mortar”. (b) Nature-inspired alumina/PMMA “brick-and-mortar” structures made by freeze-casting in the image of nacre. (c) Compared to nacre, the synthetic materials (lamellar and brick-and-mortar structures) show significant toughness improvements. Toughening is associated in part with “brick” pull-out (b) and frictional sliding at mineral interfaces coupled with deformation in the compliant polymeric layer (red arrows in (b)). In particular, the “brick-and-mortar”  $\text{Al}_2\text{O}_3/\text{PMMA}$  ceramic shows exceptional toughness  $>30 \text{ MPa}\sqrt{\text{m}}$ . (d) Freezing conditions control the structure of SiC/PMMA composites as the kinetics of crystallization affect ice morphology and porosity. At high freezing velocities, the ice crystals show a pronounced dendritic morphology. SiC scaffolds exhibit a transition in pore shape, from lamellar to columnar, as the freezing front rate increases (d).

**Theoretical modeling:** To model the behavior of these hybrid materials, we have used two physics-based approaches based on micromechanical mechanisms and numerical modeling. Damage is induced when microcracks are initiated at pores; stress redistribution around the microcracks defines behavior until the strength is reached, with friction at micro-interfaces providing for ductility. To describe the complex relationships between structure, size and properties, we are building finite-element tools for the study of hierarchical materials, applied here to the ceramic scaffold and composite brick-and-mortar structures.

Using multiple brick patterns, elastic properties are computed based on Sanchez-Palencia periodic homogenization theory to derive relationships between the Young’s and shear moduli, Poisson’s ratios and the ceramic content, as a function of the aspect ratio of the bricks; specifically, we find that finer bricks provide for higher stiffness at similar ceramic contents, although rule-of-mixtures predictions for Poisson’s ratio are poor. To model failure, damage mechanisms are introduced in the microstructures. For the ceramic scaffolds, we have considered brittle failure of the single walls and bridges, modeled with Weibull theory. For brick-and-mortar structures, we have modeled mortar plasticity, mortar cracking, debonding/friction at brick-mortar interfaces. Using multiple repetitions of these computations, at multiple loading directions, we have derived multiaxial and statistical failure criteria for these materials.

### Future Plans

Our hybrid materials derive their unique damage-tolerance through the concept of a “lubricant phase”; the ceramic provides the strength, the polymer has minimal load-bearing role but instead acts like a lubricant to relieve stress concentrations. Accordingly, our future plans continue to be focused on the use

of hard scaffolds (SiC, Al<sub>2</sub>O<sub>3</sub>) with compliant second phases, particularly using metallic additions to enhance high-temperature capability. Guided by theory, specifically MD modeling to understand processing parameters and micromechanical/numerical analyses to model mechanisms that control strength and toughness, we plan to further develop lightweight materials with nano/microstructures optimized for structural performance, namely with high toughness without compromise in strength.

### DOE-BES Sponsored Publications - 2010-2012

#### *Nature-Inspired Structural Materials: Processing and Properties*

1. ME Launey, E Munch, DH Alsem, E Saiz, AP Tomsia, RO Ritchie. A novel biomimetic approach to the design of high-performance ceramic/metal composites. *J Roy Soc Interface* 2010;7:741.
2. E Saiz, M Benhassine, J De Coninck, AP Tomsia. Early stages of dissolutive spreading. *Scripta Mater* 2010;62:934.
3. M Benhassine, E Saiz, AP Tomsia, J De Coninck. The role of the commensurability of the substrate on the nonreactive wetting kinetics of liquid metals. *Acta Mater* 2010;58:2068.
4. ME Launey, PY Chen, J McKittrick, RO Ritchie. Mechanistic aspects of the toughness of elk antler. *Acta Biomater* 2010; 6:1505.
5. DV Wilbrink, M Utz, RO Ritchie, MR Begley. Scaling of strength and ductility in bio-inspired brick and mortar composites. *Appl Phys Lett* 2010; 97:193701.
6. M Benhassine, E Saiz, AP Tomsia, J De Coninck. Nonreactive wetting kinetics of binary alloys. *Acta Mater* 2011;59:1087.
7. MR Begley, NR Philips, BG Compton, DV Wilbrink, RO Ritchie, M Utz. Mechanical models to guide the development of synthetic 'brick and mortar' composites", *J Mech Phys Solids* 2012;60:1545.

#### *Damage-Tolerance in Materials*

8. MD Demetriou, M Launey, G Garret, D Hofmann, WL Johnson, RO Ritchie. A damage tolerant glass. *Nature Mater* 2011;10:123.
9. RO Ritchie. Conflicts between strength and toughness. *Nature Mater* 2011;10:817.
10. RO Ritchie, ME Launey. Crack growth in brittle and ductile solids. *Encyclopedia of Tribology*, QJ Wang, YW Chung, eds. Springer Science, AZ Dordrecht, The Netherlands, 2012.
11. ME. Launey, RO Ritchie. Crack growth in noncrystalline solids. *Encyclopedia of Tribology*, QJ Wang, YW Chung, eds. Springer Science, AZ Dordrecht, The Netherlands, 2012.
12. I Altenberger, RK Nalla, Y Sano, L Wagner, RO. Ritchie. On the effect of deep-rolling and laser-peening on the stress-controlled low- and high-cycle fatigue behavior of Ti-6Al-4V at elevated temperatures up to 550°C. *Intl J Fatigue* 2012;44:292.

#### *Ceramic and Intermetallic Structural Materials*

13. AM Kueck, QM Ramasse, LC De Jonghe, RO Ritchie. Atomic-scale imaging and the effect of yttrium on the fracture toughness of silicon carbide ceramics. *Acta Mater* 2010;58:2999.
14. CS Lee, JA Lemberg, DG Cho, JY Roh, RO Ritchie. Mechanical properties of Si<sub>3</sub>N<sub>4</sub>-Al<sub>2</sub>O<sub>3</sub> FGM joints with 15 layers for high-temperature applications. *J Eur Ceram Soc* 2010;30:1743.
15. M Barney, D Xu, SW Robertson, V Schroeder, RO Ritchie, AR Pelton, A Mehta. Impact of thermomechanical texture on the superelastic response of Nitinol. *J Mech Beh Biomed Mater* 2011;4:1431.
16. KE Thomson, D Jiang, W Yao, RO Ritchie, AK Mukherjee. Characterization and mechanical testing of alumina-based nanocomposites reinforced with Nb and/or carbon nanotubes fabricated by spark plasma sintering. *Acta Mater* 2012; 60:622.
17. SW Robertson, AR Pelton, RO Ritchie. Mechanical fatigue and fracture of Nitinol. *Intl Mater Rev* 2012;57:1.
18. JA Lemberg, MR Middlemas, T Weingärtner, B Gludovatz, JK Cochran, RO Ritchie. On the fracture toughness of fine-grained Mo-3Si-1B (wt.%) alloys at ambient to elevated (1300°C) temperatures. *Intermetallics* 2012;20:141.
19. JA Lemberg, RO Ritchie. Mo-Si-B alloys for ultrahigh-temperature structural applications. *Adv Mater* 2012;24:3445.

#### *Materials for Energy Applications*

20. Y Murakami, RO Ritchie. Effect of hydrogen on fatigue-crack propagation in steels. *Gaseous Hydrogen Embrittlement of Materials in Energy Technologies*, RP Gangloff, BP Somerday, eds., Woodhead Publishing Ltd., Cambridge, U.K., 2012, vol. 1, pp. 379-417.
21. ML Martin, BP Somerday, RO Ritchie, P Sofronis, IM Robertson. Hydrogen-induced intergranular failure in nickel revisited. *Acta Mater* 2012;60:2739.

#### *Micron-Scale Materials*

22. DH Alsem, R van der Hulst, EA Stach, MT Dugger, JThM de Hosson, RO Ritchie. Wear mechanisms and friction parameters for sliding wear of micron-scale polysilicon sidewalls. *Sens & Actuat A* 2010;163:373.
23. RA Meirum, DH Alsem, AL Romasco, T Clark, R Polcawich, J Pulskamp, M Dubey, RO Ritchie, CL Muhlstein. Fatigue-induced grain coarsening in nanocrystalline platinum films. *Acta Mater* 2011;59:1141.
24. DH Alsem, H Xiang, RO Ritchie, K Komvopoulos. Sidewall adhesion and sliding contact behavior of polycrystalline silicon microdevices operated in high vacuum. *J MEMS* 2012;21:359.

## **Using Artificial Microstructures to Understand Microstructure-Property Relationships in Metallic Glasses**

Jan Schroers, Yale University, Mechanical Engineering and Materials Science  
Department

Materials science seeks to correlate microstructure with (mechanical) properties. This has been successfully shown in some limited cases, however, for most technological relevant materials the microstructures and their fabrication are too complex for a systematic study. Most challenging is the interconnection of microstructural features. For example, when varying the grain size of a microstructure through the cooling rate, essential all other microstructural features including volume fraction, spacing, shape, chemical composition, and dispersity are also affected. “Virtual experiments” through molecular dynamics simulations have been widely used to investigate structure-property relationships but are limited by today’s available computing power, which limits the system size and simulation time. As a consequence, on the length scale required for microstructural investigations mainly continuous modeling is feasible and the complex constitutive equations for plastic deformation limits the modeling to the elastic region.

As a novel approach, in between real microstructures and virtual experiments, we propose to study microstructure-property relationships with artificial microstructures. This approach allows us to individually and independently vary parameters and thereby determine their individual effects on mechanical properties. The artificial microstructures are fabricated through a two-step process; silicon lithography is used to fabricate the mold and thermoplastic forming to replicate the mold into a bulk metallic glass structure. A vast range of shapes comprising of length scales ranging from 10 nm to millimeters can be fabricated. Examples where this approach is useful include toughening mechanism in metallic glasses, transition from plastic deformation to elastic buckling in metallic glass heterostructures, and flaw tolerances of microstructures.

We also characterized metallic glasses on the nanoscale. Here we used a nanoimprint process, which allows us to readily fabricate test samples. Characterization includes tensile and bending testing, crystallization kinetics, and the effect of sample size on viscosity.

DOE DE-FG02-07ER46393, Cornell University  
**Deformed Materials: Towards a Theory of Materials Morphology Dynamics**  
James P. Sethna, sethna@lassp.cornell.edu

Laboratory of Atomic and Solid State Physics, Clark Hall, Cornell University, Ithaca, NY 14853-2501

**Program Scope:** Our group studies materials under external loading using two different approaches. First, we explore the behavior of a minimal continuum model of dislocation dynamics that forms striking cell-wall structures consistent with recent fractal and scaling analyses of experiments. Second, we apply methods of statistical physics to understand brittle fracture and dislocation avalanches.

**Recent Progress:**

*Avalanche Oscillator.* We have been analyzing plasticity avalanche data from Dennis Dimiduk's group for some time, trying to understand why they find rate-dependent critical exponents at very low strain rates. We hypothesized that there was a slow relaxation process competing with the avalanches, and developed several models to incorporate and explore this competition. We discovered that these models exhibited a new mechanism for avalanches – not self-organized criticality, not plain old depinning, but an oscillatory approach to the critical point. Large, rare avalanches throw one far from the critical point, leading to a quasi-periodic series of large avalanches with

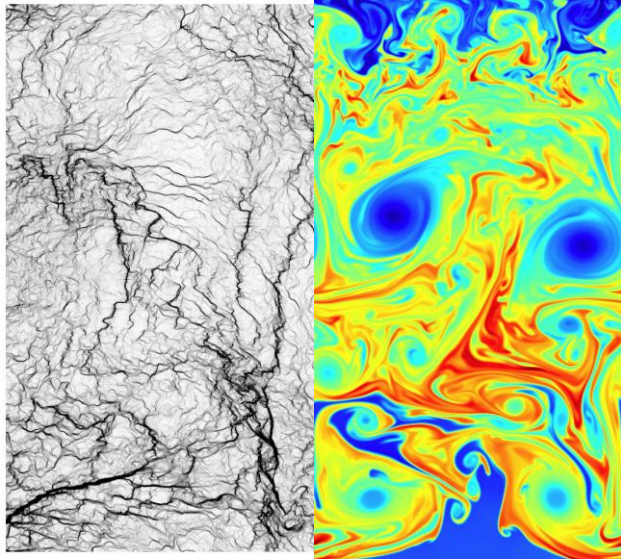


Fig. 2: Dislocation dynamics (left) has strong analogies to turbulence (right).



Fig. 1: Avalanche oscillator behavior deduced from nanopillar experiments

a build-up in between. This behavior is captured in a simple model, in more realistic simulations, is exhibited in Dimiduk's experiments, and appears also to be observed in earthquakes deep under the earth's crust.

*Turbulent Dislocations:* Our invited paper on the analogies between dislocation evolution and fully-developed turbulence, *Is dislocation flow turbulent in deformed crystals?*, was published in a special issue of CiSE (Fig. 1). It addresses in detail the subtle issues of defining good convergence in the continuum limit of theories that form delta shocks and fractals that inevitably extend to the lattice scale.

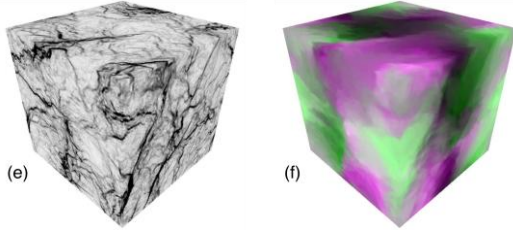


Fig. 3: 3D simulations of dislocation evolution with climb forbidden by vacancy-diffusion backpressure: dislocation density (left) and orientation field (right).

*Three Dimensions:* Our long paper, extending our 2010 PRL, is under review. It gives full descriptions of the motivation and derivations of our equations of motion. It introduces a new model for forbidding climb, by coupling climb to a vacancy field (below) and then making the vacancies expensive; this reproduces a model originally proposed by Acharya (Fig. 2). It introduces true three-dimensional simulations of our model, which continue to show realistic cellular structures and evolution (Fig. 2). The clear distinction

between cell walls (allowing climb) and grain boundaries (forbidding climb) that we reported in our PRL disappeared in three dimensions, where all three models have similar morphologies and correlation functions.

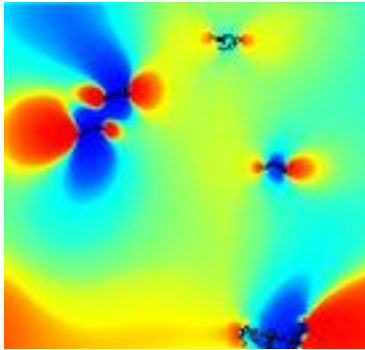


Fig. 4: Fuse network model for fracture

*Fracture and Extreme Value Statistics:* Our fuse-network model for fracture in *Physical Review Letters* (Fig. 5), addresses several key questions for rare event failure estimation. (1) The failure distribution (crucial for practical engineering applications) is not well described by the commonly used universal extreme-value distributions (Weibull, Gumbel, or Fréchet), even for relatively large systems. (2) The distribution does obey the weakest link hypothesis for rather small sizes; the long-range interactions between cracks do not qualitatively change the failure mechanisms. This hypothesis underlies the coarse-graining renormalization-group transformation that underlies extreme value statistics: why doesn't it work? (3) The failure distribution is nicely described by a

disorder-based nucleation theory (originally due to Duxbury). (4) The nucleation theory, for large enough sizes, will eventually converge to the Gumbel distribution – but very slowly. Two sigma into the tails, the convergence reaches 1% accuracy only for samples larger than the observable universe.

*Avalanche Precursors and the Fracture Phase Diagram:* The self-affine fracture surface roughness and fracture precursor events are reminiscent of avalanches at continuous transitions, even though fracture would naively be a prototype of an abrupt transition. We have developed a unified description involving a renormalization-group crossover from a percolation regime to a nucleated one. Only in the finite-size crossover regime are avalanches exhibited – in the infinite-system limit, because the fracture strength disappears, there are no precursor events.

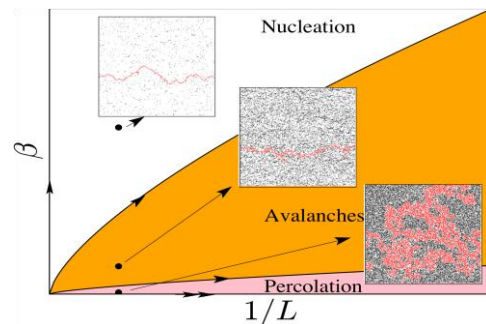


Fig. 5: Fracture phase diagram ( $\beta$  = stress vs. disorder;  $L$  = system size)

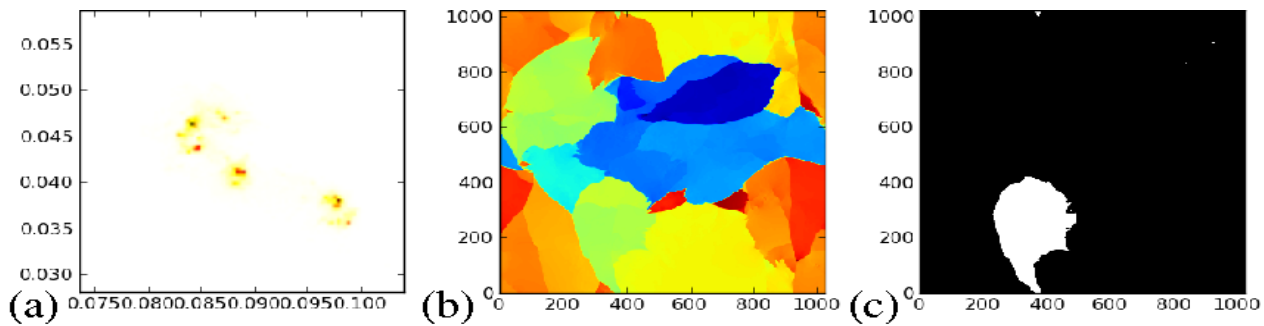


Fig. 6: Incoherent X-ray peaks and their corresponding real-space sources.

### Future Plans:

**X-ray diffraction.** We are exploring the predictions of our model for X-ray diffraction experiments. Our model was inspired by recent experiments which extract real-space morphologies, but we can use our real-space simulation to generate predictions from scattering experiments as well. On the right, we show incoherent X-ray scattering, simulating the experimental geometry of a recent

Science paper by Jakobsen et al. We show that the splitting they see in their X-ray peak, even though the latter comes from a single grain, does not reflect the splitting of a dislocation cell (at least in our simulation); indeed, the regions of a grain that scatter into the region of the peak vary with deformation and form multiply-connected regions in real space. Our work on coherent X-ray diffraction – which leads both to Bragg sidebands and also to small-angle X-ray scattering – is in its initial stages.

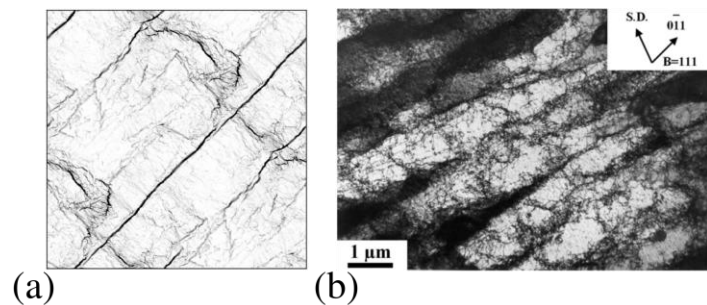


Fig. 7: Cellular structures, anisotropic loading, theory versus experiment (Gracio's group).

**Response to Loading:** We are exploring the morphological evolution under tensile and cold-rolling geometries (Figure 7), and will shortly be studying Bauschinger effects, Mughrabi's two-component composite model for plastic deformation, and cyclic loading.

**Vacancies, Solute, and Dirt.** We have implemented a coupling between dislocation climb and vacancy diffusion in our simulations – climb acting as sources and sinks for vacancies. Vacancy diffusion is often neglected in systems undergoing climb, even though the climb rate must depend roughly inversely on the distance to the nearest sink (at least for diffusion-limited dynamics). We are planning more generally to couple our dislocation dynamics to scalar fields, to represent both static disorder (inducing avalanches and metastability) and diffusing disorder (to study the PLC effect).

**Delta-Shocks & Slip System Theories.** Mathematically and numerically our continuum dislocation equations are pushing new ground – they form  $\delta$ -shocks, which are far less studied or understood than the standard step-like Riemann shocks that arise in hydrodynamics and traffic. Here these  $\delta$ -

shocks are physically representing grain boundaries and cell walls – clearly of physical interest even if dangerous mathematically. We are exploring why previous theories (Park and Arsenlis, Koslowski and LeSar) did not generate these  $\delta$ -shocks, and are studying the mathematical origin of  $\delta$ -shocks by modifying these more traditional theories to include entrainment between different slip systems.

### **Key BES-Supported Publications, 2010-2012:**

*Quasi-periodic events in crystal plasticity and the self-organized avalanche oscillator*, S. Papanikolaou, D. M. Dimiduk, W. Choi, J. P. Sethna, M. D. Uchic, C. F. Woodward, and S. Zapperi, *Nature* **490**, 517-521 (2012).

*Fracture strength of disordered media: Universality, interactions and tail asymptotics*, Claudio Manzato, Ashivni Shekhawat, Phani K. V. V. Nukala, Mikko J. Alava, James P. Sethna, and Stefano Zapperi, *Phys. Rev. Lett.* **108**, 065504 (2012),

*Avalanche Spatial Structure and Multivariable Scaling Functions; Sizes, Heights, Widths, and Views through Windows*, Yan-Jiun Chen, Stefanos Papanikolaou, James P. Sethna, Stefano Zapperi, and Gianfranco Durin, *Phys. Rev. E* **84**, 061103 (2011). (*Selected for PRE Kaleidoscope*)

*Scaling theory of continuum dislocation dynamics: Self-organized critical pattern formation*, Yong S. Chen, Woosong Choi, Stefanos Papanikolaou, and James P. Sethna, (*submitted*).

*Is dislocation flow turbulent in deformed crystals?*, Woosong Choi, Yong S. Chen, Stefanos Papanikolaou, and James P. Sethna, *Computing in Science and Engineering* **14**, 33 (2012).

*Theory of dielectric breakdown and avalanches at the non-equilibrium Mott transition*, Ashivni Shekhawat, Stefanos Papanikolaou, Stefano Zapperi, and James P. Sethna, *Phys. Rev. Lett.* **107**, 276401 (2011).

*Universality beyond power laws and the average avalanche shape*, Stefanos Papanikolaou, Felipe Bohn, Rubem L. Sommer, Gianfranco Durin, Stefano Zapperi, and James P. Sethna *Nature Physics* **7** 316-320 (2011).

*Minimal model of plasma membrane heterogeneity requires coupling cortical actin to Ising criticality*, Benjamin B. Machta, Stefanos Papanikolaou, James P. Sethna, and Sarah L. Veatch, *Biophysical Journal* **100**, 1668-1677 (2011).

*Bending crystals: the evolution of grain boundaries and fractal dislocation structures*, Yong S. Chen, Woosong Choi, Stefanos Papanikolaou, and James P. Sethna, *Phys. Rev. Lett.* **105**, 105501 (2010)

Project title: **Radiation Responses of Low Dimensional Carbon Systems**  
PI: Lin Shao  
Texas A&M University  
335R Zachry Engineering Center, College Station, TX 77845  
lshao@tamu.edu

## **Program Scope**

The project is aimed to fundamentally understand the geometry and quantum size effects on damage creation and defect clustering of ion irradiated, low-dimensional carbon systems including graphene, carbon nanotubes (CNT), carbon buckypaper, sintered carbon nanotubes which make a 300  $\mu\text{m}$  thick sheet, and their bulk counterparts. Furthermore, the project will study irradiation-induced electrical, thermal and mechanical property changes. The project integrates experiments and atomic scale modeling, in order to develop predictive multiscale modeling capabilities over time and length scales linkable to experiments.

## **Recent Progress**

Research highlights of the first two years include (a) development of a model to explain Raman signal changes upon ion irradiation, which is utilized to quantify defects in carbon nanotubes; (b) understanding amorphization mechanism of carbon nanotubes and revealing the amorphization resistance shifting at different irradiation temperatures; (c) obtaining fundamental understanding of phonon transport in ion irradiated carbon buckypapers. Both experiments and molecular dynamics simulations have shown that C displacements between tubes can dramatically enhance phonon transport.

## **Quantitative Defect Characterization**

Raman analysis has been widely used to compare defect concentrations of carbon systems, but the extracted information on defects has been qualitative instead of quantitative. The Raman spectra of carbon systems have several distinct modes, most notably the D mode (at  $\sim 1340\text{ cm}^{-1}$ ), G mode (at  $\sim 1580\text{ cm}^{-1}$ ) and the radial breathing mode ( $50\text{-}500\text{ cm}^{-1}$ ). General consensus states that D mode is related to defects including pentagon-heptagon pairs, kinks, vacancies, impurities and tube ends. Our recent study has shown that D/G intensities first increase, then decrease with ion fluence. Based on careful comparisons with transmission electron micrographs, we developed the following model [1]: with increasing defect numbers, the D intensity increases due to T-K relationship [62]. However, D intensity begins to drop at higher defect concentrations when the average distance between defects becomes comparable to the size of six-fold ring. By applying this model, Raman analysis can obtain average linear density of defects along tubes. Figure 1 compares our model fitting with experimental D/G intensities. The maximum D/G intensity ratio corresponds to defect number high enough to cause structural amorphization, which agrees with TEM characterization.

The study shows that T-K relation is still valid for nanometer-scale crystalline structures in CNTs. The study leads to a quantitative analysis method which is able to extract number of defects created in ion irradiated carbon nanotubes. The study further reveals the cause of D intensity changes and the appearance of its maximum intensity.

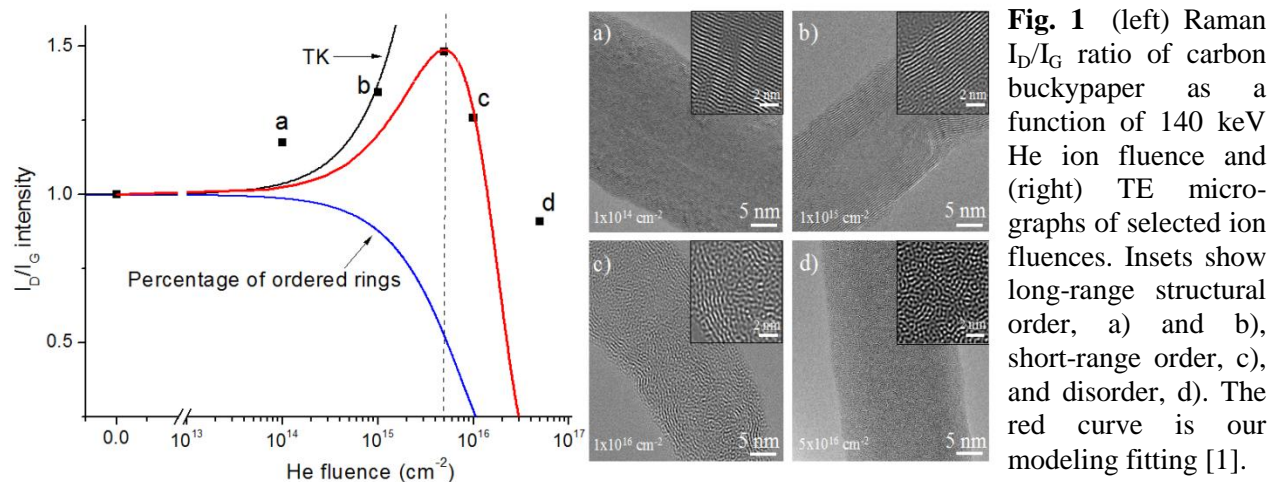


**Fig. 1** (left) Raman  $I_D/I_G$  ratio of carbon buckypaper as a function of 140 keV He ion fluence and (right) TE micrographs of selected ion fluences. Insets show long-range structural order, a) and b), short-range order, c), and disorder, d). The red curve is our modeling fitting [1].

### The temperature dependence of amorphization in CNTs

Following our findings that the appearance of maximum D/G intensity corresponds to CNT amorphization, we studied the D/G intensity changes as a function of ion fluence and ion irradiation temperature [2]. Therefore, the required ion fluence to reach amorphization, as a function of irradiation temperature, can be experimentally determined. As shown in Figure 2, when ion irradiation temperature is increased to 400 °C, the required fluence for amorphization is shifted to a higher value. This agrees with the previous observations that point defects become mobile and dynamic defect annealing becomes significant at temperatures above 350 °C, leading to a higher threshold fluence for amorphization.

### Phonon transport assisted by inter-tube carbon displacements in carbon buckypapers

Though a single carbon nanotube (CNT) possesses superior thermal conductivity, a carbon buckypaper made of randomly networked carbon nanotubes has much lower thermal conductivity due to difficulty of phonon transport from one tube to another. We found that ion bombardment can introduce inter-tube carbon displacements as stable point contacts to assist phonon transport [3,4]. The ion irradiation simultaneously introduces defects within the tube, thus the thermal conductivity of a buckypaper is determined by competing effects: inter-tube-displacement-mediated phonon transport and intra-tube-defect-caused phonon scattering. The competition leads to first increasing, then decreasing thermal conductivity as a function of ion fluences, with a peak enhancement of 540% observed. These competing effects are confirmed by our molecule dynamics simulations [4].

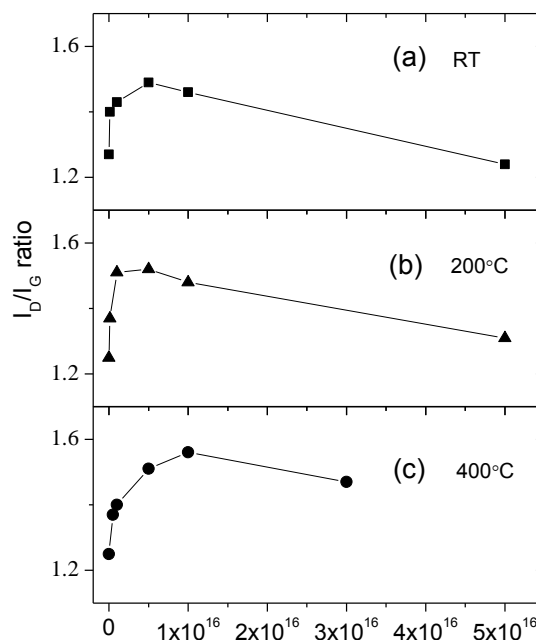


Figure 2.  $I_D/I_G$  ratio as a function of increasing ion fluence for irradiations at a) room temperature, b) 200°C, and c) 400°C [2].

Figure 3 plots experimentally obtained thermal conductivity ( $\lambda$ ) changes as a function of hydrogen ion fluence, through normalization by their corresponding nuclear stopping powers. For all three ion energies, thermal conductivities first increase and then decrease with fluence.

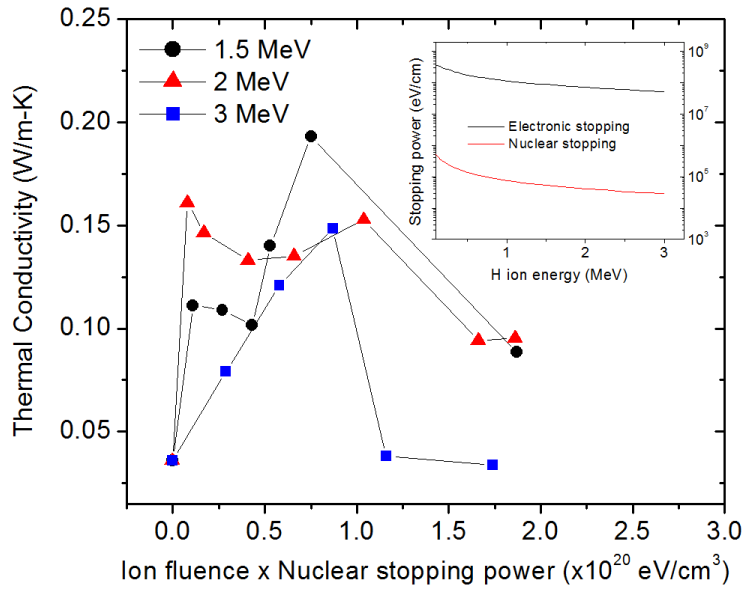


Figure 3. Thermal conductivities of buckypapers, measured at 300 K, plotted as a function of ion fluence multiplied by nuclear stopping power. The insert shows the energy dependence of electronic and nuclear stopping powers [4].

Molecular dynamics (MD) simulation code LAMMPS is used to understand what governs thermal property changes at the atomic scale [4]. The modeling includes two steps: irradiation and thermal properties determination. Radiation damage is simulated using 500 eV C ion bombardment of adjacent nanotubes and then the Müller-Plathe method is utilized to calculate thermal conductivities. Figure 4 shows evolution of calculated thermal conductivities with increasing number of bombarding ions. In an isolated CNT increasing radiation damage decreases thermal conductivity, while in two adjacent CNTs thermal conductivities first increase and then decrease at high damage levels. At low ion fluences inter-tube displacements efficiently promote tube-to-tube phonon transport between adjacent nanotubes, compensate for and exceed phonon scattering by defects, and consequently increase conductivity.

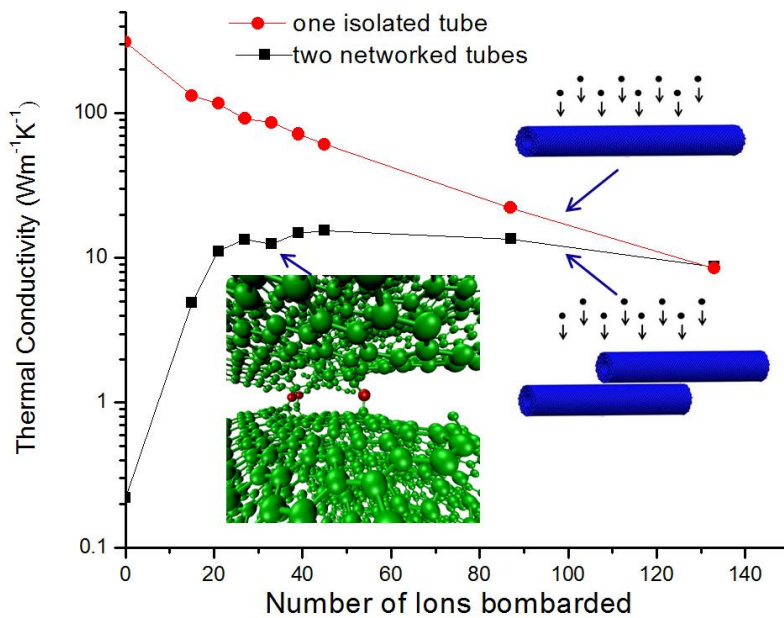


Figure 4. Calculated thermal conductivities of an individual nanotube and two adjacent MWNTs as a function of increasing number of bombarding ions [4].

### Short list of planned activities

- Start ion irradiation induced structural, electrical and thermal property changes of a single CNT tube.
- Use in situ ion irradiation and transmission electron microscopy to visualize dynamic structural changes under ion beam irradiation and compare with modeling predictions.
- Characterize CNT yarns treated by ion beams of different ion fluence and flux, and identify conditions in order to achieve two substantial structural changes: tube linking vs. tube welding. Yarns are created by continuous pulling from self-aligned nanotube arrays, and are immediately exposed to an ion beam in air.
- Study temperature dependence of yarns' electrical properties and identify the dominant electron conduction path from two possible mechanisms: hopping vs. tunneling;
- Measure mechanical property changes and understand the mechanisms of load transfers and inter-tube sliding influenced by inter-tube linking/welding;

### A list of journal publications resulting from this grant

1. Assel Aitkaliyeva, M. Martin, T.A. Harriman, D.S. Hildebrand, D.A. Lucca, M.C. McCarthy, H-K Jeong, and Lin Shao, "Raman spectroscopic responses of ion irradiated carbon nanotubes", **Phys. Rev. Lett.**, submitted and under revision.
2. Assel Aitkaliyeva and Lin Shao, "The production of amorphous regions in carbon nanotubes by 140 keV He ion irradiation", **Carbon**, 50, 4680(2012).
3. Assel Aitkaliyeva and Lin Shao, "The change of microstructure and thermal properties in ion irradiated carbon nanotube mats as a function of ion penetration depth", **Appl. Phys. Lett.** 102, 063109 (2013).
4. Aitkaliyeva, D. Chen, S. McDeavitt, L. Shao, "Phonon transport assisted by inter-tube carbon displacements in in carbon nanotube mats", **Scientific Reports**, in press

# Understanding and Controlling Toughening Mechanisms in Nanotube Reinforced Ceramic Coatings

**Brian W. Sheldon and William A. Curtin,  
School of Engineering, Brown University, Providence, RI  
Brian\_Sheldon@brown.edu**

## Program Scope

The performance of many ceramic coatings is limited by low fracture toughness. Nanoreinforcements in these materials can provide substantial toughness improvements, based in part on research at Brown University which provided the first direct evidence that ceramics can be toughened with multiwalled carbon nanotubes (MWNTs). The research in the current program focuses primarily on developing fundamental understanding of toughening mechanisms. These investigations consist of well-integrated experimental and theoretical / computational efforts. The experiments are probing ceramic coatings reinforced with nanotubes, to obtain detailed information on the relationships between materials characteristics and mechanical behavior (primarily toughness). Most of this work is being conducted with silicon nitride matrices produced by chemical vapor infiltration, where the MWNT reinforced coatings exhibit excellent mechanical properties. Electron microscopy and detailed mechanical testing of these materials provides critical information about their structure and performance. The modeling efforts are closely coupled with the experiments to gain understanding of deformation and interfacial sliding on the nanoscale. Atomistic modeling of realistic composite unit cells using chemically reliable input is being used to understand deformation mechanisms and to quantify the dependence of toughness on reinforcement dimensions (diameter, wall thickness, interface roughness) and structure (graphene ordering, density). Modeling at the mesoscale, guided by the findings of the nanoscale studies, has created parametric models for interpreting mechanical testing data.

## Recent Progress

The experimental work over the past year has focused on controlling key attributes of the carbon nanotube (CNT) reinforced ceramic coatings that are the focus of this program. All of these efforts are designed to give us the ability to conduct systematic investigations of the fundamental mechanisms that are associated with improved mechanical properties in these materials. Specific advances that have been achieved can be summarized as follows:

- *Fabrication of composites with higher CNT densities:* Our initial success with CNT reinforced silicon nitride materials was based on materials with CNT volume fractions of approximately 10%. The synthesis of materials with higher densities has proved to be a significant challenge, however, composites with a range of CNT densities have now been produced (without simultaneously altering other properties). This was achieved by using a variety of bilayer catalyst combinations and pretreatment conditions. We have also employed a novel pulsed growth technique, in collaboration with Drs. Gyula Eres and Dave Geohegan (both at Oak Ridge National Laboratory).
- *Systematic control of graphene ordering:* This effort is largely designed to test our model predictions, which indicate that interwall coupling in multiwall nanotubes will have a substantial impact on load transfer and toughening in nanocomposites. While graphene ordering can vary by changing CNT synthesis conditions, this invariably alters other attributes of the nanotubes. To avoid this difficulty, we have instead focused on annealing at very high temperatures, where the primary change in the CNTs is graphene ordering. This approach has been successful (up to 1800 C so far,

with higher temperature possible). The mechanical properties of these materials are currently being investigated.

- *Surface functionalization studies with polymer-derived ceramic matrices:* The relationship between the atomic structure of the CNT – matrix interface and the mechanical response of these composites is an open question. For example, the predicted importance of interwall defects suggests that bonding between the outer wall of the CNT's and the matrix might be a secondary consideration. While a wide range of surface functionalization strategies can be employed with CNTs, many and perhaps most of these alterations are unlikely to survive the vapor phase infiltration processing methods that we have used to synthesize most of our materials to date (for example, organic functional groups are likely to volatilize or decompose and leave only a carbon residue). Thus, for surface functionalization studies we have developed an alternative matrix fabrication approach with polymer-derived ceramics. An initial nanoindentation study with these materials shows that  $\text{CF}_4$  plasma treatments have a noticeable impact on the mechanical response.

In the current simulation work, we are analyzing the “matrix crack deflection” problem at the nanoscale. As a matrix crack approaches a fiber, the crack can either deflect along the interface (leading to toughening by other mechanisms) or penetrate into the fiber (leading to brittle behavior), depending on the relative toughness and strength of the interface and fiber, respectively. Classic work by He and Hutchinson using a continuum model has long been quoted, but its relevance at the nanoscale, and for CNTs that are only a few atom layers in thickness, has not been probed directly. Our goal here is thus to use direct atomistic models to probe this fracture process, with systematic control of the degree of interfacial bonding and sliding.

Specifically, we simulate an annular crack propagating through a diamond matrix and impinging on the interface with single-wall and double-wall defect-free nanotubes. We investigate crack impingement under quasi-static force or displacement applied to the composite, Figure 1, as a function of

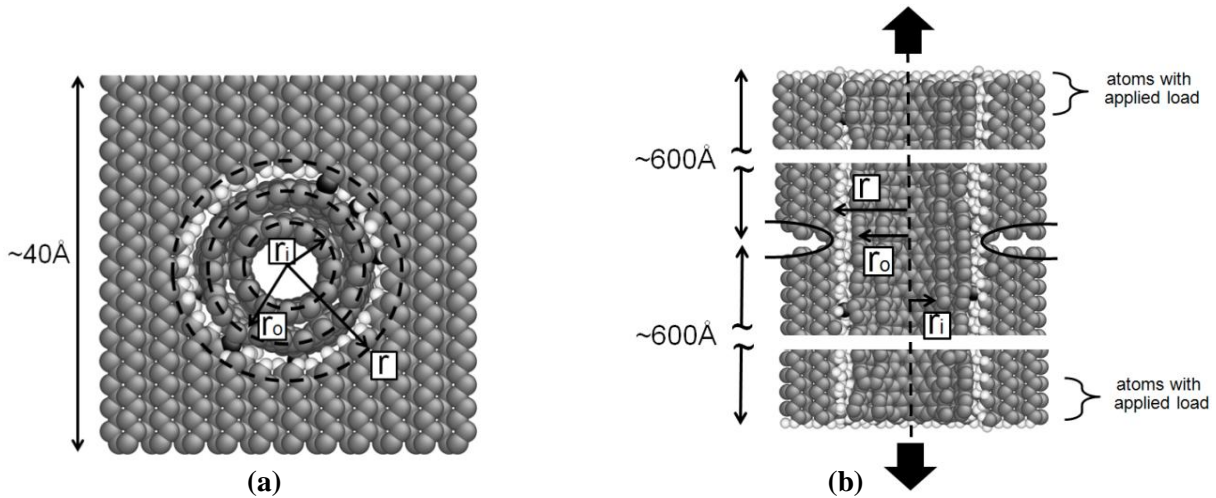


**Figure 1.** (a) Top view and (b) side view of an atomistic model of a nanocomposite unit cell composed of a diamond matrix with a hole of radius  $r = 11.22 \text{ \AA}$ , a DWNT of inner and outer shells of radii  $r_i = 4.71 \text{ \AA}$  and  $r_o = 8.22 \text{ \AA}$  at  $f = 3\%$  interwall  $sp^3$  bonding, and interstitial carbon atoms at the interface bonding matrix and nanotube. Carbon atoms in the matrix and nanotube are gray, random interstitial carbon atoms in the interface are black, and hydrogen atoms are white. In (b) an annular crack is inserted by removing the carbon atoms at the center of the matrix. During loading in direction of the tube axis, increments of displacement or force are applied to the carbon atoms at the boundary of the composite cell, subfigure (b).

the degree of interfacial bonding captured through interstitial carbon atoms located in the interface and forming bonds with both matrix and nanotube. The modeling at this level must be done very carefully. If the initial crack in the matrix is too large, then the stress exerted on the CNT after the crack grows (which will equal the entire applied force divided only by the cross-sectional area of the CNT) will exceed the strength of the CNT and it will fail immediately independent of interfacial considerations. If the matrix crack is too small, then a very large stress must be applied to make it propagate, and again the CNT can be overloaded. Thus, the molecular simulation must be tuned to achieve conditions under which a meaningful matrix crack does grow but while probing the response of the interface. The dimensions of the simulation cell used in Figure 1 satisfy these conditions.

The density of interstitial carbon atoms between the matrix and the CNT controls the interface strength, as we have demonstrated in our previous work. Here, we consider interstitial areal densities  $\rho$  with a range of  $0.13 \div 1.5 \text{ nm}^{-2}$ , so to control the strength of the interface between 800 MPa and 9 GPa and with the interface debond energy scaling similarly between 0.03 and  $0.34 \text{ J/m}^2$ . Note that the typical fracture toughness of a CNT is considerable higher, close to  $8 \text{ J/m}^2$ . Even for the strongest interface, the incident cracks do not penetrate into the nanotube immediately after crack propagation but do induce shear distortions in the interstitial/matrix or interstitial/CNT bonds.

The carbon atoms at the interface bond matrix and nanotube loosely with a typical bond energy per interstitial between  $1.1 \div 1.3 \text{ eV}$ , lower than the bond energy between two carbon atoms of a DWCNTs with 3%  $sp^3$  interwall coupling, close to  $4.2 \text{ eV}$ . However, at high values of interface strength, for densities  $\rho > 0.53 \text{ nm}^{-2}$ , the nanotubes fail before debonding and do not dissipate frictional energy by sliding against the matrix. In this regime, the resulting nanocomposite would be characterized by low fracture toughness and would behave essentially like a brittle ceramic. Moreover, in the absence of pre-existing CNT defects in the outer nanotube walls, the fracture of the tube always starts from a critical “crack-like” defect nucleated near the matrix crack faces, where the outer wall is mostly strained. In fact, when the bonds between the nanotube carbon atoms are highly stretched, the bonds with the interstitial carbon atoms become the nucleation sites for fracture by locally tearing open the outer CNT shell and driving the tube to premature fracture, as shown in Figure 2. DWCNTs with interwall coupling are relatively insensitive to the presence of “crack-like” defects nucleated on the external shell near the bonds with the interstitials: the  $sp^3$  interwall bonds restrain the propagation of the defects until the nanotube is stretched by an axial stress almost equal to the non-defective tube strength. However, the SWCNTs fail at approximately a 20% lower strength. Since DWCNTs with interwall bonds fail at the non-defective strength also at elevated densities of interstitials, we believe that in realistic MWCNT-reinforced composites the properties of the interface, such as frictional sliding and toughness, and the nanotube strength can be independently designed and optimized by adjusting the parameters of the fabrication process and by carefully controlling the density of carbon atoms between matrix and nanotube.

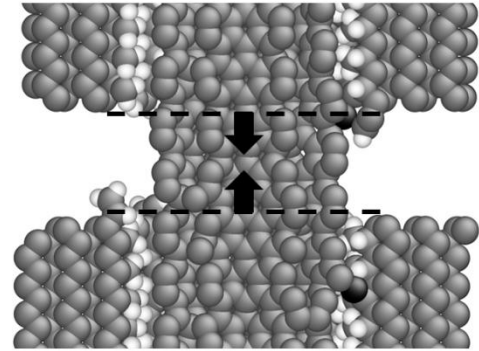


**Figure 2.** After crack propagation, while the nanotube is stretched between the opening crack surfaces, the bonds with the interstitial atoms are distorted by shear deformations. At high values of interface strength the nanotube fail before breaking bonds with the interstitials, without debonding from the diamond matrix.

## Future Plans

The experimental work for the coming year will focus on several different investigations. A major new focus is the use mechanical testing methods that make use of in situ microscopy and focused ion beam milling to create precise micro-specimens. The work on density effects will continue with

additional efforts to control and understand processing, along with mechanical testing of the resulting composites with nanoindentation. We will also initiate more detailed studies of the impact of two additional variations in the CNT structures: the effects of graphene ordering and the effects of CNT “waviness”. The first will be controlled with high-temperature annealing on SiC substrates, as outlined in the original proposal. Control of the CNT waviness will be an exploratory effort, but based on recent computational results we believe that this is a potentially important factor in the mechanical behavior of these nanocomposite materials. The basic idea here is that processing conditions can be used to vary the CNT waviness. These process variations are also likely to vary internal defect structures, thus it will be necessary to deconvolute these effects. We hope to distinguish these effects with careful Raman spectroscopy.

In the computational work for the coming year, we will further pursue atomistic modeling of matrix crack/nanotube/interface interactions. We will vary the interface bonding to establish upper limit values for this behavior, and we will vary the internal interwall coupling using interwall interstitials to establish conditions for obtaining debonding within the nanotubes. We will also work on developing complex atomistic CNT structures with roughness and/or defects. At the continuum scale, we will complete work on the interplay of fiber roughness and interfacial friction as a function of nanotube constitutive and geometric properties (tube thickness/number of graphene layers, interface friction, roughness amplitude and wavelength). We will try to quantitatively relate continuum and atomic scale models.

### **2012 / 2013 Publications**

A.K. Kothari, S. Hu, Z. Xia, B.W. Sheldon, E. Konca, "Enhanced fracture toughness in carbon nanotube reinforced amorphous silicon nitride nanocomposite coatings", *Acta Mater.* **66**, 3333-3339 (2012).

A.K. Kothari, B.W. Sheldon, G.Eres, “Thickness limitations in carbon nanotube reinforced silicon nitride coatings synthesized by vapor infiltration”, *Acta Mater* **60**, 7104-7111 (2012).

F. Pavia, W.A. Curtin, “Modeling crack impingement in nanoceramic composites”, submitted to *Compos. Sci Technol* (2012).

A.J. Kessman, J. Zhang, S. Vasudevan, J. Lou, and B.W. Sheldon, “Carbon Nanotube Pullout and Toughening in Ceramic Nanocomposites”, submitted to *Acta Mater* (2012).

S. Vasudevan, J. Rankin, B.W. Sheldon, “Synthesis and properties of carbon nanotube – nanocrystalline diamond matrix composites”, submitted to *Carbon* (2013).

# Dynamic Fracture in Dealloying Induced Stress Corrosion Cracking

Karl Sieradzki

*Fulton School of Engineering*

*Arizona State University, Tempe AZ 85287-6106*

*email: Karl.Sieradzki@asu.edu*

**Program Scope:** This research program initiated in August 2012 examines the role of unstable dynamic fracture in dealloying induced stress-corrosion cracking (DISCC) of single-phase face-centered cubic alloys. Corrosion of these alloys often results in the formation of a brittle nanoporous layer [1] which we hypothesize serves to nucleate a crack that owing to dynamic effects penetrates into the un-dealloyed parent phase alloy. Thus, since there is essentially a purely mechanical component of cracking, stress corrosion crack propagation rates can be significantly larger than that predicted from electrochemical parameters.

Central to the problem of DISCC are the dynamic fracture properties of these dealloyed nanoporous morphologies. Conveniently, nanoporous gold (NPG) serves as an excellent model system for studying the fundamental aspects of this since there has been a considerable worldwide effort in the past 10 years aimed at elucidating the mechanical and electrochemical properties of this material [for example, 2-4].

These dealloyed structures can be characterized by an average ligament and pore diameter that typically have similar dimensions. We refer to this dimension as the *length scale* of the dealloyed structure. At small enough length scale these nanoporous morphologies are extremely brittle. Twenty-five years ago we hypothesized that under tensile loading such dealloyed layers undergo brittle fracture and inject a crack into the underlying un-dealloyed parent phase alloy [5]. Two aspects of this so-called film induced “cleavage” process are the focus of this research program: (1) Can monolithic NPG support dynamic fracture and if so how does this depend on the NPG length scale and electrochemical conditions relevant to stress corrosion and (2) Can such dynamic fracture in a NPG layer of finite thickness inject a crack into the un-dealloyed parent-phase?

There are two major types of experiments being performed. One series of experiments is centered on dynamic fracture in monolithic NPG as a function of length scale and electrochemical condition. A number of these experiments are also performed on dried samples in laboratory air. Owing to ambient temperature coarsening the smallest length scale that we can examine for Ag-Au alloys in the air experiments is of order 20 nm. However, we’ve learned that the addition of a few percent of Pt into these alloys quenches surface diffusion allowing for the maintenance of ~5 nm length scales and we will employ this strategy at these smaller length scales [6]. For monolithic NPG samples maintained in electrolyte at a potential of 1.4 V (NHE) the NPG is covered with a monolayer of oxide that quenches surface diffusion coarsening and under this condition we will examine dynamic fracture at ligament length scales of 5-10 nm. We anticipate that this length scale will yield the highest crack velocity, as owing to the intrinsic size effect, plasticity will be most effectively suppressed. Post mortem fractography is performed on samples from this series of experiments.

The other set of experiments referred to as crack injection [for example, 7]. In these experiments a polycrystalline sample is dealloyed under a zero stress condition in order to form a dealloyed layer of prescribed thickness and then while the dealloying potential is maintained the sample is rapidly loaded causing intergranular fracture. The idea behind rapid loading is two-fold: first to eliminate (or minimize) conventional stress-corrosion and second to prevent any significant ligament coarsening that may occur in the NPG layer prior to application of the mechanical load. All the variants of this general scheme involve inserting a step or steps between dealloying and load application in order to eliminate the possibility of SCC occurring during load application. For example, the voltage is changed to a value for which no faradaic reaction is possible and the sample is held at this condition for a prescribed period of time (of order seconds to minutes) prior to load application. Other variants involve removing the sample from the electrolyte and placing it in DI water or just rinsing in DI water and holding the sample in air. All of these variants necessarily result in the coarsening of the NPG layer and so must hinder crack injection to various degrees. Post mortem fractography, FIB sectioning and compositional analysis is performed on this sample set to determine crack injection distances and grain boundary compositions. Additionally, FIB milling and lift out techniques are used to fabricate electron transparent cross-section membranes containing injected grain boundary cracks for subsequent analysis using aberration corrected scanning TEM (STEM).

**Recent Progress:** In the past 7 months we have been examining dynamic fracture in monolithic NPG in air and under potential control in 1.0 M HClO<sub>4</sub>. Fully annealed single edge-notched (SEN) samples (4 mm in width, 12 mm in length, and 125 μm thick) with an EDM cut notch (30 μm wide and 800 μm in length) originally containing 74 at% Ag were dealloyed using a “crack-free” recipe [8,9] for obtaining monolithic NPG. A Phantom V12 high-speed camera fitted to an optical microscope monitored the crack length as samples were loaded quasi-statically in tension under displacement control in a micrometer-controlled fixture. This fixture contains a specially designed electrochemical cell allowing for a three-electrode (reference, counter and working) configuration. The SEN sample (face-up showing the notch) is positioned directly on top of this cell allowing for the bottom portion of the sample thickness to be “immersed” in the electrolyte as the remainder of the sample was imbibed with electrolyte. Capacitance measurements were used to validate that the entire sample was exposed to electrolyte. In this manner tests were performed over a range of voltages (0.5 – 1.4 V NHE). **Figure 1 a-p**, shows the results of one such test performed at 0.5 V (NHE).

There are two primary sources of error in these tests. One is related to the “crack-free” NPG sample. These samples are delicate and we have found that even the most careful handling of these samples as they are prepared for mechanical testing can result in cracks that will reduce the effective elastic modulus of the sample and the corresponding crack velocities that we measure. The second source of error relates to the crack length measurement during fracture under electrochemical conditions. Since the samples are imbibed the top surface of the sample viewed under the microscope sometimes contains enough electrolyte droplets as to reduce the resolution of our measurement. The digital image is pixelated and as the frame speed is increased the number of pixels in an image is reduced. For the 4.34 μs per frame capture rate employed for the test results shown in Figure 1 each pixel corresponds to 20 μm which places an upper limit on the crack length

resolution at this frame rate. We were able to achieve this resolution limit for tests conducted in air and for some of the electrochemical tests, but in some testing the crack length resolution was only  $80\ \mu\text{m}$ . This yields to errors in the crack velocity ranging from  $\sim \pm 4$  to  $\pm 20\ \text{ms}^{-1}$ .

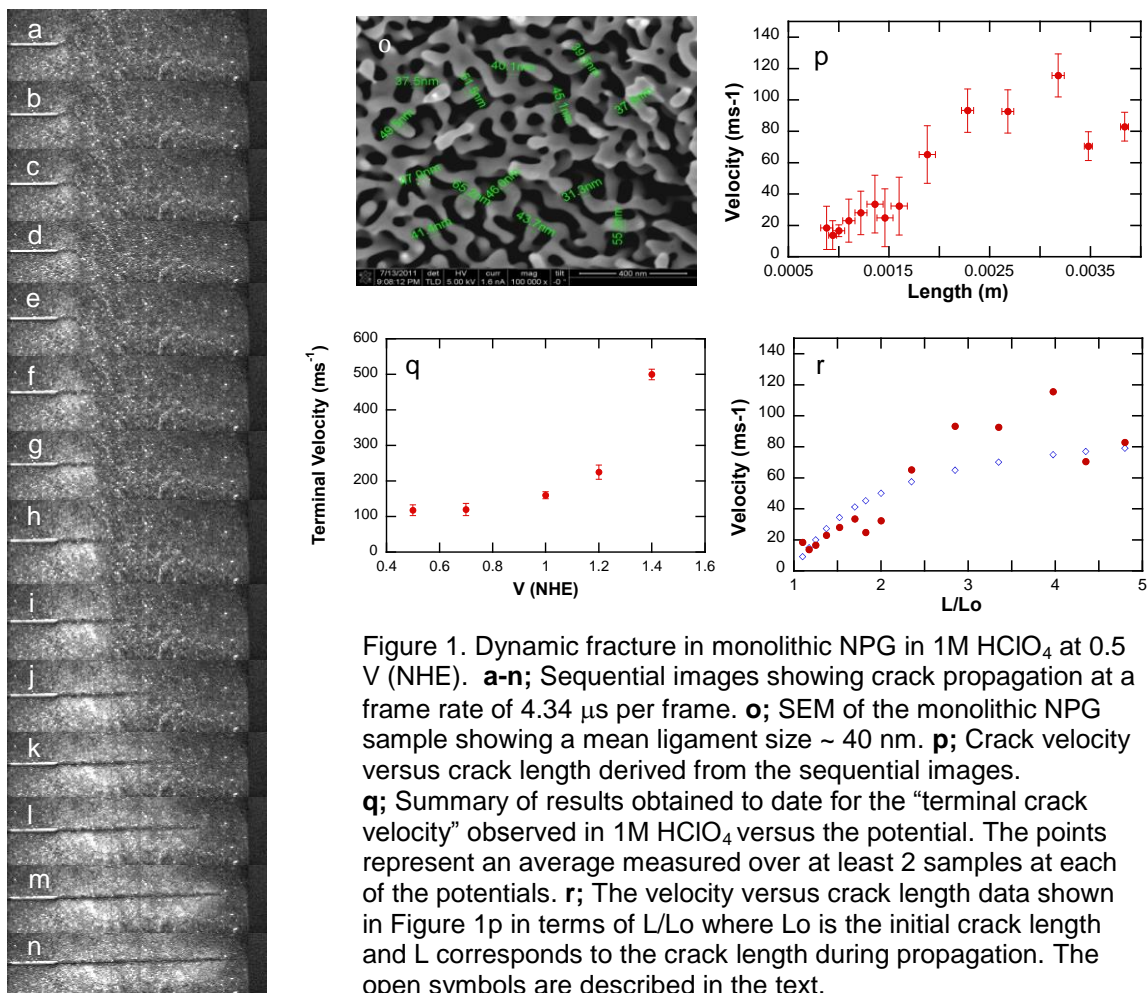


Figure 1. Dynamic fracture in monolithic NPG in 1M HClO<sub>4</sub> at 0.5 V (NHE). **a-n**; Sequential images showing crack propagation at a frame rate of 4.34  $\mu\text{s}$  per frame. **o**; SEM of the monolithic NPG sample showing a mean ligament size  $\sim 40\ \text{nm}$ . **p**; Crack velocity versus crack length derived from the sequential images. **q**; Summary of results obtained to date for the “terminal crack velocity” observed in 1M HClO<sub>4</sub> versus the potential. The points represent an average measured over at least 2 samples at each of the potentials. **r**; The velocity versus crack length data shown in Figure 1p in terms of  $L/L_0$  where  $L_0$  is the initial crack length and  $L$  corresponds to the crack length during propagation. The open symbols are described in the text.

**Figure 1q** is a summary of results obtained to date for the observed terminal crack velocities in  $\sim 40\ \text{nm}$  length scale NPG as a function of electrochemical potential. For the tests run at 1.4V only 2-3 images at the  $4.34\ \mu\text{s}$  frame rate could be obtained. The NPG ligaments on these samples were covered with 1 ML of gold oxide and were quite brittle and difficult to handle. To date we performed 5 separate experiments at 1.4V and 3 out of 5 gave us crack velocities that were only in the  $100\text{-}150\ \text{ms}^{-1}$  range. We only used the results from the other 2 experiments to arrive at the average of velocity  $\sim 500\ \text{ms}^{-1}$  plotted in this figure. Our reasoning for this is simply that experiments yielding the highest velocity were likely performed on samples containing the least number of defects as a result of sample handling. However, these results should be considered as preliminary as there are more tests underway.

**Figure 1r**, shows the data of Figure 1p in terms of the crack velocity versus the parameter  $L/L_0$ , where  $L$  is the crack length during propagation and  $L_0$  is the initial crack length. Most theories of dynamic fracture including both the original Mott theory as well as that of Freund result in the following prediction for the crack velocity-crack length relationship for an elastic solid;  $v = v_T \left(1 - L_0 / L\right)$ , where  $v_T$  is the crack tip terminal velocity taken as the Raleigh velocity. There have been several measurements of the Young's modulus of 40 nm length-scale NPG similar to that used in the experiments discussed above and a reasonable value is of order 10 GPa [3,4]. Taking a density equal to about 0.25 that of solid gold we estimate a longitudinal sound velocity,  $v_L$ , of about 1400 m/s for 40 nm length-scale NPG and a corresponding Raleigh velocity,  $v_R$  (equal to about 0.6  $v_L$ ) of 800 m/s. The terminal velocities that we measured are well below this number owing to plasticity. Nevertheless, in Figure 1r we compare our result with the theoretical prediction adjusting  $v_T$  to that measured in the experiment ( $100 \text{ ms}^{-1}$ ). The solid red points (error bars have been deleted for clarity) are the experimental results and the open blue symbols correspond to that predicted from the theoretical equation.

**Future work:** Over the next year, we will continue to examine dynamic fracture in 5-20 nm length-scale monolithic NPG as a function of electrochemical potential. Additionally we will start to perform crack injection experiments on polycrystalline Ag-Au samples. Prior to the end of this calendar year, we hope to have our first set of results for the composition analysis of grain boundary injected cracks using aberration-corrected STEM.

**Publications:** There are no publications to date resulting from this work.

## References

1. Li R. and Sieradzki K., 1992; "Ductile-brittle transition in random porous Au", *Phys. Rev. Lett.*, **68**, pp. 1168-1171.
2. Lee D., Wei X., Chen X., Zhao M., Jun S-C., Hone J., Herbert E.G., Oliver W.C., Kysar J.W., 2007; "Microfabrication and mechanical properties of nanoporous gold at the nanoscale", *Scripta Mat.*, **56**, pp. 437-440.
3. Xia R., Xu C., Wu W., Li X., Feng X-Q., Ding Y., 2009; "Microtensile tests of mechanical properties of nanoporous Au thin films", *J. Mater. Sci.*, **44**, pp. 4728-4733.
4. Mathur A. and Erlebacher J., 2007; "Size dependence of effective Young's modulus of nanoporous gold", *Appl. Phys. Lett.*, **90**, pp. 061910-1-061910-3.
5. Sieradzki K and Newman R.C., 1985; "Brittle behavior of ductile metals during stress-corrosion cracking", *Philos. Mag.* **51**, pp. 95-132; 1987; "Stress-corrosion cracking", *J. Phys. Chem. Solids*, **48**, pp.1101-1113.
6. Snyder, J., Asanithi P., Dalton A.B., Erlebacher J, 2008b; "Stabilized nanoporous metals by dealloying ternary alloy precursors", *Adv. Mat.*, **20**, pp. 4883-4886.
7. Friedersdorf F. and Sieradzki K., 1996; "Film-induced brittle intergranular cracking of silver-gold alloys", *Corrosion*, **52**, pp. 331-336.
8. Jin H-J., Kurmanaeva L., Schmauch J., Rosner H., Ivanisenko Y., Weissmuller J., 2009; "Deforming nanoporous metal: Role of lattice coherency", *Acta Mat.*, **57**, pp. 2665-2672.
9. Okman O., Lee D., Kysar J.W., 2010; "Fabrication of crack-free nanoporous gold blanket thin films by potentiostatic dealloying", *Scripta Mat.*, **63**, pp. 1005-1008.

## Program Title: Tunable Hetero-Epitaxial Shape Memory Alloys

### Principal Investigator

Alejandro Strachan ([strachan@purdue.edu](mailto:strachan@purdue.edu))  
School of Materials Engineering, Purdue University  
West Lafayette, Indiana 47907, USA

### Program Scope or Definition

Shape memory materials are used for a wide range of applications, from medicine to aerospace, due to the ability to recover their original shape after inelastic deformation and super-elasticity. The ability to engineer desired performance in these materials is of technological and basic-science importance and this project explores a novel avenue to achieve this using large-scale computer simulations. The goal of the team is to explore hetero-epitaxial integration develop composite shape memory meta-materials with improved or tunable properties.

A successful project will provide a quantitative assessment of the potential and limitations of hetero-epitaxial integration as an avenue to develop shape memory materials with tailored properties. This may address some of the limitations that currently restrict the use of SMAs as active materials. From the point of view of basic science the effort will shed light into the fundamental phenomena that govern and limit the fabrication and performance of hetero-epitaxial SMAs nanostructures: i) coherency limits in terms of materials and size, and ii) the role of strain, interfaces, and free surfaces in their martensitic transformation and thermo-mechanical response. Shape memory materials have an enormous potential for a wide range of applications from nanoscale switches for communications and low power electronics to microfluidics and this project will contribute to the knowledge base necessary for the development of next-generation materials nanoengineered to achieve specific functionalities.

### Recent Progress

We use large-scale MD simulations to characterize size effects in the martensitic transformation that governs shape memory in NiAl alloys and use this information to engineer nanostructured alloys with tunable martensite/austenite transformation hysteresis. We characterize how the reduction in specimen size affects the resulting martensite microstructure and leads to an increase in the variability in phase transition temperature, see Figure 1. We find that for specimens with size below 10 nm fluctuations in transition temperature from sample-to-sample variability reached approximately 10%, limiting their use. These results shed light into the ultimate limits of miniaturization in this class of materials.

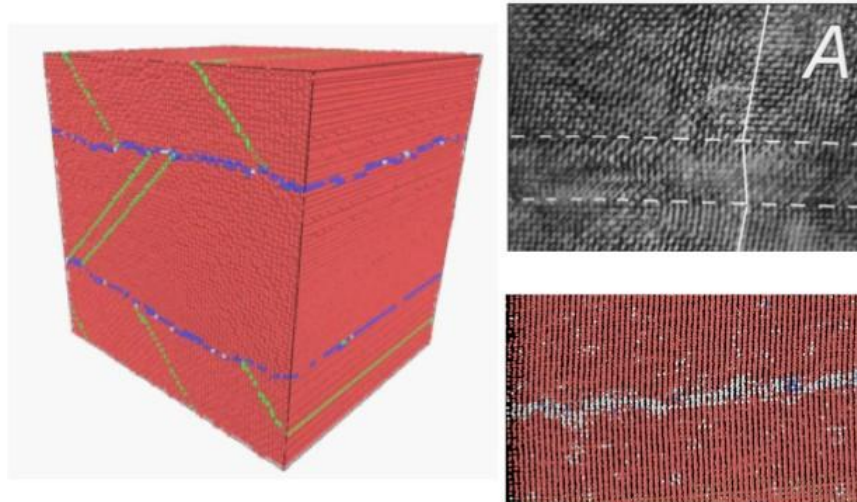


Figure 1. Martensite structure predicted by MD simulations and twinning region detail compared with TEM image from Potapov et al. *Acta Mater.* 48 3833–3845 (2000).

We also investigate the possibility of tuning the thermo-mechanical response of shape memory materials via strain engineering through hetero-epitaxial integration of metallic alloys of different composition. We use molecular dynamics simulations with an accurate many body interatomic potential to characterize hetero-epitaxial nano-laminates composed of shape memory  $\text{Ni}_x\text{Al}_{1-x}$  random alloys and B2 NiAl (which does not exhibit shape memory). We simulate cooling and heating of nanolaminate samples with various cross-sections, periodic lengths, and compositions to characterize how size and composition affect transition temperature and the associated hysteresis, see Fig. 2.

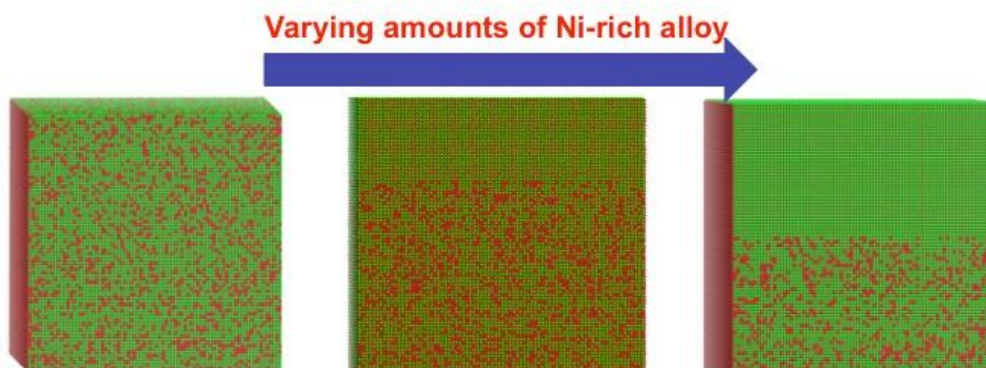


Figure 2: Atomic snapshots of a Ni rich NiAl alloy (left) and an epitaxial nanolaminates with alternating layers of  $\text{Ni}_{63}\text{Al}_{37}$  and  $\text{Ni}_{50}\text{Al}_{50}$ . (Ni and Al atoms are indicated by red and green spheres respectively) .

The right panel of Figure 3 shows how the thermal hysteresis and phase transition strain, defined as the change in lattice parameter between martensite and austenite at 50 K as a function of  $\text{Ni}_{0.63}\text{Al}_{0.37}$  alloy content in the eSL. The (desired) relative decrease in thermal hysteresis is more rapid (by a factor of approximately three) than the (undesired) relative

decrease in actuation strain showing that epitaxial integration leads to improved performance. For example, an eSL meta-material containing 70% Ni-rich alloy is predicted to exhibit only 40% of the hysteresis of the pure material with a decrease in actuation of only approximately 18%. These results indicate that such eSL meta-materials would be attractive for applications involving actuation with the potential of improved fatigue resistance.

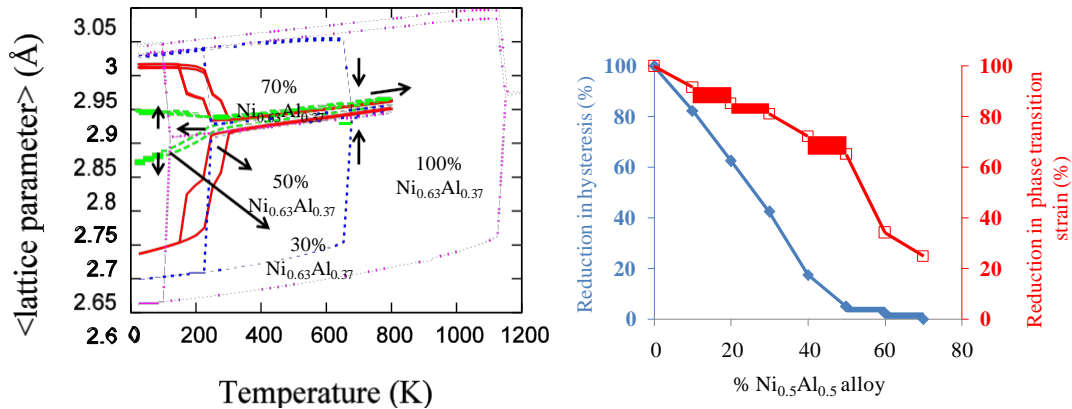


Figure 3: Left: Heating and cooling curves for pure defect free random  $\text{Ni}_{0.63}\text{Al}_{0.37}$  alloy and the family of eSL meta-materials with varying fraction of  $\text{Ni}_{0.63}\text{Al}_{0.37}$  alloy (30%, 50% and 70%). Right: Thermal hysteresis reduction (blue) and actuation strain (red open symbols) at 50 K for the eSL meta-materials with varying fractions of  $\text{Ni}_{0.63}\text{Al}_{0.37}$  alloy with respect to pure  $\text{Ni}_{0.63}\text{Al}_{0.37}$ .

### Future Plans

The team is now focusing on finishing the size-dependence of the martensite microstructure and will focus next on finite size systems where surface energetics play important roles. This work will shed light into the properties of thin films and nanowires of interested in nano-electrochemical systems (NEMS).

### References to publications of DOE sponsored research that have appeared in 2010-2012 or that have been accepted for publication.

1. "Size effects on martensitic microstructure in Zr nanowires via molecular dynamics", A. Thompson and A. Strachan, *Physical Review B*, 81, 085429 (2010).
2. "Phase stability and transformations in NiTi from density functional theory calculations", K. Guda Vishnu and A. Strachan, *Acta Materialia* 58, 745–752 (2010).
3. "Size effects in NiTi from density functional theory calculations", K. Guda Vishnu\* and A. Strachan, *Physical Review B* 85, 014114 (2012).
4. "Amorphous Ni/Al nanoscale laminates as high-energy intermolecular reactive composites" K. Guda Vishnu, M. Cherukara, H. Kim and A. Strachan, *Physical Review B*, 85, 184206 (2012).

5. "Role of nanostructure on reaction and transport in Ni/Al intermolecular reactive composites", M. Cherukara,\* K. Guda Vishnu, A. Strachan, Physical Review B, 86, 075470 (2012).
6. "Shape memory metamaterials with tunable thermo-mechanical response via hetero-epitaxial integration", K. Guda Vishnu\* and A. Strachan, Journal of Applied Physics (in press).

**Title: Radiation Effects in Nanocrystalline Ceramics: Multi-scale Model and Experiment**

**PI:** Izabela Szlufarska; **Co-PIs:** Dane Morgan, Todd Allen (through 12/31/2012); Kumar Sridharan (starting 01/01/2013)

Email: [szlufarska@wisc.edu](mailto:szlufarska@wisc.edu)

**Program scope or definition:**

The two main objectives of this project are: (i) to discover fundamental phenomena that control interaction of radiation-induced defects with the microstructure of ceramics; and (ii) to determine under what conditions nanocrystalline ceramics exhibit superior radiation resistance as compared to their polycrystalline counterparts. The project is focused on SiC as a model high-temperature ceramic and as a highly promising material for multiple nuclear reactor components (e.g., cladding). Because of the complexity of the defect energy landscape in SiC, understanding fundamental defect properties in this material is challenging. However, the complexity of SiC creates a wealth of possibilities for making exciting scientific discoveries. To meet the aforementioned objectives, we use an integrated approach that includes theory, modeling and experiments. On a modeling side, we are developing the first radiation model of SiC that is based on first principle properties of defects and that predicts long-term evolution of radiation damage as a function of microstructure and irradiation conditions. On the experimental side, we are carrying out irradiation experiments to determine the effect of grain size reduction on radiation resistance of SiC and to identify other key microstructural features that control this resistance.

**Recent progress:**

Primary radiation damage in SiC: Our studies of radiation cascades of SiC [1, 2] have demonstrated that more atomic displacements and more defects are produced in SiC with small grain sizes due to the increased volume fraction of grain boundaries (GBs). The surprising realization was that this enhancement of produced defects is almost entirely due to displacements in the GB regions and that the density of defects present in the crystalline grains shows a negligible dependence on the grain size [1]. Similarly, we have determined that the amount of primary damage produced in crystalline grains is independent of the GB type, when damage is properly normalized with respect to the velocity direction of the primary knock-on atom (PKA) [2]. Given that both our own experiments [3, 4] and those from other groups have found variation of the radiation resistance of SiC with grain size, we concluded that these differences are likely to arise during long-term damage evolution (on diffusional time scales). Since the lowest energy barriers to defect migration in SiC is believed to be about 0.67 eV (this is for C interstitial), limited diffusion is expected at room temperature during the primary damage phase, which lasts up to a few picoseconds. This result indicates that it is the defect evolution, not the total defect production in the crystalline regions that is affected by the presence of GBs. Consequently, our more recent modeling efforts have focused on predicting long-term defect evolution and radiation resistance by combining *ab initio* energetics of defects with rate theory models, and by using accelerated atomistic simulations.

Energy landscape for defect recombination in SiC: One of the unresolved questions related to the response of SiC to radiation is what fundamental mechanisms are responsible for controlling the critical amorphization temperature in this material. It has been often assumed in the literature that the temperature at which it is no longer possible to amorphize SiC through irradiation (400K +/-100K) corresponds to the temperature at which Si interstitials become mobile. This reasoning was based on the estimate of Si interstitial migration energy at about 1.5 eV. While this explanation is intuitively appealing, recent *ab initio* calculations by multiple groups (including ours) have shown that this migration barrier for Si interstitial is ~0.8 eV and that there are no migration barriers of point defects near 1.5 eV. In our studies we proposed that there are additional types of energy barriers that play a key role in defect annealing and these are defect recombination barriers. We have performed *ab initio* molecular dynamics (MD) simulations combined with the nudged elastic band (NEB) and “drag” method to determine mechanisms and barriers for binary reactions between point defects in SiC [5]. Two most important conclusions from these studies are: (i) the apparent discrepancies in energy barriers reported in the literature are related to different reactions paths explored in these studies. In all the cases we have either confirmed the barrier for

the lowest energy path or we have found a new path with a lower energy; (ii) We have found an energy barrier of  $\sim 1.34$  eV for the reaction of C interstitial with a Si antisite (Si on C sublattice) to form a Si interstitial and to recover C atom to its sublattice.

To identify the effect of recombination barriers on radiation-induced amorphization in SiC, we have developed a rate theory model [6]. This is the first rate theory model for this material that is built entirely on first principle calculations of defect energetics. Using this model we have shown that without the consideration of defect reaction barriers, the critical amorphization temperature is grossly underestimated ( $\sim 200$ K). Including barriers to defect reactions in the model, leads to an amorphization temperature of  $\sim 450$ K, which is in the regime of experimentally measured values. While all the reactions are coupled to each other, we found that the key reaction that controls the defect recovery is the aforementioned recombination of C interstitial and Si antisite defect.

Coupling of energy landscape to grain size effects

during irradiation: By performing simulations with the newly developed *ab initio* based rate theory model [6], we discovered that the presence of recombination barriers strongly couples to the grain size, producing surprising effects [7]. Specifically, we have shown that for reaction barriers comparable to those present in SiC, at low temperature nanocrystalline material is more radiation resistant than a polycrystalline material. This is in the regime where interstitials are already mobile, but they cannot recombine with vacancies due to the presence of recombination barriers. Since GBs serve as defect sinks, increased volume fraction of GBs leads to a faster damage annealing in nanocrystalline materials. At higher temperature, nanocrystalline material becomes less radiation resistant than its polycrystalline counterpart. In this regime interstitials can easily recombine with vacancies, however a fraction of the interstitials are annihilated at the GBs, leading to a so-called interstitial starvation and leaving an excess of vacancies in the lattice. Whether the interstitial starvation phenomenon will be manifested for a given material depends on the combination of defect migration barriers, recombination barriers, the temperature and the grain size.

Defect clusters in SiC: Up to this point our discussion has been focused on the role of point defects in radiation effects of SiC. While point defects are believed to be the dominant defects during electron irradiation of SiC, there exists evidence that defect clusters may be formed during ion irradiation. Using a combination of random configuration sampling, MD simulated annealing, and density functional theory (DFT) calculations, we performed an extensive search for the most stable configurations of carbon interstitial clusters in SiC [8]. Among other findings, we discovered a “magic” cluster size of 3 carbon interstitials (see Fig. 1), where the formation energy per interstitial shows a distinct minimum. We proposed this defect to be responsible for the experimentally observed DII photoluminescence center [9]. The DII center is known to be one of the most persistent defects in SiC and it is likely to provide a nucleus for growth of larger defect clusters in irradiated SiC. Interestingly, this cluster is present not only in the cubic SiC structure (relevant for nuclear applications) [10], but also in hexagonal SiC structures, which are of large interest for the semiconductor industry. The impact of our results extends therefore beyond the field of materials for nuclear energy applications.

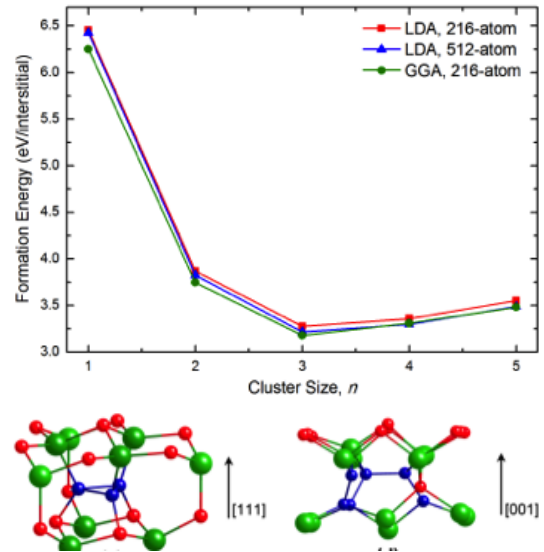


Fig. 1 (Top) Formation energy of C interstitial clusters per interstitial as a function of cluster size. (Bottom) The newly discovered ground state of the C tri-interstitial cluster (left) and the previously proposed ground state for the same defect.

We are currently carrying out simulations to determine stability (dissociation energies) and mobilities of the newly discovered clusters, which will be critical for understanding how these clusters evolve under radiation. Since formation and migration energies in SiC are relatively high (due to the covalent nature of the bonding), these phenomena are not accessible to standard atomistic simulations because of the limited time scales of these methods. We are therefore employing accelerated methods based on the kinetic activation-relaxation technique (*k*-ART)<sup>1</sup>. We have already implemented this technique for SiC and validated it for diffusion of point defects. We are now using this technique to study dynamics of defect clusters.

Microstructural dependence of radiation resistance in nc-SiC:

One of the intriguing aspects of radiation resistance of nanocrystalline (nc) SiC is that seemingly contradictory experimental results have been reported regarding the grain size effects on radiation. For instance, we have carried out Kr irradiation experiments on SiC powders and found that the dose to amorphize SiC decreases with decreasing grain size (indicating a lower radiation resistance) [4]. On the other hand our electron irradiation experiments on nc SiC samples grown by chemical vapor deposition (CVD) show an increased dose to amorphization for the nc material [5] (see Fig. 2). Similar results have been observed by other groups working on this problem<sup>2</sup>. The most likely explanation is that the microstructure (beyond grain size) of SiC has a strong effect on radiation resistance. Specifically, the only nc-SiC samples that showed a superior radiation resistance are the CVD grown films, which have a high density of stacking faults (SFs). The effect of SFs on defect evolution in SiC is still unknown and we are in the process of investigating multiple explanations. In particular, initial results suggest that the barrier which we identified as controlling amorphization (~1.34 eV for the reaction of C interstitial with a Si antisite) is reduced significantly in the SF. However, multiple other hypotheses still need to be investigated.

Effect of GB stresses on the sink strength: Our MD simulations have shown that the GB type does not have any significant effect on the defect production during radiation [2]. However, it is possible that GB type will affect defect evolution. To investigate this hypothesis, we have performed numerical simulations of defect annihilation at tilt GBs as a function of the tilt angle. We have explicitly included the effects of stresses from a network of GB dislocations. Most previous models of GB sink strengths have ignored this contribution from stresses. We found that while for coarse-grained materials the effects of the stress field are negligible, GB stresses play a significant role in the kinetics of defect annihilation in fine-grained materials. Contrary to what has been established for larger grain size, in nanomaterials there is a tilt angle that maximizes defect sink strengths and sink strengths of some GBs can exceed what is known as the “perfect” planar sink strength (Fig. 3)<sup>3</sup>.

Radiation-induced amorphization in carbides: We have performed the first fully *ab initio* study of radiation-induced amorphization of SiC by accumulation of point defects (characteristic of electron irradiation). We found that the material amorphizes at 0.25 dpa, in quantitative agreement with

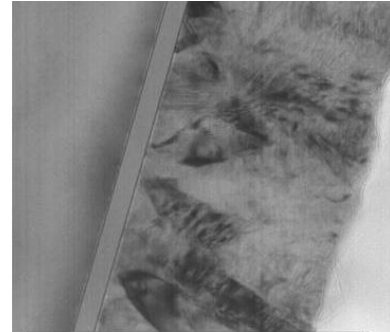
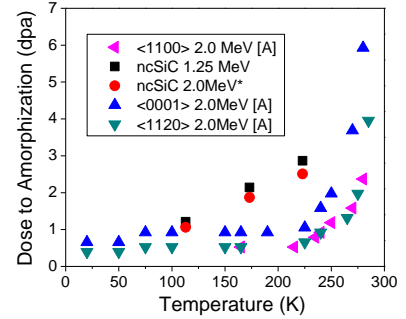


Fig. 2 (Top) Dose to amorphization vs. temperature for nc and single crystal SiC. (Bottom) CVD grown SiC showing a large concentration of stacking faults.

<sup>1</sup> F. El-Mellouhi *et al.*, Phys. Rev. B Vol. 78, 153202 (2008); Beland *et al.* Phys. Rev. E Vol. 84, 046704 (2011)

<sup>2</sup> W. Weber *et al.* To be published (2013)

<sup>3</sup> Jiang, Swaminathan, Morgan, Szlufarska, In preparation

experimental data. Similar *ab initio* analysis of ZrC reveals an increased resistance to amorphization, which is consistent with the known amorphization resistance of ZrC. We are now investigating the atomistic origins of this behavior.

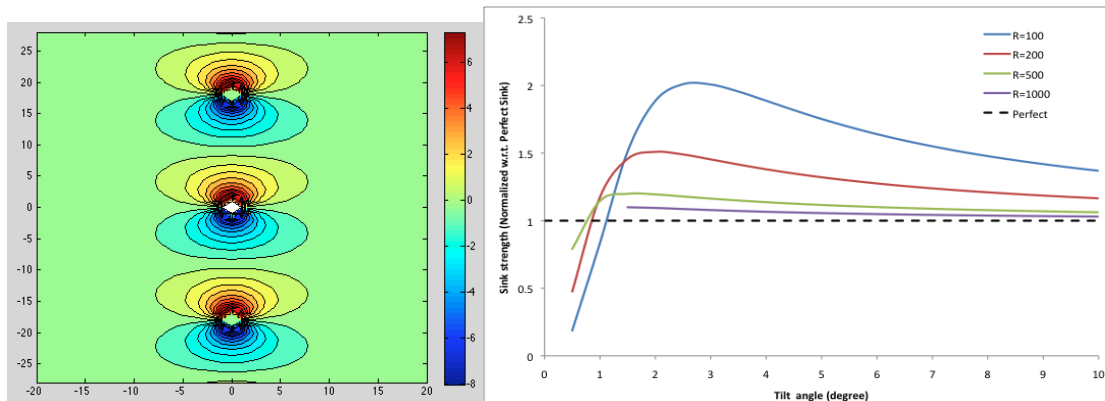


Fig. 3 (Left) Stress field from an infinite array of edge dislocations. (Right) Sink strength of small angle tilt GBs normalized by strength of a perfect sink. For small grain sizes, sink strength can be stronger than perfect due to the dominant contribution from elastic stress field to defect segregation.

**Future plans** build directly on our existing results and many of them have been already discussed in the preceding paragraphs. They include: (i) Combined experimental and modeling investigation of the role of SFs in radiation resistance of SiC (effects on mobility and formation energies of point and cluster defects); (ii) Mobility and stability of SiC clusters using accelerated atomistic techniques (*k*-ART); (iii) Mechanisms underlying amorphization of SiC via point defect accumulation (in contrast to ZrC that does not amorphize); (iv) What happens to defects when they segregate to GBs? All the analysis so far assumes that GBs are perfect sinks and we want to focus on the mechanisms of defect accommodation at GBs. For example, what happens if either C or Si preferentially segregates to GBs?; (v) Determine through experimental characterization of the irradiated microstructure how radiation-induced amorphous regions develop in SiC. Discover if the amorphization is homogeneous or heterogeneous and where does it start?

**Journal publications from this grant:** [1] *Effects of grain size and grain boundaries on defect production in nanocrystalline 3C-SiC*, N. Swaminathan, P. J. Kamenski, D. D. Morgan, I. Szlufarska, *Acta Materialia* 58, 2843-2853 (2010) (**100%**); [2] *Radiation interaction with tilt grain boundaries in beta-SiC*, N. Swaminathan, M. Wojdyr, D. D. Morgan, I. Szlufarska, *J. Appl. Phys.* 111, 054918 (2012) (**100%**); [3] *Radiation resistance of nanocrystalline silicon carbide*, L. Jamison, P. Xu, K. Sridharan, T. Allen, *Advances in Materials Science for Environmental and Nuclear Technology II - Materials Science and Technology 2010 Conference and Exhibition, MS and T'10*, American Ceramic Society, Houston, TX, United States, 2011, pp. 161-168. (**100%**); [4] *Experimental and ab initio study of enhanced resistance to amorphization of nanocrystalline silicon carbide under electron irradiation*, L. Jamison, M.-J. Zheng, S. Shannon, T. Allen, D. Morgan, I. Szlufarska, Submitted (**100%**); [5] *Energy barriers for point defect reactions in 3C silicon carbide*, M.-J. Zheng, N. Swaminathan, D. Morgan, I. Szlufarska, Submitted (**80%**); [6] *Ab initio based rate theory model of radiation induced amorphization in  $\beta$ -SiC*, N. Swaminathan, D. Morgan, I. Szlufarska, *J. Nucl. Mater.* 414, 413-439 (2011) (**100%**); [7] *The role of recombination kinetics and grain size on radiation induced amorphization*, N. Swaminathan, D. Morgan, I. Szlufarska, *Phys. Rev. B* 86, 214110 (2013) (**100%**); [8] *Structure and stability of small carbon interstitial clusters in 3C-SiC*, C. Jiang, D. Morgan, I. Szlufarska, Submitted (**100%**); [9] *Carbon tri-interstitial defect: A novel model for the  $D_{II}$  center*, C. Jiang, D. Morgan, I. Szlufarska, *Phys. Rev. B* 86, 144118 (2012) (**100%**); [10] Invited: *Radiation effects in SiC for nuclear structural applications*, Y. Katoh, L. L. Snead, I. Szlufarska, W. Weber, *Current Opinion in Solid State & Materials Science*, 16, 143-152 (2012) (**100% of Szlufarska's time; 25% of the total effort on the paper**)

# Linking the Correlated Dependence of Grain Boundary Structure and Density to Defect Evolution Mechanisms during Radiation Damage

PI: Mitra Taheri, Materials Science & Engineering, Drexel University  
3141 Chestnut Street Philadelphia, PA 19103  
[mtaheri@coe.drexel.edu](mailto:mtaheri@coe.drexel.edu)

## PROGRAM SCOPE

The aim of this project is to provide a fundamental understanding of how metallic nanocrystalline alloys can be utilized as radiation tolerant materials in future nuclear reactors. Although much is known already about the effects of radiation damage accumulation, information about its origin and mechanisms at the nanoscale and how these mechanisms evolve as a function of grain boundary character (GBC) and density (i.e., grain size) is still unclear.

Understanding and mitigating radiation damage is of paramount importance in the nuclear industry. Damage of structural materials is a major limitation to extended lifetime of current reactors, and implementation of future reactors. Although much is known about the effects damage accumulation, information about its origin and mechanisms at the nanoscale and how these mechanisms evolve as a function of grain boundary structure and density (i.e., grain size) is still unclear. Further understanding of the kinetics of the following point defect behaviors is needed: the decrease in point defect density near the grain boundary, or denuded zone, and radiation induced segregation (RIS), the preferential diffusion of solute atoms near the grain boundary that result in chemical inhomogeneity at the boundary. The precise role of interstitial diffusion is unknown due to the difficulty of separating interstitial and vacancy diffusion.

In situ and analytical transmission electron microscopy techniques will be used to study both pure and alloy materials. TEM samples prepared from thin films will be irradiated *in-situ*, allowing for dynamic observation of the behavior of the alloy under ion irradiation. Thus, this work will define a framework for understanding the origin of radiation damage mechanisms in model BCC and FCC nanocrystalline materials, on which a foundation of radiation tolerant material development can be built.

**Specific Aims.** The key questions that will be addressed by this work are:

1. What is the influence of GB density and GB character (GBC) on radiation damage accumulation near grain boundaries in model nanocrystalline FCC and BCC alloys; how are these two effects connected?
2. In the context of radiation induced segregation (RIS), what effect does species dependent interstitial diffusion have on the GB chemistry in light of these two dependencies?

## RECENT PROGRESS

Work is currently underway to define the effect of GBC and density on radiation induced defect formation and subsequent chemical segregation in BCC materials. It will employ *a suite of interfacial experimentation* to observe the formation and segregation of point defects as a function of grain size and GBC. Combined with analytical techniques such as STEM-EDS, EELS and APT, *in-situ* and *ex-situ* irradiation techniques are being used to study the effect of sink strength and density on defect clustering and behavior in relation to grain boundaries.

**Current Methodology.** Free-standing thin films of Fe and Fe-Cr alloys are deposited by physical vapor deposition on NaCl substrates at LANL. Deposition and annealing parameters are controlled to provide grain sizes as small as 10nm which enables a study of radiation damage as a function of grain size. After deposition, the films are characterized using TEM and X-ray techniques (SAXS, XRD) at Drexel University. Specimen microstructure is characterized by NanoMEGAS ASTAR precession diffraction in the TEM (20) at Drexel. This system allows the acquisition of orientation maps by rastering the electron beam across the sample with a 5nm step size, recording a diffraction pattern at each position. The diffraction patterns are matched to calculated templates to determine orientation information. From this data, information about grain size, texture, and grain boundary character are obtained, allowing for a detailed study of grain boundary character effects. After initial characterization, the samples are irradiated using high energy ions. *In-situ* irradiations are carried out using the dual beam irradiation setup at Argonne National Laboratory's IVEM Tandem facility which consists of a 650KeV ion implanter directed into a Hitachi H-9000NAR TEM at 30° from the electron beam (21). Ex-situ irradiations are also be used in conjunction with the in-situ work, and have been performed at LANL as well as SNL. Specimens were irradiated at varying dose levels (e.g. 0.5dpa, 1dpa, 5dpa) and at selected temperatures between -270°C and +600°C.

Characterization of the damage morphology in the nanocrystalline specimens after irradiation is performed using the JEOL 2100 TEM at Drexel. Conventional TEM is used to characterize the dislocation loop types (e.g. vacancy loop vs interstitial loop), habit planes, and Burger's vector. Point defect cluster size and number density are measured as a function of grain size. The interaction of defect loops with grain boundaries and the resulting effect on the irradiated microstructure are investigated using conventional microscopy techniques in conjunction with grain boundary orientation maps data acquired by precession electron (Nanomegas system).

**Results.** Much of the initial work has focused on a the behavior of nanocrystalline pure iron films with grain size between 20nm and 500nm under irradiation with 1MeV Kr<sup>2+</sup> ions at 300°C to 5 dpa. Free standing sputtered iron films display defect cluster formation mechanisms that are characteristic for the irradiation of iron. In nanocrystalline iron films annealed to a large grain size (e.g. 100-500nm), large  $\mathbf{b}=1/2\langle 111 \rangle$  type loops appear by 3dpa and continue to increase in size to the final dose around 5dpa. The irradiated microstructure begins to deviate from the bulk behavior as grain size decreases. This is principally observed as a decrease in the size of the dislocation loops in smaller grains (Figure 1). The influence of decreasing grain size on defect cluster density is more complex, and dependent on the strength of the grain boundary sinks, as well as the presence of sessile  $\mathbf{b}=\langle 100 \rangle$  type dislocation loops which can remain stable near a grain boundary. In many nanocrystalline grains, denuded zones are found near the boundaries. The denuded width is maintained as the grain size decreases so the denuded area represents a greater fraction of the grain. Preliminary results have shown that the width of this region of low defect density likely depends on the grain boundary character. A low angle boundary with 12° misorientation about (112) was found to have a denuded zone of comparable width (~20nm) in both bulk and nanocrystalline grains, while others had no visible denuded zone (Figure 2).

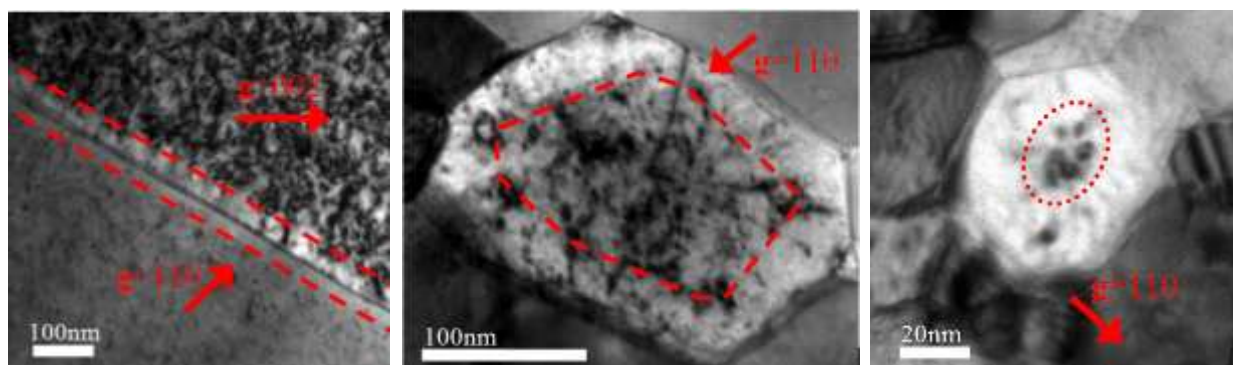


Figure 1. a) Denuded zone near a low angle grain boundary in bulk polycrystalline iron and the effect of a similar denuded zone in a) a 200nm grain and b) a 60nm grain in free standing nanocrystalline iron films.

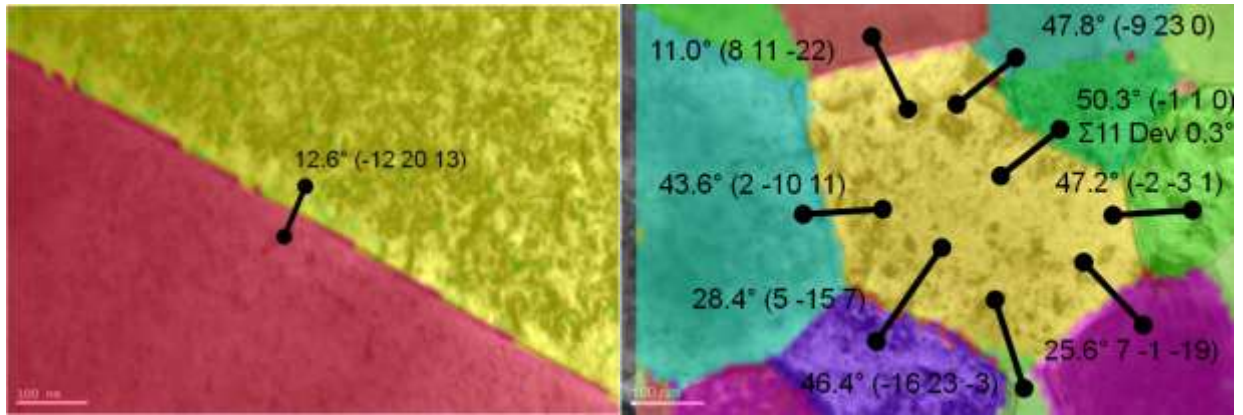


Figure 2. Orientation maps acquired by precession diffraction overlaid on TEM brightfield images showing denuded zone with variations with GBC. A low angle GB with 11° misorientation about (112) in a nanocrystalline grain shows a denuded zone with a width comparable to a low angle GB with a 12° (112) boundary in bulk iron.

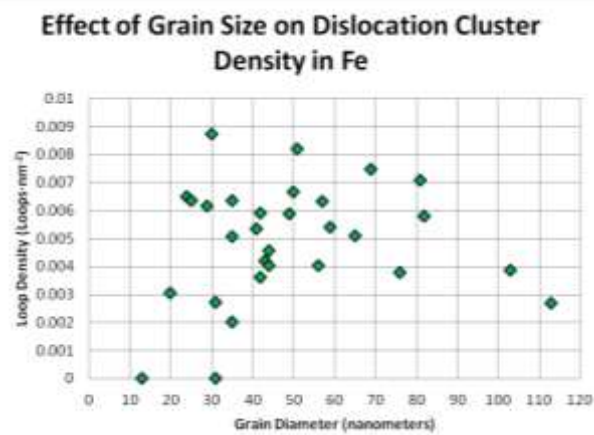


Figure 3. Dislocation cluster density as a function of grain size below 120nm. A slight decreasing trend is observed due to loss of point defects and clusters to boundaries.

boundary, but also the loss of point defect clusters by loop hop (Figure 4) and of large dislocation loops to grain boundaries by glide. The presence of a high volume fraction of grain boundaries implies that dislocation clusters that form are more likely to be close enough to a grain boundary that they will be annihilated before reaching a stable size.

## FUTURE PLANS

Preliminary results have primarily been derived from irradiations carried out in pure nanocrystalline Fe using 1MeV Kr<sup>2+</sup> ions at 300°C. Upcoming efforts will expand upon the initial results presented above on grain size effects by studying the correlation between the defect density in nanocrystalline grains and grain boundary character by correlating *ex-situ* defect counts with orientation maps. Diffraction

As a consequence of the variance in denuded zone width, a wide distribution of defect cluster densities is observed at small grain sizes (Figure 3). Grains that possess a wide denuded zone on all boundaries are nearly devoid of dislocation loops by a grain diameter of two times the width of the denuded zone. Other grains that do not have such strong boundary sinks may retain dislocation loops in the smallest measurable grains (~20nm). The dislocation cluster density remains comparable to a sinkless region, although the size of the loops is much smaller.

Using in-situ irradiation experiments it was shown that the denuded zone in iron is not only the result of diffusion of individual point defects to the grain

boundary, but also the loss of point defect clusters by loop hop (Figure 4) and of large dislocation loops to grain boundaries by glide. The presence of a high volume fraction of grain boundaries implies that dislocation clusters that form are more likely to be close enough to a grain boundary that they will be annihilated before reaching a stable size.

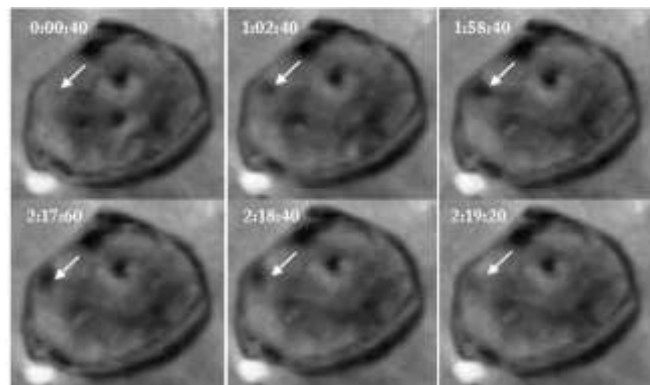


Figure 4. Unstable loop formation near GBs (time in minutes).

information will be used to examine the mechanisms for point defect clustering and dislocation loop loss to grain boundaries in terms of GBC. Future work will include detailed studies of irradiation damage as a function of temperature (Figure 5) in order to understand how the mobilities of interstitials, vacancies, and defect clusters affect the ability of nanocrystalline Fe films to resist irradiation. Defect mobility will also be controlled by the addition of solute atoms such as chromium which, in addition to allowing the study of the influence of defect trapping, will also permit a study to explore the effect of nanocrystalline grain structure on radiation induced segregation (RIS).

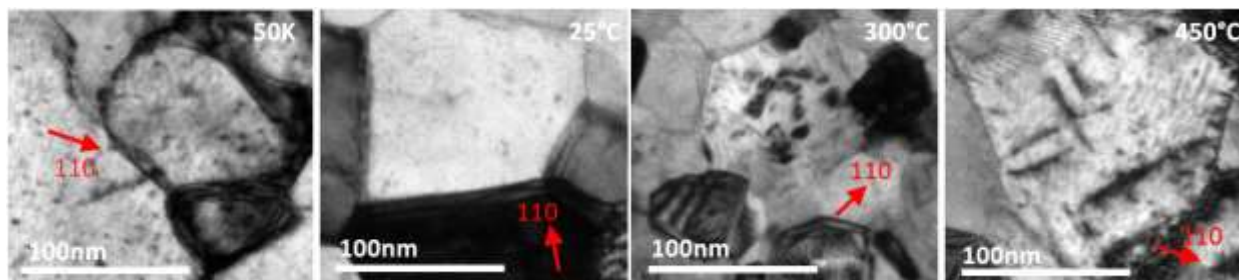


Figure 5. Defect morphology in grains of similar size in nanocrystalline Fe after being irradiated to 5dpa.

## REFERENCES

1. M. L. Jenkins, M. A. Kirk, *Characterization of Radiation Damage by Transmission Electron Microscopy* (IOP Publishing, Philadelphia, PA, 2001).
2. G. Was, *Fundamentals of Radiation Materials Science* (Springer, New York, NY, 2007)
3. B. D. Wirth. *Science*. **318**, 923-924 (2007).
4. S. J. Zinkle, J. T. Busby. *Materials Today*, **12**, 12-19 (2009).
5. R. E. Stoller, P. J. Kamenski, Yu. N. Osetsky. **1125**, 131-139 (2008).
6. J. A. Hudson, D. J. Mazey, R. S. Nelson. *J. Nucl. Mater.* **41**, 241-256 (1971).
7. S. J. Zinkle, K. Farrell. *J. Nucl. Mater.* **168**, 262-267(1989).
8. G. Ackland. *Science*. **327**, 1587-1588 (2010).
9. A. Misra, L. Thilly. *MRS Bulletin*. **35**, 965-971 (2010).
10. E. G. Fu, A. Misra, H. Wang, L. Shao, X. Zhang. *J. Nucl. Mater.* **407**, 178-188 (2010).
11. H. Van Swygenhoven, A. Caro, D. Farkas. *Scripta Mater.* **44**, 1513-1516 (2001)
12. M. Rose, A. G. Balogh, H. Hahn. *Nucl. Instr. Meth. Phys. Res., Sect. B.* **127-128**, 119-122 (1997).
13. N. Nita, R. Schaeublin, M. Victoria. *J. Nucl. Mater.* **953**, 329-333 (2004).
14. Y. Chimi, A. Iwase, N. Ishikawa, M. Kobiyama, T. Inami, S. Okuda. *J. Nucl. Mater.* **297**, 355-357 (2001).
15. T. D. Shen, S. Feng, M. Tang, J. A. Valdez, Y. Wang, K. E. Sickafus. *Appl. Phys. Lett.* **90**, 263115 (2007).
16. A. R. Kilmametov, D. V. Gunderov, R. Z. Valiev, A. G. Balogh, and H. Hahn. *Scripta Mater.* **59**, 1027-1030 (2008)
17. M. Samaras, P.M. Derlet, H. Van Swygenhoven, M. Victoria. *Phys. Rev. Let.* **88**, 125505 (2002).
18. M. Samaras, P.M. Derlet, H. Van Swygenhoven, M. Victoria. *J. Nucl. Mater.* **351**, 47-55 (2006).
19. M. Samaras, W. Hoffelner, M. Victoria. *J. Nucl. Mater.* **352**, 50-56 (2006).
20. A. D. Darbal, M. Gemmi, J. Portillo, E. Rauch, S. Nicolopoulos. *Microscopy Today*. **20**, 38-42 (2012).
21. C.W. Allen, L.L. Funk and E.A. Ryan. *Mater. Res. Soc. Symp. Proc.* **396**, 641 (1996).

## **“Stress states associated with twin nucleation and propagation in HCP materials”**

Carlos N. Tomé (PI) (tome@lanl.gov)

MST-8, MS G755, Los Alamos National Laboratory, Los Alamos, NM 87545, USA

**Program:** “Multi-scale study of the role of microstructure in the deformation behavior of hexagonal materials”

### **Participants**

- LANL Technical Staff: C. N. Tomé (PI), I. J. Beyerlein, D.W. Brown, E. Cerreta, B. Clausen, R.C. McCabe, J. Wang, R.A. Lebensohn
- LANL Postdocs: A. Kanjarla, L. Balogh, S. Niezgodna, B. Morrow
- Collaborations: S. Merkel (U. of Lille, France), H. El Kadiri (Mississippi S.U.), L. Capolungo (Georgia Tech), R.H. Wenk (U.C. Berkeley), M. Daymond (Queens U, Canada), P. D. Wu & H. Wang (McMaster U, Canada) , Y. Jiang (U Nevada Reno)
- Graduate students: P. A. Juan & N. Berlin (Georgia Tech), Qin Yu (U Nevada Reno)

### **Scope of Program**

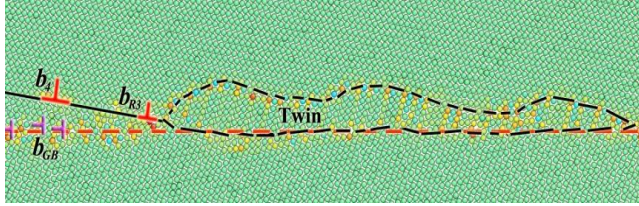
Hexagonal metals are relevant to several technologies: Zr in the nuclear industry, Mg in the automotive industry, Be and Hf in defense, Ti in aeronautics. We use experiments and modeling to characterize the deformation mechanisms and to predict the complex evolution of microstructure (dislocations, twins and their interaction) taking place in hexagonal materials during plastic deformation. Being able to predict metal flow during complex forming operations will allow us to optimize the forming operations themselves, as well as the mechanical properties of the formed materials.

Our paradigm is to develop a basic understanding of the microstructure and to establish a connection between microstructure and the macroscopic mechanical response of hexagonal materials. We foresee to achieve new levels of understanding of polycrystal plasticity by explicitly incorporating atomistic and crystallographic aspect of the microstructure (such as twin nucleation), and stochastic events (such as local neighborhood, stress fluctuations at grain boundaries, misorientation effects). We approach the issues above using a closely integrated modeling and experimental paradigm, which spans a range of length scales from the atomistic to the continuum. We are developing methodologies for characterizing the local mechanisms experimentally and theoretically, and for incorporating them into models describing the macroscopic response of the aggregate. The focus throughout this program is to identify and quantify the relevant variables at each length scale, and to ensure that the modeling and experimental components are seamlessly integrated across the length scales.

During 2011-2012 our focus has been on: (1) characterizing stress states along grain boundaries and twin boundaries using MD, local crystal plasticity models and X-ray synchrotron experiments; (2) developing constitutive models of aggregates which include twinning, strain reversals, strain rate, temperature and pressure effects; (3) connecting dislocation evolution models with experimental measurements of peak broadening. The subject of this presentation touches upon some aspects of topics (1) and (2).

## Technical Progress

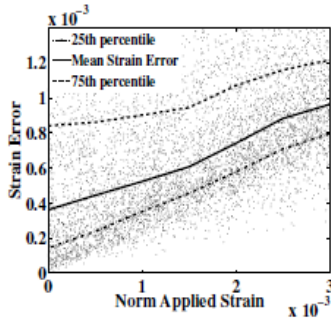
**Atomistic simulations:** Atomistic simulations address the micro length scale. During 2011 we made progress in our basic understanding of twin nucleation and twin propagation in Mg, Zr and Be. Our MD atomistic simulations reveal that stable  $(\bar{1}012)$



twin nuclei can nucleate in Mg from symmetric tilt grain boundaries following dislocation arrival and dissociations at the boundaries [Tomé et al, 2011; J. Wang and Beyerlein, 2012; J. Wang et al, 2012). The figure shows a  $30^\circ$  tilt

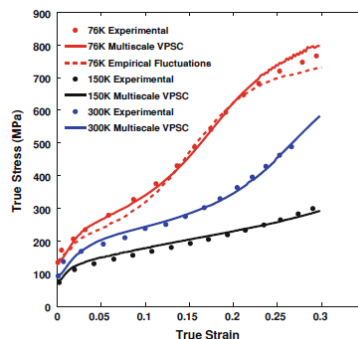
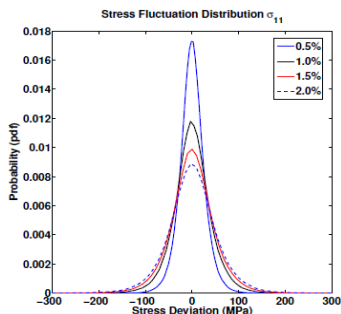
boundary and basal dislocations inducing a twin nucleus. Because all our EBSD and TEM evidence supports twin initiation at boundaries in HCP materials, we adopted it as our mechanism for twin nucleation and introduced it in our statistical mesoscale models of twinning.

**Microscopic characterization by EBSD:** During 2011 we pursued developing the technique of High Resolution Electron Back Scattering Diffraction (HR-EBSD). After systematic work, we concluded that the resolution of the technique is insufficient for



resolving the stress distributions in the vicinity of grain and twin boundaries [Niezgoda et al, 2012]. The figure on the left shows that the error in the measured strain components may vary from  $\Delta\varepsilon=10^{-4}$  to an unrealistic  $\Delta\varepsilon=10^{-2}$ , depending on the orientation under consideration. The technique still provides local misorientation information, and the measurements will be used for analyzing plastic localization near boundaries as a function of neighbor misorientation.

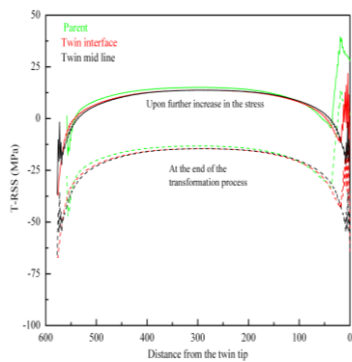
**Constitutive laws for HCP aggregates:** During 2011-2012 we made progress on developing constitutive polycrystal models that link micro, meso and macro scale. We incorporated a stochastic twin nucleation model that precedes twin propagation in the grains into our Visco Plastic Self Consistent polycrystal model (VPSC). The nucleation model is based on probabilistic stress fluctuations at grain boundaries calculated with a local plasticity model based on Fast Fourier Transform (FFT) [Kanjarla et al, 2012]. The left figure shows the deviations from average of component  $\sigma_{11}$  for an ensemble of 100



Zr polycrystals (500 grains each) having the same texture but different spatial arrangement of grains, and subjected to tension and compression. The tail of the distribution is

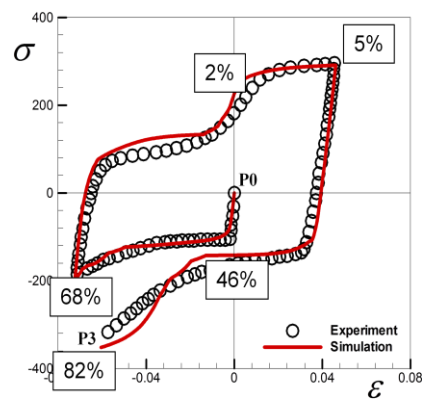
relevant to the probabilistic variations of stress responsible for local twin nucleation. A consequence of the approach is to activate macroscopically unfavorable twin variants. Results are in close agreement with twin statistic on variant distribution measured by EBSD [Capolungo et al, 2009], and also with experimentally measured stress-strain and texture evolution [Tomé et al, 2011; Niezgodna et al, 2013]. The figure on the right compares the measured and predicted stress-strain response of Zr at 76, 150 and 300K. The hardening law used in the simulations was developed within our BES Program, and is based on the evolution of prism, basal and pyramidal dislocations. It also includes twinning, strain rate and temperature effects [Beyerlein and Tomé, 2008].

We used the FFT approach to calculate local stresses inside a twin, and the stress distribution in the parent and neighbor grains induced by the localized twin shear



[Kanjara et al, 2013]. The results indicate that back stresses are induced on the twin which arrest further propagation. These stresses strongly depend on the neighbor orientation and its capability of accommodating the shear induced by the twin tip at the boundary. The variation of the resolved shear at the twin interface, along the twin is shown in the figure. Observe the dip in the profiles in the vicinity of the grain boundaries, which suggests that the back stress will arrest further growth of the twin

**Synchrotron X-ray diffraction:** An experiment done on polycrystalline Mg at the 34-ID beamline at APS (Argonne) [Balogh et al, 2013] provided evidence for stress gradients in the vicinity of twins, and suggested to modify the criterion of twin growth used in our crystal plasticity simulations. Specifically, the stress that matters for twin growth is the one acting at the twin interface, and this experiment shows that such stress is closer to the average stress in the twin than to the average stress in the parent. Consequently, we implemented such criterion in a newly developed Elasto-Visco-Plastic Self Consistent model [H. Wang et al, 2010] and used it for simulating cyclic deformation of Mg [H. Wang et al, 2012]. We also implemented a twinning-detwinning mechanism which proved to play the main role in



explaining the stress-strain response, texture evolution, and twin fraction evolution during cyclic loading. The figure shows the predicted twin volume fraction at different stages of load, which is in good agreement with experimental measurements.

## Future Research

We plan to focus future research on deriving experimental and theoretical information about local stress states in HCP materials and how they relate to slip, twin nucleation and twin propagation. Specifically:

- (1) Analyze local stress states and their fluctuations near grain and twin boundaries and characterize them using a statistical framework.
- (2) Explore the configuration of twin boundaries, with special interest paid to the appearance of serrations in otherwise coherent twin boundaries. We suspect that these serrations may control the growth of twins once formed [J. Wang et al, 2013]. Specifically, we will use a combination of Molecular Dynamics (MD) techniques and High resolution TEM to investigate such features in Mg and Zr.
- (3) We will apply Discrete Dislocation Dynamics (DDD) simulations to study dislocation interactions in HCP metals and so obtain parameters for our crystal hardening model. We will connect experimental peak broadening with the dislocation densities predicted by DDD and by our hardening models.

## References

- L. Balogh, S.R. Niezgodá, A.K. Kanjarla, D.W. Brown, B. Clausen, W. Liu, C.N. Tomé, "Spatially resolved in-situ strain measurements from an interior twinned grain in bulk polycrystalline AZ31 alloy", *Acta Metall* (2013) in press
- I.J. Beyerlein and C.N. Tomé, "A dislocation based constitutive law for pure Zr including temperature effects", *Int. J. of Plasticity* **24** (2008) 867-895
- L. Capolungo, P.E. Marshall, R.J. McCabe, I.J. Beyerlein, C.N. Tomé, "Nucleation and propagation of twins in Zr: a statistical study", *Acta Mater* **57** (2009) 6047-56
- A.K. Kanjarla, R.A. Lebensohn, C.N. Tomé, under preparation (2013)
- A.K. Kanjarla, I.J. Beyerlein, R.A. Lebensohn, C.N. Tomé, "On the role of local grain interactions on twin nucleation and texture evolution in hexagonal materials", *Mats. Sc. Forum* 702-703 (2012) 265-268
- S.R. Niezgodá, R.J. McCabe, C.N. Tomé, "Quantification of strain and orientation measurement error in cross-correlation Electron Back Scatter Diffraction in hexagonal close-packed materials", *Scripta Mater* **67** (2012) 818-821
- S.R. Niezgodá, I.J. Beyerlein, A.K. Kanjarla, C.N. Tomé, "Introducing grain boundary influenced stochastic effects into constitutive models: application to twin nucleation in hexagonal close packed metals", *J of Metals* **65** #3 (2013) 419-430
- C.N. Tomé, I. J. Beyerlein, J. Wang, R.J. McCabe, "A multi-scale statistical study of twinning in Mg", *J of Metals* **63** No. 3 (2011) 19-23
- H. Wang, P.D. Wu, C.N. Tomé, Y. Huang, "A finite strain elasto-viscoplastic self-consistent model for polycrystalline materials", *J Mech Phys Solids* **58** (2010) 594-612
- H. Wang, P.D. Wu, C.N. Tomé, J. Wang, "A constitutive model of twinning and detwinning for HCP polycrystals", *Mats Sc and Engineering* **A555** (2012) 93-98
- J. Wang, I.J. Beyerlein, "Atomistic modeling of interactions of lattice dislocation with  $[1\bar{2}10]$  symmetrical tilt grain boundaries in Mg", *Mod Sim Mats Sci Eng* **20** (2012) 024001
- J. Wang, I.J. Beyerlein, J. P. Hirth, "Nucleation of elementary  $\{\bar{1}011\}$  and  $\{\bar{1}013\}$  twinning dislocations at a twin boundary in hexagonal-close-packed crystals", *Mod Sim Mats Sci Eng* **20** (2012) 024002
- J. Wang, L. Liu, C.N. Tomé, S.X. Mao, S.K. Gong, "Twinning and de-twinning via glide and climb of twinning dislocations along Serrated Coherent Twin Boundaries in HCP metals", *Mats Research Letters*(2013) in press

## Chemomechanics of Far-From-Equilibrium Interfaces (COFFEI)

Harry L. Tuller, W. Craig Carter, Yet M. Chiang, Krystyn J. Van Vliet, Bilge Yildiz, Sidney Yip  
Massachusetts Institute of Technology ([tuller@mit.edu](mailto:tuller@mit.edu))

### *Needs, Objectives, Impact of Project*

Brittle oxide functional materials, such as those utilized in solid oxide fuel cells, permeation membranes and lithium batteries, exhibit significant operational stresses induced via chemical and electrochemical diffusion across material interfaces. Virtually all battery storage materials undergo considerable mechanical strain during Li flux at solid-liquid and solid-solid interfaces. Likewise, fuel cell components and permeation membranes, operating under steep oxygen activity gradients, often suffer from chemically induced strains. The highly variable performance of mixed conducting fuel cell electrodes is suspected to be due to polarization induced stoichiometry changes and associated mechanical deformations. At the same time, exciting new evidence suggests that certain types of highly defective oxides can relieve stresses by defect redistribution, and thereby tolerate larger deformations and/or induce enhanced charge and mass transport in the vicinity of interfaces. Furthermore, the discovery of highly active cathode materials for oxygen reduction in solid oxide fuel cells at intermediate temperatures remains an important challenge for improving materials stability and system cost. Overcoming of this challenge requires an improved understanding of the oxygen reduction reaction (ORR) mechanism at the molecular level, and of the underlying correlation between the ORR kinetics and the inherent surface structure of the cathode materials. Control of ORR activity and oxygen transport kinetics through strain-manipulation at surfaces and hetero-interfaces presents a new opportunity to enable advances in this area. Tailoring the surface chemistry, atomic and electronic structure on nonstoichiometric transition metal oxides (TMOs) and rare earth oxides (REOs) for faster oxygen reduction kinetics under harsh conditions of high temperature, reactive gas pressure and material strain state is critical. Successful development of functionally superior and long-lived battery and fuel cell systems and stress adaptable oxides requires a deeper, fundamental understanding of the coupling among the historically important subfields of solid-state electrochemistry, transport kinetics, and mechanical deformation for nonstoichiometric TMOs. In particular, the *chemomechanical coupling* of defect concentrations, ionic transport, electro-catalytic activity and stored elastic energy is particularly acute in the far-from-equilibrium conditions typical of energy device applications.

Our project employs (a) advanced *in-situ* and *ex-situ* characterization tools to characterize model materials and interfaces synthesized with molecular-level control, under both laboratory-controlled and extreme environments representative of energy device operation; and (b) computational modeling and simulation frameworks to predict transport mechanisms, reactivity and stability of these model materials and interfaces under significant chemical strains typical of energy device operation. This talk will focus on key recent results from the two Thrusts in the project. First is on chemomechanics due to cation transport in battery TMOs, while the second part focuses on chemomechanics of anion transport and electrocatalysis at fuel cell and permeation membrane TMO and REO interfaces.

### *1. Coupling between Electrochemical Driving Forces and Mechanical Stress in Battery Materials*

We have derived a fracture mechanics failure criterion for individual electrode particles and demonstrate its utility with a model system: galvanostatic charging of  $\text{Li}_x\text{Mn}_2\text{O}_4$ .(1) Fracture mechanics predicts a critical C-rate above which active particles fracture; this critical C-rate decreases with increasing particle size. We thus produced the *first-ever electrochemical shock map* (Figure 1), a graphical tool that shows regimes of failure depending on C-rate, particle size, and the material's inherent fracture toughness  $K_{Ic}$ . Fracture dynamics are sensitive to the gradient of diffusion-induced stresses at the crack tip; as a consequence, small initial flaws grow unstably and are therefore potentially more damaging than larger initial flaws, which grow stably.

The utility of these electrochemical shock maps to electrode particle design is maximized when the fracture toughness of the particular TMO is known. Surprisingly, this and other elastic and plastic properties of most TMOs have not been measured directly. Thus, we have also quantified the elastic modulus, hardness and fracture toughness of single crystal  $\text{LiCoO}_2$  (Meng, Woodford *et al.*(2)). To our

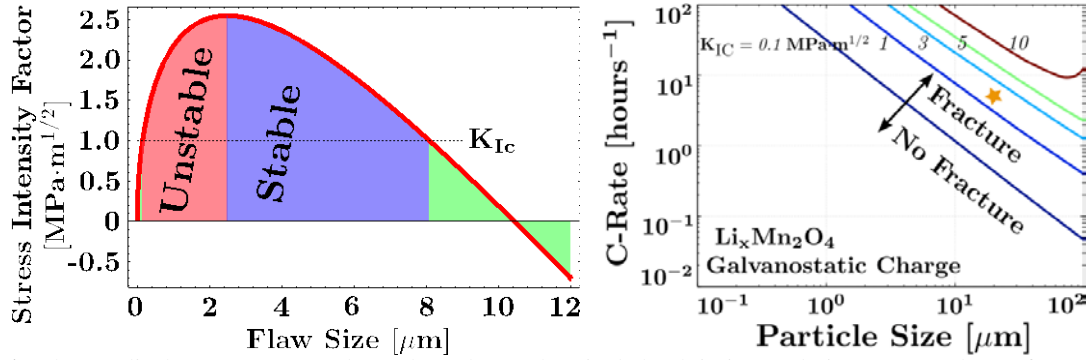
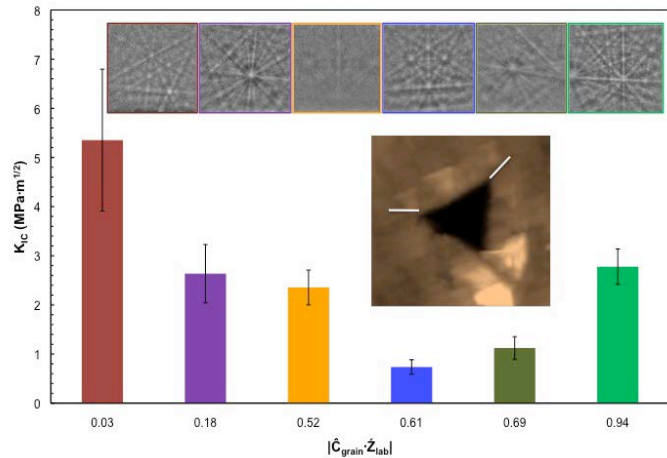


**Figure 1:** Charge-discharge or C-rate dependent electrochemical shock in intercalation compounds. Left: Stress-intensity factor – flaw size relationship for concentration induced stresses in an Li<sub>x</sub>Mn<sub>2</sub>O<sub>4</sub> particle subject to high C-rate charge. Right: Electrochemical shock map showing particle size and C-rate conditions where fracture is, and is not, expected for Li<sub>x</sub>Mn<sub>2</sub>O<sub>4</sub>. (1) Individual curves are calculated assuming the value of K<sub>IC</sub> shown; experimental values of K<sub>IC</sub> are not available for this material.

knowledge, this is the *first report of these key mechanical properties for this model TMO*. We synthesized dense, sintered compacts comprising polycrystals of 100 μm average grain diameter, such that the strain volume of indentation was small compared to grain volume. This sample format and grain size gave access to mechanical properties reasonably interpreted as those of a single crystal, and also enabled acquisition of several replicate experiments within each grain. To quantify K<sub>IC</sub>, we then calibrated and implemented a method by which large probe displacements are related to fracture events. This provided an efficient way to determine the critical stress intensity factor (hereafter, fracture toughness) K<sub>IC</sub> directly from instrumented nanoindentation load-displacement responses without the requirement of direct imaging of each indentation to estimate crack length. The experimentally measured elastic, plastic, and fracture properties can serve as useful input for the modeling of electrochemical-mechanical coupling in LCO, and also inform the design of operating conditions and microstructures that limit or prevent mechanical damage during electrochemical cycling of lithium-ion batteries.

**Figure 2:** Fracture toughness K<sub>IC</sub> of single grains within LiCoO<sub>2</sub> as a function of grain orientation, measured by electron backscattering diffraction and quantified by a grain misorientation metric relating the crystallographic c-axis to the indentation normal z<sub>lab</sub>. No statistically significant correlation was identified between fracture toughness and grain orientation among these single crystals. Color-boxed insets are EBSD patterns of crystallographic orientation; sepia inset is an AFM image quantifying crack lengths emanating from the indentation corners, of length ~ 500 nm.



## 2. Chemomechanics of Highly Nonstoichiometric Oxides and Impact on Transport and Electrocatalytic Activity at Oxide Surfaces and Hetero-Interfaces

We focus on the chemomechanics of anion (oxygen) transport into and within transition metal oxides (TMOs) and rare earth oxides (REOs) relevant to solid oxide fuel cells (SOFC), electrolyzers and gas permeation membranes. Because fast oxygen exchange and oxygen ion conduction is a key requirement for these devices, applicable materials must contain a high density of mobile oxygen defect concentrations reaching as high as 10<sup>22</sup> - 10<sup>23</sup> cm<sup>-3</sup> in relevant fluorite (MO<sub>2-δ</sub>) and perovskite (ABO<sub>3-δ</sub>)

related structures. As a result of these high levels of nonstoichiometry and oxygen vacancy densities within the crystalline lattice, these oxides exhibit oxygen “dilatational breathing modes”. This defect chemistry effect on the mechanical stresses and strains within the material constitutes the first focus to be discussed in this part. The second focus is the reverse coupling – how induced mechanical stresses affect the defect chemistry, and the kinetics of anion transport and oxygen surface exchange. The magnitude of this chemo-mechanical coupling is known to depend on composition, oxygen partial pressure ( $p_{O_2}$ ), and mechanical stress, but systematic studies probing quantitatively the mechanisms of such coupling were lacking prior to our research in COFFEI.

i) **Chemical Dilation in Fluorite and Perovskite Oxides:** The resultant lattice dilation upon reduction of the material is determined either by in-situ x-ray diffraction or dilatometry and then coupled with the knowledge of nonstoichiometry to come up with values for the chemical expansion coefficient. Finally, an atomistic picture is obtained on how ion valence change and oxygen vacancy formation during the reduction process each contribute to chemical dilation and how a deeper understanding of this process could potentially be used to control and tune the chemical coefficient of expansion.

A self consistent defect equilibria and transport model, with predictive abilities, was developed for  $Pr_xCe_{1-x}O_{2-\delta}$  system. Our group has made significant progress in measuring and understanding the origin of chemo-mechanical coupling between dilation and oxygen non-stoichiometry ( $\delta$ ), termed chemical expansion. Figure 3 shows a plot of thermo-chemical expansion of  $Pr_{0.1}Ce_{0.9}O_{2-\delta}$  (10PCO) upon heating in air. Chemical strain,  $\epsilon_C = \alpha_C \Delta\delta$  is correlated to the change in oxygen stoichiometry ( $\Delta\delta$ ), by the chemical expansion coefficient  $\alpha_C$  found for 10PCO to be  $\sim 0.084$ .(3, 4)

We were able to deconvolute, for the first time, the key contributions to chemical expansion upon reduction of oxides, e.g. in the  $Pr_xCe_{1-x}O_{2-\delta}$  system described above. In order to elucidate the origin of, and potentially reduce, chemical expansion, our group undertook a computational investigation, going beyond the prior empirical modeling. Using molecular dynamics (MD), density functional theory, and empirical analysis, chemical expansion was found to arise from two mechanisms, a lattice dilation upon reduction of cations (e.g.  $Ce^{4+} \rightarrow Ce^{3+}$ ) and charge localization on the Ce cations, and a shrinkage upon oxygen vacancy formation (shown schematically in Figure 4).(5) This approach creates the opportunity to engineer and optimize these materials towards achieving a near zero coefficient of chemical expansion by compensating more effectively the two opposite trends.

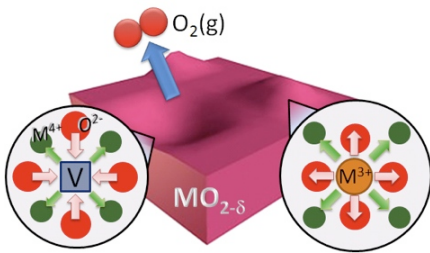


**Figure 4:** Schematic of chemical expansion origin – competition of oxygen and cation sublattice relaxations.

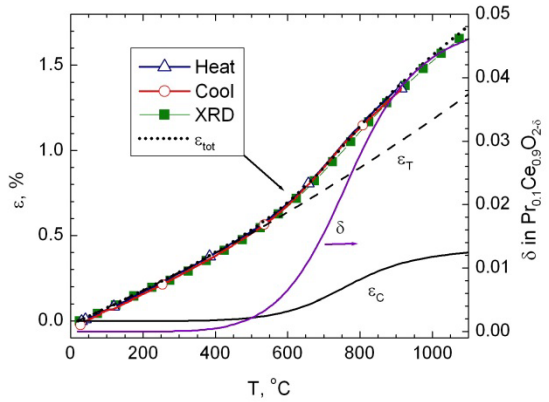


**Figure 3.** Equilibrium thermo-chemical expansion of  $Pr_{0.1}Ce_{0.9}O_{2-\delta}$  showing correlation of chemical expansion with changes in  $\delta$ .

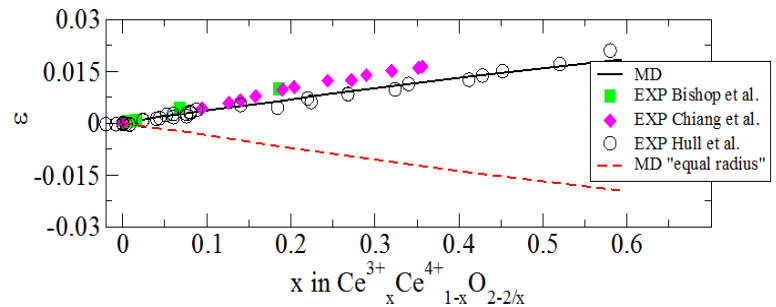


**Figure 5:** MD simulation of chemical expansion in  $CeO_{2-\delta}$  showing contributions from cation radius change and oxygen vacancy formation (solid line) and only vacancy formation (dashed line).

i) *Surface chemistry and electronic structure on SOFC cathodes – effects of high temperature and material strain state:* The surface structure and chemistry (i.e., cation concentration and oxygen non-stoichiometry) on transition metal oxides are dynamically driven by the surrounding harsh environment at high temperature, varied oxygen partial pressure and under electrochemical potentials. As a result, the surface can become quite a “different material” than the bulk phase. Cation segregation is a commonly observed and acknowledged phenomenon on the surface of SOFC cathode materials, such as on SrTiO<sub>3</sub> (STO), (La,Sr)MnO<sub>3</sub> (LSM) and SrTi<sub>1-x</sub>Fe<sub>x</sub>O<sub>3</sub> (STF)(6). Such deviations from the bulk nominal composition and phase can directly alter the surface electronic structure and the electrocatalytic activity of the surface. In addition, we have shown that lattice strain can also serve as a thermodynamic and kinetic driving force for the surface exchange and diffusion of oxygen on SOFC cathodes, by influencing the interface cation chemistry, surface oxygen stoichiometry, electrical conductivity, and surface and bulk ionic transport. However, *in situ studies of how the key descriptors of oxygen reduction reaction (ORR) activity evolve with temperature, oxygen pressure and strain state have been largely missing on SOFC cathodes, except from few recent studies, including our work.* This is because the operating conditions of SOFC cathodes at elevated temperatures and reactive gas pressures are too harsh for the traditional vacuum-based surface science techniques. In-depth probing of the surface electronic structure on SOFC cathodes, considering the effects of high temperature, oxygen pressure and material strain state, is essential towards advancing our understanding and control of the ORR activity on them. Highlights from our research are summarized below. In particular we uncovered for the first time:

- How the surface electronic structure of a model perovskite oxide system, La<sub>0.8</sub>Sr<sub>0.2</sub>CoO<sub>3</sub> thin films, evolves as a function of temperature, and how this transition is affected by lattice strain,
- How surface structure and cation chemistry affect ORR activity on the basis of electronic structure measured at high temperatures, on the model perovskite SrTi<sub>1-x</sub>Fe<sub>x</sub>O<sub>3</sub> thin films,
- How dissimilar interfaces enable vastly accelerated oxygen reduction kinetics by electron injection from one phase to another, on the model heterosystem of La<sub>0.8</sub>Sr<sub>0.2</sub>CoO<sub>3</sub> and La<sub>0.8</sub>Sr<sub>0.2</sub>CoO<sub>3</sub> (LSC<sub>214/113</sub>) multilayers (Figure 6).

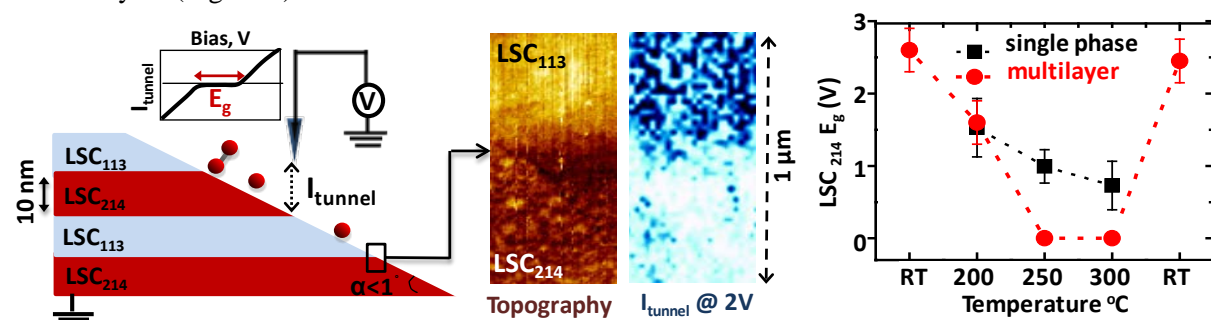


**Figure 6 :** (Left) Schematic of the novel *in situ* approach to probe the electronic structure across the interface of nanoscale multilayers at high temperature and in oxygen environment, combining grazing incidence focused ion beam milling and scanning tunneling microscopy/spectroscopy. Using this approach, we investigated the LSC<sub>214/113</sub> multilayer (Center), and discovered the electronic activation of LSC<sub>214</sub> (by disappearance of its band gap, E<sub>g</sub>) at high temperature (Right), leading to an ultra-high ORR activity. (7)

- W. H. Woodford, Y.-M. Chiang, W. C. Carter, *Journal of The Electrochemical Society* **157**, A1052 (2010).
- M. Qu, W.H. Woodford, J. M. Maloney, W.C. Carter, Y-M. Chiang, K. J. Van Vliet., *Advanced Energy Materials* (2012).
- Y. Kuru, S. R. Bishop, J. J. Kim, B. Yildiz, H. L. Tuller, *Ecs Transactions* **35**, 1131 (2011).
- S. R. Bishop, T. S. Stefanik, H. L. Tuller, *J Mater Res* **27**, 2009 (Aug, 2012).
- D. Marrocchelli, S. R. Bishop, H. L. Tuller, B. Yildiz, *Advanced Functional Materials* **22**, 1958 (2012).
- Y. Chen, W. Jung, Z.Cai, H. L. Tuller and B. Yildiz, *Energy Environmental Science*, 2012, 5, 7979, (2012).
- Y. Chen, Z. Cai, Y. Kuru, W. Ma, H L. Tuller and B. Yildiz *et al.*, *Advanced Energy Materials*, (2013).

# COMBINED ATOMISTIC AND MESOSCOPIC STUDY OF DEFORMATION OF BODY-CENTERED-CUBIC TRANSITION METALS: EFFECTS OF ALLOYING AND MAGNETISM

V. VITEK

Department of Materials Science and Engineering, University of Pennsylvania, Philadelphia, PA  
19104; e-mail: vitek@seas.upenn.edu

## 1. Program Scope

The principal goal of this research is to provide a fundamental insight into the deformation and fracture mechanisms in body-centered-cubic (BCC) transition metals. BCC transition metals and their alloys are the most important materials employed in the broad range of technologies associated with energy production and conversion. Moreover, from the perspective of fundamental science, these materials have a mixed nearly free electron and covalent bonding, which leads to significant directional bonds. This presents a formidable scientific challenge for atomic level studies of extended defects.

The basic precursor of any atomistic study is a description of atomic interactions that reflects correctly the physics of bonding in a given material. In transition metals the partially filled *d*-band invokes the dependence of the energy on bond angles and in the present research we are developing a new version of bond-order potentials (BOPs) that reflect well this bonding together with bonding by nearly free *s* and *p* electrons

The link between bonding on atomic scale and the mechanical response of a material to loading can only be established via a multiscale approach. In the case of BCC metals we concentrate on atomistic modeling of the structure and glide of  $1/2\langle 111 \rangle$  screw dislocations that control the plastic behavior of these metals. This is followed by the development of a mesoscopic model of dislocation glide at finite temperatures the part of which is determination of the Peierls barrier employing the nudged-elastic band (NEB) method. The novel concept is that the Peierls potential is a function of the applied stress tensor. Finally we also investigate the reasons for the variability of slip systems in BCC based B2 intermetallic alloys based on transition metals.

## 2. Recent Progress

### 2.1. Development of new bond-order potentials (BOPs) for BCC transition metals

In transition metals the cohesion arises from a mixture of nearly free electron bonding of *s* and *p* electrons and directional bonds resulting from the interaction between the localized valence *d*-electrons. The *d*-electrons induced bonding can be well formulated in terms of bond-order potentials (BOP) that are based on the tight-binding method. Apart from the quantum mechanical character, a very significant advantage of BOPs is that modeling can be performed in real space and periodic boundary conditions can be avoided.

Within the BOP scheme the binding energy of non-magnetic transition metals is a sum of the covalent attractive contribution and the repulsive contribution. The attractive bond energy is controlled by the matrix elements of the two-center tight-binding Hamiltonian and the bond

order, the physical meaning of which is half of the difference between the number of electrons in bonding and anti-bonding states or twice the density matrix. The latter is evaluated using the suit of computer codes available as the Order N (OXON) package that is employed in all our calculations. The Hamiltonian elements and their dependence on the distance between the atoms is obtained using DFT based calculations and thus the attractive part of the covalent energy is evaluated within the tight-binding approximation accurately and fully quantum mechanically. In contrast, the repulsive part of the bonding energy is purely empirical and cannot be deduced directly from DFT calculations. In our present research we have introduced new bond integrals that do not require any screening and a new form of the environment dependent repulsion based on the analytically derived overlap repulsion of p electrons. The latter was done by Aoki and Kurokawa (J. Phys.: Cond. Matter 19, 136228, 2007) by using the non-orthogonal TB model for the systems composed of closed-shell atoms of argon, which in this case accounts principally for the overlap repulsion of p electrons. In this way the environmentally dependent repulsive term was obtained that can be well approximated by the analytical many-body potential describing repulsion between atoms i and j:

$$\Phi_{ij}(R_{ij}; \lambda_i + \lambda_j) = \exp(-\lambda_i) \exp(-\lambda_j) V_R(R_{ij}) \quad (1)$$

where

$$\lambda_i = \sum_{k \neq i} g \exp(-\nu R_{ik})$$

is an environmentally dependent function; summation over k extends over the neighbors interacting with the atom I; constants like g and  $\nu$  are determined by fitting.  $V_R$  is a pair-wise function describing a direct interaction between atoms i and j. Our conjecture is that this functional form of the many-body repulsive potential can be employed to describe the repulsive term in BOPs for transition metals. The reason is that due to close-shell electronic configuration of argon the total energy term accounts principally for overlap repulsion of p electrons and, in transition metals, the environment dependent repulsion has the same physical origin.

In the present research we have developed BOPs for Mo, W, Ta, Nb, V and Cr. We are also in the process of developing the BOP for magnetic iron. The transferability of the potentials has to be thoroughly tested since they are to be used in environments very different than the ideal lattice. The testing has been performed by calculating the energy of alternative structures, vacancies and evaluating the energy when deforming the structure along several transformation paths. As an example of testing we show the results of calculation of tetragonal deformation path for tungsten. It is seen from Fig. 1 that there a close agreement with DFT calculations and thus the BOP is very well transferable to situations far removed from the ideal BCC lattice.

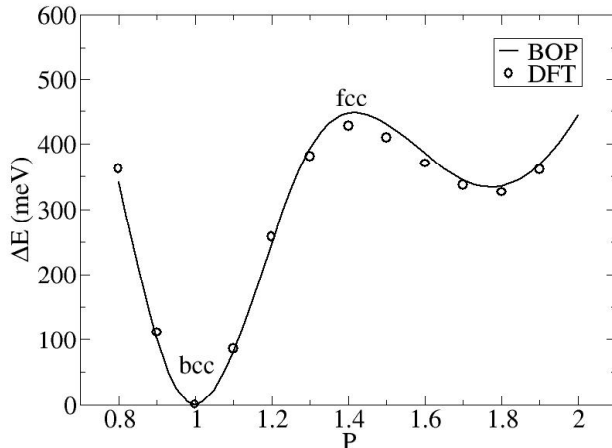


Fig. 1. The tetragonal path for W that corresponds to extension along the [001] direction and contraction along the [100] and [010] directions that leads to deformation from BCC to FCC structure. This path can be described by a parameter  $p$  so that the vector along [001] is proportional to  $p^{2/3}$  and along the [100] and [010] directions to  $p^{-1/3}$ . The BCC and FCC lattices correspond to  $p = 1$  and  $\sqrt{2}$ , respectively.

## 2.2. Study of $1/2[111]$ screw dislocations in BCC transition metals

The non-planar core of  $1/2[111]$  screw dislocations in BCC metals was fully confirmed by many atomistic studies but never observed experimentally. We addressed the question of observation by HREM in a thin foil in which the effects of the surface relaxation displacements (Eshelby twist) is very important. These relaxations are large and the conclusion is that a complete description of the core cannot be attained at present from the HREM analysis. Details of this study are summarized in our recent publication in the Philosophical Magazine.

An essential development in the studies of the glide of dislocations is the analysis of their thermally activated motion via formation and propagation of pairs of kinks. For this purpose we need to know the full shape of the Peierls barrier. We have carried out evaluation of this barrier using the Nudged Elastic Band (NEB) model and found that the usual application of the NEB does not lead to the correct Peierls barrier. Hence, we introduced a significant modification in which the NEB method is applied only to a small number of degrees of freedom that determine closely the position of the dislocation, while all the other atomic degrees of freedom are relaxed via standard molecular statics. In this case the Peierls stress determined by the barrier agrees to within 8% with that obtained in the atomistic study of the dislocation glide under the applied shear stress. In this approach the dimensionality of the problem is severely reduced and thus the calculation is much faster and at the same time more precise. Details of this study are presented in our recent paper in Modelling and Simulation in Materials Science and Engineering.

## 2.3. Factors determining the choice of the slip direction in B2 intermetallics.

Unlike in elemental metals BCC metals, in B2 intermetallics different slip directions have been observed in different B2 compounds.. In order to identify the reasons for different slip directions in different compounds we carried out calculation of (110)  $\gamma$ -surfaces for CuZn, FeAl, NiAl, FeTi CoTi, NiTi and FeGa using the DFT (VASP ). Only in CuZn and FeTi the  $1/2\langle 111 \rangle$  fault, usually considered as the APB in B2 alloys, was found to be metastable. In all other compounds studied the deviation away from  $1/2\langle 111 \rangle$  is significant. Using these results for possible stacking-fault like defects we carried out an analysis of dissociations of screw  $\langle 111 \rangle$  and  $\langle 001 \rangle$  dislocations on  $\{101\}$  planes. We associated the largest mobility of dislocations with their widest planar splitting and assumed that screw dislocations that do not dissociate are sessile. Based on this analysis we concluded that  $\langle 111 \rangle$  is the dominant slip direction in CuZn, FeGa and FeAl. On the other hand in CoTi, FeTi and NiTi the  $\langle 001 \rangle$  slip dominates and this is also the dominant slip direction in NiAl. All these predictions agree with experimental observations. Details of this study are presented in our recent paper in Acta Materialia.

## 3. Future plans

Until now most of the development dealt with elemental BCC transition metals. However, pure metals are rarely used in structural applications because they do not have the needed combination of properties such as strength, ductility, corrosion resistance, etc. Alloying is usually needed to provide the right balance. Hence, the direction of the future research will be the development of BOPs for alloys based on the BCC transition metals, which includes magnetic iron and its alloys. The substitutional alloys we shall consider are Ta-W, Mo-Nb and, in particular Fe-Cr. The very important aspect is that these alloys are disordered and this will be taken into account via composition-dependent interatomic potentials. Another class of alloys for which we plan to develop BOPs is B2 ordered compounds in which the planar faults have been investigated in our present research. All these potentials will be employed in atomistic studies of

dislocations and their glide as well as in investigations of grain boundaries and other interfaces that play important role in the mechanical behavior.

On the mesoscopic level, we shall investigate the glide of dislocations at finite temperatures by developing models with input from atomistic studies, in particular using the modified NEB method, developed in our program, to determine the Peierls barrier and its stress dependence. Besides analysis of dislocation motion in alloys we shall analyze the dislocation motion on nano scale, such as plasticity of nano pillars and on the scale encountered in nano indentation. In both cases the stress field in which dislocations move is much more complex than in the uniaxial tension/compression. As our previous studies revealed, it is the full stress tensor that plays essential role in the glide of dislocations and investigation of the effect of complex stress field encountered in nano experiments will be one of our goals.

#### 4. Publications resulting from the DOE sponsored research

1. R. Gröger and V. Vitek: Temperature and strain rate dependent flow criterion for bcc transition metals based on atomistic analysis of dislocation glide, *Int. J. Materials (Zeit. Metallkunde)* **100**, 315-321, 2009.
2. M. Cak, M. Sob, V. Paidar and V. Vitek: Stacking Faults and Dislocation Dissociation in MoSi<sub>2</sub>, in *Advanced Intermetallic-Based Alloys for Extreme Environment and Energy Applications*, edited by M. Palm, B.P. Bewlay, M. Takeyama, J.M.K. Wiezorek, Y-H. He, MRS Symposium Proceedings, Vol. **1128**, U7-10, 2009.
3. R. Gröger and V. Vitek: Directional versus central-force bonding in studies of the structure and glide of 1/2<111> screw dislocations in BCC transition metals, *Philos. Mag.* **34-36**, 3163-3178, 2009.
4. V. Paidar, M. Cak, M. Sob and V. Vitek: Theoretical analysis of dislocation splitting in MoSi<sub>2</sub>, *Journal of Physics: Conference Series* **240**, 012007-6, 2010.
5. V. Paidar, Yi-Shen Lin, M. Cak, and V. Vitek: Why is the slip direction in CuZn and FeAl different than in CoTi, *Intermetallics* **18**, 1285-1287, 2010.
6. V. Vitek: Atomic level computer modeling of crystal defects with emphasis on dislocations: Past, present and future, *Prog. Mater. Sci.* **56**, 577-585, 2011.
7. T. Kana, M. Sob and V. Vitek: Ab initio study of phase transformations in transition-metal disilicides, *Intermetallics* **19**, 919-926, 2011.
8. T. Kana, M. Sob and V. Vitek: Transformation Paths in Transition-metal Silicides, *Key Engineering Materials* **465**, 61-64, 2011.
9. R. Gröger, K. J. Dudeck, P.D. Nelist, V. Vitek, P. B. Hirsch and D. J. H. Cockayne: Effect of Eshelby twist on core structure of screw dislocations in molybdenum: atomic structure and electron microscope image simulations, *Philos. Mag.* **91**, 2364-2381, 2011.
10. Yi-Shen Lin, M. Cak, V. Paidar, and V. Vitek: Why is the slip direction different in different B2 alloys?, *Acta Materiala* **60**, 881-888, 2012.
11. R. Gröger and V. Vitek: Constrained nudged elastic band calculation of the Peierls barrier with atomic relaxations, *Modelling Simul. Mater. Sci. Eng.* **20**, 035019-13, 2012.
12. Yi-Shen Lin, M. Mrovec, and V. Vitek: New bond-order potentials for study of defects in BCC transition metals, Materials Research Society, Symposium TT: Defects and Microstructure Complexity in Materials, Boston 2012.
13. R. Gröger and V. Vitek: Stress dependence of the Peierls barrier of 1/2<111> screw dislocations in BCC metals, *Acta Materiala*, to be published.

## Localized Deformation and Intergranular Fracture of Irradiated Alloys under Extreme Environmental Conditions

Gary S. Was

2355 Bonisteel Blvd., University of Michigan, Ann Arbor, MI 48109 [gsw@umich.edu](mailto:gsw@umich.edu)

Ian M. Robertson

1304 West Green Street MC-246, University of Illinois, Urbana, IL 61801 [ianr@uiuc.edu](mailto:ianr@uiuc.edu)

Diana Farkas

201A Holden Hall, Virginia Tech, Blacksburg, VA 24061, [diana@vt.edu](mailto:diana@vt.edu)

### Program Scope

The objective of this project is to determine the processes by which localized deformation in irradiated materials leads to intergranular cracking in alloys in aggressive environments at high temperature. We will use the Fe-Cr-Ni-based austenitic alloy system as the model system for studying the interaction between localized deformation bands and grain boundaries as these alloys are well-characterized and exhibit a widely varying IASCC response. We will use proton irradiation to induce localized deformation in the form of well-defined dislocation channels that will pre-determine the location of channel-boundary interactions. Having a small number of known sites for dislocation-grain boundary interactions greatly facilitates their study. We will employ electron-backscattered diffraction including using cross-correlation based techniques to determine strains, focused ion-beam milling and transmission electron microscopy to identify, select, fabricate samples for detailed microstructural characterization as well as for in-situ deformation at high temperature in the TEM. The experimental effort will be combined with atomic level molecular statics and molecular dynamics studies using massively parallel simulations to model the exact configuration and orientation used in the experiments. The simulations will provide much needed insight as to how grain boundaries operate as dislocation sources, ejecting vast numbers of dislocations into the grain. Specifically, this project will combine simulation and experiments to achieve the following sub-objectives:

- Determine the modes of interaction between dislocations and grain boundaries as a function of temperature.
- Identify the role of defect-free dislocation channels as the deformation mode in irradiated metals.
- Determine how dislocation channels nucleate at grain boundaries as a function of temperature.
- Identify the importance of dislocation emission vs. channel termination at grain boundaries in establishing the conditions favoring crack initiation.
- Elucidate the role of grain boundary orientation on dislocation – grain boundary interaction.
- Determine the impact of local strains on the resulting failure mechanism.
- Mechanistically couple intergranular stress corrosion cracking to localized deformation at grain boundaries.

Our approach is to couple TEM characterization of dislocation interactions with grain boundaries; *in situ* deformation experiments at high temperature in the TEM; EBSD for misorientation determination coupled with cross-correlation analysis methods to determine the strain tensor, and atomic force microscopy to measure surface displacement with molecular statics and molecular dynamics to determine the underlying mechanisms controlling irradiation-assisted stress corrosion cracking that is assessed by experiments on irradiated samples in a high temperature, aggressive environment. Austenitic Fe-Cr-Ni-based alloys with a systematic and predetermined localized deformation structure will be used as these are well characterized and the susceptibility to cracking controlled through the composition. As solute additions are known to have profound effects on the grain boundary deformation and cracking behavior, their effect will also be determined. Through this multiscale and multidisciplinary approach, the modes of

grain boundary-dislocation interaction will be directly related to IGSCC susceptibility. In the current project period, we will focus on two specific sub-objectives: 1) Channel dislocation creation and termination at grain boundaries, and 2) linkage between channel – grain boundary interaction and IASCC.

### Recent Progress

Recent work has shown that irradiation assisted stress corrosion cracking in irradiated austenitic alloys follows several well defined dependencies. The strongest dependence is that the closer is the grain boundary surface trace is to the normal to the applied tensile stress, the higher the incidence of cracking. This behavior differs substantially from SCC in nickel-base alloys in which cracking is maximized on boundaries with their trace at 45° to the tensile stress. Beyond this, the following are also observed [1]:

- Random high-angle grain boundaries exhibit a cracking frequency 4 times that of special boundaries,
- Boundaries in which adjacent grains are characterized by low (high) Schmid (Taylor) factors are much more likely to crack than those with high (low) Schmid (Taylor) factors.
- Grain boundary cracking is 2.5 more likely when a dislocation channel terminates at the boundary than when there is clear slip transmission across the boundary.
- Cracks nucleate directly at grain boundary-channel intersections.

The Schmid Modified Grain Boundary Stress (SMGBS) model [2] predicts that cracking also peaks for grain boundaries oriented normal to the tensile stress and that the stress at required for cracking is between 0.4 and 0.6 of the yield stress, in agreement with a large database on the stress required for cracking of irradiated stainless steels in primary water. These data collectively indicate that the normal stress is controlling and that local stresses may be well above the nominal applied stress at the dislocation-channel intersection. As a result, attention has focused on the stress and strain states at the vicinity of this intersection.

Scaling between the atomistic simulation results and the macroscale assessment of slip trace interactions and cracking of grain boundaries is achieved by two approaches: post-mortem characterization of the bulk deformed material and dynamic deformation experiments in the TEM of irradiated material. For the former, the samples are extracted from specific locations using focused ion beam machining. For the latter, the samples are irradiated and strained in-situ in the IVEM-accelerator facility at Argonne National Laboratory. This approach allows the interaction of the channel dislocations with the grain boundary to be directly observed with the process of slip transfer being analyzed in terms of the established slip transfer criteria. The basic premise being probed through this effort is that it is the interaction of the channel dislocations with the grain boundaries and the inability of slip to be transferred that contributes to the local disruption of the oxide and the nucleation and propagation of the incipient intergranular crack. Figure 1 shows the outcome of interactions of dislocations with two different grain boundaries in irradiated material. The first interaction shows dislocations impinging on a  $\Sigma 3$  twin boundary, which produced three interactions identified as 1a – 1c. Dynamic observations show that system 1b operates but emits only a few dislocations before systems 1a and 1c dominate the response. Analysis shows that system b experiences the highest resolved shear stress, but generates a grain boundary dislocation with a large Burgers vector. Despite the high local resolved shear stress, limited activity of this system is anticipated because of the increase in strain energy density in the grain boundary. System 1a experiences a smaller resolved shear stress and generates a grain boundary dislocation with a small Burgers vector. System 1c is glissile along the twin plane. This result, which in general is consistent with analysis of other interactions, suggests the criteria for predicting the activated slip systems is as in unirradiated material but the activated slip system must experience a shear stress high enough to drive the nucleated dislocations through the obstacle field. It also suggests that if system 1a did not experience a sufficiently high resolved shear stress, no or very limited transmission would occur. The second interaction shows a much different response, Figure 1c and 1d, as there is no evidence of slip transmission through the grain boundary, just the formation of dislocations against the boundary. Instead of relieving the accumulated stress by the absorption of dislocations, a small crack is observed to nucleate. This new result was unexpected and

analysis to determine why this particular boundary responded differently to all others that have been observed is in progress.

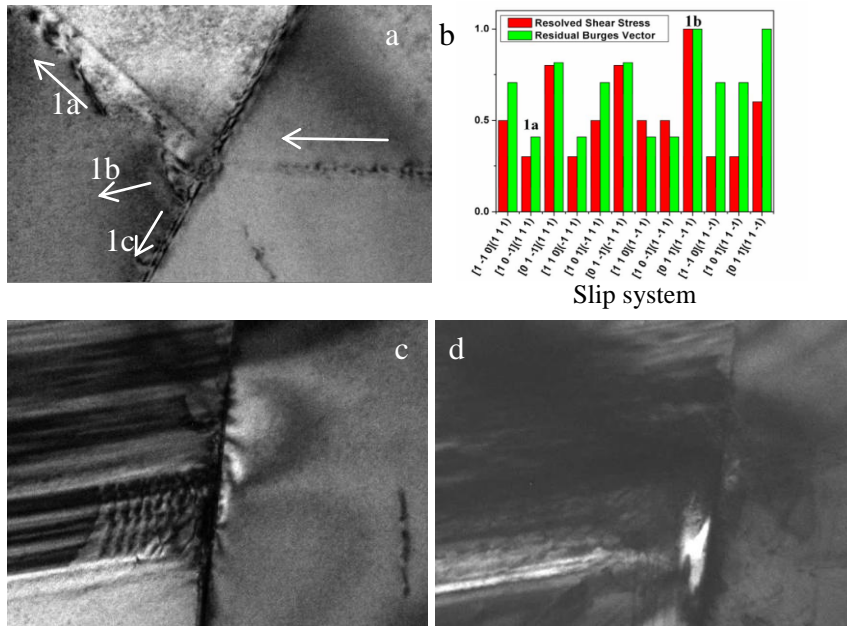


Figure 1. a) Slip transmission through a  $\Sigma 3$  twin boundary; b) the magnitude of the residual grain boundary dislocation created by the transmission event and the local resolved shear stress. c) dislocation pile-up being formed at a random grain boundary; and d) the nucleation of a crack at the grain boundary. There was no evidence of

Since the local stresses and strains at the dislocation channel-grain boundary (DC-GB) intersection are deemed critical to understanding slip transfer and cracking at the grain boundary, we have developed DIC and high-resolution electron backscattering detection (HR-EBSD) to provide a quantitative description in irradiated samples. A 304SS sample was irradiated to 5 dpa at 360°C and EBSD was used to characterize the grain boundary character followed by deposition of gold nanoparticles prior to straining to 3.5% in an Ar environment at 288°C. Digital image correlation (DIC) coupled with confocal laser microscopy were

used to quantify the plastic strain tensor in the channel-boundary intersection. High-resolution electron backscattering detection (HR-EBSD) was used to quantify the elastic stress and strain tensors. A total of 25 DC-GB intersections were characterized. Of these, 10 exhibited slip transmission across the boundary and 15 exhibited discontinuous slip. Displacement along the grain boundary was used as an indication of the amount of plastic strain and it was found to be higher in boundaries across which slip was characterized as discontinuous. The same was true for elastic strains in that DC-GB intersections. Boundaries at which slip was discontinuous exhibited higher elastic strains than when slip was continuous. An example of a DC-GB exhibiting discontinuous slip and with high plastic and elastic strains is shown in Figure 2. Figure 3 shows that of the 10 DC-GB intersections exhibiting continuous slip, only 3 had high values of both elastic and plastic strains. Of the 15 DC-GB intersections exhibiting continuous slip, 9 had high values of both elastic and plastic strains. Also shown is the fraction of boundaries that cracked as a function of slip continuity following straining of a companion sample in 288°C normal water chemistry (NWC) to 6%.

Simulations of strain localization and crack formation were performed in digital samples created to mimic the experimental ones. The samples were created with exactly the same misorientations and similar grain boundary planes as the ones tested experimentally. The samples were clusters of about 8 grains and typically contained about 4 million atoms. The grain boundary structures were first relaxed using molecular dynamics and an empirical interatomic potential describing fcc materials. Computational limitations dictated a grain size of about 30 nm and a strain rate for deformation along the horizontal axis of  $3.3 \times 10^8 \text{ s}^{-1}$ . Figure 4 shows an example of a cluster (cluster D) where the experimentally measured microstructure (a) was recreated (b) and subject to horizontal tensile deformation of 9% (c).

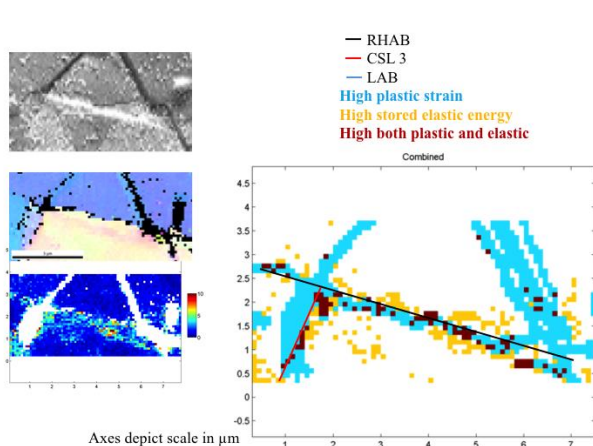


Figure 2. Discontinuous DC-GB intersection in irradiated 304SS following 3.5% strain in 288°C Ar.

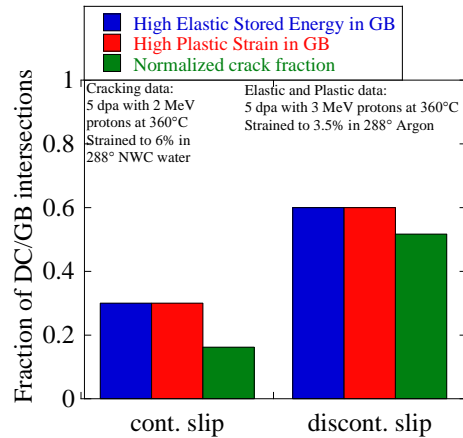


Figure 3. Fraction of grain boundaries showing high elastic strain, high plastic strain and IG fracture by slip continuity.

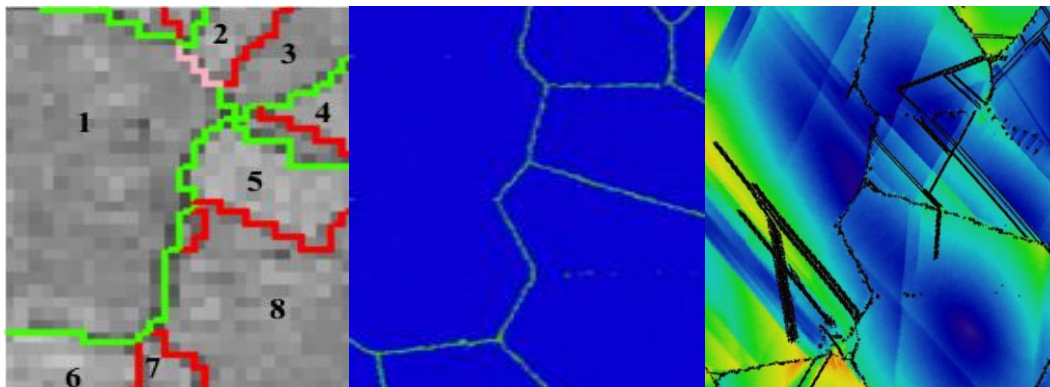


Figure 4. Experimentally measured microstructure (left) was recreated (center) and subject to horizontal tensile deformation of 9% (right).

Three main features were analyzed in these clusters: 1) Dislocation transmission through a  $\Sigma=3$  boundary 2) strain localization in the grain boundary region and 3) crack nucleation along the boundaries. Dislocation transmission through a  $\Sigma=3$  boundary in this cluster (Grain boundary 5-8 in cluster D) was analyzed in a geometry that corresponded to one observed experimentally in TEM samples (Fig. 1a). The boundary is of the same misorientation. The relationship of the incoming and outgoing Burgers vector and the magnitude of the residual Burgers vector in the boundary match that in the experiment.

### Future Plans

Future plans include extension of DIC and HR-EBSD to characterize additional DC-GB intersections and SCC tests to correlate cracking with the local stress fields. Simulation will concentrate on the role of additional defects and/or impurities present in the grain boundaries and inside the grains.

### References

1. M. D. McMurtrey, G. S. Was, L. Patrick and D. Farkas, "Relationship Between Localized Strain and Irradiation Assisted Stress Corrosion Cracking in an Austenitic Alloy," *Mater. Sci. Engin. A* 528 (2011) 3730-3740.
2. E. A. West and G. S. Was, "A Model for the Normal Stress Dependence of Intergranular Cracking of Irradiated 316L Stainless Steel in Supercritical Water," *J. Nucl. Mater.* 408 (2011) 142-152.

## Electronic and Atomic Response of Ceramic Structures to Irradiation

**Principal Investigator:** Weber, William J.

**Email:** [weberwj@ornl.gov](mailto:weberwj@ornl.gov)

**Address:** Oak Ridge National Laboratory  
1 Bethel Valley Road  
Oak Ridge, TN 37831-6138

**Senior Investigators:** Chisholm, Matthew F. (Oak Ridge National Laboratory)  
Cooper, Valentino R. (Oak Ridge National Laboratory)  
Specht, Eliot D. (Oak Ridge National Laboratory)  
Zhang, Yanwen (Oak Ridge National Laboratory)  
Xiao, Haiyan (University of Tennessee)

**Students:** 3 Postdoctoral Fellows, 1 Graduate Student

### Scope:

The overarching goal of this research is to understand, predictively model, and ultimately control the dynamic response of ceramic structures to irradiation at the level of electrons and atoms. The design of radiation tolerant materials and creation of new functional materials by ion beam modification demand a comprehensive understanding and predictive models of energy transfer and exchange processes at the level of electrons and atoms. To achieve this goal, this research will focus on two specific aims: (1) the dynamic and coupled response of electronic and atomic structures to single ion events; and (2) the collective effects from the coupled dynamics of electronic and atomic processes on damage accumulation, phase transformations and recovery processes for multiple ion events over a broad range of conditions. Novel experimental techniques and computational approaches are integrated to investigate the separate and coupled dynamics of electronic and atomic processes over a range of irradiation conditions to elucidate the underlying mechanisms. This research will leverage unique experimental capabilities for measuring *in situ* the response of ceramics to ion irradiation and to individual single ion events, as well as the unique materials synthesis, characterization and modeling resources at Oak Ridge National Laboratory. The scientific advances from the work will not only lead to the design of self-healing and radiation tolerant materials for advance nuclear energy systems, but will provide the foundation for the design and control of material properties that enable broad advances in sustainable energy technologies and national security.

### Recent Progress:

A new ion irradiation capability has been made available and being utilized to investigate the fundamental nature of ion-solid interactions in ceramics and the role of energy loss by energetic ions to target electrons on fundamental damage production, accumulation and recovery processes. Recent results confirm that the electronic energy loss from 20 MeV Pt<sup>+</sup> ions induces recovery of a pre-damaged state created by 550 keV Si<sup>+</sup> ions.

A novel large-scale molecular dynamics approach has been developed and applied to investigate the effects of electronic and nuclear energy loss of Au ions, with energies from 0.5 to 100 MeV, on damage production in amorphous silica; the results confirm the experimentally observed synergy of electronic and nuclear energy loss on damage production in amorphous silica. A similar molecular dynamics

approach has demonstrated that electronic energy loss by ions can induce defect recovery and epitaxial recrystallization in silicon carbide, confirming experimental observations of irradiation-induced recovery in silicon carbide from the electronic energy loss.

Density functional theory has been used to investigate the effects of Ti point defects on the electronic structure of  $Y_2Ti_2O_7$ , and the results reveal distorted geometries around the Ti vacancy and interstitial, along with oxygen holes and Ti electrons. Analysis of the electronic structure suggests that the Ti vacancy and interstitial are acceptor and donor type defects, respectively.

*Ab initio* molecular dynamics is a powerful tool in the study of low-energy recoil events in ceramics, both for determining threshold displacement energies with *ab initio* accuracy and for understanding the role of charge transfer and redistribution on defect production and stable defect configurations. This method has been employed in the study of low-energy recoil events in  $Gd_2Zr_2O_7$  and  $Gd_2Ti_2O_7$ . Due to charge transfer processes between the recoil and lattice atoms, the threshold displacement energies are lower than those determined by classical molecular dynamics methods using fixed-charge interatomic potentials. In addition to normal interstitial configurations found by molecular dynamics, two additional stable configurations for cation interstitials are found in these structures due to charge redistribution: Gd, Zr and Ti interstitials occupying bridge sites between cations; and Zr and Ti interstitials occupying the vacant 8a oxygen site.

A hybrid functional has been optimized in order to accurately describe the nature of neutral and charged defects in silicon carbide within the framework of density functional theory. It provides a better description of the band structures in silicon carbide than conventional exchange-correlation functionals and other popular hybrid functionals. High transferability has been demonstrated for different silicon carbide polytypes, silicon and diamond. This hybrid functional is being employed to determine formation energies and electronic structures of neutral and charged intrinsic defects in silicon carbide.

#### **Future Plans:**

The additive and competitive radiation effects due to electronic and nuclear energy loss from energetic ions over the range from 0.5 MeV to 1 GeV will be investigated through the integration of experimental and computational methods. *In situ* measurements, based on Rutherford Backscattering in channeling geometry, will characterize the effects of single and multiple ion events in the range of 0.5 to 30 MeV at temperatures from 160 to 500 K using our new ion irradiation capabilities. The separate effects of electronic energy loss on damage production and recovery will be explored using unique pre-damaged states in single crystals. Benchmarking experiments on the effects of purely electronic energy loss will be performed with ions at energies from 100 to 1 GeV using collaborator facilities in France, Germany, Australia and China. Initial studies will focus on SiC, MgO,  $ZrO_2$ , and  $SrTiO_3$ .

The novel large-scale molecular dynamics approach that has been developed will be used to model the combined effects of atomic displacement processes and electronic energy losses in these same materials over the energy range from 0.5 MeV to 1 GeV.

In ceramics with strong luminescence signatures for vacancy defects, *in situ* luminescence measurements at cryogenic temperatures will be used to study the nature, production and recovery of vacancy defects. In the future, this will be combined with *in situ* Raman spectroscopy.

The formation, migration and electronic structures of neutral and charged intrinsic defects in silicon carbide will be determined using the hybrid functional developed under this project. In particular, the change in electronic structure at stacking faults, faulted loops and grain boundaries on intrinsic defect behavior will be investigated.

The formation and migration energies of neutral and charged intrinsic defects in  $\text{ZrO}_2$  and  $\text{MgO}$  will be investigated using density functional theory approaches in order to better understand the faster kinetics of some irradiation effects processes at lower temperatures.

Low energy recoil events, interstitial defect configurations, and charge redistribution will be investigated in  $\text{MgO}$  and  $\text{SrTiO}_3$  using *ab initio* molecular dynamics and density functional theory. A hybrid density functional for  $\text{SrTiO}_3$  from the literature will be employed to study the electronic structure of neutral and charged defects in  $\text{SrTiO}_3$ .

#### Publications:

1. J.-M. Costantini, F. Beuneu, S. Morrison-Smith, R. Devanathan, and W. J. Weber, "Paramagnetic defects in electron-irradiated yttria-stabilized zirconia: Effect of yttria content," *J. Applied Physics* **110** [12], 123506 (2011).
2. W. J. Weber, Y. Zhang, H. Y. Xiao, and L. M. Wang, "Dynamic recovery in silicate-apatite structures under irradiation and implications for long-term immobilization of actinides," *RSC Advances* **2** [2], 595-604 (2012).
3. M. Ishimaru, I. O. Usov, Y. Zhang, and W. J. Weber, "Superlattice-like stacking fault array in ion-irradiated GaN," *Philosophical Magazine Letters*, **92** [1], 49-55 (2012).
4. W. J. Weber, Y. Zhang, and L. M. Wang, "Review of dynamic recovery effects on ion irradiation damage in ionic-covalent materials," *Nucl. Instrum. and Methods in Physics Research B* **277**: 1-5 (2012).
5. J. Du, R. Devanathan, L. R. Corrales, and W. J. Weber, "First-principles calculations of the electronic structure, phase transition and properties of  $\text{ZrSiO}_4$  polymorphs," *Computational and Theoretical Chemistry* **987**: 62-70 (2012).
6. H. Y. Xiao, Y. Zhang, and W. J. Weber, "Enhanced electronic conductivity by controlled self-doping in pyrochlores," *Phys. Chem. Chem Phys.* **14** [18]: 6556-6560 (2012).
7. Y. Katoh, L. L. Snead, I. Szlufarska, and W. J. Weber, "Radiation effects in SiC for nuclear structural applications," *Current Opinion in Solid State and Materials Science* **16** [3]: 143-152 (2012).
8. H. Y. Xiao, Y. Zhang, and W. J. Weber, "Impact of point defects on electronic structure in  $\text{Y}_2\text{Ti}_2\text{O}_7$ ," *RSC Advances* **2** [18]: 7235-7240 (2012).
9. C. Lan, J. M. Xue, Y. Zhang, J. R. Morris, Z. Zhu, Y. Gao, Y. G. Wang, S. Yan, and W. J. Weber, "Molecular dynamics simulations of ion range profiles for heavy ions in light targets," *Nucl. Instrum. and Methods in Physics Research B* **286**: 45-50 (2012).
10. A. Debelle, M. Backman, L. Thomé, W. J. Weber, M. Toulemonde, S. Mylonas, A. Boule, O. H. Pakarinen, N. Juslin, F. Djurabekova, K. Nordlund, F. Garrido, and D. Chaussende, "Combined experimental and computational study of the recrystallization process induced by electronic interactions of swift heavy ions with silicon carbide crystals," *Physical Review B* **86** [10]: 100102 (2012).
11. M. Backman, F. Djurabekova, O. H. Pakarinen, K. Nordlund, Y. Zhang, M. Toulemonde, and W. J. Weber, "Cooperative effect of electronic and nuclear stopping on ion irradiation damage in silica," *J. Physics D: Applied Physics* **45** [50]: 505305 (2012).

12. M. Backman, M. Toulemonde, O. H. Pakarinen, N. Juslin, F. Djurabekova, K. Nordlund, A. Debelle, and W. J. Weber, "Molecular dynamics simulations of swift heavy ion induced defect recovery in SiC," *Computational Materials Science* **67** (2013) 261-265.
13. X. J. Wang, H. Y. Xiao, X. T. Zu, Y. Zhang, and W. J. Weber, "Ab initio molecular dynamics simulations of ion-solid interactions in Gd<sub>2</sub>Zr<sub>2</sub>O<sub>7</sub> and Gd<sub>2</sub>Ti<sub>2</sub>O<sub>7</sub>," *J. Materials Chemistry C* **1** (2013) 1665-1673.
14. M. Backman, F. Djurabekova, O. H. Pakarinen, K. Nordlund, Y. Zhang, M. Toulemonde, and W. J. Weber, "Atomistic simulations of MeV ion irradiations of silica," *Nucl. Instrum. and Methods in Physics Research B* (2013) in press. <http://dx.doi.org/10.1016/j.nimb.2012.10.020>
15. P. Liu, Y. Zhang, X. Wang, X. Xiang, and W. J. Weber, "Response Properties of YAlO<sub>3</sub>:Ce Scintillation Crystal under Ion Irradiation," *Nucl. Instrum. and Methods in Physics Research B* (2013) in press. <http://dx.doi.org/10.1016/j.nimb.2013.01.018>

## Investigating Deformation and Failure Mechanisms in Nanoscale Multilayer Metallic Composites

H. M. Zbib, Washington State University, Pullman, WA 99164-2920; zbib@wsu.edu  
D.F. Bahr, Purdue University, West Lafayette, IN, 47907; dfbahr@purdue.edu

**Scope:** In this investigation we are studying a new class of materials composed of trimetallic nanoscale multilayer metallic (NMM) composites comprising hybrid coherent/incoherent interfaces. Our investigation has involved the following: a) Fabricate and characterize the structure of trimetallic NMM composites (CuNiNb, MoPtNi, Ni/N-n, and Cr/Cu;) with minor interfacial impurities. b) Perform mechanical tests, including uniaxial and biaxial bulge fatigue, creep-fatigue, and monotonic tests of trimetallic NMM composites. c) Perform MD analyses of interface mechanics in trimetallic NMM; investigate possible interface imperfections and interface chemistry. d) Perform DD analysis of dislocation mechanisms in trimetallic NMM composites with/without radiation effects. e) Perform large scale analysis of interface crack-dislocations interaction using DD, under cyclic loading conditions.

### Recent Progress:

The result of our work has been reported in 34 publications and 4 more have been submitted. In summary, we have developed experimental methods, theoretical models and numerical techniques to study trimetallic NMM composites. Guided by results from molecular dynamics (MD) investigations as well as dislocation dynamics analyses (DD), multilayer thin films of CuNbNi with various layer thickness were fabricated at LANL and tested at WSU using bulge testing, microtensile and nanoindentation. The results (Figure 1) showed that the trimetallic system is stronger than the CuNi system, exhibits more strain hardening, displays ductile behavior, and can be as strong as the CuNb system at an optimum layer design - the optimum design is a trilayer CuNiNb system with a layer thickness scheme of 3nm/5nm/5nm respectively. Furthermore, this trimetallic system has high resistance to fatigue.

In order to explain the strengthening effects in the trilayer system that we have observed in our experimental work, a series of atomistic simulations of nanoindentation have been performed on several multilayer structures with different material composition, individual layer thicknesses and indenter radii and the results are reported in. Based on the MD simulations, we discovered that the presence of the Cu-Nb interface plays an important role on the plastic deformation of the NMM composites – it has shown its significance in both the surface pile-up deformation and the strain hardening effect of the NMM. First, for the surface deformation (pile-up and sink-in), the pile-up height is inversely related to the strain hardening rate. Two surface deformation mechanisms have been discovered, they are all affected by the presence of incoherent interfaces. Second, the hardening exponent of the NMM under nanoindentation is closely related to the shear deformation of the Cu/Ni-Nb interface. Such shear deformation, quantified by interfacial dislocation density  $\bar{\rho}$ , is mainly due to the dislocation-interface interactions. The amount of the shear deformation of such incoherent interfaces, in turn, is related to the effective thickness ( $h^*/R$ ) of the

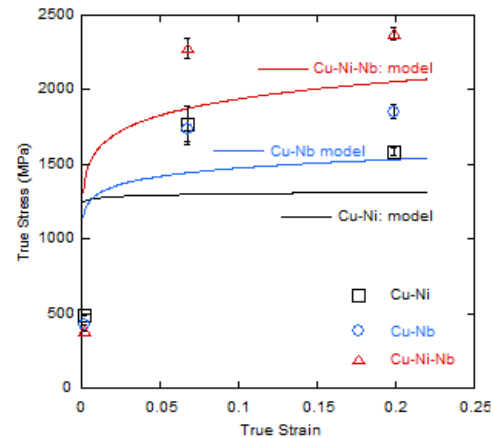


**Figure 1.** Effective flow stress at different strains for the three multilayered chemistries estimated using bulge testing and nanoindentation. Fits follow a power law model with fixed values of strain hardening exponents.

FCC layers. Based on these results we developed a constitutive for the hardness of the NMM composites taking the length scales, such as indenter radii and effective FCC layer thickness, as parameters, leading to a the following scaling relationship:  $\ln H^* = \ln H + \bar{\beta} \left( \frac{R}{h^*} \right)^m \ln(e^\alpha \varepsilon^{n_0})$ , suggesting that the hardness of a

Nb, Cu and (or) Ni based multilayer has an inverse power law dependence on the individual layer thickness, which is qualitatively consistent with recent experimental observations [A1, A15]. Although this model is constructed based on a very narrow range of material combinations and individual layer thicknesses, it should apply to most of the multilayers composed of fcc and bcc material with the similar stacking setup

These discoveries led us to investigate other bilayer and trilayer material systems (MoPtNi, Ni/Np-Au and CrCu), and consider developing more complex multilayer nanostructured metallic systems, NNM with nano-precipitates and into three-dimensional foams with nanolayered struts. We have shown first numerically through MD and DD simulations (Figure 2) and then experimentally (Figure 3), that by adding nano-precipitates within the NMM system one has the opportunity to further enhance strengthening and enlarge the design size-space.

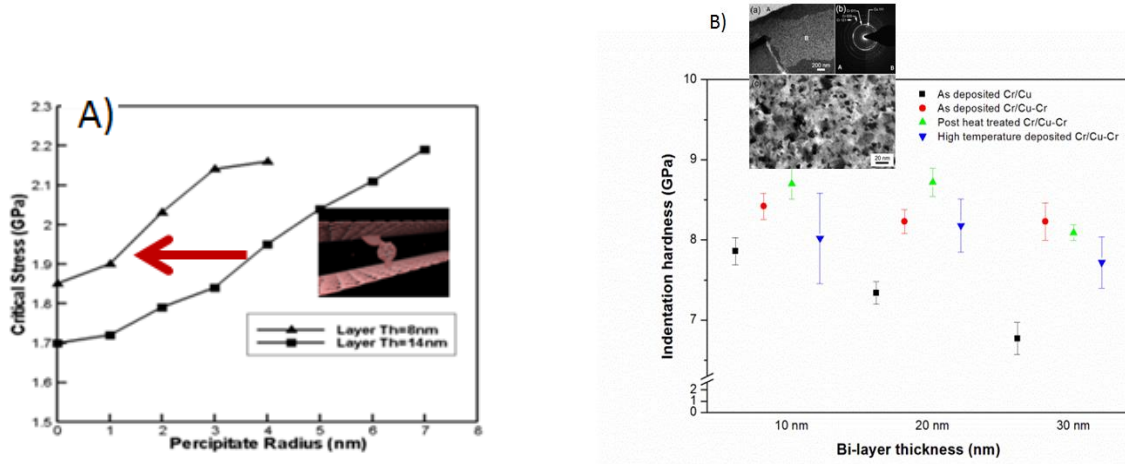


Figure 2. A) Critical stress as function of the precipitate size for two different structures, one with 8 nm and one with 14 nm copper layer thickness respectively. The arrow depicts the ability of the precipitates to strengthen the thicker structure to the point that it exhibits the same strength with a thinner structure without precipitates. B) Nanoindentation hardness of samples deposited at four different conditions having bi-layer thickness of 10 nm, 20 nm and 30 nm. Each data point is the mean hardness of more than 80 indentations. Inset: Bright field TEM image showing multilayer structure in a part of a 20nm as-deposited thin film.

To explain this strengthening effect we developed a model based on dislocation interaction with a rigid particle in a confined channel, yielding the analytical expression

$$\tau_{crit} = \frac{b\mu}{4\pi} \frac{[2 - \nu(1 - \cos\theta)]}{(1 - \nu)} \ln \left[ \frac{HD}{b^2} \left( \frac{H - D}{H + D} \right)^2 \right] \frac{1}{H - D}$$

where  $\mu$  is the shear modulus and  $\nu$  the Poisson ratio. In the limit as  $D/H \rightarrow 0$ , and  $D \rightarrow b$ , the equation reduces to the confined layer plasticity model. The upper limit based on this equation,  $D/H \rightarrow 1$ , e.g.  $D = H$  corresponds to the complete blockage of the channel by the precipitate and the stress becomes singular, corresponding to the breakdown of the elastic solution. However, the upper threshold is determined by the shear strength of the interface and or the precipitate as shown by the MD results. Moreover, this relation shows that both the channel width and the precipitate size control strength with

inverse dependence on the mean free path “ $H$ - $D$ ” and logarithmic dependence on both the channel width  $H$  and precipitate size  $D$ .

In the case of foam structures, we have shown, again first numerically then experimentally, that it is possible to increase the overall strength of nanoporous materials by forming a core-shell structure with composite ligaments. Specifically, adding thin layers of Ni onto a NP-Au foam can increase the strength of the film by approximately five times in the core-shell foam. The addition of Ni does not only impact the hardness, but also significantly decreases creep during the indentation process. The simulations have suggested these effects, and have been coupled with experimental studies to verify and drive new simulations as well as new experiments.

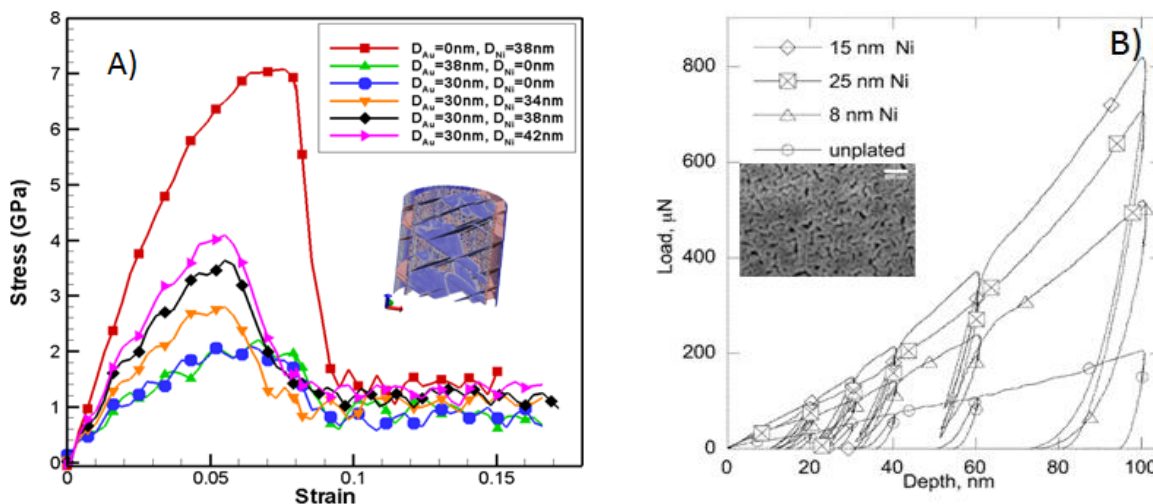


Figure 3. A) Stress-strain curves from MD simulated tensile behavior of pure Au and Au-Ni ligaments. Ligaments of pure Au at 30 and 38 nm diameters, as well as 30 nm of Au with plating thicknesses of 2, 4, and 6 nm are shown. There is no size effect demonstrated for pure Au; the behavior is independent of ligament thickness. Insert: Nucleation of dislocations from the interface of Au-Ni composite ligaments. Typical load-depth curves for indentations into NP-Au and Ni plated NP-Au for nominal plating thicknesses of 8, 15, and 25 nm on a ligament size of nominally 30 nm. Inset: Ni plated nanoporous gold, 10 nm of Ni on 50 nm thick ligaments.

### Future Plans

This year we are focusing on investigating the effect of interfacial impurities (chemistry and interfacial properties) temperature and atmosphere on NMM. Deposition with gaseous impurities (O and N) will be carried out on various NMM. To isolate the effects of impurities we use bilayers of CuNb, CuNi, NbNi, PtMo, MoNi, and NiPt. We continue to perform MD analyses of interface mechanics in trimetallic NMM to further investigate interface imperfections, interface chemistry, and irradiation damage.

As we move forward with this project, we intend to *design* a new type of metal/ceramic nanocomposites with engineered nanolaminate structures that will exhibit higher strength, self healing, high temperature tolerance, and thermal stability under harsh environments which has not been attempted. There are two fundamental issues that we intend to investigate to move this area of research forward: Understanding the interaction of the ceramic with the metal and the influence of the interface structure on the initial deformation of the metal. Understanding the influence the complex loading state has on the subsequent deformation of nanostructured systems.

List of publications of DOE sponsored research that have appeared in 2010-2012 or that have been accepted/submitted for publication.

1. Thermal stability and strength of Mo/Pt multilayered films, A. Bellou, L. Scudiero, D.F. Bahr, *Journal of Materials Science*, vol. 45, pp. 354-362 (2010) DOI:10.1007/s10853-009-3943-4.
2. Strength and aging behavior of Mo/Pt multilayers, A. Bellou, D.F. Bahr, *Journal of Materials Science*, vol. 46, pp. 108-116 (2011) DOI: 10.1007/s10853-010-4845-1.
3. Deformation mechanisms in nano-composite metallic structures. Mastorakos, I., Abdolrahim, N. and Zbib, H.M. *Int. J. Mechanical Science*, 52, 295-302, 2010.
4. Deformation mechanisms and pseudoelastic behavior in trilayer composite metal nanowires. Abdolrahim, N., Mastorakos, I and Zbib, H.M. *Physical Review B* 81, 054117, 2010.
5. Strain hardening behavior in nanolayered metallic multilayers. Bellou, A., C. Overman, Zbib, H.M. Bahr, D. and A. Misra. *Scripta Metallurgica*, 64, 641-644 (2011).
6. Size dependent strength in nanolaminate metallic systems. I.N. Mastorakos, A. Bellou, D.F. Bahr and H.M. Zbib, *Invited Feature Paper*, 26 (10), 1179 – 1187, 2011. Featured in *MRS Material 360 Newsletter*.
7. Analysis of plastic deformation in nanoscale metallic multilayers with coherent and incoherent interfaces. Zbib, H.M., Overman, C., Akasheh, F., Bahr, D.F. *Int. J. Plasticity*, 27, 1618-1623, 2011.
8. Challenges below the Grain Scale and Multiscale Models. Zbib, H.M. and Bahr. In: *Computational Methods for Microstructure-Property Relations*. In: *Computational methods for Microstructure-property relations*. Eds. Ghosh, S. and Dimiduk, D., Springer, 555-590, 2011.
9. Treating internal surfaces and interfaces in discrete dislocation dynamics. Mastorakos, I. N., Akasheh, F. E., and Zbib, H.M. *J. Mech, Behavior of Mater*, 20, 13-20, 2011.
10. Precipitate strengthening in nanometallic composites. Abdolrahim, N, Mastorakos, I. and Zbib, H.M. *Phil Mag Letters* 1-11, 2012. DOI:10.1080/09500839.2012.704153.
11. Interfacial Properties of Cu-Nb Multilayers as a Function of Dislocation/Disconnection Content. Abdolrahim, N., Mastorakos, I.N., Zbib, H.M., Bahr, D.F. In: *Volume 2; Materials Fabrication, Properties, Characterization and Modeling*. 75-82, TMS Annual Meeting Proceedings, 2011.
12. Deformation mechanisms, size effects, and strain hardening in nanoscale multilayered metallic composites under nanoindentation. Shao, S., Zbib, H.M., Mastorakos, I., Bahr, D.F. *J. Appl. Phys.*, 112, 044307, 2012.
13. The mechanical response of core-shell structures for nanoporous metallic materials. Bahr, D.F, Abdolrahim, N., Revard, B., Reilly, C., Balk, T.J., Zbib, H.M., *Phil Mag*, 1-13, 2012. DOI:10.1080/14786435.2012.731528
14. Effect of interfaces in the work hardening of nanoscale multilayer metallic composites during nanoindentation: A Molecular Dynamics Investigation. S. Shao, H.M. Zbib, D.F. Bahr and I.N. Mastorakos, *Journal of Engineering Materials and Technology*, in press, 2013.
15. The failure strengths of the Cu-Ni-Nb- based nanoscale metallic multilayers under high strain rate tensile loadings. Shao, S., Zbib, H.M., Mastorakos, I.N., and Bahr, D.F., *MSMSE*, submitted, 2012.
16. Multiscale modeling and simulation of deformation in nanoscale metallic multilayer systems. Abdolrahim, N., Zbib, H.M., and Bar, D.F. *Int. J. Plasticity*, submitted, 2013
17. Precipitation strengthening in nanocomposite Cr/Cu multilayer films. Wo, P.C., Abdolrahim, N., Zhu, Y., Mastorakos, I., Bahr, D.F., Zbib, H.M. submitted. *Phil Mag*, 2013.
18. The effect of interfacial geometry and chemistry on the strengthening of Nanoscale Multilayer Metallic Composites. I.N. Mastorakos, N. Abdolrahim, D.F. Bahr and H.M. Zbib, to be submitted to *Phil. Mag.*, 2013

# ***EFRC Abstracts***



## **EFRC Center for Materials Science of Nuclear Fuel**

Todd Allen, Director

Idaho National Laboratory, Idaho Falls, ID 83415

Partner Institutions

Oak Ridge National Laboratory, University of Florida, University of Wisconsin-Madison,  
Colorado School of Mines, Purdue University

### **Center Objectives**

The Center for Materials Science of Nuclear Fuel (CMSNF) has been established in 2009 as part of the U.S. Department of Energy's Energy Frontier Research Centers (EFRCs) program [1]. CMSNF is tasked with creating new knowledge on the connection between microstructure and thermal transport properties of oxide nuclear fuels. The center's effort is geared toward the development of a first-principles-based understanding of the impact of complex defect structure on thermal transport in irradiated nuclear fuel. The model material of interest is uranium dioxide,  $\text{UO}_2$ . The center's research is based on the premise that thermal transport in crystalline  $\text{UO}_2$  is a phonon-mediated process that is influenced by the scattering mechanisms associated with the defect disorder and microstructural changes caused by irradiation.

The thermal transport problem undertaken by the CMSNF team is tackled in steps. At the most basic level, a reference  $\text{UO}_2$  material (high-purity, stoichiometric  $\text{UO}_2$ ) is considered and a wide range of modeling and experimental tools are used to understand the physics of thermal transport within this material as a function of temperature, from room temperature to about 1200 K. Next,  $\text{UO}_2$  with an impurity representative of a solid fission product (e.g., cerium) and a noble gas is considered and the same thermal transport investigations are repeated. At this level, the complexity of irradiation-induced defect clusters or large microstructure features is avoided. Finally, the investigation of thermal transport in an irradiated material is carried out, considering the addition of the unique microstructural features.

The center brings together an internationally renowned, multi-institutional team of experimentalists and computational materials theorists from Idaho National Laboratory, Oak Ridge National Laboratory, Colorado School of Mines, University of Florida, University of Wisconsin-Madison, and Purdue University. This team of experimentalists and theoreticians has established a unique paradigm of integrating theory and experiments to understand the physics of thermal transport in oxides with complex microstructure, such as irradiated  $\text{UO}_2$ .

### **Research Highlights**

The research goals of CMSNF are:

- To develop an understanding of the impact of complex defect structures on thermal transport in irradiated oxide fuel from first principles.
- To achieve the above for the case of irradiation induced defects in oxide fuel, which will also achieve a first-principles-based understanding of the effects of irradiation on stoichiometry and microstructure in oxide fuel.

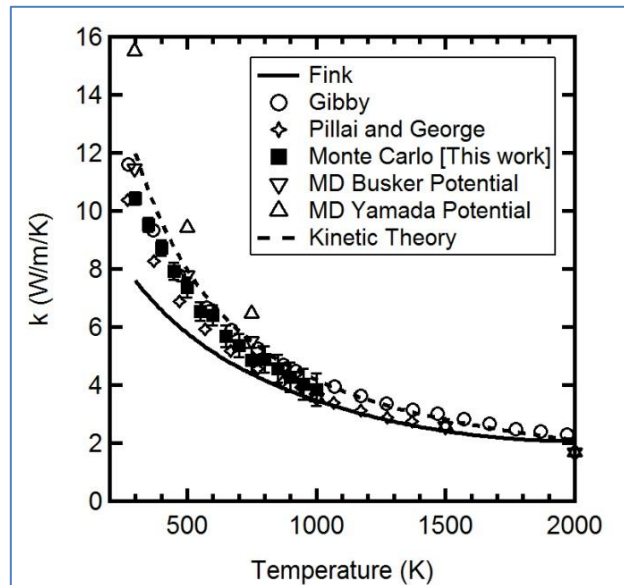
- By reaching the above two goals through a program of combined theory and experiment, the center will also establish a new research direction that integrates the physics of thermal transport and the physics of defect and microstructure in irradiated oxide fuel.

Some research highlights illustrating the progress toward these objectives are given below.

### 1. Anharmonicity and Thermal Transport in $\text{UO}_2$

A central goal of CMSNF is to build a predictive capability for thermal transport based on phonon dynamics in  $\text{UO}_2$ , by solving Boltzmann transport equation (BTE) for phonons. This capability will ultimately be used to predict the collective phonon dynamics in  $\text{UO}_2$  with complex microstructure. A robust Monte Carlo (MC) solver of BTE has been developed and tested for defect-free single crystals [2]. This solver is now being generalized to  $\text{UO}_2$  with defects. Figure 1 shows the predicted thermal conductivity of  $\text{UO}_2$  from phonon dynamics. In parallel, neutron scattering and density functional theory were used to, respectively, measure and calculate the dispersion curves and phonon lifetime [3]. Phonon lifetime, which is used as input to the MC/BTE approach, captures the anharmonic effects in crystals. The dispersion relations measured at different temperatures enable the determination of the branch-specific Grüneisen parameter, which is a fundamental property of crystals. The availability of both Grüneisen parameter and phonon lifetime data obtained from neutron scattering allows us to confront the predictions of the classical perturbation theory [4] with experiments at the level of phonon lifetime for the first time. This task is currently underway.

**Figure 1. Temperature dependence of  $\text{UO}_2$  thermal conductivity as predicted by a Monte Carlo solution of Boltzmann transport equation [2].**



### 2. Effect of Microstructure on Thermal Transport

A critical part of our thermal transport investigations focuses on the prediction and measurement of the effect of defects and microstructure on thermal conductivity in  $\text{UO}_2$  and surrogate materials. Several measurements of the conductivity of film and bulk configurations using laser based modulated thermo-reflectance technique were already performed [5]. Of particular interest, however, is the deterioration of thermal conductivity as a result of phonon scattering by irradiation-induced microstructure. A recent post-irradiation investigation

performed on surrogate ceria samples confirms the detrimental effect of dislocation loops and voids; see figure 2. Establishing the connection between such measurements and MC/BTE framework is now underway to reveal the relative contributions of these phonon scatterers. The effect of dislocations on conductivity has been already predicted by molecular dynamics [6].

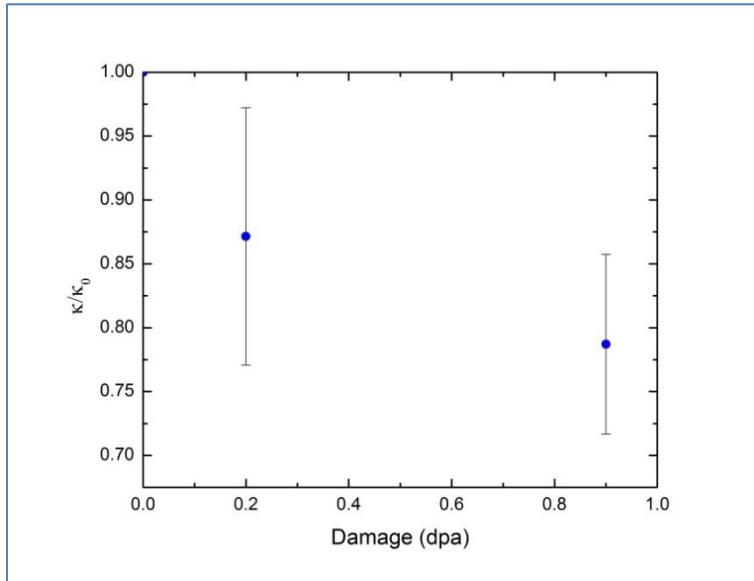


**Figure 2. Preliminary assessment of conductivity reduction in He-irradiated ceria as a function of dpa. The dislocation loops, voids and point defects proved to be efficient phonon scatterers even at modest levels of damage [Marat Khafizov, INL].**

### 3. Electrochemical Effects of Microstructure in $UO_2$

CMSNF researchers have discovered that charged point defects form clouds around surfaces and voids in  $UO_2$ , resulting in strong spatial variations in local off-stoichiometry in the material. This discovery was made in connection with investigating the thermodynamic basis of defect disorder in single crystals. The thermodynamic framework used to make this discovery also led to the observation that voids in  $UO_2$  must contain oxygen gas. Because of the abundance of oxygen in  $UO_2$  and the enhanced mobility of oxygen atoms under irradiation, this important finding is judged to be extremely relevant to explaining the possible stabilization of voids in  $UO_2$  by oxygen in the absence of fission gases [7]. If proven, this will change a long history of hypotheses in investigating fission-gas bubble formation and related swelling irradiated fuel.

### 4. Irradiation-Induced Microstructure in $UO_2$

Obtaining experimental data on the formation of dislocation loops and fission-gas bubbles is a critical part of CMSNF investigation for two purposes, gathering information on the salient features of microstructure evolution, both during irradiation and annealing, and providing data for model validation. Irradiation of  $UO_2$  and  $CeO_2$  using a variety of ions (H, He, Kr and Xe) has already been performed and a great deal of data was obtained in these systems. Figure 3 shows a sample result for dislocation loop formation in Kr-irradiated  $CeO_2$ . Dislocation loops were found to grow quickly at low ion dose, transform to segments as dose increases, and finally transform to dislocation networks at higher doses through coalescence/coarsening mechanisms. Irradiated samples are now being characterized chemically and thermally and the microstructure observations are being connected with defect chemistry and microstructure evolution models.

## 5. Other Important Research Areas

Additional investigations carried out as part of the center's research include molecular dynamics simulation of defect clusters and their diffusion [8], atom probe measurement of local off-stoichiometry and fission gas distribution in  $\text{UO}_2$  and  $\text{CeO}_2$ , the synthesis of  $\text{UO}_2$  polycrystalline films using magnetron sputtering, and grain growth experiments and modeling.

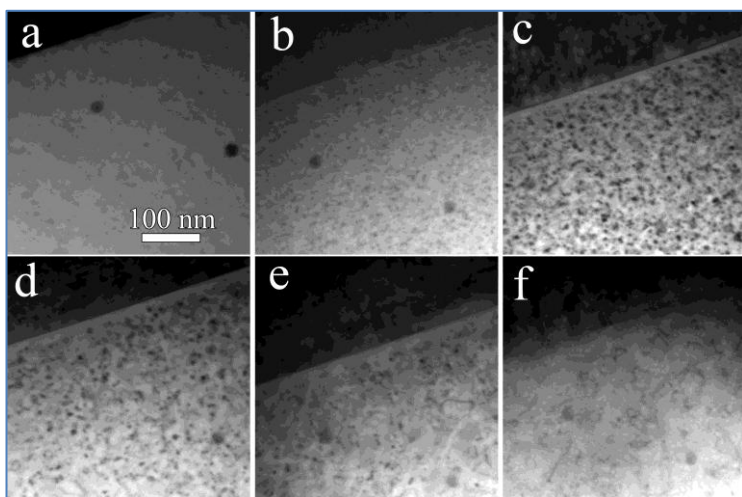


**Figure 3. TEM images showing the nucleation and growth of loops in  $\text{UO}_2$  irradiated with 1 MeV Kr at 800 °C. (a) un-irradiated, (b)  $5 \times 10^{14}$ , (c)  $1 \times 10^{15}$ , (d)  $2 \times 10^{15}$ , (e)  $3 \times 10^{15}$ , (f)  $5 \times 10^{15}$  ions/cm<sup>2</sup> (observations along [111] direction with  $g_{220}$  reflection) [Lingfeng He, UW].**

## Acknowledgement

This material is based on work supported as part of the Center for Materials Science of Nuclear Fuel, an Energy Frontier Research Center funded by the U.S. Department of Energy, Office of Basic Energy Sciences under award number FWP 1356.

## References

1. Energy Frontier Research Centers (EFRCs); see <http://science.energy.gov/bes/efrc/>.
2. WR Deskins and A El-Azab, Monte Carlo simulation of phonon transport in  $\text{UO}_2$  single crystals, *Modell Simul Mater Sci Engng*, in the press
3. JWL Pang, WJL Buyers, A Chernatynskiy, MD Lumsden, BC Larson and SR Phillpot, Phonon lifetime investigation of anharmonicity and thermal conductivity in  $\text{UO}_2$  by neutron scattering and theory, *Phys Rev Lett*, submitted
4. PG Klemens, in: *Solid State Physics* vol 7 ed F Seitz and D Turnbull (1958) 1.
5. Khafizov et al, Thermal conductivity of nanocrystalline ceria films, *J Amer Ceram Soc*, submitted
6. B Deng, A Chernatynskiy, P Shukla, SB Sinnott, SR Phillpot, *J Nucl Mater* (2012) doi: <http://dx.doi.org/10.1016/>
7. A-R Hassan, A El-Azab, C Yablinsky and TR Allen, Defect disorder in  $\text{UO}_2$ , *J Solid State Chem*, submitted.
8. XM Bai, A El-Azab, J Yu, TR Allen, Migration mechanisms of oxygen interstitial clusters in  $\text{UO}_2$ , *J Phys: Cond Matter* 25 (2013) 015003

## **EFree – An Energy Research Frontier Center**

Executive Committee: H-k Mao<sup>1</sup> (EFree Director), R.J. Hemley<sup>1</sup> (Assoc. Director), S. Gramch<sup>1</sup> (Managing Director), J. Badding<sup>2</sup>, R. Boehler<sup>1</sup>, M. Guthrie<sup>1</sup> & V. Struzhkin<sup>1</sup> (Science Thrust Leaders), S. Mysen (Project Administrator)

Contact: mguthrie@ciw.edu

<sup>1</sup> *Geophysical Laboratory, 5251 Broad Branch Rd, NW, Washington DC 20015.*

<sup>2</sup> *Pennsylvania State University, University Park, PA 16802.*

The Center for Energy Frontier Research in Extreme Environments (EFree) is an Energy Frontier Research Center (EFRC) that is focused on fundamental materials research under extreme conditions. In EFree, high pressures and temperatures are used to explore structure/property relationships by making structure the experimental variable. Extreme conditions are also used to synthesize new materials with optimal properties for energy applications. The science of the Center spans three broad Thrust Areas: Chemical Energy, Electromagnetic Frontiers, and Structural Limits of Performance. A fourth technical thrust, supports the scientific thrust by delivering state-of-the-art experimental capabilities to underpin the scientific research. We will present recent research highlights that demonstrate the powerful utility of extreme conditions research for energy-focused material science.

**Center for Materials at Irradiation and Mechanical Extremes (CMIME),  
an Energy Frontier Research center**

Los Alamos National Laboratory	A. Misra (Director), I.J. Beyerlein (Co-Director), <u>Co-investigators</u> : B.P. Uberuaga (team leader), N.A. Mara (team leader), J.A. Caro, S.M. Valone, E.K. Cerreta, T.C. Germann, G.T. Gray, Q. Jia, S.A. Maloy, A.F. Voter.
Carnegie Mellon University, Pittsburgh	<u>Co-investigator</u> : A.D. Rollett
University of Illinois, Urbana Champaign	<u>Co-investigators</u> : R.S. Averback, P. Bellon
MIT, Cambridge, MA	<u>Co-investigator</u> : M.J. Demkowicz (team leader)
University of Nebraska, Lincoln	<u>Co-investigator</u> : M. Nastasi

*Mission Statement: To understand, at the atomic scale, the interactions of defects at interfaces in materials subjected to extreme radiation doses and mechanical stress in order to synthesize new interface-dominated materials with tailored response under such extreme conditions.*

The challenge to developing materials with radically extended performance limits at irradiation and mechanical extremes will require designing and perfecting atom- and energy- efficient syntheses of revolutionary new interface-dominated materials where the atomic structures of the interfaces are used to tailor the interactions of point and line defects with interfaces and hence, the macroscopic material properties. The key deliverables from this research program will be quantitative relationships between the atomic structure and energetics of interfaces and radiation or mechanical damage evolution in materials. These quantitative relations are *figures-of-merit* that can be used to rank different solid-solid interfaces in terms of the ability of an interface to control defect evolution.

CMIME has two thrust areas in *irradiation extremes* and *mechanical extremes* respectively. The irradiation extremes thrust studies a range of radiation damage phenomena relevant to fusion and fission energy over a broad range of metal-metal, metal-oxide and oxide-oxide interfaces. The mechanical extremes thrust explores severe plastic deformation processing such as accumulative roll bonding (ARB) to design nanocomposites with interfaces that are crystallographically and morphologically stable at large plastic strains. The behavior of these ARB-processed nanocomposites is explored in a variety of conditions such as shock, high-pressure torsion, irradiation, fatigue, etc. Besides ARB, physical vapor deposition is used to synthesize model bi-layer or multi-layer systems for ion irradiation studies. Given the focus on mechanistic understanding at the level of atomic structure of interfaces, we study model systems such as Cu-Nb, Cu-Ag, SrTiO<sub>3</sub>-TiO<sub>2</sub>, etc where accurate interatomic potentials are available so that experimental results can be integrated with theory. For other more complex systems such as metal-oxide (Fe-Y<sub>2</sub>O<sub>3</sub>, Fe-TiO<sub>2</sub>, etc) efforts are underway to develop charge-transfer based interatomic potentials. Likewise for long-time-scale simulation defect cluster evolution, method development activities involve atomistically-informed kinetic Monte Carlo approaches.

# ***Author Index***



## Author Index

Allen, Todd.....	135, 167	King, William.....	9
Allison, John.....	1	Koslowski, Marisol .....	58
Anderson, P. M.....	82	Kramer, Matthew.....	66
Averback, Robert.....	9	Kumar, Mukul .....	62
Badding, J.....	171	Lagrange, Thomas .....	62
Bahr, D. F. ....	163	Lang, Maik .....	39
Baker, I. ....	5	LeSar, Richard.....	66
Bei, H.....	43	Li, Q.....	78
Bellon, Pascal .....	9	Li, Qizhen.....	70
Bernier, Joel.....	62	Li, Shiu Fai .....	62
Beyerlein, I. J.....	172	Lienert, Ulrich .....	74
Bieler, Thomas R.....	13	Mao, H-k .....	171
Boehler, R.....	171	Mason, Jeremy.....	62
Boehlert, Carl J.....	13	Mendelev, Mikhail .....	66
Boyce, B. L.....	17	Miller, Matt .....	74
Bruemmer, Stephen M. ....	18	Miller, Michael K.....	78
Bulatov, Vasily .....	62	Mills, M. J. ....	78, 82
Carter, W. Craig .....	147	Misra, Amit .....	86, 172
Castro, Ricardo.....	22	Morgan, Dane.....	135
Chiang, Yet M.....	147	Morris, J. R.....	43
Ciobanu, Cristian.....	102	Müllner, Peter.....	90
Clark, B. G.....	17	Mysen, S.....	171
Crimp, Martin A.....	13	Nix, William D.....	94
Curtin, William A.....	123	Obstalecki, Mark .....	74
Daly, Samantha .....	26	Olszta, Matthew J.....	18
Dauskardt, Reinhold H.....	30	Osetskyy, Y. N. ....	43
Dawson, Paul.....	74	Ott, Ryan .....	66
Demkowicz, Michael J.....	34	Parish, C. M.....	78
Dillon, Shen.....	9	Park, Jun-Sang.....	74
Dunand, David C.....	35	Pharr, G. M.....	43
Edmondson, P. D.....	78	Raj, Rishi .....	98
Ewing, Rodney C. ....	39	Rajan, Krishna .....	66
Farkas, Diana.....	155	Reed, Bryan .....	62
Foiles, S. M. ....	17	Reimanis, Ivar .....	102
Fu, C. L.....	78	Riedo, Elisa .....	106
Gao, Y. F. ....	43	Ritchie, Robert O.....	110
George, E. P.....	43	Robertson, Ian M.....	155
Gianola, Daniel S. ....	47	Rollett, Anthony .....	66
Gramch, S.....	171	Rosso, Kevin M.....	18
Greer, Julia .....	51	Schreiber, Daniel K.....	18
Guthrie, M. ....	171	Schroers, Jan.....	114
Hattar, K. M.....	17	Seidman, David N. ....	35
Hemker, Kevin .....	54	Sethna, James P.....	115
Hemley, R. J.....	171	Shao, Lin .....	119
Holm, E. A.....	17	Sharon, J. A. ....	17
King, Alexander .....	66	Sheldon, Brian W. ....	123

Sieradzki, Karl.....	127
Sridharan, Kumar .....	135
Strachan, Alejandro .....	131
Struzhkin, V.....	171
Szlufarska, Izabela.....	135
Taheri, Mitra.....	139
Tang, Ming .....	62
Tomé, Carlos N. ....	143
Tomsia, Antoni P.....	110
Trinkle, Dallas .....	9
Tuller, Harry L. ....	147
Van Vliet, Krystyn J.....	147
Viswanathan, G. B.....	78
Vitek, V. ....	151
Wang, Chongmin.....	18
Wang, X.-L.....	78
Wang, Y.....	82
Was, Gary S.....	18, 155
Weber, William J.....	159
Williams, Jim.....	74
Wolverton, Chris .....	35
Wong, Su Leen .....	74
Yao, L.....	78
Yildiz, Bilge .....	147
Yip, Sidney.....	147
Zbib, H. M.....	163
Zhang, Y.....	78
Zhang, Z. W.....	78

# ***Participant List***



## Participant List

Name	Organization	E-Mail Address
Allison, John	University of Michigan	johnea@umich.edu
Bahr, David	Purdue University	dfbahr@purdue.edu
Baker, Ian	Dartmouth College	ian.baker@dartmouth.edu
Bellon, Pascal	University of Illinois	bellon@illinois.edu
Beyerlein, Irene	Los Alamos National Laboratory	irene@lanl.gov
Boehlert, Carl	Michigan State University	boehlert@egr.msu.edu
Boyce, Brad	Sandia National Laboratories, New Mexico	blboyce@sandia.gov
Bruemmer, Stephen	Pacific Northwest National Laboratory	stephen.bruemmer@pnl.gov
Castro, Ricardo	University of California, Davis	rhrcastro@ucdavis.edu
Christen, Hans	Oak Ridge National Laboratory	christenhm@ornl.gov
Click, Tammy	Oak Ridge Institute for Science and Education	tammy.click@orise.orau.gov
Crockett, Teresa	U.S. Department of Energy	teresa.crockett@science.doe.gov
Daly, Samantha	University of Michigan	samdaly@umich.edu
Dauskardt, Reinhold	Stanford University	dauskardt@stanford.edu
Dawson, Paul	Cornell University	prd5@cornell.edu
Demkowicz, Michael	Massachusetts Institute of Technology	demkowicz@mit.edu
Dunand, David	Northwestern University	dunand@northwestern.edu
Easo, George	Oak Ridge National Laboratory	georgeep@ornl.gov
El-Azab, Anter	Purdue University	aelazab@purdue.edu
Ewing, Rodney	University of Michigan	rodewing@umich.edu
Foiles, Stephen	Sandia National Laboratories, New Mexico	foiles@sandia.gov
Gianola, Daniel	University of Pennsylvania	gianola@seas.upenn.edu
Greer, Julia	California Institute of Technology	jrgreer@caltech.edu
Guthrie, Malcolm	Efree, Geophysical Laboratory	mguthrie@ciw.edu
Hemker, Kevin	Johns Hopkins University	hemker@jhu.edu
Horton, Linda	U.S. Department of Energy	linda.horton@science.doe.gov
Jiang, Chao	University of Wisconsin at Madison	cjiang32@wisc.edu
Koslowski, Marisol	Purdue University	marisol@purdue.edu
Kumar, Mukul	Lawrence Livermore National Laboratory	mukul@llnl.gov
Lang, Maik	University of Michigan	mklang@umich.edu
LeSar, Richard	Ames Laboratory / Iowa State University	lesar@iastate.edu
Li, Qizhen	University of Nevada, Reno	qizhenl@unr.edu
Marzouk, Youssef	Massachusetts Institute of Technology	ymarz@mit.edu
Miller, Matthew	Cornell University	mpm4@cornell.edu
Miller, Michael	Oak Ridge National Laboratory	millermk@ornl.gov
Mills, Michael	The Ohio State University	Mills.108@osu.edu

Misra, Amit	Los Alamos National Laboratory	amisra@lanl.gov
Mullner, Peter	Boise State University	petermullner@boisestate.edu
Naglieri, Valentina	Lawrence Berkeley National Laboratory	vnaglieri@lbl.gov
Nix, William	Stanford University	nix@stanford.edu
Ott, Ryan	Ames Laboratory	rtott@ameslab.gov
Parish, Chad	Oak Ridge National Laboratory	parishcm@ornl.gov
Pharr, George	Univ. of Tennessee /Oak Ridge National Laboratory	pharr@utk.edu
Piccione, Brian	University of Pennsylvania	bpic@seas.upenn.edu
Raj, Rishi	University of Colorado at Boulder	rishi.raj@colorado.edu
Reed, Bryan	Lawrence Livermore National Laboratory	reed12@llnl.gov
Reimanis, Ivar	Colorado School of Mines	reimanis@mines.edu
Riedo, Elisa	Georgia Institute of Technology	elisa.riedo@physics.gatech.edu
Ritchie, Robert	Lawrence Berkeley National Laboratory	roritchie@lbl.gov
Rottmann, Paul	Johns Hopkins University	paul.rottman@jhu.edu
Schreiber, Daniel	Pacific Northwest National Laboratory	daniel.schreiber@pnl.gov
Schroers, Jan	Yale University	jan.schroers@yale.edu
Sethna, James	Cornell University	sethna@lassp.cornell.edu
Shao, Lin	Texas A&M University	lshao@tamo.edu
Shekhawat, Ashivni	Cornell University	as2249@cornell.edu
Sheldon, Brian	Brown University	Brian_Sheldon@brown.edu
Sieradzki, Karl	Arizona State University	karl.sieradzki@asu.edu
Strachan, Alejandro	Purdue University	strachan@purdue.edu
Szlufarska, Izabela	University of Wisconsin	szlufarska@wisc.edu
Sundararaghavan, Veera	University of Michigan, Ann Arbor	veeras@umich.edu
Taheri, Mitra	Drexel University	mtaheri@coe.drexel.edu
Tome, Carlos	Los Alamos National Laboratory	tome@lanl.gov
Vetrano, John	U.S. Department of Energy	john.vetrano@science.doe.gov
Vitek, Vaclav	University of Pennsylvania	vitek@seas.upenn.edu
Wang, Jian	Los Alamos National Laboratory	wangj6@lanl.gov
Was, Gary	University of Michigan	gsw@umich.edu
Wat, Amy	Lawrence Berkeley National Laboratory	awat@lbl.gov
Weber, William	Oak Ridge National Laboratory	weberwj@ornl.gov
Wilk, Philip	U.S. Department of Energy	philip.wilk@science.doe.gov
Woodford, William	Massachusetts Institute of Technology	woodford@mit.edu
Yildiz, Bilge	Massachusetts Institute of Technology	byildiz@mit.edu
Zbib, Hussein	Washington State University	zbib@wsu.edu
Zhang, Chen	Michigan State University	zhangc43@egr.msu.edu
Zhang, Yanwen	Oak Ridge National Laboratory	zhangy1@ornl.gov